MODELING AND CONTROL OF A DOUBLY-FED INDUCTION GENERATOR FOR WIND TURBINE-GENERATOR SYSTEMS

by

Xin Jing

A Thesis submitted to the Faculty of the Graduate School,
Marquette University,
in Partial Fulfillment of the Requirements for
the Degree of Master of Science

Milwaukee, Wisconsin

December 2012

ABSTRACT

MODELING AND CONTROL OF A DOUBLY-FED INDUCTION GENERATOR FOR WIND TURBINE-GENERATOR SYSTEMS

Xin Jing, M.S.E.E

Marquette University, 2012

Wind energy plays an increasingly important role in the world because it is friendly to the environment. During the last decades, the concept of a variable-speed wind turbine (WT) has been receiving increasing attention due to the fact that it is more controllable and efficient, and has good power quality. As the demand of controllability of variable speed WTs increases, it is therefore important and necessary to investigate the modeling for wind turbine-generator systems (WTGS) that are capable of accurately simulating the behavior of each component in the WTGS. Therefore, this thesis will provide detailed models of a grid-connected wind turbine system equipped with a doubly-fed induction generator (DFIG), which includes the aerodynamic models of the wind turbine, the models of the mechanical transmission system, the DFIG models and the three-phase two-level PWM voltage source converter models.

In order to obtain satisfying output power from the WTGS, control strategies are also necessary to be developed based on the previously obtained WTGS models. These control schemes include the grid-side converter control, the generator-side converter control, the maximum power point tracking control and the pitch angle control. The grid-side converter controller is used to keep the DC-link voltage constant and yield a unity power factor looking into the WTGS from the grid-side. The generator-side converter controller has the ability of regulating the torque, active power and reactive power. The maximum power point tracking control is used to provide the reference values for the active power at the stator terminals. The pitch angle control scheme is used to regulate the pitch angle and thus keep the output power at rated value even when the wind speed experiences gusts.

Various studies in the literature have reported that two-level converters have several disadvantages compared with three-level converters. Among the disadvantages are high switching losses, high dv/dt, and high total harmonic distortion (THD). Hence, the models and field oriented control schemes for three-level neutral-point-clamped (NPC) converters are also investigated and applied to a WTGS. Besides, an advanced modulation technology, namely, space vector PWM (SVPWM), is also investigated and compared to traditional sinusoidal PWM in a WTGS.

ACKNOWLEDGMENTS

Xin Jing, M.S.E.E

I wish to express special gratitude to my family members for their encouragement, support and belief in me all these years. Also, I would like to thank my wife, Qianqian, for her understanding, support, patience, belief in me and true love. Moreover, I would like to dedicate this work to the memory of my father, Zhensheng, who gave me life, taught me about life, gave me support, believed in and encouraged me all these years; may he rests in peace.

I would like to express my sincerely appreciation to my advisor, Prof. Nabeel A.O. Demerdash, for his supervision, and for the valuable knowledge that he shared with me. I have learned valuable lessons from his wisdom, carefulness, and visions.

I would like also to express my sincerely appreciation to my committee members, Prof. Dan M. Ionel, Prof. Edwin E. Yaz and Prof. Susan C. Schneider for their time dedicated to examine and review my work and also for their valuable feedback, as well as useful suggestions that helped to make this thesis a more complete document.

Finally, I wish to express special thanks to my laboratory team-mates and friends, Jiangbiao He, Peng Zhang, Gennadi Y. Sizov and Alia Manarik, for their enjoyable discussions, valuable comments and assistance in my research work.

TABLE OF CONTENTS

TABLE OF CONTENTS

LIST OF TABLES

LIST OF FIGURES

LIST OF SYMBOLS AND ACRONYMS

WTGS	Wind turbine-generator systems
WT	Wind turbine
DFIG	Doubly-fed induction generator
THD	Total harmonic distortion
PWM	Pulse-width modulation
DPC	Direct power control
VSC	Voltage source converter
SVPWM	Space vector PWM
PMSG	Permanent magnet synchronous generator
MPPT	Maximum power point tracking
FOC	Field oriented control
DTC	Direct torque control
IGBT	Insulated-gate bipolar transistor
NPC	Neutral-point-clamped
VSI	Voltage source inverter
$P_{\omega t}$	The captured power of the wind turbine
ρ	Air density
R	Rotor blade radius
v_{ω}	Wind speed

C_p	Power coefficient of a wind turbine
β	Pitch angle
λ	Tip speed ratio
J_{B1}, J_{B2}, J_{B3}	Three blade inertias
J_H	Hub inertia
J_{GB}	Gearbox inertia
J_G	Generator inertia
K_{HB}	Spring constant between the hub and the blade
K_{HGB}	Spring constant between the hub and the gearbox
K_{GBG}	Spring constant between the gearbox and the generator
d_{HB}	Mutual damping between the hub and the blade
d_{HGB}	Mutual damping between the hub and the gearbox
d_{GBG}	Mutual damping between the gearbox and the generator
D_{B1}, D_{B2}, D_{B3}	Self-damping of the three blades
D_H	Self-damping of the hub
D_{GB}	Self-damping of the gearbox
D_G	Self-damping of the generator
T_{B1}, T_{B2}, T_{B3}	Three individual aerodynamic torques acting on the three blades
T_G	Generator torque
$\theta_{B1}, \theta_{B2}, \theta_{B3}, \theta_H, \theta_{GB}, \theta_G$	Angular positions of the three blades, the hub, the gearbox and the generator

$\omega_{B1}, \omega_{B2}, \omega_{B3}, \omega_H, \omega_{GB}, \omega_G$	Angular velocities of the three blades, the hub, the gearbox and the generator
J_{wt}	Combined wind turbine inertia
D_{wt}	Combined wind turbine self-damping
T_w	Combined wind turbine torque
θ_{wt}	Angular positions of the combined wind turbine
ω_{wt}	Angular velocities of the combined wind turbine
J_G^{2m}	Combined generator inertia
K_{2m}	Spring constant between the combined wind turbine and the combined generator
D_G^{2m}	Combined generator self-damping
d_{2m}	Mutual damping between the combined wind turbine and the combine generator
θ_G^{2m}	Angular positions of the combined generator
ω_G^{2m}	Angular velocities of the combined generator
S_B	Base power (VA)
ω_0	Base electrical angular velocity (rad/s)
P	Number of pole of the generator
N_{GB}	Gearbox speed ratio
ω_B'	Base mechanical speed (rad/sec) at the high-speed side
T_B'	Base torque (Nm) at the high-speed side
θ_B'	Base mechanical angle (rad) at the high-speed side

J'_B	Base inertia (Nm/(rad/sec)) at the high-speed side
K'_B	Base stiffness coefficient (Nm/(rad/sec)) at the high-speed side
D'_B, d'_B	Base damping coefficient (Nm/(rad/sec)) at the high-speed side
σ	Angle between the magnetic axes of stator phase winding, A, and rotor phase winding, a,
ω_r	Speed of the rotor
v_A, v_B, v_C	Terminal voltages of the stator
v_a, v_b, v_c	Terminal voltages of the rotor
i_A, i_B, i_C	Stator phase currents in the ABC reference frame
i_a, i_b, i_c	Rotor phase currents in the ABC reference frame
r_s	Resistance of a stator phase winding
r_r	Resistance of a rotor phase winding
L_{ss}	Self-inductance of a stator phase winding
L_{sm}	Mutual inductance between any two stator phase windings
L_{rr}	Self-inductance of a rotor phase winding
L_{rm}	Mutual inductance between any two rotor phase windings
L_{srm}	Maximum mutual-inductance between the stator phase windings and rotor phase windings
$\underline{V}_{ABC}$	Stator voltage vector
$\underline{V}_{abc}$	Rotor voltage vector

$\underline{I}_{ABC}$	Stator current vector
$\underline{I}_{abc}$	Rotor current vector
$\underline{\Lambda}_{ABC}$	Stator flux linkage vector
$\underline{\Lambda}_{abc}$	Rotor flux linkage vector
$\underline{R}_{ss}$	Stator resistance matrix
$\underline{R}_{rr}$	Rotor resistance matrix
$\underline{L}_{ss}$	Stator self and mutual inductance matrix
$\underline{L}_{ss}$	Rotor self and mutual inductance matrix
$\underline{L}_{sr}$	Mutual inductance matrix between stator and rotor phase windings
$\underline{T}_{sro}$	Stator transformation matrix for the reference frame fixed on the rotor
$\underline{T}_{rro}$	Rotor transformation matrix for the reference frame fixed on the rotor
$v_{Dro}, v_{Qro}, v_{Oro}$	Stator terminal voltages expressed in the DQO rotor reference frame
$v_{dro}, v_{qro}, v_{oro}$	Rotor terminal voltages expressed in the dqo rotor reference frame
$i_{Dro}, i_{Qro}, i_{Oro}$	Stator phase currents expressed in DQO rotor reference frame
$i_{dro}, i_{qro}, i_{oro}$	Rotor phase currents expressed in dqo rotor reference frame

$\underline{T}_{sst}$	Stator transformation matrix for the stationary stator reference frame
$\underline{T}_{rst}$	Rotor transformation matrix for the stationary stator reference frame
$v_{Dst}, v_{Qst}, v_{Ost}$	Stator terminal voltages expressed in the DQO stationary stator reference frame
$v_{dst}, v_{qst}, v_{ost}$	Rotor terminal voltages expressed in the dqo stationary stator reference frame
$i_{Dst}, i_{Qst}, i_{Ost}$	Stator phase currents expressed in DQO stationary stator reference frame
$i_{dst}, i_{qst}, i_{ost}$	Rotor phase currents expressed in dqo stationary stator reference frame
ω_s	Synchronous speed
$\underline{T}_s$	Stator transformation matrix for the synchronously rotating reference frame
$\underline{T}_r$	Rotor transformation matrix for the synchronously rotating reference frame
v_D, v_Q, v_O	Stator terminal voltages expressed in the DQO synchronously rotating reference frame
v_d, v_q, v_o	Rotor terminal voltages expressed in the dqo synchronously rotating reference frame
i_D, i_Q, i_O	Stator phase currents expressed in DQO synchronously

	rotating reference frame
i_d, i_q, i_o	Rotor phase currents expressed in dqo synchronously rotating reference frame
ω_{rm}	Mechanical rotational speed
T_{dev}	Develop torque
P_s	Active power of the DFIG
Q_s	Reactive power of the DFIG
$v_{ds}, i_{ds}, \lambda_{ds}$	Stator d-axis terminal voltage, current and flux linkage in the fourth order model expressed in the synchronously rotating reference frame
$v_{qs}, i_{qs}, \lambda_{qs}$	Stator q-axis terminal voltage, current and flux linkage in the fourth order model expressed in the synchronously rotating reference frame
$v_{dr}, i_{dr}, \lambda_{dr}$	Rotor d-axis terminal voltage, current and flux linkage in the fourth order model expressed in the synchronously rotating reference frame
$v_{qr}, i_{qr}, \lambda_{qr}$	Rotor d-axis terminal voltage, current and flux linkage in the fourth order model expressed in the synchronously rotating reference frame
L_s	Stator leakage inductance
L_r	Rotor leakage inductance
L_m	Magnetizing inductance

$e_a(t), e_b(t), e_c(t)$	Voltage sources of a three-phase PWM rectifier
R_g	AC side resistance of a three-phase PWM rectifier
L_g	AC side inductance of a three-phase PWM rectifier
i_{ag}, i_{bg}, i_{cg}	Input currents of a three-phase PWM rectifier
C	DC-link capacitor of a three-phase PWM rectifier
R_L	Load resistance of a three-phase PWM rectifier
i_{dc}	DC-link current
i_L	Load current
v_{dc}	DC-link voltage
$S_k\left(k = a, b, c\right)$	Switch function of phase, k
$v_{(a,0)}$, $v_{(b,0)}$, $v_{(c,0)}$	Voltages from the AC side of the PWM rectifier to the power neutral point, *0*
$v_{(N,0)}$	Voltage from point, N , to neutral point, *0*, of a PWM rectifier
$v_{(a,N)}$, $v_{(b,N)}$, $v_{(c,N)}$	Voltages from the AC side of the PWM rectifier to point, N
T	Transformation matrix for a three-phase PWM rectifier
θ	Angle between the stationary reference frame to synchronous reference frame
ω_{gs}	Synchronous speed of the three-phase input voltages or the grid-side voltages
s_d, s_q	Switching functions expressed in the DQ synchronous

	reference frame
i_{dg}, i_{qg}	Input currents expressed in the DQ synchronous reference frame
e_d, e_q	Input voltages expressed in the DQ synchronous reference frame
m	Modulation index
P_g	Active power of a grid-side converter
Q_g	Reactive power of a grid-side converter
θ	Angle between the α-axis of the stationary reference frame and the D-axis of the synchronous reference frame
e_α, e_β	Grid-side voltages expressed in the stationary reference frame
v_d, v_q	Control signals of a grid-side converter
$\overline{V_{La}}$	AC side inductance voltage drop of phase, a
$\overline{V_{(a,0)}}$	Voltage from the AC side of the grid-side converter to the power neutral point, 0, of phase-a
E_m	Magnitude of the AC side input voltage
V_m	Magnitude of the voltage from AC side to the power neutral point, 0
I_m	Magnitude of the AC side current of the grid side converter
v_{ma}	Modulation signal for phase-a

v_r	Carrier signal of the SPWM
V_{ma}	Magnitude of the modulation signal for phase-a
V_T	Magnitude of the carrier signal
v_{a1}	Fundamental component of the voltage from the AC side of the grid side converter to the power neutral point, *0*
$\lambda_{\alpha s}$, $\lambda_{\beta s}$	Stator flux linkages expressed in the stationary α, β reference frame
λ_s	Resultant stator flux
θ_s	Stator flux angular position
$i_{\alpha s}$, $i_{\beta s}$	Stator α-axis and β-axis currents expressed in the stationary reference frame
$i_{\alpha r}$, $i_{\beta r}$	Rotor α-axis and β-axis currents expressed in the stationary reference frame
λ_{xs}, λ_{ys}	DQ-axes stator flux linkages expressed in the stator flux reference frame
λ_{xr}, λ_{yr}	DQ-axes rotor flux linkages expressed in the stator flux reference frame
i_{xs}, i_{ys}	DQ-axes stator phase currents expressed in the stator flux reference frame
i_{xr}, i_{yr}	DQ-axes rotor phase currents expressed in the stator flux reference frame
i_{ms}	Magnetizing current of the generator

v_{xr}, v_{yr}	DQ-axes rotor terminal voltages expressed in the stator flux reference frame
ω_s	Electrical angular velocity of the stator flux
v_{xr}, v_{yr}	Control signals of a generator-side converter
P_{max}	Captured maximum power
β_{ref}	Pitch angle reference
$\vec{V}^*$	Output reference voltage vector
$\vec{V}_0, \vec{V}_1, \ldots, \vec{V}_7$	Voltage vectors of a two-level inverter
$T_0, T_1, \ldots, T_7$	Turn-on time of the vectors, $\vec{V}_0$ through $\vec{V}_7$
$m_{\max}$	Maximum value for the modulation index
S_a	Switching state of a three-level converter for phase-a

Chapter 1

Introduction

1.1 Background

In recent years, the environmental pollution has become a major concern in people daily life and a possible energy crisis has led people to develop new technologies for generating clean and renewable energy. Wind power along with solar energy, hydropower and tidal energy are possible solutions for an environmentally-friendly energy production. Among these renewable energy sources, wind power has the fastest growing speed (approximately 20% annually) in the power industry [1].

With the concern of environmental pollution, wind power is being established in many countries by way of government-level policy. It is reported that by 2020, Europe will achieve 20% of power consumed in there supplying by large-scale offshore wind farms. Besides, Europe is now planning for enlarging the capacity of the large-scale offshore wind farms to more than 30 GW power by 2015 [2]. Besides Europe, other countries such as China and USA also have promising offshore wind power resources and similar plans for wind farm installation.

In the past decades, wind power generation has experienced a very fast development. Therefore, in this thesis, the focus is put on the wind power generation as it is said to encounter large integration obstacles and possible solutions in the near future.

1.1.1 Components of a Wind Turbine-Generator System

The major components of a wind turbine-generator system are shown in Figure.1. The wind turbine (WT) is composed of three blades, the rotor hub and the nacelle located immediately behind the rotor hub which houses the gearbox, generator and other components.

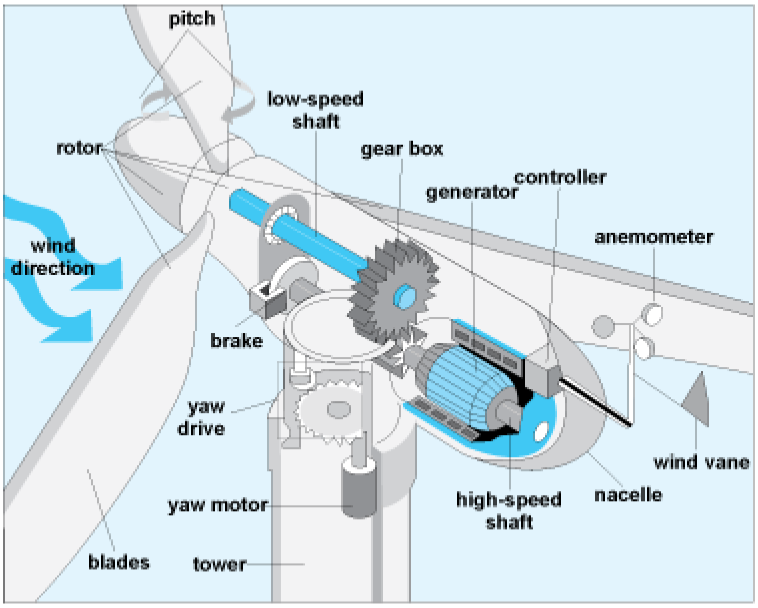

Figure 1.1 Components of a wind turbine-generator system [3]

The drive train system consists of three blades, a low-speed shaft, a gearbox, a high-speed shaft and a generator. The low-speed shaft connects the low-speed shaft to a two or three-stage gearbox, followed by a high-speed shaft connected to the generator [3]. The process of how the wind turbine system generates electrical power will be briefly summarized as follows: 1) the wind strikes the wind turbine blades, causes them to spin and further makes the low-speed shaft rotate, 2) the rotating low-speed shaft transfers the kinetic energy to the gearbox, which has the function of stepping up the rotational speed and rotating the high-speed shaft, 3) the high-speed shaft causes the generator to spin at high speed which is close to the rated speed of the generator, 4) the rotating generator converts the mechanical power to electrical power.

Usually, the output voltages of the generator are low, and hence there will be the need for a transformer to step up the generator output voltage for the purpose of directly connecting to the grid.

Based on the wind direction, the yaw system will rotate the nacelle to make the wind turbine face into the wind. An emergency mechanical brake is equipped at the high-speed shaft to protect the drive train system from the mechanical stress when experiencing wind gusts [4].

In addition, there are extensive on-board controllers that can change the pitch angle of the rotor blades, and regulate the yaw system and drive train system as well as power control components. Besides, these on-board controllers can brake the rotor in possible runaway situations, such as high wind speeds and power-grid outages [3].

Other components of a wind turbine-generator system are wind vane, cooling fan and different sensors. These sensors include the anemometer, speed or position sensors as well as voltage and current sensors. The wind vane is used to measure the wind directions and then decide the operation of the yaw control system. Electric cooling fans are used to cool the gearbox, generator, power converters and the on-board controllers. The anemometer is used to measure the wind speed for tracking the maximum power or protection purposes. For example, when the wind speed experiences gusts, the wind speed signal sensed by the anemometer will be sent to the on-board controllers, which will make the wind turbine shut down through the brake for safety considerations. Other sensors such as speed sensors and current sensors in wind turbine systems are used for control purposes, and should be specified according to the control schemes.

1.1.2 Wind Turbine Concepts

Generally speaking, wind power generation uses either fixed speed or variable speed turbines which can be categorized into four major types. The main differences between these wind turbine types are the ways how the aerodynamic efficiency of the rotor would be limited for different wind speed conditions. These four types are briefly described below [5]:

1. Fixed Speed Wind Turbines (WT Type A)

   This type of wind turbine uses an asynchronous squirrel-cage induction generator (SCIG) directly connected to the grid via a transformer. The so-called “fix speed WT” comes from the fact that the rotational speed of the wind turbine cannot be automatically regulated and will only vary with the wind speed. This type of wind turbine needs a switch to prevent motoring operation during low wind speeds, and also suffers a major drawback of reactive power consumption since there is no reactive power control. Besides, this type of wind turbine transfers the wind fluctuations to mechanical fluctuations and further converts these into electrical power fluctuations due to the fact that there are no speed or torque control loops. These electrical power fluctuations can lead to an impact at the point of connection in the case of a weak grid.

2. Partial Variable Speed Wind Turbine with Variable Rotor Resistance (WT Type B)

This type of wind turbine uses a wound rotor induction generator (WRIG) directly connected to the grid. The rotor phase windings of the generator are connected in series with controlled resistances. In this way, the total rotor resistances can be regulated, and thus the slip and the output power can be controlled. Due to the limitation of the serial resistance sizes, the variable speed range is usually small, typically 0-10% above synchronous speed [5].

3. Variable Speed Wind Turbine with Partial-Scale Power Converter (WT Type C)

   This configuration, known as the doubly-fed induction generator (DFIG) concept, uses a variable speed controlled wind turbine. The stator phase windings of the doubly-fed induction generator are directly connected to the grid, while the rotor phase windings are connected to a back-to-back converter via slip rings. The power converters could control the rotor frequency and thus the rotor speed. Here, the speed range for the DFIG is around ±30% of the synchronous speed. The power rating of the power converters is typically rated ±30% around the rated power since the rotor of the DFIG would only deal with slip power. The smaller rating of the power converters makes this concept attractive from an economical point of view. Besides, this type of wind turbine can also achieve the desired reactive power compensation.

4. Variable Speed Wind Turbine with Full-Scale Power Converter (WT Type D)

   This configuration usually uses a permanent magnet synchronous generator (PMSG) and a full-scale power converter. The stator phase windings are connected to the grid through a full-scale power converter. Some of this type of wind turbines adopt a gearless concept, which means that instead of connecting a gearbox to the generator, a direct driven multi-pole generator is used without a gearbox.

The first two types of wind turbines have many disadvantages. Examples of these disadvantages are: 1) they do not support any speed control, 2) they do not have reactive compensation, 3) they require a stiff grid, 4) their mechanical construction must be able to support high mechanical stress caused by wind gusts, and so on. Therefore, this thesis does not show any detailed work about these considerations. The advantages and disadvantages of type C and type D wind turbine systems are summarized next.

Advantages of the DFIG-based wind turbine-generator system:

- It has the ability of decoupling the control of the active and reactive power by controlling the rotor terminal voltages. Hence, the power factor control can be implemented in this system.
- The DFIG is usually a wound rotor induction generator, which is simple in construction and cheaper than a PMSG.
- In a DFIG-based wind turbine-generator system, the power rating of the power converters is typically rated ±30% around the rated power, and this characteristic leads to many merits, such as, reduced converter cost, reduced filter volume and cost, less switching losses, less harmonic injections into the connected grid, and improved overall

efficiency (approx. 2-3% more than full-scale frequency converter) if only the generator and power converters are considered [6].

Disadvantages of the DFIG-based wind turbine-generator system [4]:

- Needs slip-rings and gearbox, which will require frequent maintenance.
- Has limited fault ride through capability and needs protection schemes
- Has complex control schemes

Advantages of the PMSG-based wind turbine-generator system [7]:

- The PMSG can achieve full speed regulation.
- The PMSG makes it possible to avoid a gearbox, therefore, there are no mechanical stress issues when experiencing wind gusts.
- The PMSG does not need the slip-rings and brushes, hence, less maintenance will be needed. Therefore, a PMSG-based wind turbine will be more stable than a DFIG-based one.
- The PMSG can also achieve active power and reactive power control. The control schemes are relatively simple and easy to implement.

Disadvantages of the PMSG-based wind turbine-generator system [7] [8]:

- The power converters of a PMSG-based wind turbine-generator system have a full-scale power rating, which means that the power converters will cause high losses, generate high harmonic components, and have high cost.
- The PMSG is usually a multi-polar generator, which is relatively large

and heavy, and causes inconvenience for the installation.

- The PMSG naturally needs permanent magnets, which will increase the cost for this wind turbine concept considering the current market.
- The permanent magnets run the risk of demagnetization at high temperature.

Nowadays, DFIGs are most commonly used in the wind turbine industry for large wind turbines. Considering these merits of the DFIG-based wind turbine-generator systems, this thesis will only focus on DFIGs and then provide some detailed work about the modeling and control schemes of such wind turbine-generator systems.

1.1.3 Operating Regions of a Wind Turbine-Generator System

The wind turbine always operates with different dynamics, from minimum wind speed to maximum wind speed, and the operating regions of the wind turbine can be illustrated by their power curve shown as in Figure 1.2. Three wind speeds and two operation modes are shown in this power curve, and their definitions are as given below [9] [10]:

- Cut-in speed: The cut-in speed is the minimum wind speed at which the wind turbine will generate usable power. This wind speed is typically between 3.13 and 4.47 m/sec for most turbines.
- Rated speed: The rated speed is the minimum wind speed at which the wind turbine will generate its designated rated power. At wind speeds between the cut-in speed and the rated speed, the wind turbine will

operate at the "maximum power point tracking (MPPT) mode", and the output power of a wind turbine will increase as the wind speed increases.

- Cut-out speed: At very high wind speeds, typically between 22 and 45 m/sec, most wind turbines cease power generation and are shut down for protection purposes. The wind speed at which shut down operation occurs is called the cut-out speed. When the wind turbine experiences high wind speed, the mechanical part of the wind turbine may be damaged, and hence having a cut-out speed is a safety consideration. When the wind speed drops back to a safety level, the wind turbine operation usually resumes.

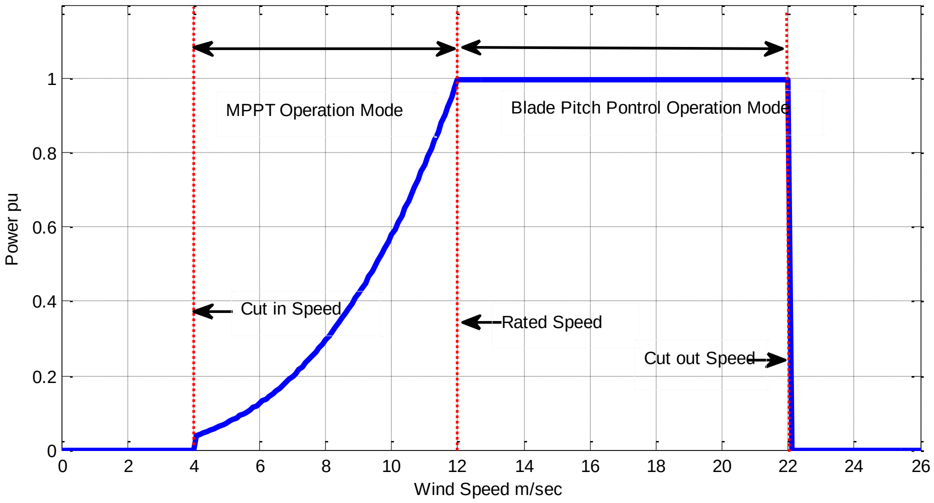

Figure 1.2 Power verse wind speed curve

In the MPPT operation mode, the speed of the turbine is adjusted in such a way that the wind turbine can capture the maximum power based on the given wind speed. However, this operation has the drawback of generating fluctuated power due to the variations in wind speed. At the rated wind speed point, the controller attempts to maintain the generator speed at its rated speed (typically around 15-20 percent above synchronous speed), and the output power at its rated power. This maximum power tracking regulation is mainly achieved by means of the generator-side converter control.

In the blade pitch control operation mode, if the wind speed exceeds its rated value, it would be detrimental for the wind turbine to operate at such high wind speed. Hence, the generator speed must be limited by reducing the aerodynamic torque. This can be done through regulating the pitch angle of the blades, so that the aerodynamic conversion efficiency is reduced, and thus less mechanical torque acts on the generator, and finally the speed can be maintained at a constant level.

1.2 Literature review

In this section, a detailed literature review describing doubly-fed induction generator (DFIG)-based wind turbine-generator systems will be presented. More specifically, the related previous studies and researches on the modeling, the control strategies, and the state of the art converter topologies applied in DFIG-based wind turbine-generator systems will be presented.

1.2.1 Modeling of a Wind Turbine-Generator System

As mentioned in last section, the modeling of a wind turbine-generator system consists of the aerodynamic modeling, the drive train system modeling, the DFIG modeling, and the power converter modeling, see Figure 1.1. Hence, this part of the study will only focus on the modeling of such system.

- Aerodynamic modeling

In [11], Tao sun deduced the maximum energy that a wind turbine system can extract from the air system under ideal conditions. In [12], the authors derived the relationship between the mechanical power input and the wind speed passing through a turbine rotor plane, which can be expressed by the power coefficient of the turbine. There are three most commonly used methods to simulate the power coefficient which is provided by the wind turbine manufacturer. The first two methods are given in references [11], [13] and [14]. The third method is the lookup table method, and given in references [10] and [15]. There are two other methods to approximate the power efficiency curve, but they are not commonly used. Interested readers can find them in [16-17].

- Drive train modeling

For the drive train system modeling, the work in reference [18] elaborately explained the reduced mass conversion method and compared a six-mass model with reduced mass models for transient stability analysis. In [19], Stavros A. Papathanassiou used a six-mass drive train model to analyze the transient processes during faults and other disturbances. In [20], three different drive train models and different power electronic converter topologies were considered to study the harmonic assessment. Reference [21] compared the transient stabilities of a three-mass model, a two-mass model, and a one-mass model. In addition, the effects of different bending flexibilities, blade and hub inertias on the transient stabilities of large wind turbines were also analyzed. In [22], a three-mass model, which took into account the shaft flexibility and blade flexibility in the structural dynamics, was developed and then used to derive a two-mass model. In [18] and [23], the authors concluded that a two-mass drive train model was sufficient for transient stability analysis of wind turbine-generator systems. Besides, the two-mass model is widely used in references [24-29]. Other references, such as [14, 30-33] focused their study on the generator control and modeling, where the drive train system was simply expressed by single mass models.

- DFIG modeling

The doubly-fed induction machines can be categorized into four types. These types are: the standard doubly-fed induction machine, the cascaded doubly-fed induction machine, the single-frame cascaded doubly-fed induction machine and the brushless doubly-fed induction machine [34]. However, only the standard type and brushless type of doubly-fed induction machines have been applied in wind turbine-generator systems. In reference [35], the authors developed the brushless doubly-fed induction generator by employing two cascaded induction machines to eliminate the brushes and copper rings, and used a closed-loop stator flux oriented control scheme to achieve active and reactive power control. In [36], Yongchang Zhang proposed a direct power control (DPC) strategy for cascaded brushless doubly-fed induction generators which featured quick dynamic responses and excellent steady state performances.

The doubly-fed induction generator model can be expressed in the stationary stator reference frame, the reference frame rotating at rotor speed and the synchronously rotating reference frame. In [31] and [37], the authors adopted the synchronously rotating reference frame in order to simplify the controller design because of the fact that all the currents and voltages expressed under this reference frame will be of a dc nature. While, in [38], both stator and rotor variables were referred to their corresponding natural reference frames, and the machine model expressed in such reference frame is called the “Quadrature-Phase Slip-Ring” model.

The DFIG model can usually be expressed by reduced order models, which can yield a third order model by neglecting the derivative terms of the stator flux and first order model by neglecting both the derivative terms of the stator flux and rotor flux [39]. But in [37], the authors proposed an enhanced third order model which considered the dc-components of the stator currents, and gave a comparison between a full order model and the proposed model for wind ramp conditions. Alvaro Luna, in [40], deduced a new reduced third order model by ignoring the stator resistances and inductances through applying the Laplace transformation, and compared the proposed model with a full order model for transient analysis.

There are many references which made the comparison between the full order model and reduced order models [41-43]. In [44], the authors even considered the saturated conditions, and made a detailed comparison among these unsaturated and saturated full order models and reduced order models. Pablo Ledesma, in [45], compared a third order model with a full order model in two extreme operation points under short-circuit fault conditions. These points are sub-synchronous speed and super-synchronous speed, respectively. As known, the difference between the model of a squirrel-cage induction generator and a doubly-fed induction generator is the rotor input. Hence, the simplified models of squirrel-cage induction generators may be helpful for understanding the reduced order models of DFIGs. Interested readers can find them in [46] and [47].

- Power converter modeling

The traditional power converter used in wind turbine-generator systems is a back-to-back two-level PWM converter. The three-phase voltage source PWM converter model can be expressed in the ABC reference frame and the DQO synchronous reference frame which is deduced for control purposes. The mathematical model based on space vectors expressed in the ABC reference frame was derived in [48]. In [49-51], the authors showed the detailed work about the transformation of a PWM converter model from the ABC reference frame to the DQO synchronous reference frame. For wind turbine applications, some researchers simplified the power converter model by employing an equivalent ac voltage source that generates the fundamental frequency [32]. In [52], José R. Rodríguez gave the detailed description for the working principles, control strategies, and made comparisons for three-phase voltage source and current source PWM converters.

1.2.2 Control Strategies for a Wind Turbine-Generator System

The control schemes for a wind turbine-generator system include the pitch angle control, maximum power point tracking control, and the DFIG control. The traditional control techniques and advanced control techniques for wind turbine-generator systems are reviewed in this section.

1. Pitch angle control

The pitch angle control is a mechanical method of controlling the blade angle of the wind turbine when the captured wind power exceeds its rated value or wind speed exceeds its rated value. In this way, pitch angle control is enabled to limit the maximum output power to be equal to the rated power, and thus protect the generator when the wind speed experiences gusts. The pitch angle controller is only activated at high wind speeds.

There are numerous pitch angle regulation techniques described in the literatures [53-59]. The conventional pitch angle control usually uses PI controllers [53-55]. However, several advanced pitch control strategies were proposed. A new approach for the pitch angle control, which worked well for unstable and noisy circumstance, was presented in [56]. Besides, a fuzzy logic pitch angle controller was developed in [57], which did not need much knowledge about the system. Furthermore, a pitch angle controller using a generalized predictive control was presented in [58], whose strategy was based on the average wind speed and the standard deviation of the wind speed. Another pitch control scheme was proposed in [59], in which a self-tuning regulator adaptive controller that incorporated a hybrid controller of a linear quadratic Gaussian neuro-controller and a linear parameter estimator, was developed for the pitch angle control. In [60], the authors only applied a fuzzy logic pitch angle controller in a wind turbine-generator system to achieve the maximum power point tracking control and power control.

2. Maximum power point tracking control

In order to achieve the maximum power point tracking (MPPT) control, some control schemes have been presented. The maximum power point tracking control can be mainly divided into two types. They are the conventional control schemes and intelligent control schemes.

- Conventional control schemes

The conventional control schemes can also be divided into current mode control and speed mode control, which depends on the setting of reference values. The reference values are the active power and electromagnetic torque for current mode control [61-63], and the rotational speed for the speed mode control [64-65]. In [66], the author compared these two control strategies for dynamic transient analysis, and concluded that the current mode control has slow response with simple construction, while the speed mode control has fast response with complex construction. The discussions and limitations of these two control schemes were presented in [67].

In fact, the wind speeds in above conventional control schemes need to be exactly measured. However, the anemometer cannot precisely measure the wind speed because of the flow distortion, complex terrain and tower shadow influence [68]. Hence, some studies on maximum wind energy tracking without wind velocity measurement had been developed in [24], [69] and [70].

- Intelligent control

The intelligent control strategies usually apply the hill-climbing control and the fuzzy logic control to the maximum power point tracking control. The traditional hill-climbing control uses a fixed-step speed disturbance optimal control method to determine the speed, perturbation size and direction according to the changes in the power before and after sampling [71]. However, this control method is usually slow in speed because the step disturbance is fixed. Therefore, some improved hill-climbing control methods were proposed. For example, a method of using variable-step wind energy perturbation method to control the captured wind power was analyzed in [67]. Another advanced hill-climbing searching method with an on-line training process, which can search for the maximum wind turbine power at variable wind speeds, even without the need for knowledge of wind turbine characteristics, wind speed and turbine rotor speed, was developed in [72].

Fuzzy logic control based MPPT strategies have the advantages of having robust speed control against wind gusts and turbine oscillatory torque, having superior dynamic and steady performances, and being independent of the turbine parameters and air density, see [68] and [73].

- Other control strategies

In [74], the authors presented a novel adaptive MPPT control scheme in which the wind speed was estimated by the output power and the efficiency of the generator, and the maximum efficiency was estimated by the maximum tip-speed ratio tracker. A novel MPPT strategy that was based on directly adjusting the dc/dc converter duty cycle according to the results of comparisons between successively monitored wind turbine output powers was proposed in [75], in which there was no requirement for the knowledge of wind turbine characteristic and measurements of the wind speed.

3. DFIG control

Control of the DFIGs is more complicated than the control of a squirrel-cage induction generator, because the DFIGs can operate at sub-synchronous speed and super-synchronous speed by regulating the rotor terminal voltages. Through the years, many researchers have presented various types of DFIG control strategies, such as field oriented control, direct torque/power control, predictive control, sensorless control and nonlinear control.

- Field oriented control

Field oriented control (FOC) or vector control is commonly used in doubly-fed induction generator controls due to its ability of controlling the motor speed more efficiently, and the low economic cost to build an FOC system. Field oriented control also provides the ability of separately controlling the active and reactive power of the generator. Currently, there are mainly two types of field oriented control in DFIGs, which are stator voltage oriented control and stator flux oriented control, respectively. The stator flux oriented control is widely used in the DFIG control designs [24], [38], [65], in which the q-axis current component is used for active power control and the d-axis component is used for reactive power control. While for the stator voltage oriented control, the situation is on the contrary [76-77], the d-axis component is used for active power control and the q-axis current component is used for reactive power control. In [78], the author compared real and reactive power control for a DFIG-based wind turbine system using stator voltage and stator flux oriented control, respectively, and the simulation results illustrated same performances.

- Direct torque/power control

Recently, a new technique for directly control of the induction motors’ torque or power was developed, which included direct torque control (DTC) and direct power control (DPC). Direct torque control scheme was first developed and presented by I. Takahashi and T. Nogouchi [79-80]. Based on the principles of DTC for electrical machines, direct power control for a three-phase PWM converter was introduced in [81].

Direct torque control techniques do not require current regulators, coordinate transformations, specific modulations and current control loops [82]. Thus, direct torque control has the ability of directly controlling the rotor flux linkage magnitude and generator torque through properly selecting the inverter switching states [83]. To show the advantages of DTC, the comparison between the field oriented control and direct torque control was made in [84]. Direct torque control using space vector modulation technology was presented in [85]. In [86-88], the authors applied basic direct torque control to a doubly-fed induction generator. Direct torque control which was achieved without PI controller and only required the knowledge of grid voltages, rotor currents, and rotor position as was proposed in [82]. Z. Liu, in [89], proposed a novel direct torque control scheme which was developed based on the control of the rotor power factor.

Direct power control has the merits of being simple, requiring fewer sensors, having low computational complexity, fast transient response and low machine model dependency compared with direct torque control [90]. In [91], the comparison between field oriented control and direct power control for a PWM rectifier was presented, and the simulation results showed that the virtual-flux-based direct power control was superior to the voltage-based direct power control and field oriented control. Direct power control has been applied in DFIG-based wind turbine-generator systems in recent years [92-95]. In [93] and [94], the authors used direct power control in a DFIG-based wind turbine system under unbalanced grid voltage conditions. A new direct power control, which was based on the stator flux and only needed the stator resistance values of the machine parameters, was proposed in [95].

- Other control strategies

In recent years, increasing attention is being paid to the application of predictive control in the field of the DFIG-based wind turbine-generator systems [96-98]. Several predictive direct power control strategies were studied and compared for ac/dc converters in [99]. Sensorless control is usually achieved by estimating the rotor position, so that there is no need for the rotor position encoder. There are many studies worked on the sensorless control, see reference [100-102]. Moreover, direct torque/power control strategies can be considered as “sensorless type” control techniques because direct torque/power control could obtain a good dynamic control of the torque/power without any mechanical transducers on the machine shaft [84]. A nonlinear control approach, which used the nonlinear static and dynamic state feedback controllers with a wind speed estimator in a wind turbine-generator system, was proposed in [23].

1.2.3 Power Converter Topologies for a Wind Turbine-Generator System

Power electronics, being the technology of efficiently converting electric power, plays an important role in wind power systems. In recent years, the multi-level converters and matrix converters became main solutions for medium voltage drives. In this section, the application of multi-level converters and matrix converters in wind turbine-generator systems is reviewed.

- Multi-level converters

Compared with traditional two-level converters, multi-level converters have many advantages, such as, more sinusoidal output voltage waveforms, lower total harmonic distortion (THD), reduced filter size and cost, reduced switching losses in the IGBTs, lower dv/dt, and so on [103-104]. This is due to the fact that the output voltages can be formed using more than two voltage levels [105].

Generally speaking, multi-level converters can be classified in three categories [106]: neutral-point-clamped (NPC) converters, flying capacitor converters and cascaded H-bridge (CHB) converters. Multi-level neutral-point-clamped converters are most widely used in wind turbine-generator systems. In [107] and [108], three-level NPC converters were applied in PMSG-based wind turbine systems with field oriented control. In [109], the author used a three-level neutral-point-clamped PWM converter to drive a permanent magnet synchronous generator, in which a space vector modulated direct power control was applied. In [110], a new application of the predictive direct power control was presented for a doubly-fed induction machine equipping with three-level NPC converters, in which constant switching frequency technology was achieved. In [111], the active and passive components of a NPC converter, such as insulated-gate bipolar-transistors, free-wheeling diodes, clamping diodes, grid filters, dc-bus capacitors, were designed for a wind turbine system equipped with a squirrel-cage induction generator. A comparison between traditional two-level converters and three-level NPC converters for a wind power system was made in [105] and [112]. In [113] and [114], the authors made comparisons between the neutral-point-clamped converters, flying capacitor converters and cascaded H-bridge converters for wind power generation. The application of cascaded H-bridge converters in wind turbine-generator systems was developed in recent years; interested readers can find them in [115-116].

- Matrix converters

The matrix converter concept, which was first introduced by A. Alesina and M. G. B. Venturini [117], has become increasingly attractive for wind power applications. When compared with back-to-back two-level converters, matrix converters have some significant advantages, such as, sinusoidal input and output currents, absence of a DC-link capacitor, fewer IGBT switches, simple and compact power circuit, operation with unity power factor for any load, and regeneration capability [118-119]. Numerous works have been published for the application of matrix converters in wind turbine-generator systems. The application of a matrix converter for power control of a DFIG-based wind turbine system can be found in [120-121]. In [122], a wind turbine system, which was composed by a squirrel-cage induction generator and a matrix converter, was presented. For the applications of PMSG-based wind turbine systems, one can easily find them in [123-124].

1.3 Thesis contributions

In this thesis, the development of the modeling and control of a DFIG-based wind turbine-generator system is carried out. First, the method of deducing reduced mass models of the drive train system, the way of transforming the doubly-fed induction generator model from the ABC reference frame to different DQO reference frames are reviewed, and the way of modeling a three-phase PWM rectifier is presented in this thesis. Moreover, the comparison of the full order model to reduced order models of a doubly-fed induction generator is made.

Second, for the control of a wind turbine system, the controller for a three-phase two-level grid-side converter, which can achieve a unity power factor looking from the grid side while keeping the DC-link voltage constant, is developed. Then, another controller which has the ability of decoupled controlling the active power and reactive power of a doubly-fed induction generator is implemented. The simulation results show the feasibility of these controllers.

Third, a relatively new modulation technology, which is called “space vector PWM” [52], is studied and then applied to a wind turbine system. The space vector PWM technology [52] is compared with the traditional sinusoidal PWM [105], and the simulation results show that the space vector PWM has lower THD and higher peak values of the fundamental component of the output phase voltages.

Moreover, three-level neutral-point-clamped converters [106] are applied to a wind turbine system, in which the space vector PWM is implemented for three-level converters. The comparison between the two-level converters and three-level converters is made, and the simulation results show that the three-level converters have more sinusoidal voltage waveform, lower THD and less harmonic components in the active and reactive power profiles.

1.4 Thesis organization

Including this introductory chapter, this thesis is organized in six chapters. In the second chapter, the modeling for a wind turbine-generator system is presented. More specifically, several methods to model the aerodynamics of a wind turbine rotor, the six-mass model and reduced mass models for the drive train system, the detailed doubly-fed induction generator models expressed in the ABC reference frame and various DQO reference frames, and the PWM converter models expressed in the ABC and the DQO synchronous reference frame are developed and analyzed. In Chapter 3, different control schemes for a wind turbine system are presented, which include the grid-side converter control, generator-side converter control, maximum power point tracking strategy and pitch angle control. The simulation results as well as the corresponding analysis and discussion of these results will be also presented in this chapter. In Chapter 4, a space vector PWM technology is introduced and compared with the traditional sinusoidal PWM for a two-level inverter. Besides, a three-level neutral-point-clamped converter is studied, and the corresponding space vector modulation is developed. The simulation results and discussion for three-level converters and two-level converters modulated by space vector PWM will be presented. In Chapter 5, the modeling and field oriented control scheme for a wind turbine-generator system using three-level neutral-point-clamped converters will be studied, and the simulation results and discussion will be presented. Finally, in Chapter 6, conclusions and recommendations will be presented.

Chapter 2

Modeling of a Wind Turbine-Generator System

In wind turbine-generator systems (WTGSs), the kinetic wind energy is converted to electrical energy through doubly-fed induction generators (DFIGs) and then fed into the grid. In order to investigate the power quality issues of variable speed wind turbine-generator systems, such as their interaction with the grid and different control scheme configurations, a proper model of the grid-connected variable speed WTGS should be established first.

In this chapter, a general introduction to the WTGSs is first given, in which a wind energy conversion system is discussed briefly. Second, several methods of calculating the WTGS captured power from the wind are proposed, which are the aerodynamic models of wind turbines. Third, a detailed six-mass drive train system model and several reduced mass models, such as, three-mass, two-mass and one-mass model, are discussed. In addition, a six-mass to reduced mass conversion method is introduced. Fourth, a DFIG model expressed in the ABC reference frame is developed, and then several DFIG models expressed in various DQO-dqo reference frames are deduced from the ABC model by classical DQO transformations. Moreover, the reduced order models are also derived based on the DFIG model expressed in a synchronously rotating reference frame. Finally, the mathematical models of three-phase PWM voltage source converters are developed in the ABC reference frame and DQO synchronous reference frame.

2.1 Introduction

A variable speed wind turbine-generator system (WTGS) schematic is shown in Figure 2.1. The stator phase windings of the doubly-fed induction generator (DFIG) are directly connected to the grid, while the rotor phase windings are connected to a back-to-back converter via slip rings. The back-to-back converter consists of two converters, i.e., generator-side converter and grid-side converter, and a DC-link capacitor placed between the two converters. The main objective for the grid-side converter is to keep the variation of the DC-link voltage small. With control of the generator-side converter, it is possible to control the torque, the speed of the DFIG as well as its active and reactive power at the stator terminals.

Since the back-to-back power converters could be operated in bi-directional mode, the DFIG could thus be operated either in sub-synchronous speed mode or super-synchronous speed mode. Here, the speed range for the DFIG is around ±30% of the synchronous speed [10]. The DFIG stator sides always feed active power to the grid, whereas active power is fed into or out of the rotor depending on the operating condition of the DFIG. In super-synchronous speed mode, the active power flows from the rotor via the back-to-back converter to the grid, whereas it flows in the opposite direction in sub-synchronous speed mode. In this thesis, the model of the variable speed wind turbine with a DFIG was developed in a Matlab/Simulink environment.

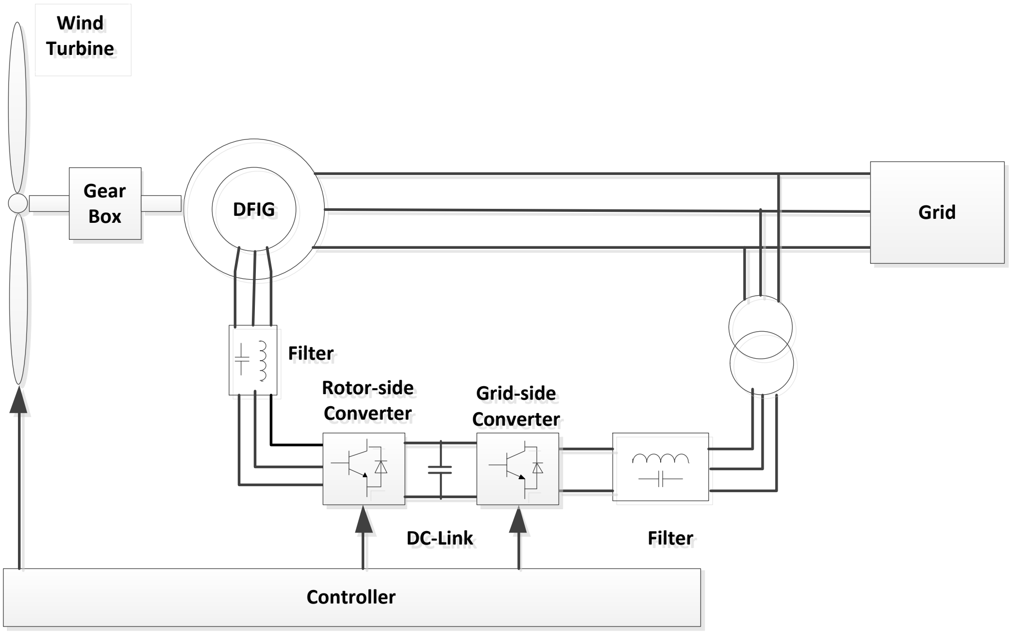

Figure 2.1 DFIG wind turbine scheme

2.2 Aerodynamic Model

A WTGS is a structure that transforms the kinetic energy of the incoming air stream into electrical energy. The conversion takes places by using two devices. The first one is the extraction device, which harvests the mechanical power by the wind stream turning the wind turbine rotor. The other one is the generator which transforms the rotational mechanical power to electrical power. The relationship between the mechanical input power and the wind speed passing through a turbine rotor plane can be written as follows [12]:

$$P_{\omega t} = {}^{1}\!/_{2}\,\rho \pi R^{2} v_{\omega}^{3} C_{p}(\lambda, \beta) \qquad (2.1)$$

where, $P_{\omega t}$, is the captured power of the wind turbine, ρ, is the air density, R, is the rotor blade radius, and v_{ω}, is the wind speed. Here, C_p, is the power coefficient of the turbine, which is a function of the pitch angle, β, and the tip speed ratio, λ. Here, C_p coefficient describes the power extraction efficiency of a wind turbine.

The tip speed ratio of a wind turbine is a variable expressing the ratio between the peripheral tip blade speed and the wind speed, and it is expressed as $\lambda = R\omega_t / v_\omega$. The C_p character in a wind turbine aerodynamic model can be approximated by several different possible non-linear functions. The most commonly used methods are the following three methods. The function of the first method is given by [11] and [13], and written as follows:

$$C_p = 0.22\left(\frac{116}{\lambda_i} - 0.4\beta - 5\right)\exp^{-12.5/\lambda_i} \tag{2.2}$$

where,

$$\lambda_i = \left(\frac{1}{\lambda + 0.08\beta} - \frac{0.035}{\beta^3 + 1}\right)^{-1}$$

The second method is given by [14], and expressed in equation (2.3):

$$C_p = 0.73\left(\frac{115}{\lambda_i} - 0.58\beta - 0.002\beta^{2.14} - 13.2\right)\exp^{-18.4/\lambda_i} \tag{2.3}$$

where,

$$\lambda_i = \left(\frac{1}{\lambda - 0.02\beta} - \frac{0.03}{\beta^3 + 1}\right)^{-1}$$

The third way to calculate the C_p coefficient is the lookup table method [40] [15], and given as follows:

$$C_p(\lambda, \beta) = \sum_{i=0}^{4}\sum_{j=0}^{4}\alpha_{i,j}\beta^i\lambda^j \tag{2.4}$$

The coefficients, $\alpha_{i,j}$, are given in the Table 2.1, where the approximation is only valid for $2 < \lambda < 13$.

Table 2.1 Coefficients $\alpha_{i,j}$

i/j	0	1	2	3	4
0	-4.19×10^{-1}	2.18×10^{-1}	-1.24×10^{-2}	-1.34×10^{-4}	1.15×10^{-5}
1	-6.79×10^{-2}	6.04×10^{-2}	-1.39×10^{-2}	1.07×10^{-3}	-2.39×10^{-5}
2	1.57×10^{-2}	-1.1×10^{-2}	2.15×10^{-3}	-1.49×10^{-4}	2.79×10^{-6}
3	-8.6×10^{-4}	5.7×10^{-4}	-1.05×10^{-4}	5.99×10^{-6}	-8.92×10^{-8}
4	-1.48×10^{-5}	-9.48×10^{-6}	1.62×10^{-6}	-7.15×10^{-8}	4.97×10^{-10}

Figure 2.2 shows the relationship between the C_p coefficient and λ for these three methods when the pitch angle, β, equals zero. Therefore, in practice, one needs to choose a approximation method that is most close to the manufacture's C_p curve. In the following chapter, the third method is chosen because all the wind turbine data were acquired from [15]. Besides, there are also two other methods to approximate the C_p curve, but they are not commonly used. Interested readers can find them in [16] [17].

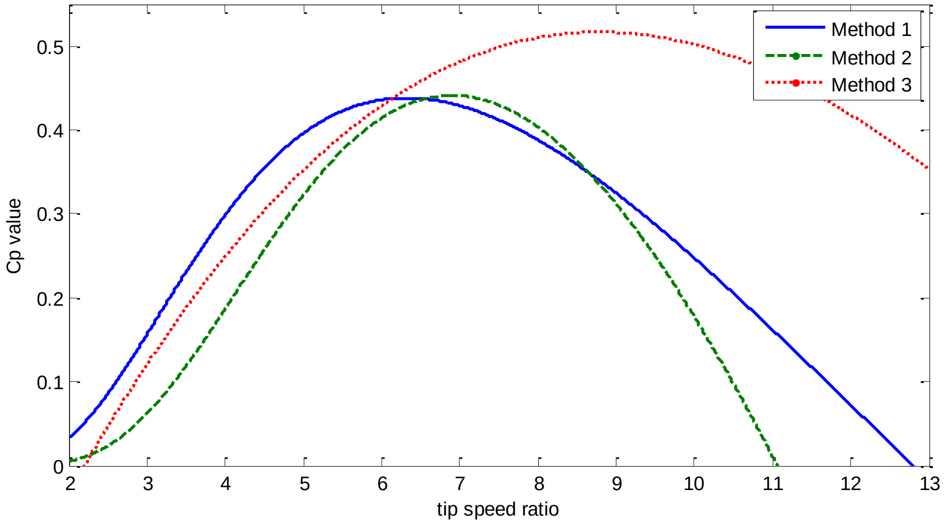

Figure 2.2 Three method comparisons when pitch angle equals zero

2.3 Drive Train Model

The drive train system of the WTGS can be represented either by a three-mass model, two-mass model, single lumped-mass model or even a six-mass model. It has already been reported that for precise transient analysis of WTGSs, a six-mass drive train model is needed. However, a six-mass drive train model increases the simulation time due to the complex and lengthy mathematical computation with small time-steps. Therefore, reduced mass models are considered to simplify the computation while preserving a reasonable accuracy of transient processes. This section gives an overview of the four above mentioned types of drive train models and elaborately explains the reduced mass conversion method based on [18].

2.3.1 Six-Mass Model

The basic six-mass drive train model is presented in Figure. 2.3. The six-mass model system has six inertias [18]: three blade inertias (J_{B1}, J_{B2}, and J_{B3}), hub inertia (J_H), gearbox inertia (J_{GB}), and generator inertia (J_G). Spring constants, K_{HB1}, K_{HB2}, K_{HB3}, K_{HGB} and K_{GBG}, represent the elasticity between adjacent masses. The mutual damping between adjacent masses is expressed as d_{HB1}, d_{HB2}, d_{HB3}, d_{HGB} and d_{GBG}. The torque losses acting on individual masses can be expressed by the self-damping of these masses, D_{B1}, D_{B2}, D_{B3}, D_H, D_{GB} and D_G. The inputs of the drive train system are the generator torque, T_G, and three individual aerodynamic torques acting on three blades, (T_{B1}, T_{B2} and T_{B3}).

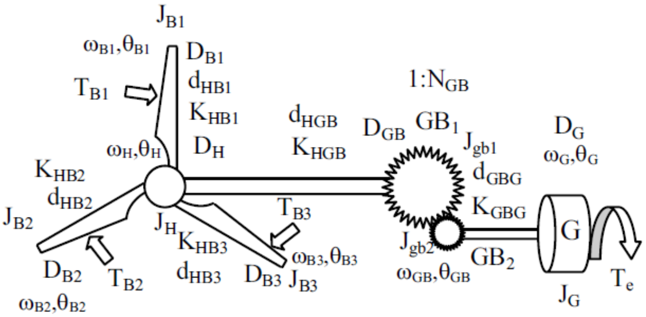

Figure 2.3 Six-mass model scheme [18]

The state equation of the six-mass drive train model is given in the following equation [19]:

$$\frac{d}{dt}\begin{bmatrix}\underline{\theta}\\ \underline{\omega}\end{bmatrix}=\begin{bmatrix}[0] & [I]\\ -[J]^{-1}[K] & -[J]^{-1}[D]\end{bmatrix}\begin{bmatrix}\underline{\theta}\\ \underline{\omega}\end{bmatrix}+\begin{bmatrix}[0]\\ [J]^{-1}\end{bmatrix}\underline{T} \tag{2.5}$$

where, $[\theta]=[\theta_{B1},\theta_{B2},\theta_{B3},\theta_H,\theta_{GB},\theta_G]^t$ and $[\omega]=[\omega_{B1},\omega_{B2},\omega_{B3},\omega_H,\omega_{GB},\omega_G]^t$, are the vectors of the angular positions and angular velocities of the blades, hub, gearbox and generator, respectively. Here, $[J]=diag[J_{B1},J_{B2},J_{B3},J_H,J_{GB},J_G]$, is the diagonal inertia matrix, $[T]=[T_{B1},T_{B2},T_{B3},0,0,T_G]^t$, is the vector of the three blade torques and generator torque, while $[K]$ and $[D]$, are the 6×6 spring constant matrix and damping matrix, respectively, whose expressions are given as follows [19]:

$$[K]=\begin{bmatrix}K_{HB} & 0 & 0 & -K_{HB} & 0 & 0\\ 0 & K_{HB} & 0 & -K_{HB} & 0 & \\ 0 & 0 & K_{HB} & -K_{HB} & 0 & 0\\ -K_{HB} & -K_{HB} & -K_{HB} & K_{HGB}+3K_{HB} & -K_{HGB} & 0\\ 0 & 0 & 0 & -K_{HGB} & K_{HGB}+K_{GBG} & -K_{GBG}\\ 0 & 0 & 0 & 0 & -K_{GBG} & K_{GBG}\end{bmatrix} \tag{2.6}$$

and

$$[D]=\begin{bmatrix} D_B+d_{HB} & 0 & 0 & -d_{HB} & 0 & 0 \\ 0 & D_B+d_{HB} & 0 & -d_{HB} & 0 & \\ 0 & 0 & D_B+d_{HB} & -d_{HB} & 0 & 0 \\ -d_{HB} & -d_{HB} & -d_{HB} & D_H+d_{HGB}+3d_{HB} & -d_{HGB} & 0 \\ 0 & 0 & 0 & -d_{HGB} & D_{GB}+d_{HGB}+d_{GBG} & -d_{GBG} \\ 0 & 0 & 0 & 0 & -d_{GBG} & D_g+d_{GBG} \end{bmatrix} \tag{2.7}$$

where, in this model, $K_{HB1}=K_{HB2}=K_{HB3}=K_{HB}$, $d_{HB1}=d_{HB2}=d_{HB3}=d_{HB}$, and $D_{B1}=D_{B2}=D_{B3}=D_B$.

In the drive train system, all the data used in the state equation are needed to be converted to a per-unit system. Here, let us define S_B as the base power (VA), ω_0 as the base electrical angular velocity (rad/s) and P as the number of poles of the generator. Then, the base values of the per-unit system at the high-speed side of the drive train system are defined as follows [125]:

$\omega'_B = {}^{\omega_0}\!/_{0.5P}$ the base mechanical speed (rad/sec)

$T'_B = {}^{S_B}\!/_{\omega'_b}$ the base torque (Nm)

$\theta'_B = \omega'_B$ the base mechanical angle (rad)

$J'_B = \dfrac{S_B}{0.5\omega'^2_B}$ the base inertia (Nm/(rad/sec))

$K'_B = \dfrac{S_B}{\omega'^2_B}$ the base stiffness coefficient (Nm/(rad/sec))

$D'_B = d'_B = \dfrac{S_B}{\omega'^2_B}$ the base damping coefficient (Nm/(rad/sec))

The above equations use a single prime to denote the high-speed side values. The low-speed side (turbine-side) base quantities can be calculated from the high-speed side (generator-side) base quantities, but the gearbox ratio, N_{GB}, is needed for the calculation. The double prime denotes the low-speed side values, which are given as follows:

$$\omega_B'' = \omega_B' / N_{GB} \tag{2.8}$$

$$\theta_B'' = \theta_B' / N_{GB} \tag{2.9}$$

$$T_B'' = N_{GB} T_B' \tag{2.10}$$

$$J_B'' = N_{GB}^2 J_B' \tag{2.11}$$

$$D_B'' = N_{GB}^2 D_B' = d_B'' \tag{2.12}$$

$$K_B'' = N_{GB}^2 K_B' \tag{2.13}$$

2.3.2 Reduced Mass Models

It has already been reported that for precise transient analysis of WTGSs, a six-mass drive train model is needed. However, the six-mass drive train model increases the simulation time due to the complex and lengthy mathematical computation with small time-steps. Therefore, reduced mass models are considered to simplify the computation while keeping reasonably accurate transient processes.

In reference [18], the authors analyzed the transient stability of a WTGS using a six-mass, three-mass, and two-mass drive train models. The influence of different drive train data on the transient stability was analyzed. It has been also shown that the six-mass model can be transformed to a two-mass model, and this will be briefly explained later in this section. In [20], three different drive train models and different power electronic converter topologies were considered to study the harmonic assessment. Reference [21] compared the transient processes of a three-mass model, a two-mass model, and a single-mass model. In addition, the effects of different bending flexibilities, blade and hub inertias on the transient stabilities of large wind turbines were also analyzed. In [22], a three-mass model, in which the shaft flexibility and blade flexibility in the structural dynamics were taken into account, was first developed and then used to derive a two-mass model.

The basic three-mass model can be derived from the six-mass model by combining the weights of the three blades and hub together. Hence, the new turbine inertia will be the sum of the three blade inertias and hub inertia. The input torque will be the summation of the three blade torques. Besides, the new turbine self-damping will be the sum of the three blades self-damping and hub self-damping. The mutual-damping and the spring constants between the blades and hub are ignored in the three-mass model. The expressions of such three-mass model are accordingly written as follows:

$$\frac{d\theta_{wt}}{dt} = \omega_{wt} \tag{2.14}$$

$$\frac{d\theta_{GB}}{dt} = \omega_{GB} \tag{2.15}$$

$$\frac{d\theta_{G}}{dt} = \omega_{G} \tag{2.16}$$

$$\frac{d\omega_{wt}}{dt} = (T_{wt} - K_{HGB} \times (\theta_{wt} - \theta_{GB}) - d_{HGB} \times (\omega_{wt} - \omega_{GB}) - D_{wt}\omega_{wt}) / J_{wt} \tag{2.17}$$

$$\frac{d\omega_{GB}}{dt} = \left. \begin{array}{l} (K_{HGB} \times (\theta_{wt} - \theta_{GB}) + d_{HGB} \times (\omega_{wt} - \omega_{GB}) - K_{GBG} \times (\theta_{GB} - \theta_{G}) - \\ d_{GBG} \times (\omega_{GB} - \omega_{G}) - D_{GB}\omega_{GB}) \end{array} \right/ J_{GB} \tag{2.18}$$

$$\frac{d\omega_{g}}{dt} = (K_{GBG} \times (\theta_{GB} - \theta_{G}) + d_{GBG} \times (\omega_{GB} - \omega_{G}) - D_{G}\omega_{G} + T_{G}) / J_{G} \tag{2.19}$$

where,

$$\left. \begin{array}{c} J_{wt} = J_{B1} + J_{B2} + J_{B3} + J_{H} \\ D_{wt} = D_{B1} + D_{B2} + D_{B3} + D_{H} \\ T_{wt} = T_{B1} + T_{B2} + T_{B3} \end{array} \right\} \tag{2.20}$$

The shaft system of the WTGS can also be represented by a two-mass model system, which is widely used in the reference [27-33]. In the two-mass model, each mass is used to represent the low-speed turbine and the high-speed generator, and the connecting resilient shaft is modeled as a spring and a damper. The three-mass system can be converted to a two-mass system by two ways. One way is by adding one gear of the gearbox to the low-speed turbine, and the other way is by adding the other gear of the gearbox to the high-speed generator. However, reference [18] showed that the gearbox and generator inertias should be added together because the spring constant of the low-speed side is lower than that of the high-speed side. Besides, the self-damping of the generator and gearbox can be simply added together, and the mutual-damping between the gearbox and generator is neglected in such a two-mass shaft model. Therefore, the deduction of the spring constant, inertial constant and the self-damping of the two-mass model can be written as follows [18]:

$$\frac{1}{K_{2m}} = \frac{1}{\left(K_{HGB} / N_{GB}^2\right)} + \frac{1}{\left(K_{GBG}\right)} \tag{2.21}$$

$$D_G^{2m} = D_G + D_{GB} \tag{2.22}$$

$$J_G^{2m} = J_G + J_{GB} \tag{2.23}$$

$$d_{2m} = d_{HGB} \tag{2.24}$$

Accordingly, the two-mass model can be written as follows:

$$\frac{d\theta_{wt}}{dt} = \omega_{wt} \tag{2.25}$$

$$\frac{d\theta_G^{2m}}{dt} = \omega_G^{2m} \tag{2.26}$$

$$\frac{d\omega_{wt}}{dt} = (T_{wt} - K_{2m} \times (\theta_{wt} - \theta_G^{2m}) - d_{2m} \times (\omega_{wt} - \omega_G^{2m}) - D_{wt}\omega_{wt}) / J_{wt} \qquad (2.27)$$

$$\frac{d\omega_G^{2m}}{dt} = (K_{2m} \times (\theta_{wt} - \theta_G^{2m}) + d_{2m} \times (\omega_{wt} - \omega_G^{2m}) - D_G^{2m}\omega_G^{2m} + T_G) / J_G^{2m} \qquad (2.28)$$

where, d_{2m}, is the mutual damping between the hub and generator and is equal to d_{HGB}, due to the fact that the mutual-damping between the gearbox and generator, d_{GBG}, is neglected in the two-mass shaft model.

From the previous discussion, it is already known that more than two-mass models may be more appropriate for short-time transient stability analysis during faults, however, in the literature, it is reported that the drive train model can be expressed by a two-mass model with an acceptable accuracy. The reasons of adopting the two-mass model are motivated by the following factors [23]:

1) The use of a two-mass model will decrease the mathematical computation complexity, reduce simulation time and simplify the controller's design.
2) The high-speed shaft rotates N_{GB} times more quickly than the low-speed shaft. Under the condition of no power losses, the low-speed shaft encounters a torque N_{GB} times greater than the high-speed shaft. Therefore, the low-speed shaft which encounters a higher torque, is subject to more deviation and needed to be taken into consideration.
3) Many authors used a two-mass model to largely simplify the controller's design [27-33].

A simplified single-mass drive train model can be obtained by removing the shaft stiffness and mutual-damping from the two-mass drive train model. Hence, there is only a single inertia, which is equivalent to the sum of the generator and the turbine inertias. This thesis focuses its study on the generator control and modeling, and the drive train system in the work is simply expressed by a single-mass model. The mathematical equation of the one-mass model is given as follows [14]:

$$\frac{d\omega_{wt}}{dt} = (T_{wt} + T_G)/J_{wt} \tag{2.29}$$

2.4 Doubly-fed Induction Generator (DFIG) Models

For the purposes of better understanding and designing vector control schemes in a wind turbine-generator system, it is necessary to know the dynamic model of the machine subjected to control. A model of the electrical machine which is adequate for designing the control system must preferably incorporate all the important dynamic effects occurring during steady state and transient operations [126]. It should be valid for any arbitrary time variations of the voltages and currents generated by the converter which supplies the machine. In this section, such a model which is valid for any instantaneous variations of the voltages and currents, and can adequately describe the performance of the machine under both steady state and transient operations, will be developed in both the ABC reference frame and several different DQO reference frames.

2.4.1 DFIG Model Expressed in the ABC Reference Frame

For simplicity, a wound rotor induction machine is considered with symmetrical two poles and three-phase windings. Figure 2.4 shows the cross-sectional view of the machine under consideration, where the effects of slotting have been neglected.

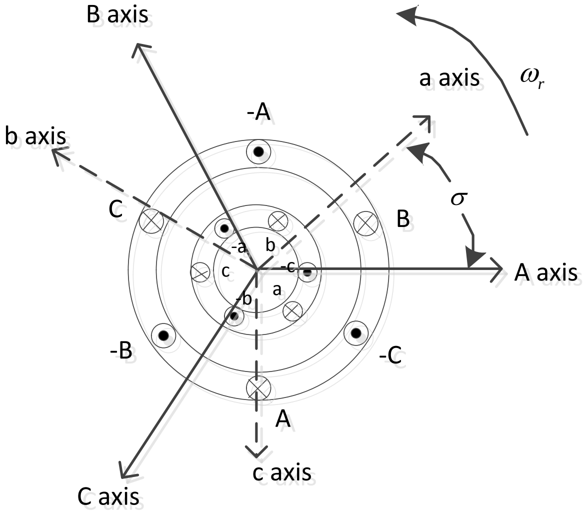

Figure 2.4 Cross-sectional view of a wound rotor induction machine

In Figure 2.4, the stator phase windings are displaced by 120 electrical degrees from each other, and the rotor phase windings are also displaced by 120 electrical degrees from each other. The angle between the magnetic axes of stator phase winding, A, and rotor phase winding, a, is σ. The speed of the rotor is, $\omega_r = d\sigma/dt$, and its direction is also shown in Figure 2.4, in the counter-clockwise direction.

The following assumptions are adopted for developing the ABC model [11]:

- The stator and rotor phase windings of the DFIG are assumed symmetrically distributed, which means that the resistances, magnetizing and leakage inductances for all three phases are equal.
- The produced magnetomotive force is sinusoidally distributed around the circumference of the stator of the DFIG. Therefore, no harmonic components will be present.
- The air-gap is assumed constant, which means constant air-gap reluctance around the circumference of the mid air-gap circle. As a consequence, the

mutual inductances between two stator phase windings and between two rotor phase windings are constant. Only the mutual inductances between the stator phase windings and rotor phase windings vary with the angular rotor position, σ.

- Saturation of the mutual inductances is neglected.
- Skin effect in the stator and rotor phase winding conductors is neglected. When the frequency of the current increases, skin effect will firstly increase the reluctance of the leakage flux permeances of the DFIG, which will further increase the resistances and decrease the leakage inductances.
- Core losses are neglected, and only the power losses on the stator and rotor phase resistances are considered.
- Cross-saturation effect, that is, the coupling between two perpendicular axes, is neglected.

Consider phase A, this phase is represented by a coil as shown in Figure 2.4. The terminal voltage of phase A, v_A, can be expressed based on Faraday's law as follows [127]:

$$v_A = r_A i_A + \frac{d}{dt}\left(\lambda_A\right) \tag{2.30}$$

$$v_A = r_A i_A + \frac{d}{dt}\left(L_{AA} i_A + L_{AB} i_B + L_{AC} i_C + L_{Aa} i_a + L_{Ab} i_b + L_{Ac} i_c\right) \tag{2.31}$$

For phases B and C, similar expressions are written as follows:

$$v_B = r_B i_B + \frac{d}{dt}\left(L_{AB} i_A + L_{BB} i_B + L_{BC} i_C + L_{Ba} i_a + L_{Bb} i_b + L_{Bc} i_c\right) \tag{2.32}$$

$$v_C = r_C i_C + \frac{d}{dt}\left(L_{AC} i_A + L_{BC} i_B + L_{CC} i_C + L_{Ca} i_a + L_{Cb} i_b + L_{Cc} i_c\right) \tag{2.33}$$

For a symmetrical condition, the stator resistances can be expressed as follows:

$$r_A = r_B = r_C = r_s \tag{2.34}$$

where, r_s, is resistance of a stator phase winding.

Similar expressions can be written for the coils representing phases, a, b and c, on the rotor, and given as follows:

$$v_a = r_a i_a + \frac{d}{dt}\left(L_{Aa} i_A + L_{Ba} i_B + L_{Ca} i_C + L_{aa} i_a + L_{ab} i_b + L_{ac} i_c\right) \tag{2.35}$$

$$v_b = r_b i_b + \frac{d}{dt}\left(L_{Ab} i_A + L_{Bb} i_B + L_{Cb} i_C + L_{ab} i_a + L_{bb} i_b + L_{bc} i_c\right) \tag{2.36}$$

$$v_c = r_c i_c + \frac{d}{dt}\left(L_{Ac} i_A + L_{Bc} i_B + L_{Cc} i_C + L_{ac} i_a + L_{bc} i_b + L_{cc} i_c\right) \tag{2.37}$$

Again, the rotor resistances can be expressed as follows:

$$r_a = r_b = r_c = r_r \tag{2.38}$$

where, r_r, is resistance of a rotor phase winding.

From the geometries shown in Figure 2.4, the inductance coefficients, L_{AA}, L_{BB} and L_{CC}, are equal since the flux path for three phase windings, A, B and C, are identical. Also, these inductances are independent of the rotor position, σ. Hence, L_{AA}, L_{BB} and L_{CC}, can be expressed as follows:

$$L_{AA} = L_{BB} = L_{CC} = L_{ss} \tag{2.39}$$

where, L_{ss}, is the self-inductance of a stator phase winding.

Similarity, it can be seen from Figure 2.4 that the inductances, L_{AB}, L_{BC} and L_{AC}, are equal in magnitude, and that they are independent of the rotor position, σ. Hence, these inductances can be expressed as follows:

$$L_{AB} = L_{BC} = L_{AC} = L_{sm} \tag{2.40}$$

where, L_{sm}, is the mutual inductance between any two stator phase windings.

Similarly, for the rotor inductance coefficients, L_{aa}, L_{bb}, L_{cc}, L_{ab}, L_{bc} and L_{ac}, can be deduced that they are all independent of the rotor position, σ, hence,

$$L_{aa} = L_{bb} = L_{cc} = L_{rr} \tag{2.41}$$

$$L_{ab} = L_{bc} = L_{ac} = L_{rm} \tag{2.42}$$

where, L_{rr}, is the self-inductance of a rotor phase winding, and L_{rm}, is the mutual inductance between any two rotor phase windings.

All other coefficients of inductance are dependent on the angular position of the rotor phase windings with respect to the stator phase windings. From the geometries shown in Figure 2.4, it can be easily deduced that all these coefficients vary correspondingly with the rotor angular position, σ, with phase differences. The expressions for these inductances are written as follows:

$$L_{Aa} = L_{Bb} = L_{Cc} = L_{srm}\cos(\sigma) \tag{2.43}$$

$$L_{Ab} = L_{Bc} = L_{Ca} = L_{srm}\cos\left(\sigma + {}^{2\pi}\!/_{3}\right) \tag{2.44}$$

$$L_{Ac} = L_{Ba} = L_{Cb} = L_{srm}\cos\left(\sigma + {}^{4\pi}\!/_{3}\right) \tag{2.45}$$

where, L_{srm}, is the maximum mutual-inductance between the stator phase windings and rotor phase windings, and σ, is the angle between the a-axis on the rotor and the A-axis on the stator, which is equal to $\sigma = \sigma_0 + \int_0^t \omega_r(t)dt$.

From equation (2.31), it can be seen that the phase variable flux linkages contain six flux linkage terms, a self-flux linkage component produced by one stator current in the stator winding, two mutual stator flux linkage components due to the other two stator currents and three stator to rotor mutual flux linkage components, which are due to the three rotor currents.

Therefore, by substituting all the inductance and resistance expressions into the stator and rotor voltage equations, the model for a wound rotor induction machine expressed in the ABC reference frame can be written as follows:

$$\begin{bmatrix} v_A \\ v_B \\ v_C \\ \cdots \\ v_a \\ v_b \\ v_c \end{bmatrix} = \begin{bmatrix} r_s & 0 & 0 & \vdots & 0 & 0 & 0 \\ 0 & r_s & 0 & \vdots & 0 & 0 & 0 \\ 0 & 0 & r_s & \vdots & 0 & 0 & 0 \\ \cdots & \cdots & \cdots & \vdots & \cdots & \cdots & \cdots \\ 0 & 0 & 0 & \vdots & r_r & 0 & 0 \\ 0 & 0 & 0 & \vdots & 0 & r_r & 0 \\ 0 & 0 & 0 & \vdots & 0 & 0 & r_r \end{bmatrix} \begin{bmatrix} i_A \\ i_B \\ i_C \\ \cdots \\ i_a \\ i_b \\ i_c \end{bmatrix}$$

$$+\frac{d}{dt}\left\{\left[\begin{matrix} L_{ss} & L_{sm} & L_{sm} & \vdots \\ L_{sm} & L_{ss} & L_{sm} & \vdots \\ L_{sm} & L_{sm} & L_{ss} & \vdots \\ \cdots\cdots\cdots & \cdots\cdots\cdots & \cdots\cdots\cdots & \vdots \\ L_{srm}\cos(\sigma) & L_{srm}\cos\left(\sigma+{}^{4\pi}\!/_{3}\right) & L_{srm}\cos\left(\sigma+{}^{2\pi}\!/_{3}\right) & \vdots \\ L_{srm}\cos\left(\sigma+{}^{2\pi}\!/_{3}\right) & L_{srm}\cos(\sigma) & L_{srm}\cos\left(\sigma+{}^{4\pi}\!/_{3}\right) & \vdots \\ L_{srm}\cos\left(\sigma+{}^{4\pi}\!/_{3}\right) & L_{srm}\cos\left(\sigma+{}^{2\pi}\!/_{3}\right) & L_{srm}\cos(\sigma) & \vdots \end{matrix}\right.\right.$$

$$\left.\left.\begin{matrix} \vdots & L_{srm}\cos(\sigma) & L_{srm}\cos\left(\sigma+{}^{2\pi}\!/_{3}\right) & L_{srm}\cos\left(\sigma+{}^{4\pi}\!/_{3}\right) \\ \vdots & L_{srm}\cos\left(\sigma+{}^{4\pi}\!/_{3}\right) & L_{srm}\cos(\sigma) & L_{srm}\cos\left(\sigma+{}^{2\pi}\!/_{3}\right) \\ \vdots & L_{srm}\cos\left(\sigma+{}^{2\pi}\!/_{3}\right) & L_{srm}\cos\left(\sigma+{}^{4\pi}\!/_{3}\right) & L_{srm}\cos(\sigma) \\ \vdots & \cdots\cdots\cdots & \cdots\cdots\cdots & \cdots\cdots\cdots \\ \vdots & L_{rr} & L_{rm} & L_{rm} \\ \vdots & L_{rm} & L_{rr} & L_{rm} \\ \vdots & L_{rm} & L_{rm} & L_{rr} \end{matrix}\right] \begin{bmatrix} i_A \\ i_B \\ i_C \\ \cdots \\ i_a \\ i_b \\ i_c \end{bmatrix}\right\} \quad (2.46)$$

From equation (2.46), it can be seen that the inductance matrix in this model is rotor position dependent and hence time dependent, which means that the inductance matrix needs to be calculated at each time step, and thus this increases the computation time. Therefore, the induction machine model expressed in various DQO reference frames will be chosen because of the advantages of simplicity of formulation, fast simulation time and ease of implementation.

2.4.2 DFIG Model Expressed in a DQO-dqo Reference Frame Fixed on the Rotor

A dynamic model is set up in the form of the DQO reference frame rotating at rotor speed type of representation. Thereby, the complexity of the inductance matrix in the ABC model, where the inductances vary with the rotor position or time, is avoided.

From equation (2.46), the induction machine model can also be written in an abbreviated matrix format, and given as follows:

$$\underline{V}_{ABC} = \underline{R}_{ss} \bullet \underline{I}_{ABC} + \frac{d}{dt}\left(\underline{\Lambda}_{ABC}\right) \tag{2.47}$$

$$\underline{V}_{abc} = \underline{R}_{rr} \bullet \underline{I}_{abc} + \frac{d}{dt}\left(\underline{\Lambda}_{abc}\right) \tag{2.48}$$

where,

$$\underline{\Lambda}_{ABC} = \underline{L}_{ss} \bullet \underline{I}_{ABC} + \underline{L}_{sr} \bullet \underline{I}_{abc} \tag{2.49}$$

$$\underline{\Lambda}_{abc} = \underline{L}_{sr}^{t} \bullet \underline{I}_{ABC} + \underline{L}_{rr} \bullet \underline{I}_{abc} \tag{2.50}$$

Here, $\underline{V}_{ABC}$, is the stator voltage vector, $\underline{V}_{abc}$, is the rotor voltage vector, $\underline{I}_{ABC}$, is the stator current vector, and $\underline{I}_{abc}$, is the rotor current vector. Here, $\underline{\Lambda}_{ABC}$, is the stator flux linkage vector, $\underline{\Lambda}_{abc}$, is the rotor flux linkage vector, $\underline{R}_{ss}$, is the stator resistance matrix, and $\underline{R}_{rr}$, is the rotor resistance matrix. Here also, $\underline{L}_{ss}$, is the stator self and mutual inductance matrix, $\underline{L}_{rr}$, is the rotor self and mutual inductance matrix, while $\underline{L}_{sr}$ is the mutual inductance matrix between stator and rotor phase windings.

Choosing a transformation for the stator, $\underline{T}_s$, such that:

$$\underline{I}_{DQO} = \underline{T}_s \bullet \underline{I}_{ABC} \tag{2.51}$$

$$\underline{V}_{DQO} = \underline{T}_s \bullet \underline{V}_{ABC} \tag{2.52}$$

$$\underline{\Lambda}_{DQO} = \underline{T}_s \bullet \underline{\Lambda}_{ABC} \tag{2.53}$$

and choosing a transformation for the rotor, $\underline{T}_r$, such that:

$$\underline{I}_{dqo} = \underline{T}_r \bullet \underline{I}_{abc} \tag{2.54}$$

$$\underline{V}_{dqo} = \underline{T}_r \bullet \underline{V}_{abc} \tag{2.55}$$

$$\underline{\Lambda}_{dqo} = \underline{T}_r \bullet \underline{\Lambda}_{abc} \tag{2.56}$$

where, the transformation matrices, $\underline{T}_s$ and $\underline{T}_r$, must be nonsingular matrices, and by substituting equations (2.51) through (2.56) into equations (2.47) through (2.50), one can easily deduce the following equation, which is the transformed DQO model expressed in an arbitrary DQO-dqo reference frame. Detailed deduction will not be shown here.

$$\begin{gathered}\left[\begin{array}{c}\underline{V_{DQO}}\\ \underline{V_{dqo}}\end{array}\right] = \left[\begin{array}{cc}\underline{T_s} \bullet \underline{R_{ss}} \bullet \underline{T_s^{-1}} & \underline{0}\\ \underline{0} & \underline{T_r} \bullet \underline{R_{rr}} \bullet \underline{T_r^{-1}}\end{array}\right]\left[\begin{array}{c}\underline{I_{DQO}}\\ \underline{I_{dqo}}\end{array}\right] + \\ \frac{d}{dt}\left\{\left[\begin{array}{cc}(\underline{T_s} \bullet \underline{L_{ss}} \bullet \underline{T_s^{-1}}) & (\underline{T_s} \bullet \underline{L_{sr}} \bullet \underline{T_r^{-1}})\\ (\underline{T_r} \bullet \underline{L_{sr}^{t}} \bullet \underline{T_s^{-1}}) & (\underline{T_r} \bullet \underline{L_{rr}} \bullet \underline{T_r^{-1}})\end{array}\right]\left[\begin{array}{c}\underline{I_{DQO}}\\ \underline{I_{dqo}}\end{array}\right]\right\} - \left[\begin{array}{cc}\underline{\dot{T}_s} \bullet \underline{L_{ss}} \bullet \underline{T_s^{-1}} & \underline{\dot{T}_s} \bullet \underline{L_{sr}} \bullet \underline{T_r^{-1}}\\ \underline{\dot{T}_r} \bullet \underline{L_{sr}^{t}} \bullet \underline{T_s^{-1}} & \underline{\dot{T}_r} \bullet \underline{L_{rr}} \bullet \underline{T_r^{-1}}\end{array}\right]\left[\begin{array}{c}\underline{I_{DQO}}\\ \underline{I_{dqo}}\end{array}\right]\end{gathered} \tag{2.57}$$

For the wound rotor induction machine model expressed in a DQO-dqo reference frame fixed on the rotor, one needs to consider the schematic in Figure (2.5) to deduce the transformation matrices, $\underline{T}_{sro}$ and $\underline{T}_{rro}$. Here, $\underline{T}_{sro}$, is the stator transformation matrix, and $\underline{T}_{rro}$, is the rotor transformation matrix for the reference frame fixed on the rotor.

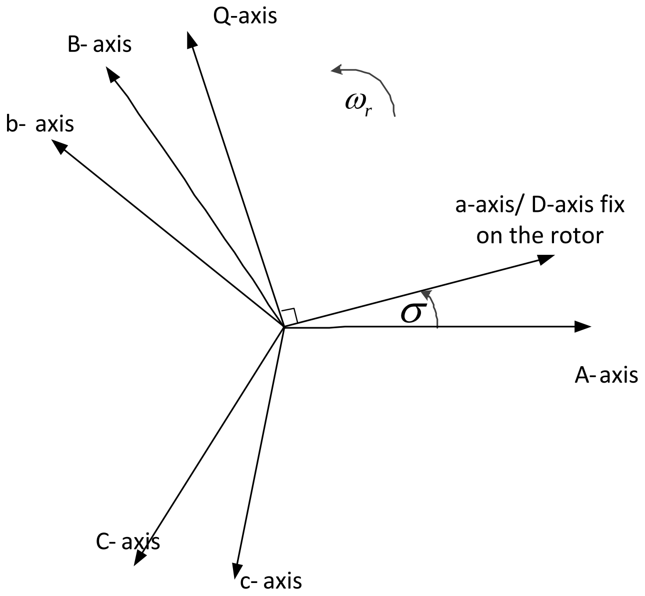

Figure 2.5 Schematic diagram of the ABC to DQO-dqo reference frame fixed on the rotor transformation

From Figure 2.5, one can easily deduce the stator and rotor transformation matrices by projecting the stator and rotor variables on the D and Q axes fixed on the rotor. The transformation matrices, $\underline{T}_{sro}$ and $\underline{T}_{rro}$, are written as follows:

$$\underline{T}_{sro} = \frac{2}{3}\begin{bmatrix} \cos(\sigma) & \cos\left(\sigma - {}^{2\pi}\!/_{3}\right) & \cos\left(\sigma - {}^{4\pi}\!/_{3}\right) \\ -\sin(\sigma) & -\sin\left(\sigma - {}^{2\pi}\!/_{3}\right) & -\sin\left(\sigma - {}^{4\pi}\!/_{3}\right) \\ {}^{1}\!/_{2} & {}^{1}\!/_{2} & {}^{1}\!/_{2} \end{bmatrix} \tag{2.58}$$

$$\underline{T}_{rro} = \frac{2}{3}\begin{bmatrix} 1 & -{}^{1}\!/_{2} & -{}^{1}\!/_{2} \\ 0 & {}^{\sqrt{3}}\!/_{2} & -{}^{\sqrt{3}}\!/_{2} \\ {}^{1}\!/_{2} & {}^{1}\!/_{2} & {}^{1}\!/_{2} \end{bmatrix} \tag{2.59}$$

Substituting equations (2.58) and (2.59) into equation (2.57), the induction motor model expressed in a DQO-dqo abbreviated matrix format can be written as follows:

$$\begin{bmatrix} \underline{V_{DQO}} \\ \underline{V_{dqo}} \end{bmatrix} = \begin{bmatrix} \underline{T_{sro}} \bullet \underline{R_{ss}} \bullet \underline{T_{sro}^{-1}} & \underline{0} \\ \underline{0} & \underline{T_{rro}} \bullet \underline{R_{rr}} \bullet \underline{T_{rro}^{-1}} \end{bmatrix} \begin{bmatrix} \underline{I_{DQO}} \\ \underline{I_{dqo}} \end{bmatrix} +$$

$$\frac{d}{dt}\left\{ \begin{bmatrix} (\underline{T_{sro}} \bullet \underline{L_{ss}} \bullet \underline{T_{sro}^{-1}}) & (\underline{T_{sro}} \bullet \underline{L_{sr}} \bullet \underline{T_{rro}^{-1}}) \\ (\underline{T_{rro}} \bullet \underline{L_{sr}^{t}} \bullet \underline{T_{sro}^{-1}}) & (\underline{T_{rro}} \bullet \underline{L_{rr}} \bullet \underline{T_{rro}^{-1}}) \end{bmatrix} \begin{bmatrix} \underline{I_{DQO}} \\ \underline{I_{dqo}} \end{bmatrix} \right\} - \begin{bmatrix} \underline{\dot{T}_{sro}} \bullet \underline{L_{ss}} \bullet \underline{T_{sro}^{-1}} & \underline{\dot{T}_{sro}} \bullet \underline{L_{sr}} \bullet \underline{T_{rro}^{-1}} \\ \underline{\dot{T}_{rro}} \bullet \underline{L_{sr}^{t}} \bullet \underline{T_{sro}^{-1}} & \underline{\dot{T}_{rro}} \bullet \underline{L_{rr}} \bullet \underline{T_{rro}^{-1}} \end{bmatrix} \begin{bmatrix} \underline{I_{DQO}} \\ \underline{I_{dqo}} \end{bmatrix} \tag{2.60}$$

Therefore, the wound rotor induction machine model expressed in the DQO-dqo reference frame fixed on the rotor can be derived, and written as follows:

$$\begin{bmatrix} v_{Dro} \\ v_{Qro} \\ v_{Oro} \\ \cdots \\ v_{dro} \\ v_{qro} \\ v_{oro} \end{bmatrix} = \left[\begin{array}{ccccccc} r_s & 0 & 0 & \vdots & 0 & 0 & 0 \\ 0 & r_s & 0 & \vdots & 0 & 0 & 0 \\ 0 & 0 & r_s & \vdots & 0 & 0 & 0 \\ \cdots & \cdots & \cdots & \vdots & \cdots & \cdots & \cdots \\ 0 & 0 & 0 & \vdots & r_r & 0 & 0 \\ 0 & 0 & 0 & \vdots & 0 & r_r & 0 \\ 0 & 0 & 0 & \vdots & 0 & 0 & r_r \end{array}\right] \begin{bmatrix} i_{Dro} \\ i_{Qro} \\ i_{Oro} \\ \cdots \\ i_{dro} \\ i_{qro} \\ i_{oro} \end{bmatrix}$$

$$+ \left[\begin{array}{ccccccc} L_{ss} - L_{sm} & 0 & 0 & \vdots & \frac{3}{2} L_{srm} & 0 & 0 \\ 0 & L_{ss} - L_{sm} & 0 & \vdots & 0 & \frac{3}{2} L_{srm} & 0 \\ 0 & 0 & L_{ss} + 2L_{sm} & \vdots & 0 & 0 & 0 \\ \cdots\cdots\cdots & \cdots\cdots\cdots & \cdots\cdots\cdots & \vdots & \cdots\cdots\cdots & \cdots\cdots\cdots & \cdots\cdots\cdots \\ \frac{3}{2} L_{srm} & 0 & 0 & \vdots & L_{rr} - L_{rm} & 0 & 0 \\ 0 & \frac{3}{2} L_{srm} & 0 & \vdots & 0 & L_{rr} - L_{rm} & 0 \\ 0 & 0 & 0 & \vdots & 0 & 0 & L_{rr} + 2L_{rm} \end{array}\right] \begin{bmatrix} \dot{i}_{Dro} \\ \dot{i}_{Qro} \\ \dot{i}_{Oro} \\ \cdots \\ \dot{i}_{dro} \\ \dot{i}_{qro} \\ \dot{i}_{oro} \end{bmatrix}$$

$$+\omega_r \left[\begin{array}{ccccccc} 0 & -(L_{ss} - L_{sm}) & 0 & \vdots & 0 & -\frac{3}{2} L_{srm} & 0 \\ (L_{ss} - L_{sm}) & 0 & 0 & \vdots & \frac{3}{2} L_{srm} & 0 & 0 \\ 0 & 0 & 0 & \vdots & 0 & 0 & 0 \\ \cdots\cdots\cdots & \cdots\cdots\cdots & \cdots & \vdots & \cdots\cdots\cdots & \cdots\cdots\cdots & \cdots \\ 0 & 0 & 0 & \vdots & 0 & 0 & 0 \\ 0 & 0 & 0 & \vdots & 0 & 0 & 0 \\ 0 & 0 & 0 & \vdots & 0 & 0 & 0 \end{array}\right] \begin{bmatrix} i_{Dro} \\ i_{Qro} \\ i_{Oro} \\ \cdots \\ i_{dro} \\ i_{qro} \\ i_{oro} \end{bmatrix} \tag{2.61}$$

2.4.3 DFIG Model Expressed in a DQO-dqo Stationary Stator Reference Frame

Instead of fixing the D-axis on the rotor, the induction machine model expressed in a stationary stator reference frame with the D-axis fixed on the stator. Now, considering the schematic diagram of the ABC to DQO-dqo stationary reference frame, shown in Figure 2.6.

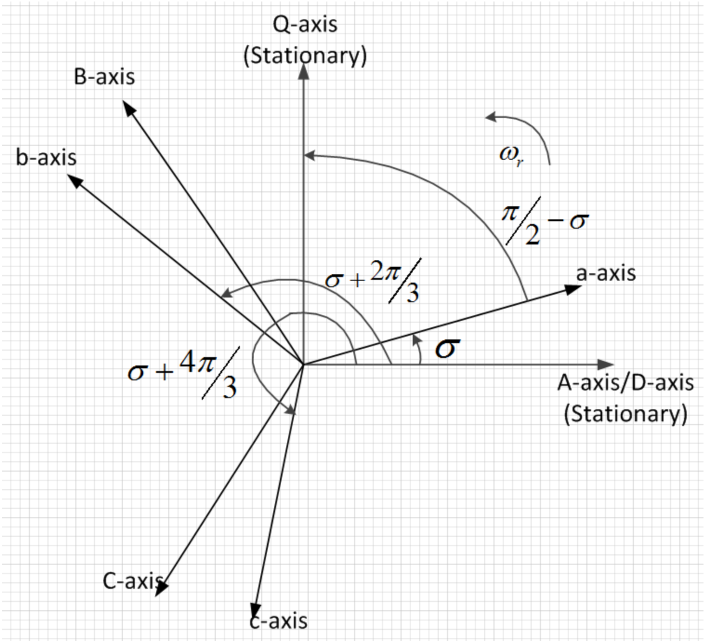

Figure 2.6 Schematic diagram of the ABC to DQO-dqo stationary reference frame transformation

One can deduce the stator and rotor transformation matrices, $\underline{T}_{sst}$ and $\underline{T}_{rst}$, for the stationary stator reference frame. This is done by projecting the stator and rotor variables on the D and Q axes fixed on the stator, and the transformation matrices, $\underline{T}_{sst}$ and $\underline{T}_{rst}$, are accordingly given as follows:

$$\underline{T}_{sst} = \frac{2}{3}\begin{bmatrix} 1 & -1/2 & -1/2 \\ 0 & \sqrt{3}/2 & -\sqrt{3}/2 \\ 1/2 & 1/2 & 1/2 \end{bmatrix} \tag{2.62}$$

$$\underline{T}_{rst} = \frac{2}{3}\begin{bmatrix} \cos(\sigma) & \cos\left(\sigma + {}^{2\pi}\!/_{3}\right) & \cos\left(\sigma + {}^{4\pi}\!/_{3}\right) \\ \sin(\sigma) & \sin\left(\sigma + {}^{2\pi}\!/_{3}\right) & \sin\left(\sigma + {}^{4\pi}\!/_{3}\right) \\ {}^{1}\!/_{2} & {}^{1}\!/_{2} & {}^{1}\!/_{2} \end{bmatrix} \tag{2.63}$$

Substituting from equations (2.62) and (2.63) into the above equation (2.57), the induction motor model expressed in a DQO-dqo abbreviated matrix format can be written as follows:

$$\begin{bmatrix} \underline{V_{DQO}} \\ \underline{V_{dqo}} \end{bmatrix} = \begin{bmatrix} \underline{T_{sst}} \bullet \underline{R_{ss}} \bullet \underline{T_{sst}^{-1}} & \underline{0} \\ \underline{0} & \underline{T_{rst}} \bullet \underline{R_{rr}} \bullet \underline{T_{rst}^{-1}} \end{bmatrix} \begin{bmatrix} \underline{I_{DQO}} \\ \underline{I_{dqo}} \end{bmatrix} + \tag{2.64}$$

$$\frac{d}{dt}\left\{ \begin{bmatrix} (\underline{T_{sst}} \bullet \underline{L_{ss}} \bullet \underline{T_{sst}^{-1}}) & (\underline{T_{sst}} \bullet \underline{L_{sr}} \bullet \underline{T_{rst}^{-1}}) \\ (\underline{T_{rst}} \bullet \underline{L_{sr}^{t}} \bullet \underline{T_{sst}^{-1}}) & (\underline{T_{rst}} \bullet \underline{L_{rr}} \bullet \underline{T_{rst}^{-1}}) \end{bmatrix} \begin{bmatrix} \underline{I_{DQO}} \\ \underline{I_{dqo}} \end{bmatrix} \right\} - \begin{bmatrix} \underline{\dot{T}_{sst}} \bullet \underline{L_{ss}} \bullet \underline{T_{sst}^{-1}} & \underline{\dot{T}_{sst}} \bullet \underline{L_{sr}} \bullet \underline{T_{rst}^{-1}} \\ \underline{\dot{T}_{rst}} \bullet \underline{L_{sr}^{t}} \bullet \underline{T_{sst}^{-1}} & \underline{\dot{T}_{rst}} \bullet \underline{L_{rr}} \bullet \underline{T_{rst}^{-1}} \end{bmatrix} \begin{bmatrix} \underline{I_{DQO}} \\ \underline{I_{dqo}} \end{bmatrix}$$

Therefore, the induction motor model expressed in the stationary stator reference frame can be deduced, and written as follows:

$$
\begin{aligned}
\begin{bmatrix} v_{Dst} \\ v_{Qst} \\ v_{Ost} \\ \cdots \\ v_{dst} \\ v_{qst} \\ v_{ost} \end{bmatrix}
&=
\begin{bmatrix}
r_s & 0 & 0 & \vdots & 0 & 0 & 0 \\
0 & r_s & 0 & \vdots & 0 & 0 & 0 \\
0 & 0 & r_s & \vdots & 0 & 0 & 0 \\
\cdots & \cdots & \cdots & \vdots & \cdots & \cdots & \cdots \\
0 & 0 & 0 & \vdots & r_r & 0 & 0 \\
0 & 0 & 0 & \vdots & 0 & r_r & 0 \\
0 & 0 & 0 & \vdots & 0 & 0 & r_r
\end{bmatrix}
\begin{bmatrix} i_{Dst} \\ i_{Qst} \\ i_{Ost} \\ \cdots \\ i_{dst} \\ i_{qst} \\ i_{ost} \end{bmatrix} \\
&+
\begin{bmatrix}
L_{ss}-L_{sm} & 0 & 0 & \vdots & \frac{3}{2}L_{srm} & 0 & 0 \\
0 & L_{ss}-L_{sm} & 0 & \vdots & 0 & \frac{3}{2}L_{srm} & 0 \\
0 & 0 & L_{ss}+2L_{sm} & \vdots & 0 & 0 & 0 \\
\cdots\cdots\cdots & \cdots\cdots\cdots & \cdots\cdots\cdots & \vdots & \cdots\cdots\cdots & \cdots\cdots\cdots & \cdots\cdots\cdots \\
\frac{3}{2}L_{srm} & 0 & 0 & \vdots & L_{rr}-L_{rm} & 0 & 0 \\
0 & \frac{3}{2}L_{srm} & 0 & \vdots & 0 & L_{rr}-L_{rm} & 0 \\
0 & 0 & 0 & \vdots & 0 & 0 & L_{rr}+2L_{rm}
\end{bmatrix}
\begin{bmatrix} \dot{i}_{Dst} \\ \dot{i}_{Qst} \\ \dot{i}_{Ost} \\ \cdots \\ \dot{i}_{dst} \\ \dot{i}_{qst} \\ \dot{i}_{ost} \end{bmatrix} \\
&+\omega_r
\begin{bmatrix}
0 & 0 & 0 & \vdots & 0 & 0 & 0 \\
0 & 0 & 0 & \vdots & 0 & 0 & 0 \\
0 & 0 & 0 & \vdots & 0 & 0 & 0 \\
\cdots\cdots\cdots & \cdots\cdots\cdots & \cdots & \vdots & \cdots\cdots\cdots & \cdots\cdots\cdots & \cdots \\
0 & \frac{3}{2}L_{srm} & 0 & \vdots & 0 & (L_{rr}-L_{rm}) & 0 \\
-\frac{3}{2}L_{srm} & 0 & 0 & \vdots & -(L_{rr}-L_{rm}) & 0 & 0 \\
0 & 0 & 0 & \vdots & 0 & 0 & 0
\end{bmatrix}
\begin{bmatrix} i_{Dst} \\ i_{Qst} \\ i_{Ost} \\ \cdots \\ i_{dst} \\ i_{qst} \\ i_{ost} \end{bmatrix}
\end{aligned}
\tag{2.65}
$$

2.4.4 DFIG Model Expressed in a DQO-dqo Synchronously Rotating Reference Frame

The DFIG model expressed in a synchronously rotating reference frame has the advantage that the time varying variables of the three-phase system, such as stator currents and voltages, rotor currents and voltages, become constants. This feature will be very useful in formulating and implementing any digital control systems. In this thesis, for control purposes, the DFIG model expressed in a synchronously rotating reference frame will be chosen, and the deduction of the develop torque, active power and reactive power expressed in a synchronously rotating reference frame will be given later in this section.

Instead of fixing the D-axis on the rotor or on the stator, the D-axis in the induction machine model expressed in a synchronously rotating reference frame will rotate at synchronous speed. Consider the schematic diagram of the ABC to DQO-dqo synchronously rotating reference frame transformation, which is shown in Figure 2.7.

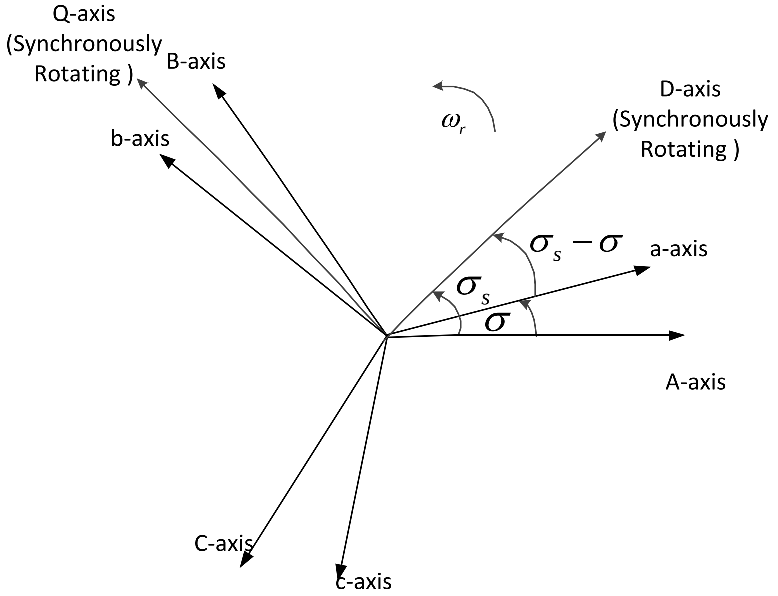

Figure 2.7 Schematic diagram of the ABC to DQO-dqo synchronously rotating reference frame transformation

Here, σ_s , is the angle between the stator A-axis and the synchronously rotating D-axis, and is equal to $\sigma_s = \sigma_{s0} + \int_0^t \omega_s(t)dt$, or $\sigma_s = \sigma_{s0} + \omega_s t$, for a fixed operation angular speed/frequency.

where, ω_s , is the synchronous speed.

By using the same logic and steps of DQO-dqo models developed as in the two previous cases, the stator and rotor transformation matrices, $\underline{T}_s$ and $\underline{T}_r$, can be deduced and given as follows.

$$\underline{T}_s = \frac{2}{3}\begin{bmatrix} \cos(\sigma_s) & \cos\left(\sigma_s - {}^{2\pi}\!/_{3}\right) & \cos\left(\sigma_s - {}^{4\pi}\!/_{3}\right) \\ -\sin(\sigma_s) & -\sin\left(\sigma_s - {}^{2\pi}\!/_{3}\right) & -\sin\left(\sigma_s - {}^{4\pi}\!/_{3}\right) \\ {}^{1}\!/_{2} & {}^{1}\!/_{2} & {}^{1}\!/_{2} \end{bmatrix} \tag{2.66}$$

$$\underline{T}_r = \frac{2}{3}\begin{bmatrix} \cos(\sigma_s - \sigma) & \cos\left((\sigma_s - \sigma) - {}^{2\pi}\!/_{3}\right) & \cos\left((\sigma_s - \sigma) - {}^{4\pi}\!/_{3}\right) \\ -\sin(\sigma_s - \sigma) & -\sin\left((\sigma_s - \sigma) - {}^{2\pi}\!/_{3}\right) & -\sin\left((\sigma_s - \sigma) - {}^{4\pi}\!/_{3}\right) \\ {}^{1}\!/_{2} & {}^{1}\!/_{2} & {}^{1}\!/_{2} \end{bmatrix} \tag{2.67}$$

Substituting the equations (2.66) and (2.67) into the above equation (2.57), the induction motor model expressed in the synchronously rotating reference frame can be deduced, and written as follows:

$$\begin{bmatrix} v_D \\ v_Q \\ v_O \\ \cdots \\ v_d \\ v_q \\ v_o \end{bmatrix} = \begin{bmatrix} r_s & 0 & 0 & \vdots & 0 & 0 & 0 \\ 0 & r_s & 0 & \vdots & 0 & 0 & 0 \\ 0 & 0 & r_s & \vdots & 0 & 0 & 0 \\ \cdots & \cdots & \cdots & \vdots & \cdots & \cdots & \cdots \\ 0 & 0 & 0 & \vdots & r_r & 0 & 0 \\ 0 & 0 & 0 & \vdots & 0 & r_r & 0 \\ 0 & 0 & 0 & \vdots & 0 & 0 & r_r \end{bmatrix} \begin{bmatrix} i_D \\ i_Q \\ i_O \\ \cdots \\ i_d \\ i_q \\ i_o \end{bmatrix}$$

$$+ \begin{bmatrix} L_{ss} - L_{sm} & 0 & 0 & \vdots & \frac{3}{2} L_{srm} & 0 & 0 \\ 0 & L_{ss} - L_{sm} & 0 & \vdots & 0 & \frac{3}{2} L_{srm} & 0 \\ 0 & 0 & L_{ss} + 2L_{sm} & \vdots & 0 & 0 & 0 \\ \cdots\cdots\cdots & \cdots\cdots\cdots & \cdots\cdots\cdots & \vdots & \cdots\cdots\cdots & \cdots\cdots\cdots & \cdots\cdots\cdots \\ \frac{3}{2} L_{srm} & 0 & 0 & \vdots & L_{rr} - L_{rm} & 0 & 0 \\ 0 & \frac{3}{2} L_{srm} & 0 & \vdots & 0 & L_{rr} - L_{rm} & 0 \\ 0 & 0 & 0 & \vdots & 0 & 0 & L_{rr} + 2L_{rm} \end{bmatrix} \begin{bmatrix} \dot{i}_D \\ \dot{i}_Q \\ \dot{i}_O \\ \cdots \\ \dot{i}_d \\ \dot{i}_q \\ \dot{i}_o \end{bmatrix}$$

$$+ \begin{bmatrix} 0 & -\omega_s \left(L_{ss} - L_{sm} \right) & 0 & \vdots & 0 & -\frac{3}{2} \omega_s L_{srm} & 0 \\ \omega_s \left(L_{ss} - L_{sm} \right) & 0 & 0 & \vdots & \frac{3}{2} \omega_s L_{srm} & 0 & 0 \\ 0 & 0 & 0 & \vdots & 0 & 0 & 0 \\ \cdots\cdots\cdots\cdots & \cdots\cdots\cdots\cdots & \cdots & \vdots & \cdots\cdots\cdots\cdots\cdots\cdots\cdots & \cdots\cdots\cdots\cdots\cdots\cdots\cdots & \cdots \\ 0 & -\frac{3}{2} \left(\omega_s - \omega_r \right) L_{srm} & 0 & \vdots & 0 & -\left(\omega_s - \omega_r \right) \left(L_{rr} - L_{rm} \right) & 0 \\ \frac{3}{2} \left(\omega_s - \omega_r \right) L_{srm} & 0 & 0 & \vdots & \left(\omega_s - \omega_r \right) \left(L_{rr} - L_{rm} \right) & 0 & 0 \\ 0 & 0 & 0 & \vdots & 0 & 0 & 0 \end{bmatrix} \begin{bmatrix} i_D \\ i_Q \\ i_O \\ \cdots \\ i_d \\ i_q \\ i_o \end{bmatrix} \tag{2.68}$$

The torque expression in the synchronously rotating reference frame can be developed from the input power, P_{in}, and the deduction processes are given as follows [127]:

$$P_{in} = \underline{I}^{t}_{ABC} \bullet \underline{V}_{ABC} + \underline{I}^{t}_{abc} \bullet \underline{V}_{abc} \tag{2.69}$$

The corresponding mechanical power, P_{mech}, is given in the ABC, abc reference frames as follows:

$$P_{mech} = P_{in} - \underline{I}_{ABC}^{t} \bullet \underline{R}_{ss} \bullet \underline{I}_{ABC} - \underline{I}_{abc}^{t} \bullet \underline{R}_{rr} \bullet \underline{I}_{abc} \tag{2.70}$$

Considering equations (2.47) and (2.48), which constitute the DFIG model expressed in the ABC reference frame, one can easily write:

$$P_{mech} = \underline{I}_{ABC}^{t} \bullet \left(\frac{d}{dt} \underline{\Lambda}_{ABC} \right) + \underline{I}_{abc}^{t} \bullet \left(\frac{d}{dt} \underline{\Lambda}_{abc} \right) \tag{2.71}$$

Substituting equations (2.51) through (2.56) into equation (2.71), the mechanical power can be expressed in an arbitrary DQO-dqo reference frame, and given as follows:

$$P_{mech} = \left(\underline{T}_s^{-1} \bullet \underline{I}_{DQO} \right)^{t} \bullet \left[\frac{d}{dt} \left(\underline{T}_s^{-1} \bullet \underline{\Lambda}_{DQO} \right) \right] + \left(\underline{T}_r^{-1} \bullet \underline{I}_{dqo} \right)^{t} \bullet \left[\frac{d}{dt} \left(\underline{T}_r^{-1} \bullet \frac{d}{dt} \underline{\Lambda}_{dqo} \right) \right] \tag{2.72}$$

$$\begin{aligned} P_{mech} = {} & \underline{I}_{DQO}^{t} \bullet \left(\underline{T}_s^{-1} \right)^{t} \bullet \left(\underline{T}_s^{-1} \bullet \frac{d}{dt} \underline{\Lambda}_{DQO} - \underline{T}_s^{-1} \bullet \dot{\underline{T}}_s \bullet \underline{T}_s^{-1} \bullet \underline{\Lambda}_{DQO} \right) \\ & + \underline{I}_{dqo}^{t} \bullet \left(\underline{T}_r^{-1} \right)^{t} \bullet \left(\underline{T}_r^{-1} \bullet \frac{d}{dt} \underline{\Lambda}_{dqo} - \underline{T}_r^{-1} \bullet \dot{\underline{T}}_r \bullet \underline{T}_r^{-1} \bullet \underline{\Lambda}_{dqo} \right) \end{aligned} \tag{2.73}$$

In order to obtain the mechanical power expression in the DQO-dqo synchronously rotating reference frame, the stator and rotor transformation matrices, $\underline{T}_s$ and $\underline{T}_r$, need to be substituted into equation (2.73). Here, the inverses of these transformation matrices are given as follows:

$$\underline{T}_s^{-1} = \begin{bmatrix} \cos(\sigma_s) & -\sin(\sigma_s) & \\ \cos\left(\sigma_s - 2\pi/3\right) & -\sin\left(\sigma_s - 2\pi/3\right) & 1 \\ \cos\left(\sigma_s - 4\pi/3\right) & -\sin\left(\sigma_s - 4\pi/3\right) & 1 \end{bmatrix} \tag{2.74}$$

$$\underline{T}_r^{-1} = \begin{bmatrix} \cos(\sigma_s - \sigma) & -\sin(\sigma_s - \sigma) & \\ \cos\left((\sigma_s - \sigma) - 2\pi/3\right) & -\sin\left((\sigma_s - \sigma) - 2\pi/3\right) & 1 \\ \cos\left((\sigma_s - \sigma) - 4\pi/3\right) & -\sin\left((\sigma_s - \sigma) - 4\pi/3\right) & 1 \end{bmatrix} \tag{2.75}$$

Then, the following equations can be obtained:

$$\left(\underline{T}_s^{-1}\right)^t \bullet \underline{T}_s^{-1} = \begin{bmatrix} 3/2 & 0 & 0 \\ 0 & 3/2 & 0 \\ 0 & 0 & 3 \end{bmatrix} = K_s \underline{G}_s \tag{2.76}$$

$$\left(\underline{T}_r^{-1}\right)^t \bullet \underline{T}_r^{-1} = \begin{bmatrix} 3/2 & 0 & 0 \\ 0 & 3/2 & 0 \\ 0 & 0 & 3 \end{bmatrix} = K_r \underline{G}_r \tag{2.77}$$

Here, from equations (2.76) and (2.77), one can write:

$$K_s = K_r = 3/2\,, \qquad \underline{G}_s = \underline{G}_r = \begin{bmatrix} 1 & 0 & 0 \\ 0 & 1 & 0 \\ 0 & 0 & 2 \end{bmatrix} \tag{2.78}$$

where, K$_s$ and K$_r$, are scalar constants, while $\underline{G}_s$ and $\underline{G}_r$, are matrices with constant coefficients. Thus, equation (2.73) becomes:

$$\begin{aligned} P_{mech} = {} & K_s \bullet \underline{I}_{DQO}^t \bullet \underline{G}_s \bullet \frac{d}{dt} \underline{\Lambda}_{DQO} - K_s \bullet \underline{I}_{DQO}^t \bullet \underline{G}_s \bullet \left(\dot{\underline{T}}_s \bullet \underline{T}_s^{-1}\right) \bullet \underline{\Lambda}_{DQO} \\ & + K_r \bullet \underline{I}_{dqo}^t \bullet \underline{G}_r \bullet \frac{d}{dt} \underline{\Lambda}_{dqo} - K_r \bullet \underline{I}_{dqo}^t \bullet \underline{G}_r \bullet \left(\dot{\underline{T}}_r \bullet \underline{T}_r^{-1}\right) \bullet \underline{\Lambda}_{dqo} \end{aligned} \tag{2.79}$$

Here, the transformer voltage terms in equation (2.79) above are neglected due to their small contribution to the torque profile when compared with the rotational voltage contributions, and their non-existent (zero) contribution to the average torque. Then, the mechanical power, P$_{mech}$, becomes:

$$P_{mech} = -K_s \bullet \underline{I}_{DQO}^t \bullet \underline{G}_s \bullet \left(\dot{\underline{T}}_s \bullet \underline{T}_s^{-1}\right) \bullet \underline{\Lambda}_{DQO} - K_r \bullet \underline{I}_{dqo}^t \bullet \underline{G}_r \bullet \left(\dot{\underline{T}}_r \bullet \underline{T}_r^{-1}\right) \bullet \underline{\Lambda}_{dqo} \tag{2.80}$$

where,

$$\dot{\underline{T}}_s = \frac{2}{3}\omega_s \begin{bmatrix} -\sin(\sigma_s) & -\sin\left(\sigma_s - 2\pi/3\right) & -\sin\left(\sigma_s - 4\pi/3\right) \\ -\cos(\sigma_s) & -\cos\left(\sigma_s - 2\pi/3\right) & -\cos\left(\sigma_s - 4\pi/3\right) \\ 0 & 0 & 0 \end{bmatrix} \tag{2.81}$$

$$\dot{\underline{T}}_r = \frac{2}{3}(\omega_s - \omega_r)\begin{bmatrix} -\sin(\sigma_s - \sigma) & -\sin\left((\sigma_s - \sigma) - {}^{2\pi}\!/_{3}\right) & -\sin\left((\sigma_s - \sigma) - {}^{4\pi}\!/_{3}\right) \\ -\cos(\sigma_s - \sigma) & -\cos\left((\sigma_s - \sigma) - {}^{2\pi}\!/_{3}\right) & -\cos\left((\sigma_s - \sigma) - {}^{4\pi}\!/_{3}\right) \\ 0 & 0 & 0 \end{bmatrix} \quad (2.82)$$

Therefore, the develop torque, T_{dev}, becomes [127]:

$$T_{dev} = \frac{P_{mech}}{\omega_{rm}} = -\frac{k_s}{\omega_{rm}} \cdot \underline{I}_{DQO}^{t} \cdot \underline{G}_s \cdot \left(\dot{\underline{T}}_s \cdot \underline{T}_s^{-1}\right) \cdot \underline{\Lambda}_{DQO} - \frac{k_r}{\omega_{rm}} \cdot \underline{I}_{dqo}^{t} \cdot \underline{G}_r \cdot \left(\dot{\underline{T}}_r \cdot \underline{T}_r^{-1}\right) \cdot \underline{\Lambda}_{dqo} \quad (2.83)$$

Here, ω_{rm}, is the mechanical rotational speed and has following relationship to the rotor speed in electrical measure:

$$\omega_{rm} = \frac{\omega_r}{P/2} \quad (2.84)$$

where, P, is the number of poles of the DFIG.

From equation (2.68), the stator flux linkages and rotor flux linkages can be written as follows:

$$\underline{\Lambda}_{DQO} = \begin{bmatrix} \lambda_D \\ \lambda_Q \\ \lambda_O \end{bmatrix} = \begin{bmatrix} L_{ss} - L_{sm} & 0 & 0 \\ 0 & L_{ss} - L_{sm} & 0 \\ 0 & 0 & L_{ss} + 2L_{sm} \end{bmatrix}\begin{bmatrix} i_D \\ i_Q \\ i_O \end{bmatrix} + \begin{bmatrix} \frac{3}{2}L_{srm} & 0 & 0 \\ 0 & \frac{3}{2}L_{srm} & 0 \\ 0 & 0 & 0 \end{bmatrix}\begin{bmatrix} i_d \\ i_q \\ i_o \end{bmatrix} \quad (2.85)$$

$$\underline{\Lambda}_{dqo} = \begin{bmatrix} \lambda_d \\ \lambda_q \\ \lambda_o \end{bmatrix} = \begin{bmatrix} \frac{3}{2}L_{srm} & 0 & 0 \\ 0 & \frac{3}{2}L_{srm} & 0 \\ 0 & 0 & 0 \end{bmatrix}\begin{bmatrix} i_D \\ i_Q \\ i_O \end{bmatrix} + \begin{bmatrix} L_{rr} - L_{rm} & 0 & 0 \\ 0 & L_{rr} - L_{rm} & 0 \\ 0 & 0 & L_{rr} + 2L_{rm} \end{bmatrix}\begin{bmatrix} i_d \\ i_q \\ i_o \end{bmatrix} \quad (2.86)$$

Substituting $\underline{G}_s$, $\underline{G}_r$, K_s, K_r, $\dot{\underline{T}}_s$, $\underline{T}_s^{-1}$, $\dot{\underline{T}}_r$, $\underline{T}_r^{-1}$, $\underline{\Lambda}_{DQO}$ and $\underline{\Lambda}_{dqo}$ into equation (2.83) will yield:

$$T_{dev} = -\frac{3/2}{\omega_{rm}}\left[\omega_s\left(i_D\lambda_Q - i_Q\lambda_D\right) + \left(\omega_s - \omega_r\right)\left(i_d\lambda_q - i_q\lambda_d\right)\right] \tag{2.87}$$

Equation (2.87) can be further simplified, and the corresponding deduction processes are detailed as follows. Here, the equation (2.87) is rewritten as follows:

$$T_{dev} = -\frac{3/2}{\omega_{rm}}\left[\omega_s\left(i_D\lambda_Q - i_Q\lambda_D + i_d\lambda_q - i_q\lambda_d\right) - \omega_r\left(i_d\lambda_q - i_q\lambda_d\right)\right] \tag{2.88}$$

Here, the following relationship can be developed by substituting the flux linkages in equations (2.85) and (2.86) into equation (2.88) above:

$$\omega_s\left(i_D\lambda_Q - i_Q\lambda_D + i_d\lambda_q - i_q\lambda_d\right) = 0 \tag{2.89}$$

Considering equation (2.84), the torque expression becomes:

$$T_{dev} = \frac{3}{2}\left(\frac{P}{2}\right)\left(i_d\lambda_q - i_q\lambda_d\right) \tag{2.90}$$

In term of currents, one can write the following:

$$\begin{aligned} T_{dev} &= \frac{3}{2}\left(\frac{P}{2}\right)\left(i_d\left(\frac{3}{2}L_{srm}i_Q + \left(L_{rr} - L_{rm}\right)i_q\right) - i_q\left(\frac{3}{2}L_{srm}i_D + \left(L_{rr} - L_{rm}\right)i_d\right)\right) \\ \Rightarrow T_{dev} &= \frac{3}{2}\left(\frac{P}{2}\right)\left(\frac{3}{2}L_{srm}\right)\left(i_Qi_d - i_Di_q\right) \end{aligned} \tag{2.91}$$

The torque expression can also be expressed in terms of stator currents and flux linkages. The developments are given as follows:

$$\begin{aligned} T_{dev} &= \frac{3}{2}\left(\frac{P}{2}\right)\left(\frac{3}{2}L_{srm}\right)\left(i_Qi_d - i_Di_q\right) \\ &= \frac{3}{2}\left(\frac{P}{2}\right)\left[\frac{3}{2}L_{srm}i_Qi_d + i_Q\left(L_{ss} - L_{sm}\right)i_D - \frac{3}{2}L_{srm}i_Di_q - i_Q\left(L_{ss} - L_{sm}\right)i_D\right] \\ &= \frac{3}{2}\left(\frac{P}{2}\right)\left[i_Q\left(\left(L_{ss} - L_{sm}\right)i_D + \frac{3}{2}L_{srm}i_d\right) - i_D\left(\left(L_{ss} - L_{sm}\right)i_Q + \frac{3}{2}L_{srm}i_q\right)\right] \end{aligned} \tag{2.92}$$

Considering equations (2.85) and (2.86), the torque expression can be simplified as follows:

$$T_{dev} = \frac{3}{2}\left(\frac{P}{2}\right)\left[i_Q\lambda_D - i_D\lambda_Q\right] \tag{2.93}$$

For a three-phase wound rotor induction machine, the active power and reactive power at the stator terminals can be deduced as follows:

$$\begin{aligned} P_s &= \frac{3}{2}\mathrm{Re}\left(\vec{V}\bullet\vec{I}^*\right) = \frac{3}{2}\mathrm{Re}\left(v_D + jv_Q\right)\bullet\left(i_D - ji_Q\right) \\ &= \frac{3}{2}\mathrm{Re}\left[\left(v_Di_D + v_Qi_Q\right) + j\left(v_Qi_D - v_Di_Q\right)\right] = \frac{3}{2}\left(v_Di_D + v_Qi_Q\right) \end{aligned} \tag{2.94}$$

$$\begin{aligned} Q_s &= \frac{3}{2}\mathrm{Im}\left(\vec{V}\bullet\vec{I}^*\right) = \frac{3}{2}\mathrm{Im}\left(v_D + jv_Q\right)\bullet\left(i_D - ji_Q\right) \\ &= \frac{3}{2}\mathrm{Im}\left[\left(v_Di_D + v_Qi_Q\right) + j\left(v_Qi_D - v_Di_Q\right)\right] = \frac{3}{2}\left(v_Qi_D - v_Di_Q\right) \end{aligned} \tag{2.95}$$

where, v_D, v_Q, i_D and i_D, are instantaneous time-domain voltage and current D and Q components, respectively.

2.4.5 Two Reduced Order Models Expressed in the DQO-dqo Synchronously Rotating Reference Frame

Since the stator and rotor phase windings of the DFIG are symmetric, this means that the zero-sequence components of the DFIG model expressed in the DQO synchronously rotating reference frame could be eliminated. Hence, the equation (2.68) is expanded and rewritten as follows:

$$v_D = r_s\bullet i_D + \left(L_{ss} - L_{sm}\right)\bullet\dot{i}_D + \frac{3}{2}L_{srm}\bullet\dot{i}_d - \omega_s\bullet\left(L_{ss} - L_{sm}\right)\bullet i_Q - \frac{3}{2}\omega_s\bullet L_{srm}\bullet i_q \tag{2.96}$$

$$v_Q = r_s\bullet i_Q + \left(L_{ss} - L_{sm}\right)\bullet\dot{i}_Q + \frac{3}{2}L_{srm}\bullet\dot{i}_q + \omega_s\bullet\left(L_{ss} - L_{sm}\right)\bullet i_D + \frac{3}{2}\omega_s\bullet L_{srm}\bullet i_d \tag{2.97}$$

$$v_d = r_r\bullet i_d + \frac{3}{2}L_{srm}\bullet\dot{i}_D + \left(L_{rr} - L_{rm}\right)\bullet\dot{i}_d - \frac{3}{2}\left(\omega_s - \omega_r\right)L_{srm}\bullet i_Q - \left(\omega_s - \omega_r\right)(L_{rr} - L_{rm})\bullet i_q \tag{2.98}$$

$$v_q = r_r\bullet i_q + \frac{3}{2}L_{srm}\bullet\dot{i}_Q + \left(L_{rr} - L_{rm}\right)\bullet\dot{i}_q + \frac{3}{2}\left(\omega_s - \omega_r\right)L_{srm}\bullet i_D + \left(\omega_s - \omega_r\right)(L_{rr} - L_{rm})\bullet i_d \tag{2.99}$$

Here, let us redefine the inductances in equations (2.96) through (2.99) as follows:

$$L_s = L_{ss} - L_{sm} \tag{2.100}$$

$$L_r = L_{rr} - L_{rm} \tag{2.101}$$

$$L_m = 1.5 L_{srm} \tag{2.102}$$

where, Ls, is the stator leakage inductance, Lr, is the rotor leakage inductance, and Lm, is the magnetizing inductance. Thus, the DFIG model expressed in the DQO synchronously rotating reference frame can be written as follows:

$$v_D = r_s \bullet i_D + L_s \bullet \dot{i}_D + L_m \bullet \dot{i}_d - \omega_s \bullet L_s \bullet i_Q - \omega_s \bullet L_m \bullet i_q \tag{2.103}$$

$$v_Q = r_s \bullet i_Q + L_s \bullet \dot{i}_Q + L_m \bullet \dot{i}_q + \omega_s \bullet L_s \bullet i_D + \omega_s \bullet L_m \bullet i_d \tag{2.104}$$

$$v_d = r_r \bullet i_d + L_m \bullet \dot{i}_D + \bullet \dot{L}_r \; i_d (\omega \quad \omega_s) \; \bullet_r L \;_m (i - \omega_Q \quad \omega)_s \; \bullet \tag{2.105}$$

$$v_q = r_r \bullet i_q + L_m \bullet \dot{i}_Q + L_r \bullet \dot{i}_q + (\omega_s - \omega_r) L_m \bullet i_D + (\omega_s - \omega_r) L_r \bullet i_d \tag{2.106}$$

Observing the right hand side of equations (2.103) through (2.106) and ignoring the resistive voltage drops, the remaining terms should be the flux linkages and derivatives of the flux linkages. Therefore, based on these considerations, the flux linkages can be rewritten as follows:

$$\lambda_D = L_s i_D + L_m i_d \tag{2.107}$$

$$\lambda_Q = L_s i_Q + L_m i_q \tag{2.108}$$

$$\lambda_d = L_r i_d + L_m i_D \tag{2.109}$$

$$\lambda_q = L_r i_q + L_m i_Q \tag{2.110}$$

Here, in order to distinguish the new model from the model which includes the zero-sequence components, different subscripts are used in this model. Here, ds and qs, are the stator direct and quadrature axes components, while dr and qr, are the rotor direct and quadrature axes components. Let us take the voltages as a example, the following relationship should be stated:

$$v_D \equiv v_{ds}\,,\quad v_Q \equiv v_{qs}\,,\quad v_d \equiv v_{dr}\,,\quad v_q \equiv v_{qr} \tag{2.111}$$

The same procedure will be also implemented for the currents and flux linkages. Then, substituting from equations (2.107) through (2.110) into equations (2.103) through (2.106) and using the new subscripts mentioned above, the DFIG model, in which the zero-sequence components are eliminated, can be derived as follows:

$$v_{ds} = r_s i_{ds} + \frac{d\lambda_{ds}}{dt} - \omega_s \lambda_{qs} \tag{2.112}$$

$$v_{qs} = r_s i_{qs} + \frac{d\lambda_{qs}}{dt} + \omega_s \lambda_{ds} \tag{2.113}$$

$$v_{dr} = r_r i_{dr} + \frac{d\lambda_{dr}}{dt} - \left(\omega_s - \omega_r\right)\lambda_{qr} \tag{2.114}$$

$$v_{qr} = r_r i_{qr} + \frac{d\lambda_{qr}}{dt} + \left(\omega_s - \omega_r\right)\lambda_{dr} \tag{2.115}$$

The flux linkages are given as follows:

$$\lambda_{ds} = L_s i_{ds} + L_m i_{dr} \tag{2.116}$$

$$\lambda_{qs} = L_s i_{qs} + L_m i_{qr} \tag{2.117}$$

$$\lambda_{dr} = L_{\mathrm{r}} i_{dr} + L_m i_{ds} \tag{2.118}$$

$$\lambda_{qr} = L_{\mathrm{r}} i_{qr} + L_m i_{qs} \tag{2.119}$$

Here, equations (2.112) through (2.115) constitute the DFIG fourth order model which is widely used in wind turbine-generator systems, and usually called the “full order model”. The expressions of the torque, active power and reactive power of the stator using the new subscript expressions can be rewritten as follows:

$$T_{dev} = \frac{3}{2}\left(\frac{P}{2}\right)\left[\lambda_{ds} i_{qs} - \lambda_{qs} i_{ds}\right] \tag{2.120}$$

$$P_s = \frac{3}{2}\left(v_{ds} i_{ds} + v_{qs} i_{qs}\right) \tag{2.121}$$

$$Q_s = \frac{3}{2}\left(v_{qs} i_{ds} - v_{ds} i_{qs}\right) \tag{2.122}$$

Equations (2.112) through (2.115) and equations (2.120) through (2.122) are the DFIG model and expressions for the torque, active and reactive power, and will be used in the controller design in the next chapter.

From equations (2.112) through (2.115), one can easily obtain the reduced second order model by ignoring the stator transients, they are, the derivatives of the stator flux linkage terms. By setting the derivatives of the stator flux linkages to zero, the following relationships can be obtained:

$$\dot{\lambda}_{ds} = 0 = L_s \dot{i}_{ds} + L_m \dot{i}_{dr} \Rightarrow \dot{i}_{ds} = -\frac{L_m}{L_s} \dot{i}_{dr} \tag{2.123}$$

$$\dot{\lambda}_{qs} = 0 = L_s \dot{i}_{qs} + L_m \dot{i}_{qr} \Rightarrow \dot{i}_{qs} = -\frac{L_m}{L_s} \dot{i}_{qr} \tag{2.124}$$

Thereby, substituting from equations (2.116) and (2.117) into equations (2.112) and (2.113), the following set of equations can be derived, in which the derivatives of the stator flux linkages are neglected:

$$v_{ds} = r_s i_{ds} - \omega_s L_s i_{qs} - \omega_s L_m i_{qr} \tag{2.125}$$

$$v_{qs} = r_s i_{qs} + \omega_s L_s i_{ds} + \omega_s L_m i_{dr} \tag{2.126}$$

From equations (2.125) and (2.126), the stator currents, i_{ds} and i_{qs}, can be obtained by expressing the stator currents as functions of the rotor d-axis and q-axis currents. From equation (2.126), the following equation can be derived:

$$i_{qs} = \left(v_{qs} - \omega_s L_s i_{ds} - \omega_s L_m i_{dr} \right) \big/ r_s \tag{2.127}$$

Substituting from equation (2.127) into equation (2.125), the stator d-axis current can be obtained from following equation:

$$v_{ds} = r_s i_{ds} - \omega_s L_s \left(\frac{\left(v_{qs} - \omega_s L_s i_{ds} - \omega_s L_m i_{dr} \right)}{r_s} \right) - \omega_s L_m i_{qr} \tag{2.128}$$

Then, the stator q-axis current can also be deduced by substituting the stator d-axis current into equation (2.126). Here, the stator d- and q- axes currents are calculated as follows:

$$i_{ds} = \frac{r_s v_{ds} + \omega_s L_s v_{qs} - \omega_s^2 L_s L_m i_{dr} + \omega_s r_s L_m i_{qr}}{\omega_s^2 L_s^2 + r_s^2} \tag{2.129}$$

$$i_{qs} = \frac{r_s v_{qs} - \omega_s L_s v_{ds} - \omega_s^2 L_s L_m i_{qr} - \omega_s r_s L_m i_{dr}}{\omega_s^2 L_s^2 + r_s^2} \tag{2.130}$$

Substituting the rotor flux linkages in equations (2.118) through (2.119) into equations (2.114) and (2.115), one can write:

$$v_{dr} = r_r i_{dr} + \frac{d\left(L_r i_{dr} + L_m i_{ds} \right)}{dt} - \left(\omega_s - \omega_r \right)\left(L_r i_{qr} + L_m i_{qs} \right) \tag{2.131}$$

$$v_{qr} = r_r i_{qr} + \frac{d\left(L_r i_{qr} + L_m i_{qs} \right)}{dt} + \left(\omega_s - \omega_r \right)\left(L_r i_{dr} + L_m i_{ds} \right) \tag{2.132}$$

Considering equations (2.123) and (2.124), the rotor voltage expressions in equations (2.131) and (2.132) can be rewritten as follows:

$$v_{dr} = r_r i_{dr} + (L_r - \frac{L_m^2}{L_s}) \frac{di_{dr}}{dt} - \left(\omega_s - \omega_r \right)(L_r i_{qr} + L_m i_{qs}) \tag{2.133}$$

$$v_{qr} = r_r i_{dr} + (L_r - \frac{L_m^2}{L_s}) \frac{di_{qr}}{dt} + \left(\omega_s - \omega_r \right)(L_r i_{dr} + L_m i_{ds}) \tag{2.134}$$

By substituting the stator currents in equations (2.129) and (2.130) into the equations (2.133) and (2.134), the reduced second order model can be deduced. From equations (2.125) through (2.126) and equations (2.133) through (2.134), it can be seen that the derivative terms in the stator voltage equations are eliminated, and only two rotor current derivative terms exist in the rotor voltage equations.

The steady state DFIG model can be easily acquired by neglecting both stator and rotor transients, which can be done by setting the derivatives of the stator and rotor flux linkage terms to zero, which yields the following:

$$v_{ds} = r_s i_{ds} - \omega_s \lambda_{qs} \tag{2.135}$$

$$v_{qs} = r_s i_{qs} + \omega_s \lambda_{ds} \tag{2.136}$$

$$v_{dr} = r_r i_{dr} - \left(\omega_s - \omega_r\right) \lambda_{qr} \tag{2.137}$$

$$v_{qr} = r_r i_{qr} + \left(\omega_s - \omega_r\right) \lambda_{dr} \tag{2.138}$$

From equations (2.135) through (2.138), it can be seen that there is no derivative terms in the DFIG steady state model, and one can easily obtain the currents by solving these four equations if the stator voltages, rotor voltages and rotational speed are known.

2.4.6 Comparison Between a DFIG Fourth Order Model and Reduced Order Models Expressed in the DQO-dqo Synchronously Rotating Reference Frame

In order to show the different transient processes of the fourth order model and reduced order models, the comparison was made in a Matlab/Simulink environment. In this case, the rotor voltages will suddenly decrease from 575v to 480v when t=0.6 seconds, see Figure 2.8. The simulation results for the fourth order, second order and steady state models are given in Figure 2.9.

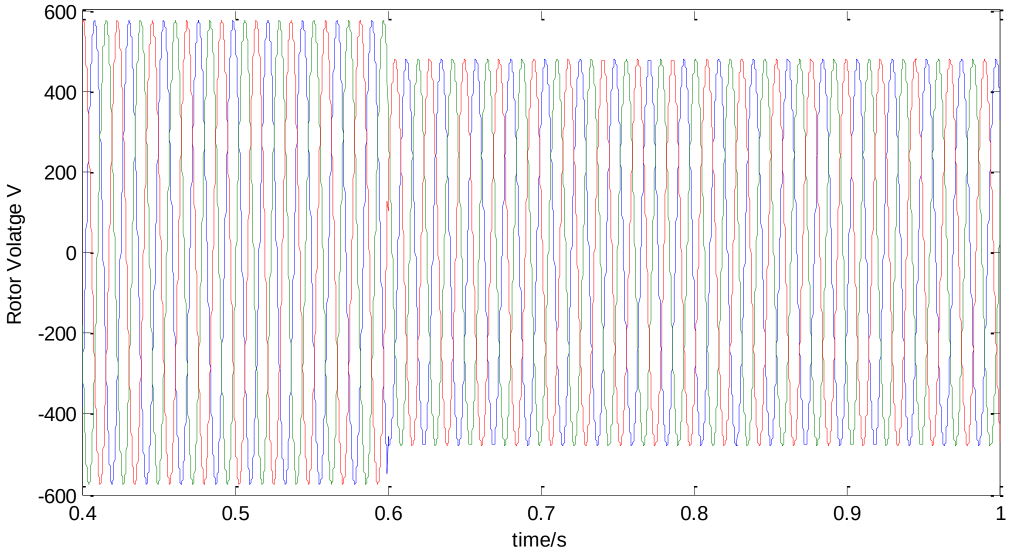

Figure 2.8 The DFIG rotor terminal voltage profiles

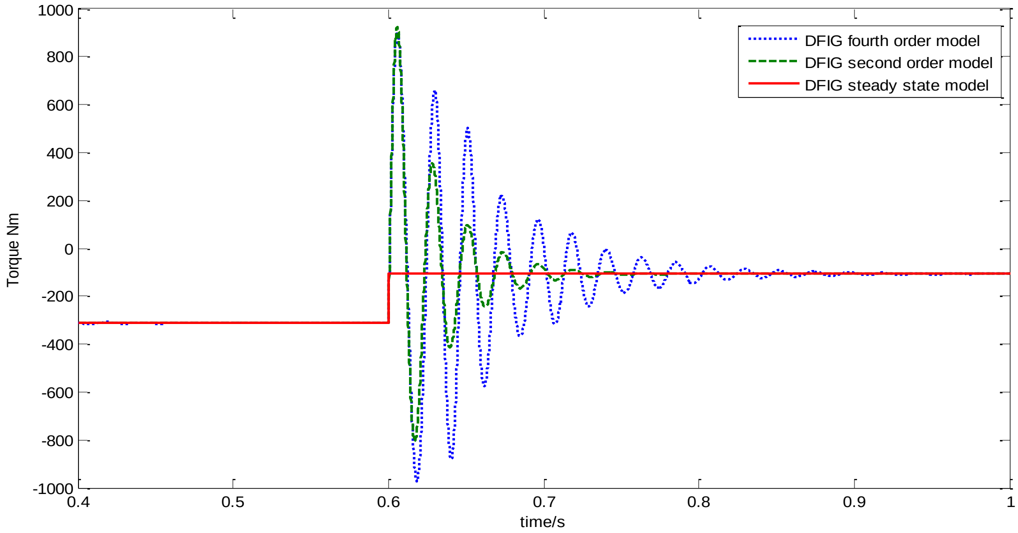

Figure 2.9 The torque profiles of different DFIG models

From Figure 2.9, it can be seen that the fourth order model has the longest starting transient time and largest starting transient magnitudes. The starting transient time and transient magnitudes are decreased in the second order model. For the steady state model, there is no transient at all because of the fact that the steady state model does not include any derivative terms.

2.5 Back-to-Back Voltage Source Converter (VSC) Models

PWM voltage source converters are commonly used in AC motor drives where the objective is to produce sinusoidal AC output voltages whose magnitudes and frequency can both be controlled. Since in DFIG-based wind turbine-generator systems, a DFIG needs to be operated either in sub-synchronous speed mode or super-synchronous speed mode according to various wind speeds. Therefore, the back-to-back power converter configurations become necessary due to their bi-directional operation ability.

A back-to-back converter consists of two converters, i.e., generator-side converter and grid-side converter with a DC-link capacitor which is placed between the two converters. The main objective for the grid-side converter is to keep the variation of the DC-link voltage small. With the control of the generator-side converter, it is possible to control the torque, the speed of a DFIG as well as its active and reactive power at the stator terminals.

In order to achieve the above objectives, it would be necessary to study the back-to-back converter model. In this section, a grid-side converter which actually plays the same role as a PWM rectifier is considered for the modeling study. A three-phase PWM voltage source rectifier model is first established in a straightforward ABC reference frame, and the ABC model is transformed to a DQO synchronous reference frame to simplify the controller design.

2.5.1 Three-Phase Voltage Source Converter (VSC) Model Expressed in the ABC Reference Frame

The main power circuit of a three-phase PWM voltage source converter is shown in Figure 2.10. It consists of six IGBTs with six antiparallel freewheeling diodes, three-phase AC input inductances and resistances, and a DC output capacitor.

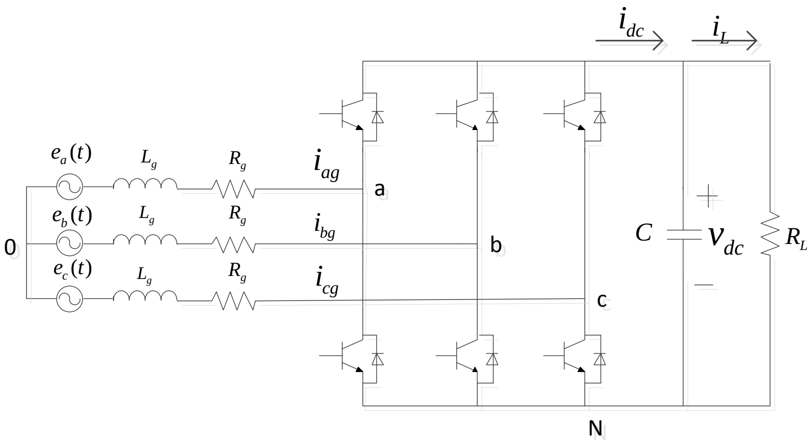

Figure 2.10 Configuration of a PWM voltage source rectifier

Here, $e_a(t)$, $e_b(t)$ and $e_c(t)$, are the three-phase voltage sources simulating an infinite-bus as a feed node in the power system, R_g 's, are the AC side resistances, and L_g 's, are the AC side inductances. Here, C, is the DC-link capacitor, R_L, is the load resistance, while, i_{ag}, i_{bg} and i_{cg}, are the input currents of a three-phase PWM rectifier. Here also, i_{dc}, is the DC-link current, i_L, is the load current, and v_{dc}, is the DC-link voltage.

The modeling and circuit analysis of the PWM rectifier is given next. First, let us define $S_k\left(k=a,b,c\right)$ as the switch function of phase, *k*. Based on the principle that any two switches in the same leg cannot be on at the same time, one can write the following definition [128]:

$$S_k=\begin{Bmatrix} 1 & The \quad upper \quad IGBT \quad is \quad on \\ 0 & The \quad upper \quad IGBT \quad is \quad off \end{Bmatrix} \tag{2.139}$$

Applying Kirchhoff’s laws to the circuit of Figure 2.10, the instantaneous values of the currents can be obtained, and written as following:

$$\begin{cases} L_g \dfrac{di_{ag}}{dt} = e_a - R_g i_{ag} - v_{(a,0)} \\ L_g \dfrac{di_{bg}}{dt} = e_b - R_g i_{bg} - v_{(b,0)} \\ L_g \dfrac{di_{cg}}{dt} = e_c - R_g i_{cg} - v_{(c,0)} \end{cases} \tag{2.140}$$

Here, $v_{(a,0)}$, $v_{(b,0)}$ and $v_{(c,0)}$, are the voltages from the AC side of the PWM rectifier to the power neutral point *0*, and can be obtained by using the following equations:

$$\begin{cases} v_{(a,0)} = v_{(a,N)} + v_{(N,0)} \\ v_{(b,0)} = v_{(b,N)} + v_{(N,0)} \\ v_{(c,0)} = v_{(c,N)} + v_{(N,0)} \end{cases} \tag{2.141}$$

where, $v_{(N,0)}$, is the voltage from point *N* to point *0*. Here, $v_{(a,N)}$, $v_{(b,N)}$ and $v_{(c,N)}$, are the voltages from the AC side of the PWM rectifier to point *N*.

For a balanced three-phase system, one can write:

$$v_{(a,0)} + v_{(b,0)} + v_{(c,0)} = 0 \tag{2.142}$$

Substituting from equation (2.141) into (2.142), the following equation can be deduced:

$$v_{(N,0)} = -\frac{v_{(a,N)} + v_{(b,N)} + v_{(c,N)}}{3} \tag{2.143}$$

Considering phase, a, when the upper IGBT is on and lower IGBT is off, one can derive; $S_a = 1$ and $v_{(a,N)} = v_{dc}$. Similarity, when the upper IGBT is off and lower IGBT is on, one can also write; $S_a = 0$ and $v_{(a,N)} = 0$. Therefore, based on the above characteristic, one can write $v_{(a,N)} = v_{dc} \bullet S_a$. Here, $v_{(a,N)}$, $v_{(b,N)}$, $v_{(c,N)}$ and $v_{(N,0)}$, can be rewritten as follows [129]:

$$\begin{cases} v_{(a,N)} = S_a v_{dc} \\ v_{(b,N)} = S_b v_{dc} \\ v_{(c,N)} = S_c v_{dc} \\ v_{(N,0)} = -\frac{1}{3}\left(S_a + S_b + S_c\right) v_{dc} \end{cases} \tag{2.144}$$

Substituting from equations (2.141) and (2.144) into equation (2.140), the following set of equations can be derived:

$$\begin{cases} L_g \dfrac{di_{ag}}{dt} = e_a - R_g i_{ag} - v_{dc}\left(S_a - \dfrac{1}{3}\sum\limits_{k=a,b,c} S_k\right) \\ L_g \dfrac{di_{bg}}{dt} = e_b - R_g i_{bg} - v_{dc}\left(S_b - \dfrac{1}{3}\sum\limits_{k=a,b,c} S_k\right) \\ L_g \dfrac{di_{cg}}{dt} = e_c - R_g i_{cg} - v_{dc}\left(S_c - \dfrac{1}{3}\sum\limits_{k=a,b,c} S_k\right) \end{cases} \tag{2.145}$$

Under the assumption that the power switch resistances of a balanced three-phase system could be neglected, the power relationship between the AC side and DC side is given as follows:

$$\sum_{k=a,b,c} i_{kg}(t) v_{kN}(t) = i_{dc}(t) v_{dc} \tag{2.146}$$

By combining equation (2.144) with (2.146), one can write:

$$i_{dc}(t) = i_{ag}(t) S_a + i_{bg}(t) S_b + i_{cg}(t) S_c \tag{2.147}$$

By applying Kirchhoff's laws to the positive node of the DC-link capacitor, one can easily reach the following equations:

$$\begin{cases} i_c = C \dfrac{dv_{dc}}{dt} \\ i_{dc} = i_c + I_L \\ i_{dc} = S_a i_{ag} + S_b i_{bg} + S_c i_{cg} \\ I_L = \dfrac{v_{dc}}{R_L} \end{cases} \tag{2.148}$$

Equation (2.148) can also be expressed by a single equation, and given as follows [48]:

$$C\frac{dv_{dc}}{dt}=S_a i_{ag}+S_b i_{bg}+S_c i_{cg}-\frac{v_{dc}}{R_L} \tag{2.149}$$

For a balanced three-phase system, one can write:

$$e_a+e_b+e_c=0 \tag{2.150}$$

$$i_{ag}+i_{bg}+i_{cg}=0 \tag{2.151}$$

Therefore, equation (2.145) along with equations (2.149) through (2.151) constitute the three-phase PWM voltage source rectifier model expressed in the ABC reference frame, and are rewritten as follows [49]:

$$\begin{cases} C\dfrac{dv_{dc}}{dt}=\sum\limits_{k=a,b,c} S_k i_{kg}-i_L \\ L_g\dfrac{di_{kg}}{dt}+R_g i_{kg}=e_k-v_{dc}\left(S_k-\dfrac{1}{3}\sum\limits_{j=a,b,c} S_j\right), k=a,b,c \\ \sum\limits_{k=a,b,c} e_k=\sum\limits_{k=a,b,c} i_{kg}=0 \end{cases} \tag{2.152}$$

2.5.2 Three-Phase Voltage Source Converter (VSC) Model Expressed in the DQ Synchronous Reference Frame

Although the PWM voltage source converter model expressed in the ABC frame has straightforward meanings, all the components in the ABC model are time variant, which will bring troubles and difficulties to controller designs. Hence, it is necessary to transform the ABC model to a DQ model which rotates at synchronous speed, so that the three-phase voltage inputs and the current components will be transformed to DC values.

Reconsidering the stator transformation matrix in equation (2.66), for the

DFIG model expressed in the DQO-dqo synchronously rotating reference frame, one can easily deduce the transformation matrix for this PWM voltage source rectifier due to their similarities, which is written as follows:

$$T = \frac{2}{3}\begin{bmatrix} \cos(\theta) & \cos(\theta - \frac{2\pi}{3}) & \cos(\theta - \frac{4\pi}{3}) \\ -\sin(\theta) & -\sin(\theta - \frac{2\pi}{3}) & -\sin(\theta - \frac{4\pi}{3}) \\ \frac{1}{2} & \frac{1}{2} & \frac{1}{2} \end{bmatrix} \tag{2.153}$$

where, θ is the angle between the stationary reference frame and synchronous reference frame, and is equal to $\theta = \omega_{gs} t + \theta_0$. Here, ω_{gs}, is the synchronous speed of the three-phase input voltages or the grid-side voltages.

Applying the transformation matrix in equation (2.153) to equation (2.152) and eliminating the zero-sequence components due to a balanced three-phase system, the PWM rectifier model expressed in the DQ synchronous reference frame can be deduced and given as follows [50][51]:

$$\begin{cases} C\dfrac{dv_{dc}}{dt} = \dfrac{3}{2}\left(i_{dg}s_d + i_{qg}s_q\right) - i_L \\ L_g\dfrac{di_{dg}}{dt} - \omega_{gs}L_g i_{qg} + R_g i_{dg} = e_d - v_d \\ L_g\dfrac{di_{qg}}{dt} + \omega_{gs}L_g i_{dg} + R_g i_{qg} = e_q - v_q \end{cases} \tag{2.154}$$

where, $v_d = v_{dc}s_d$ and $v_q = v_{dc}s_q$. Here, s_d and s_q, are the switching functions expressed in the DQ synchronous reference frame, while, i_{dg}, i_{qg}, e_d and e_q, are the input currents and voltages of the PWM rectifier expressed in the DQ synchronous reference frame.

From equation (2.154), it can be seen that the three-phase PWM rectifier model expressed in the DQ synchronous reference frame has coupled terms, $\omega_{gs}L_g i_{qg}$ and $\omega_{gs}L_g i_{dg}$. Hence, a feed forward controller will be designed to achieve a decoupled control of the PWM rectifier, and will be presented in detail in chapter 3.

2.5.3 Simulation Results for a Three-Phase Voltage Source Rectifier - Open Loop Condition

The three-phase PWM rectifier module was built in a Matlab/Simulink environment, and shown in Figure 2.11.

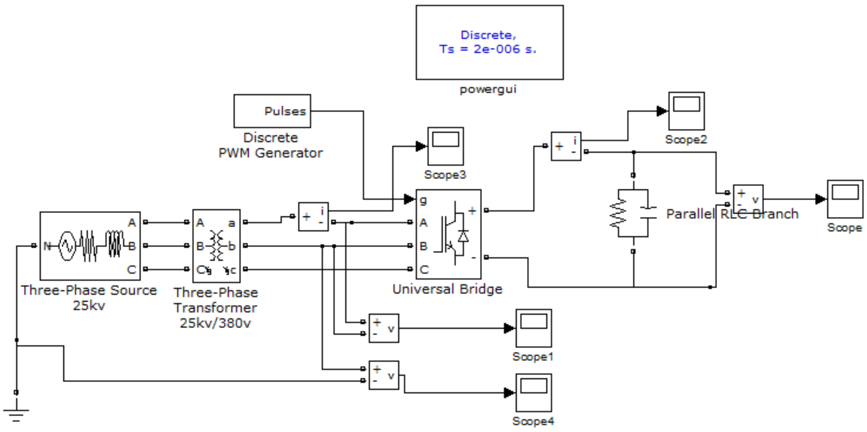

Figure.2.11 Three-phase PWM rectifier module in a Matlab/Simulink environment

In the simulation, the input line-to-line RMS voltage is 380 volts, the capacitor is 5mF, the load resistance is 100 Ohms and the modulation index is 0.5. The simulation result for the output DC-link voltage is shown in Figure 2.12.

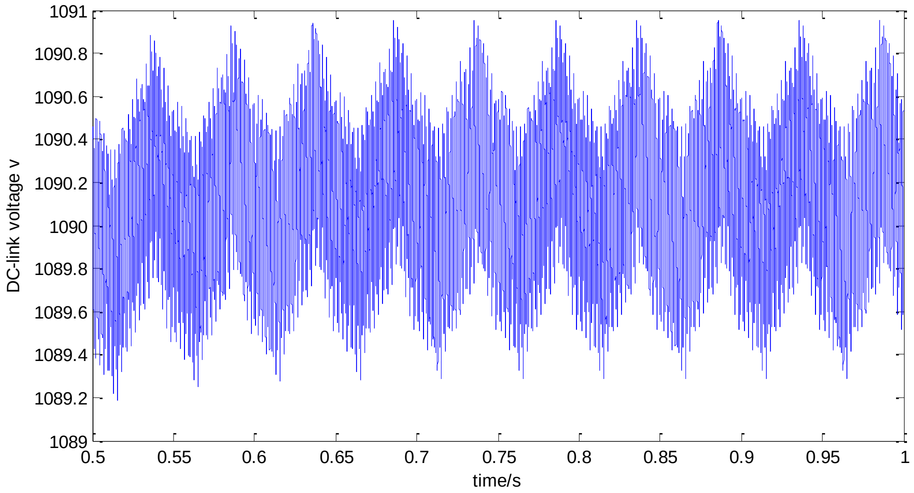

Figure 2.12 Output DC-link voltage profile of a three-phase PWM rectifier

From Figure 2.12, the steady state ripple for the DC-link voltage is 0.147%. Another thing that should be noted is that the average value of the DC-link voltage is 1090 volts, which nearly doubles the maximum value of the input line-to-line voltages. Hence, the three-phase PWM rectifier is a boost converter due to the following equation [51]:

$$v_{dc} \propto \frac{\sqrt{2}V_a(t)}{m} \tag{2.155}$$

where, m is the modulation index, and $V_a(t)$, is the RMS value for the input line-to-line voltages.

Chapter 3

Control Strategies of a Doubly-fed Induction Generator (DFIG) for Wind Turbine-Generator Systems (WTGS)

Generally speaking, variable speed wind turbine-generator systems (WTGSs) have two different control objectives, depending on the wind speed. For low wind speeds, the maximum power point tracking (MPPT) is desired so that the output power can be maximized according to the specific wind speed. For high wind speeds, the pitch angle regulation should be achieved to keep the output power at its rated value.

For the maximum power point tracking objective, it is possible to control the doubly-fed induction generator (DFIG) torque so that the speed of the turbine rotor can be varied proportional to the wind speed. In this way, the optimal tip speed ratio can be maintained, and thus the maximum power coefficient as well as the maximum output power can be achieved. The pitch angle control in a WTGS is used to regulate the pitch angle when the captured wind power exceeds its rated value, or the wind speed exceeds its rated value. Therefore, the output power can be kept at rated value even when the wind speed experiences gusts.

To achieve the two control goals mentioned above, several control schemes are implemented in the variable speed wind turbine model developed in Chapter 2. For the MPPT objective, the grid-side and generator-side PWM voltage source converter controllers will be designed. In addition, a maximum power point tracking control strategy will be described, which plays a role of providing a reference value for the generator-side converter control. For purposes of limiting the output power at its rated value, a pitch angle controller will be designed.

In this chapter, different control schemes and performances of a DFIG-based wind turbine-generator system will be presented. First, the grid-side converter control scheme which can achieve a unity power factor looking from the grid-side, while keeping the DC-link voltage constant, will be introduced. Second, a stator flux oriented control for the generator-side converter, which decouples the control of the stator side active and reactive power drawn from the grid, will be studied in detail. Third, a maximum power point tracking control strategy, using a current mode control, will be presented. Fourth, the operation principles of the pitch angle control will be described. Finally, the simulation results and discussion for a DFIG-based wind turbine-generator system will be given.

3.1 Grid-side Converter Control

3.1.1 Vector Control of a Grid-side Converter

The objective of the grid-side converter controller is to keep the DC-link voltage constant regardless of the magnitudes of the grid-side voltages, and to yield a unity power factor looking into the WTGS from the grid-side. In order to acquire better control performances, a feed forward control is used to decouple the D- and Q-axes components for the grid-side converter. Moreover, a vector control scheme, with a reference frame oriented along the grid voltage vector position, is used to independently control the active and reactive power flow between the grid and the grid-side converter.

As mentioned in Chapter 2, the grid-side converter plays the same role as a

PWM rectifier. Hence, the model of the PWM rectifier that was developed in Chapter 2 can be directly used here. Now, reconsider the scheme of a grid-side PWM voltage source converter shown in Figure 3.1, in which, e_a, e_b and e_c, are the grid voltages.

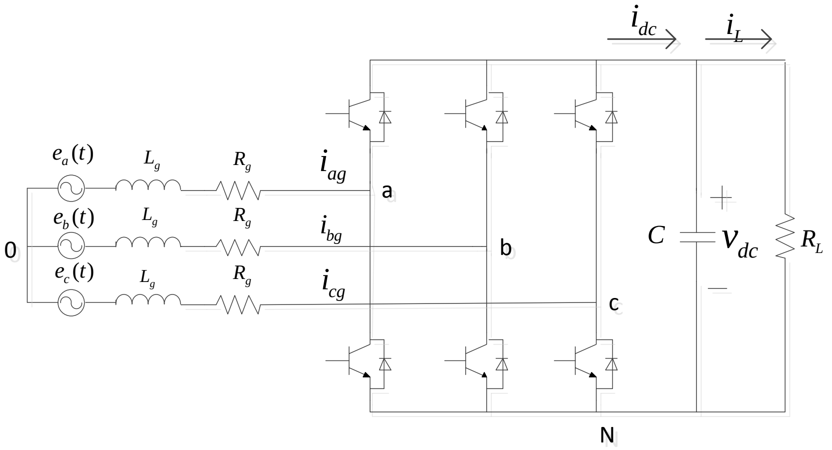

Figure 3.1 Grid-side PWM voltage source converter scheme

In order to achieve a unity power factor looking into the WTGS from the grid-side, it is necessary to study the power flow first. Applying similar technologies of deducing the formulas of the output active and reactive power for a doubly-fed induction generator expressed in the DQO-dqo synchronously rotating reference frame, the active and reactive power of a grid-side converter expressed in the DQ synchronous reference frame are given as follows:

$$P_g = \frac{3}{2}\left(e_d i_{dg} + e_q i_{qg}\right) \tag{3.1}$$

$$Q_g = \frac{3}{2}\left(e_q i_{dg} - e_d i_{qg}\right) \tag{3.2}$$

Aligning the reference frame along the D-axis in the synchronous reference frame, as shown in Figure 3.2, the Q-axis of the grid voltage, e_q , will be zero, while the D-axis of the grid voltage, e_d , will be a constant and can be written as follows:

$$e_d = e_g = \sqrt{e_\alpha^2 + e_\beta^2} \tag{3.3}$$

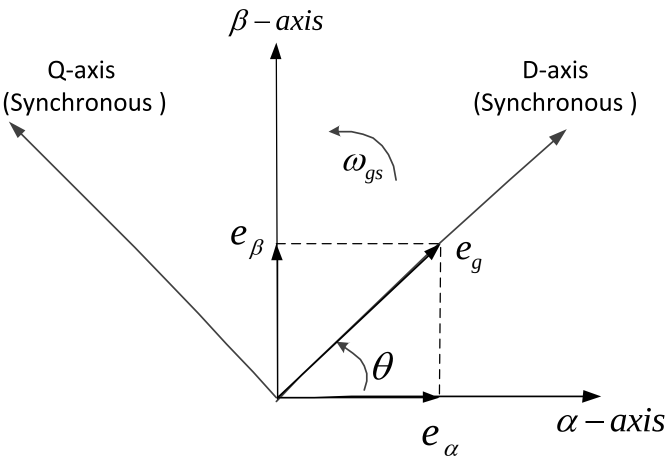

Figure 3.2 Vector diagram of the DQ synchronous reference frame for a grid-side converter

Here, in Figure 3.2, θ, is the angle between the α-axis of the stationary reference frame and the D-axis of the synchronous reference frame, and can be calculated as follows:

$$\theta = \int \omega_{gs} dt = \omega_{gs} t + \theta_0 = \tan^{-1}\left(\frac{e_\beta}{e_\alpha}\right) \tag{3.4}$$

where, e_α and e_β, are the grid-side voltages expressed in the stationary reference frame, while, θ_0, is the initial angle.

From the above analysis and equations (3.1) and (3.2), the active and reactive power of a grid-side converter under such reference frame will be proportional to the currents, i_{dg} and i_{qg}, respectively. The relationships are given as follows [11]:

$$P_g = \frac{3}{2} e_d i_{dg} \tag{3.5}$$

$$Q_g = -\frac{3}{2} e_d i_{qg} \tag{3.6}$$

Since the objective is to yield a unity power factor looking into the WTGS from the grid-side, the reactive power should be zero, and thus the reference value for the Q-axis current is zero. Hence, through controlling the D-axis and Q-axis currents, the active and reactive power flow between the grid and the grid-side converter can be regulated.

With reference to Figure 3.1, neglecting the harmonics due to the switching and ignoring the losses in the AC-side resistances and IGBTs, the input power should be equal to the output power, and the following expression can be obtained [130]:

$$Cv_{dc}\frac{dv_{dc}}{dt}+\frac{v_{dc}^2}{R_L}=\frac{3}{2}e_d i_{dg} \tag{3.7}$$

where, v_{dc}, is the instantaneous value of the DC-link voltage, which the control system tries to maintain at a constant value.

From equation (3.7), it can be seen that the DC-link voltage can be controlled by regulating the D-axis current, i_{dg}. Now, the problem which needs to be considered is how to control the D-axis and Q-axis currents to regulate the DC-link voltage and the power factor. Here, rewriting the grid-side converter model expressed in the DQ synchronous reference frame, gives the following:

$$\begin{cases} C\dfrac{dv_{dc}}{dt}=\dfrac{3}{2}\left(i_{dg}s_d+i_{qg}s_q\right)-i_L \\ L_g\dfrac{di_{dg}}{dt}-\omega_{gs}L_g i_{qg}+R_g i_{dg}=e_d-v_d \\ L_g\dfrac{di_{qg}}{dt}+\omega_{gs}L_g i_{dg}+R_g i_{qg}=e_q-v_q \end{cases} \tag{3.8}$$

where, $v_d=v_{dc}s_d$ and $v_q=v_{dc}s_q$. Here, s_d and s_q, are the switching functions expressed in the DQ synchronous reference frame, while, i_{dg}, i_{qg}, e_d and e_q, are the input currents and the grid voltages expressed in the DQ synchronous reference frame, respectively.

From equation (3.8), it can be seen that D- and Q- axes equations have coupling components, $\omega_{gs} L_g i_{qg}$ and $\omega_{gs} L_g i_{dg}$. Therefore, a decoupled control scheme is recommended, and the corresponding control signals are given as follows [50] [65]:

$$\begin{aligned} v_d &= \omega_{gs} L_g i_q + e_d + \Delta v_d \\ v_q &= -\omega_{gs} L_g i_d + e_q + \Delta v_q \end{aligned} \tag{3.9}$$

Here, the AC side resistances, R_g 's, are neglected. Substituting from equation (3.9) into equation (3.8), the desired decoupled control can be achieved, and the decoupled state equation is written as follows:

$$\begin{aligned} L_g \frac{di_{dg}}{dt} + \Delta v_d &= 0 \\ L_g \frac{di_{qg}}{dt} + \Delta v_q &= 0 \end{aligned} \tag{3.10}$$

where, Δv_d and Δv_q, are defined as follows:

$$\begin{aligned} \Delta v_d &= k_p \left(i_{dg}^* - i_{dg} \right) + k_i \int \left(i_{dg}^* - i_{dg} \right) dt \\ \Delta v_q &= k_p \left(i_{qg}^* - i_{qg} \right) + k_i \int \left(i_{qg}^* - i_{qg} \right) dt \end{aligned} \tag{3.11}$$

Here, the reference value of the Q-axis current is zero. The difference between the reference value of the DC-link voltage and measured DC-link voltage passing through a PI controller will yield the reference value of the D-axis current, which can be written as follows:

$$i_{dg}^* = k_p \left(v_{dc}^* - v_{dc} \right) + k_i \int \left(v_{dc}^* - v_{dc} \right) dt \tag{3.12}$$

From equations (3.9) through (3.11), it can be seen that the grid-side converter model is decoupled, and the D-axis and Q-axis currents can be separately regulated by controlling the Δv_d and Δv_q, so that the DC-link voltage and the reactive power of the grid-side converter can be controlled. Here, the D-axis current is used to regulate the DC-link voltage, while the Q-axis current is used to regulate the reactive power.

3.1.2 Modulation Signal Deduction

From the previous analysis, the control signals, v_d and v_q, are deduced. Hence, the relationships between these control signals and the modulation signals of the grid-side converter should be discussed and analyzed. Therefore, through these control signals, v_d and v_q, the modulation signals of the grid-side converter can be obtained.

For phase, *a*, Figure 3.3 shows the phasor diagram of a grid-side converter, which is drawn based on equation (3.13).

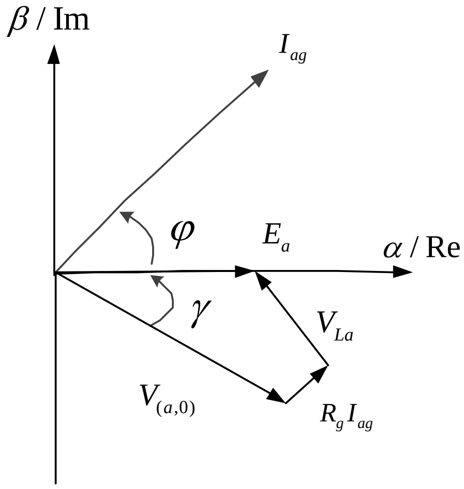

Figure 3.3 Phasor diagram of a grid-side converter

$$\overrightarrow{V_{(a,0)}} = \overrightarrow{E_a} - \overrightarrow{V_{La}} - R_g \overrightarrow{I_{ag}} \tag{3.13}$$

where, $\overrightarrow{V_{La}}$, is the AC side inductance voltage drop of phase *a*, $\overrightarrow{V_{(a,0)}}$, is the voltage from the AC side of the grid-side converter to the power neutral point *0* of phase *a*, see Figure 3.1, while $\overrightarrow{I_{ag}}$, is the current of phase *a*.

From Figure 3.3, the following set of equations can be deduced:

$$\begin{aligned} e_a &= E_m \cos \omega t \\ v_{(a,0)} &= V_m \cos(\omega t - \gamma) \\ i_{ag} &= I_m \cos(\omega t + \varphi) \end{aligned} \tag{3.14}$$

where, E_m, V_m and I_m, are the magnitudes of the AC side input voltages, the voltages from AC side to the power neutral point *0*, and the AC side phase-a current of the grid-side converter, respectively.

Now, consider the waveform for the SPWM control shown in Figure 3.4. In this Figure, v_{ma} and v_r, are the modulation signal and the carrier signal of phase *a*, respectively.

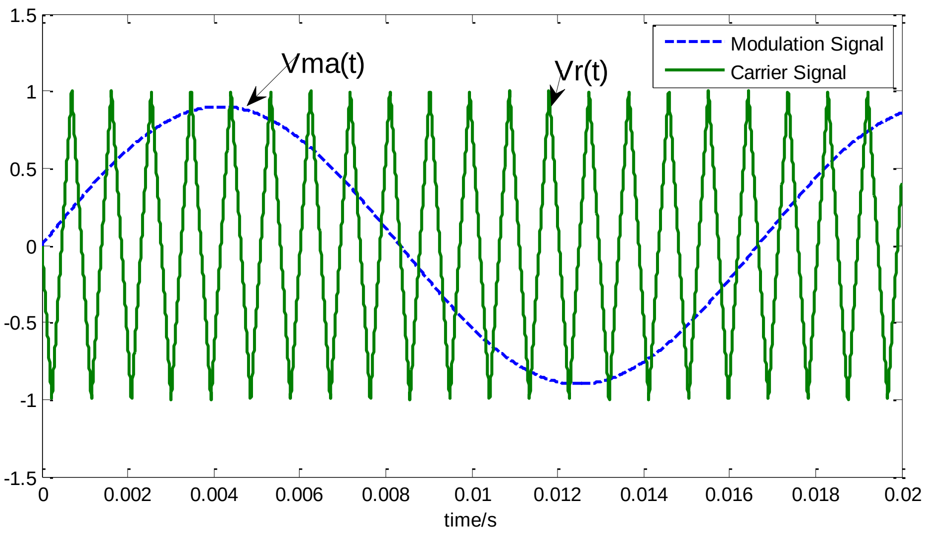

Figure 3.4 SPWM modulation waveform

According to reference [131], the modulation signal should be similar to the waveform of $v_{(a,0)}$, which is given in equation (3.14). Here, the modulation signal for phase-a can be defined as follows:

$$v_{ma} = V_{ma} \cos(\omega t - \gamma) \tag{3.15}$$

For phase-*a*, if the switching frequency of the SPWM is high, then only considering the fundamental component of the voltage from AC side to the power neutral point 0, $v_{(a,0)}$, would be feasible. Under the above assumption, the fundamental component of the AC side voltage of the grid-side converter, $v_{a1}(t)$, can be expressed as follows [131]:

$$v_{a1}(t) = \frac{1}{2}\frac{V_{ma}}{V_T} v_{dc} \cos(\omega t - \gamma) \tag{3.16}$$

where, V_{ma}, is the magnitude of the modulation signal, V_T, is the magnitude of the carrier signal, while v_{a1}, is the fundamental component of $v_{(a,0)}$, which is the voltage from the AC side of the grid-side converter to the power neutral point *0*.

According to equation (3.16), the modulation signal for phase *a* can be derived and given as follows:

$$v_{ma} = V_{ma} \cos(\omega t - \gamma) = \frac{2 v_{a1}(t) V_T}{v_{dc}} \tag{3.17}$$

Since the voltage, v_{a1}, is the fundament component of the voltage, $v_{(a,0)}$, therefore, it would be convenient to obtain the modulation signal by using the voltage, $v_{(a,0)}$, according to equation (3.17). Through comparing the PWM converter models expressed in the ABC reference frame and the DQ synchronous reference frame, it can be seen that the control signals, v_d and v_q, are the transformed voltages expressed in the DQ synchronous reference frame for the AC side voltages, $v_{(a,0)}$, $v_{(b,0)}$ and $v_{(c,0)}$. From previous analysis in Section 3.1.1, only the voltages, v_d and v_q, are known. Therefore, in order to obtain the modulation signals, it is necessary to transform the voltages, v_d and v_q, back to the ABC reference frame.

From the above analysis, the grid-side converter control scheme can be schematically drawn as follows, see Figure 3.5:

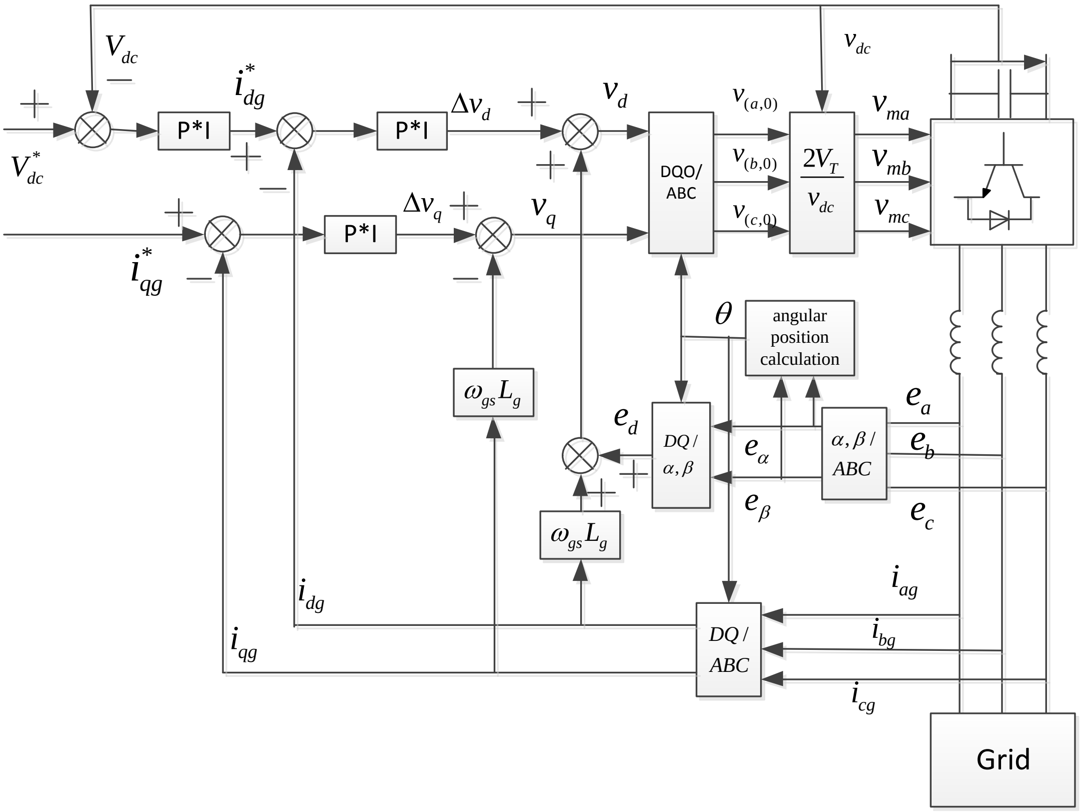

Figure 3.5 Grid-side converter control scheme

In order to test the grid-side converter control scheme, a grid-side converter is built in a Matlab/Simulink environment and simulated under a three-phase voltage sag condition. The three-phase grid-side converter control scheme built in the Matlab/Simulink is shown in Figure 3.6, and the corresponding system parameters for this simulation are given in Table 3.1.

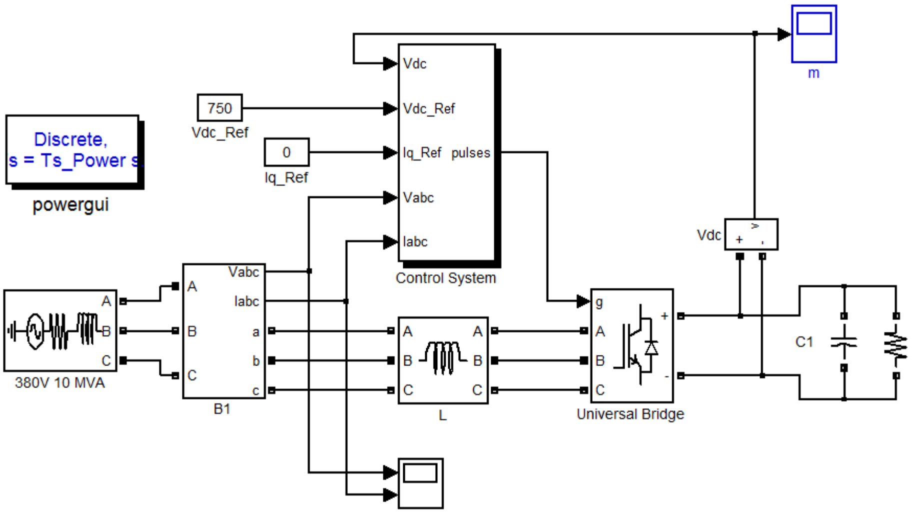

Figure 3.6 Three-phase grid-side converter control scheme in a Matlab/Simulink environment

Table 3.1 Grid-side converter simulation data

Parameter	Value	Units
RMS value of the grid-side line-to-line voltage	380	V
Inductance	2.1	mH
DC-link capacitor	2.3	mF
Load resistance	37.5	ohm

In this simulation, the three-phase input voltages will decrease to 228 V when t=0.15 seconds. After 0.1 seconds, they will be restored to their rated value, as shown in Figure 3.7. Figure 3.8 shows the DC-link voltage response of the grid-side converter under a three-phase input voltage sag condition. It can be seen that no matter what the input voltages are, the grid-side converter control scheme will try to keep the DC-link voltage constant.

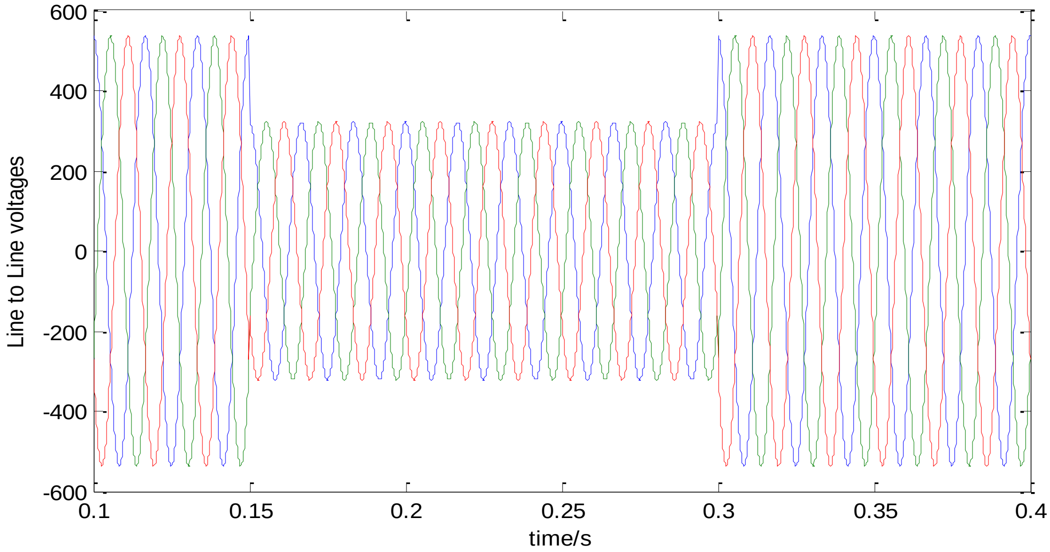

Figure 3.7 Three-phase input voltage profiles for a grid-side converter

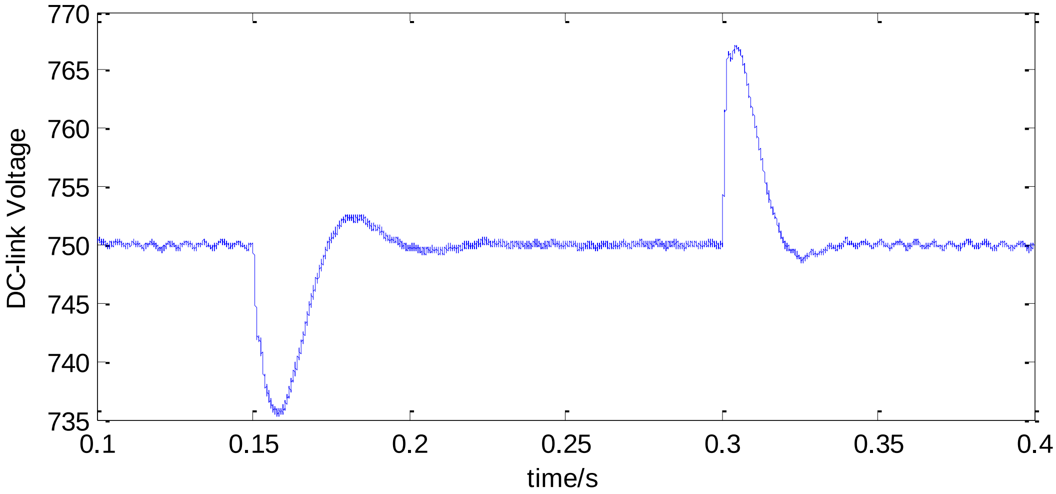

Figure 3.8 DC-link voltage profile

3.2 Generator-side Converter Control

The wound rotor induction generator is controlled using a synchronously rotating reference frame, with the direct axis oriented along the stator flux vector position. In this manner, a decoupled control between the stator side active and reactive power can be achieved, which will be explained later-on in this section. In this system simulation, the generator-side PWM converter control scheme requires the measurements of the stator and rotor currents, stator voltages and the rotor position.

Under the stator flux control scheme, all the stator and rotor variables are needed to be converted to the synchronously rotating stator flux reference frame. The space vector diagram which shows the relationship between the stator flux reference frame and the stationary reference frame is shown in Figure 3.9.

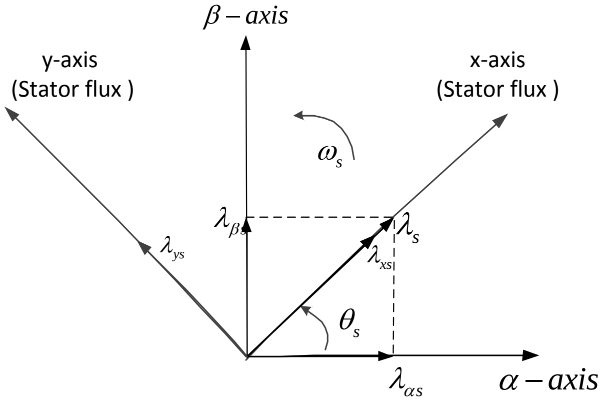

Figure 3.9 Space vectors of the stationary and stator flux reference frame

where, $\lambda_{\alpha s}$ and $\lambda_{\beta s}$, are the stator flux linkages expressed in the stationary α, β reference frame, and λ_s, is the resultant stator flux under such reference frame. The stator flux angular position, θ_s, can be obtained by following equation:

$$\theta_s = \arctan\frac{\lambda_{\beta s}}{\lambda_{\alpha s}} = \arctan\left(\frac{L_s i_{\beta s} + L_m i_{\beta r}}{L_s i_{\alpha s} + L_m i_{\alpha r}}\right) \tag{3.18}$$

where, based on the developments in [38],

$$\lambda_{\alpha s} = L_s i_{\alpha s} + L_m i_{\alpha r} \tag{3.19}$$

$$\lambda_{\beta s} = L_s i_{\beta s} + L_m i_{\beta r} \tag{3.20}$$

Hence,

$$\theta_s = \arctan\left(\frac{L_s i_{\beta s} + L_m i_{\beta r}}{L_s i_{\alpha s} + L_m i_{\alpha r}}\right) \tag{3.21}$$

Here, $i_{\alpha s}$, $i_{\beta s}$, $i_{\alpha r}$ and $i_{\beta r}$, are the stator α-axis, β-axis currents and rotor α-axis, β-axis currents expressed in the stationary reference frame, respectively. One can easily obtain these currents by using Clarke transformation.

After obtaining the angular position of the stator flux, θ_s, all the stator and rotor variables of the DFIG can be transformed to the stator flux reference frame by considering the schematic of the space vector diagram shown in Figure 3.10.

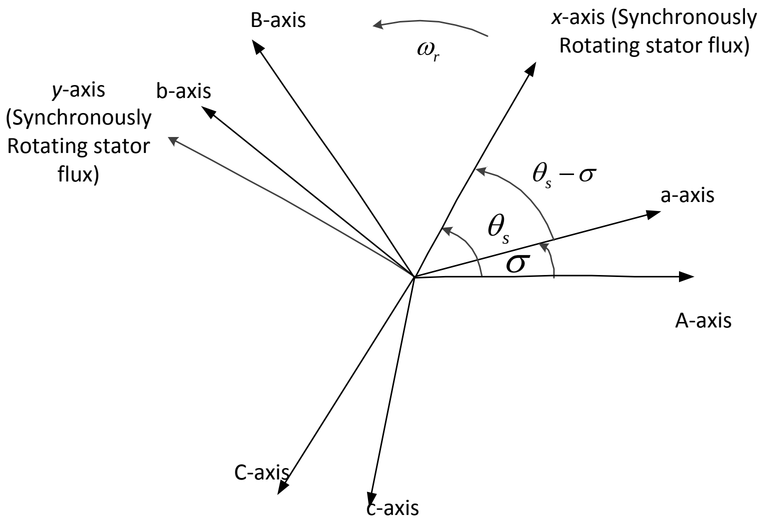

Figure 3.10 Schematic diagram of the ABC to DQO-dqo synchronously rotating stator flux reference frame transformation

Here, the stator and rotor transformation matrices, $\underline{T}_{ssf}$ and $\underline{T}_{rsf}$, for the synchronously rotating stator flux reference frame are given as follows:

$$\underline{T}_{ssf} = \frac{2}{3}\begin{bmatrix} \cos(\theta_s) & \cos\left(\theta_s - 2\pi/3\right) & \cos\left(\theta_s - 4\pi/3\right) \\ -\sin(\theta_s) & -\sin\left(\theta_s - 2\pi/3\right) & -\sin\left(\theta_s - 4\pi/3\right) \\ 1/2 & 1/2 & 1/2 \end{bmatrix} \tag{3.22}$$

$$\underline{T}_{rsf} = \frac{2}{3}\begin{bmatrix} \cos(\theta_s - \sigma) & \cos\left((\theta_s - \sigma) - 2\pi/3\right) & \cos\left((\theta_s - \sigma) - 4\pi/3\right) \\ -\sin(\theta_s - \sigma) & -\sin\left((\theta_s - \sigma) - 2\pi/3\right) & -\sin\left((\theta_s - \sigma) - 4\pi/3\right) \\ 1/2 & 1/2 & 1/2 \end{bmatrix} \tag{3.23}$$

Through aligning the direct axis of the reference frame along the stator flux vector position, see Figure 3.9, the following relationships can be derived:

$$\begin{aligned} \lambda_{xs} &= |\lambda_s| = \sqrt{\lambda_{\alpha s}^2 + \lambda_{\beta s}^2} \\ \lambda_{ys} &= 0 \end{aligned} \tag{3.24}$$

where, the subscripts, *x* and *y*, mean the direct axis and quadrature axis of the stator flux reference frame, respectively. Here, λ_{xs}, is the *x*-axis stator flux linkage, λ_{ys}, is the *y*-axis stator flux linkage, while $|\lambda_s|$, is the magnitude of the stator flux linkage.

Since the stator of the DFIG is directly connected to the grid, and the influence of the stator resistances is small, the *x*-axis stator flux linkage can be considered as constant and the *y*-axis stator flux linkage can be treat as zero. Under this consideration, the DFIG model expressed in the stator flux reference frame can be deduced based on equations (2.112) through (2.119) and can be written as follows [24]:

$$|\lambda_s| = L_m i_{ms} = \lambda_{xs} = L_s i_{xs} + L_m i_{xr} \tag{3.25}$$

Hence,

$$i_{xs} = \frac{L_m i_{ms} - L_m i_{xr}}{L_s} \tag{3.26}$$

$$\lambda_{ys} = 0 = L_s i_{ys} + L_m i_{yr} \tag{3.27}$$

Hence,

$$i_{ys} = -\frac{L_m}{L_s} i_{yr} \tag{3.28}$$

and,

$$\lambda_{xr} = L_{\mathrm{r}} i_{xr} + L_m i_{xs} = \frac{L_m^2}{L_s} i_{ms} + \sigma_r L_r i_{xr} \tag{3.29}$$

$$\lambda_{yr} = L_{\mathrm{r}} i_{yr} + L_m i_{ys} = \sigma_r L_r i_{yr} \tag{3.30}$$

$$v_{xr} = r_r i_{xr} + \frac{d\lambda_{xr}}{dt} - \left(\omega_s - \omega_r\right)\lambda_{yr} = r_r i_{xr} + \sigma_r L_r \frac{di_{xr}}{dt} - (\omega_s - \omega_r)\sigma_r L_r i_{yr} \tag{3.31}$$

$$v_{yr} = r_r i_{yr} + \frac{d\lambda_{yr}}{dt} + \left(\omega_s - \omega_r\right)\lambda_{xr} = r_r i_{yr} + \sigma_r L_r \frac{di_{yr}}{dt} + (\omega_s - \omega_r)(\frac{L_m^2}{L_s} i_{ms} + \sigma_r L_r i_{xr}) \tag{3.32}$$

where,

$$\sigma_r = 1 - \frac{L_m^2}{L_s L_r} \tag{3.33}$$

Here, λ_{xr} and λ_{yr}, are the *xy*-axes rotor flux linkages, i_{xs} and i_{ys}, are the *xy*-axes stator currents, while i_{xr} and i_{yr}, are the *xy*-axes rotor currents. Here, i_{ms}, is the magnetizing current of the DFIG, while v_{xr} and v_{yr}, are the *xy*-axes rotor terminal voltages. Here also, ω_s, is the electrical angular velocity of the stator flux, which is equal to the synchronous speed.

Equations (3.31) and (3.32) constitute the DFIG model expressed in the stator flux reference frame, in which the stator voltage equations in the DFIG fourth order model are eliminated due to the fact that under this reference frame, the direct axis stator terminal voltage will be equal to zero and quadrature axis stator terminal voltage will be a constant.

The stator *xy*-axes terminal voltage expressions as well as the relationships between the torque, power and the *xy*-axes stator currents, rotor currents expressed in the stator flux reference frame can be deduced as follows:

$$\left.\begin{array}{c} |\lambda_s| = \lambda_{xs} = Cons \\ \lambda_{ys} = 0 \\ v_{xs} = r_s i_{xs} + \dfrac{d\lambda_{xs}}{dt} - \omega_s \lambda_{ys} \\ v_{ys} = r_s i_{ys} + \dfrac{d\lambda_{ys}}{dt} + \omega_s \lambda_{xs} = Cons \end{array}\right\} \tag{3.34}$$

Hence,

$$\left.\begin{array}{c} v_{xs} = 0 \\ v_{ys} = |v_s| = Cons\tan t \end{array}\right\} \tag{3.35}$$

Accordingly, the develop torque as well as the active and reactive power, based on earlier developments, see equations (2.120) through (2.122), can be written as follows:

$$T_{dev} = \frac{3}{2}\left(\frac{P}{2}\right)\left[\lambda_{xs} i_{ys} - \lambda_{ys} i_{xs}\right] = \frac{3}{2}\left(\frac{P}{2}\right)\lambda_{xs} i_{ys} = -\frac{3}{2}\left(\frac{P}{2}\right)\frac{L_m^2}{L_s} i_{ms} i_{yr} \tag{3.36}$$

$$P_s = \frac{3}{2}\left(v_{xs} i_{xs} + v_{ys} i_{ys}\right) = \frac{3}{2} v_{ys} i_{ys} = -\frac{3}{2}|v_s|\frac{L_m}{L_s} i_{yr} \tag{3.37}$$

$$Q_s = \frac{3}{2}\left(v_{ys} i_{xs} - v_{xs} i_{ys}\right) = \frac{3}{2} v_{ys} i_{xs} = \frac{3}{2}|v_s|\frac{L_m}{L_s}(i_{ms} - i_{xr}) \tag{3.38}$$

From equation (3.35), it can be seen that the stator terminal voltage equations are eliminated, which means that the DFIG fourth order model is reduced to a second order model expressed in the stator flux reference frame. Due to the constant stator voltages, the stator active power and reactive power can be controlled in a decoupled manner via the stator currents, i_{ys} and i_{xs}, and further via the rotor currents, i_{yr} and

i_{xr}, respectively. This is because the stator currents can be directly regulated by the rotor currents, being observed from equations (3.26) through (3.28). The develop torque can also be directly controlled by the rotor *y*-axis current, i_{yr}.

From the DFIG model written in the equations (3.31) and (3.32), it can be seen that the *x*-axis and *y*-axis equations have coupling terms, namely, $(\omega_s - \omega_r)\sigma_r L_r i_{yr}$ and $(\omega_s - \omega_r)(\frac{L_m^2}{L_s} i_{ms} + \sigma_r L_r i_{xr})$. Hence, by using the same logic and algorithms for deducing the control signals of the grid-side converter, the control signals for the generator-side converter can be developed and written as follow:

$$\begin{aligned} v_x &= \Delta v_{xr} - (\omega_s - \omega_r)\sigma_r L_r i_{yr} \\ v_y &= \Delta v_{yr} + (\omega_s - \omega_r)(\frac{L_m^2}{L_s} i_{ms} + \sigma_r L_r i_{xr}) \end{aligned} \tag{3.39}$$

where,

$$\begin{aligned} \Delta v_{xr} &= k_p \left(i_{xr}^* - i_{xr}\right) + k_i \int \left(i_{xr}^* - i_{xr}\right) dt \\ \Delta v_{yr} &= k_p \left(i_{yr}^* - i_{yr}\right) + k_i \int \left(i_{yr}^* - i_{yr}\right) dt \end{aligned} \tag{3.40}$$

After obtaining the control signals, v_x and v_y, the modulation signals for the generator-side converter can be derived by using the same procedure as mentioned in Section 3.1.2. However, it should be noticed that the control signals here are expressed in the stator flux reference frame, and it is necessary to transform them to the rotor abc reference frame.

Figure 3.11 shows the vector control scheme for the generator-side PWM voltage source converter. The control scheme utilizes a cascade control, i.e. the inner current control loops are used for controlling the *x*- and *y*-axes rotor currents, and the outer power control loops are used to control the active and reactive power at the stator terminals. The power control loops generate the reference values of the *x*- and *y*-axes rotor currents for the current control loops. Here, the reference value for the active power will be obtained from the maximum power point tracking control, and will be explained in next section. Since a unity power factor is considered in this thesis, the reference value for the reactive power will be a zero value.

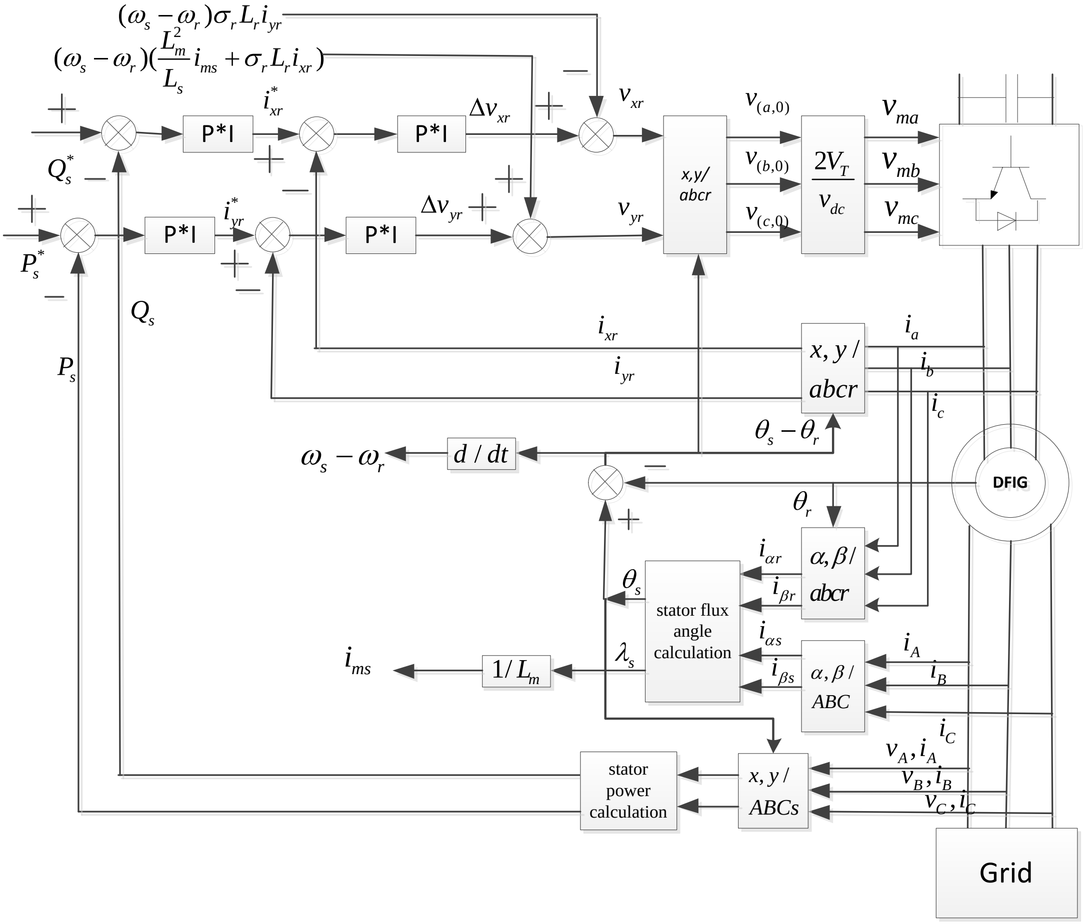

Figure 3.11 Generator-side converter control scheme

3.3 Maximum Power Point Tracking Control

When the wind velocity doesn’t reach its rated value, the output power of the DFIG cannot reach its rated power, either. Therefore, capturing as much the wind power as possible becomes the major control task for under-rated wind speed conditions. For maximum power point tracking purposes, it is possible to control the doubly-fed induction generator torque so that the speed of the turbine rotor can be varied with the wind speed in such a manner that yields an optimal tip speed ratio. In this way, the maximum power coefficient as well as the maximum output power can be obtained. Here, a current mode control will be applied in the MPPT, in which the reference value is the captured wind power. Now, reconsider the relationship between the mechanical power input and the wind speed passing through a turbine rotor plane, given in equation (3.41).

$$P_{\omega t} = \frac{1}{2}\rho\pi R^2 v_\omega^3 C_p(\lambda,\beta) \tag{3.41}$$

Here, the C_p coefficient in the wind turbine aerodynamic model is obtained through a “lookup table” method, and its profile is shown in Figure 3.12.

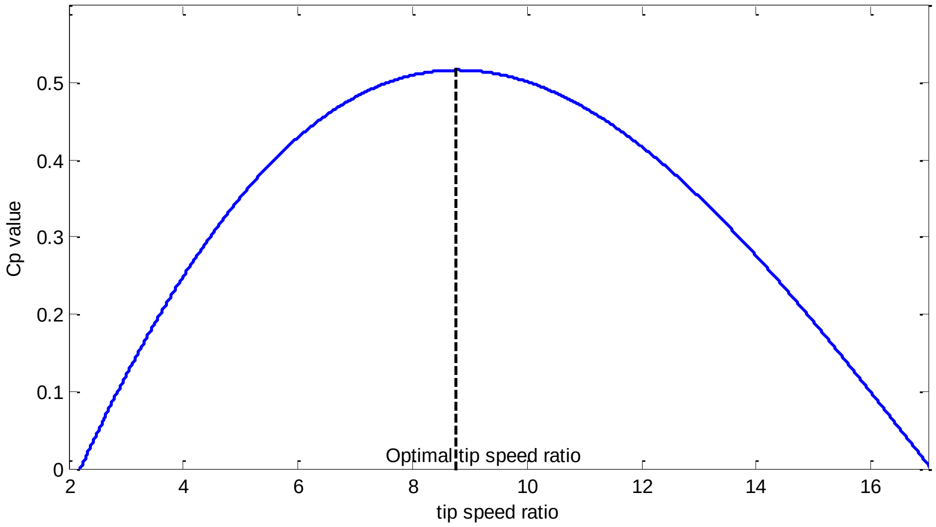

Figure 3.12 $C_p - \lambda$ curve

By maintaining the tip speed ratio at its optimum value, the captured power can be maximized and calculated as follows:

$$P_{\max} = \tfrac{1}{2}\rho\pi R^2 v_\omega^3 C_p(\lambda,\beta) = K v_\omega^3 \tag{3.42}$$

where, K is a constant and is equal to ($\tfrac{1}{2}\rho\pi R^2 v_\omega^3 C_p\left(opt\right)$). The obtained maximum power, P_{max}, will be set as the reference value of the active power for the generator-side converter control, and thus by regulating the rotor y-axis current, the maximum power can be tracked.

3.4 Pitch Angle Control

In recent years, wind turbine-generator systems equipped with a pitch angle adjusting device have become the dominating type of annually installed wind turbines. When the wind speed is below its rated speed, the pitch angle will be kept as zero value to maximize the power coefficient of the wind turbine. For wind gust conditions, the controller will regulate the pitch angle in such a manner that the output power of the wind turbine can be limited to its rated value. Therefore, the gird will suffer from minimum power variations due to the continued installation of additional wind turbines.

Based on earlier work in the literature, the pitch angle reference, β_{ref}, can be obtained by various input parametric values, which are summarized as follows [138]:

1) Wind speed. Ideally, the pitch angle reference, β_{ref}, can be obtained from the curve of the pitch angle versus wind speed. This control strategy is simple if the wind speed can be directly measured.
2) Generator rotor speed. The difference between the controlled rotor speed and its reference value will pass through a PI controller, and then produce the reference value of the pitch angle, β_{ref}.

3) Generator power. The difference between the generator power and its rated power will be sent through a PI controller, whose output will yield the reference value of the pitch angle, β_{ref}.

In this thesis, the input parameter is the generator power, and the structure of the pitch angle controller is shown in Figure 3.13.

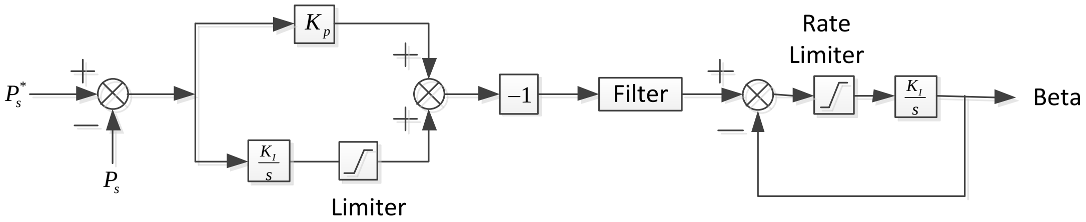

Figure 3.13 Pitch angle control scheme [56]

Adjusting the pitch angle of the blades, provides an effective mean of regulating or limiting turbine performance in strong wind speed conditions. To put the blades into the necessary position, pitch servos are employed which may be hydraulic or electrical systems. During normal operation, blade pitch adjustments with rotational speeds of approximately 5-10º per second are expected [132]. Here, the pitch angle regulating rate is 8º per second.

3.5 Performance of a Doubly-fed Induction Generator (DFIG) for Wind Turbine-Generator Systems

In order to investigate the performance of these control strategies mentioned earlier in this chapter, a wind turbine-generator system is developed in a Matlab/Simulink environment and simulated under various wind speed conditions. Here, the rated wind speed is 12 m/s. In low wind speed conditions that are below rated value, the maximum power point tracking objective can be achieved by the generator-side converter control. At high wind speed conditions above rated speed, the pitch angle can be regulated to provide proper value for the power coefficient, so that the output power of the wind turbine is approximately maintained at its rated value. The objective of the vector-control scheme for the grid-side PWM voltage source converter is to keep the DC-link voltage constant under various wind speed conditions.

The models and control strategies which are used in this simulation study are given in Table 3.2.

Table 3.2 Models and control strategies in the WTGS

DFIG	Fourth order model
Drive train	One-mass model
Generator-side converter control	Stator flux oriented control
MPPT	Current mode control

The wind turbine-generator system parameters used in this simulation study are given in Table 3.3 [15].

Table 3.3 Wind turbine-generator system parameters

Parameter	Value	Units
Wind turbine rotor radius	91.2	m
Number of poles	6	
Rated power	1.5	MVA
Rated voltage	575	V
Stator resistance	0.023	ohm

Rotor resistance	0.016	ohm
Stator inductance	0.18	H
Rotor inductance	0.16	H
Magnetizing inductance	2.9	H

The functional block diagram of the simulation scheme of a 1.5 MW doubly-fed induction generator wind turbine-generator system (WTGS) in the Matlab/Simulink environment is shown in Figure 3.14.

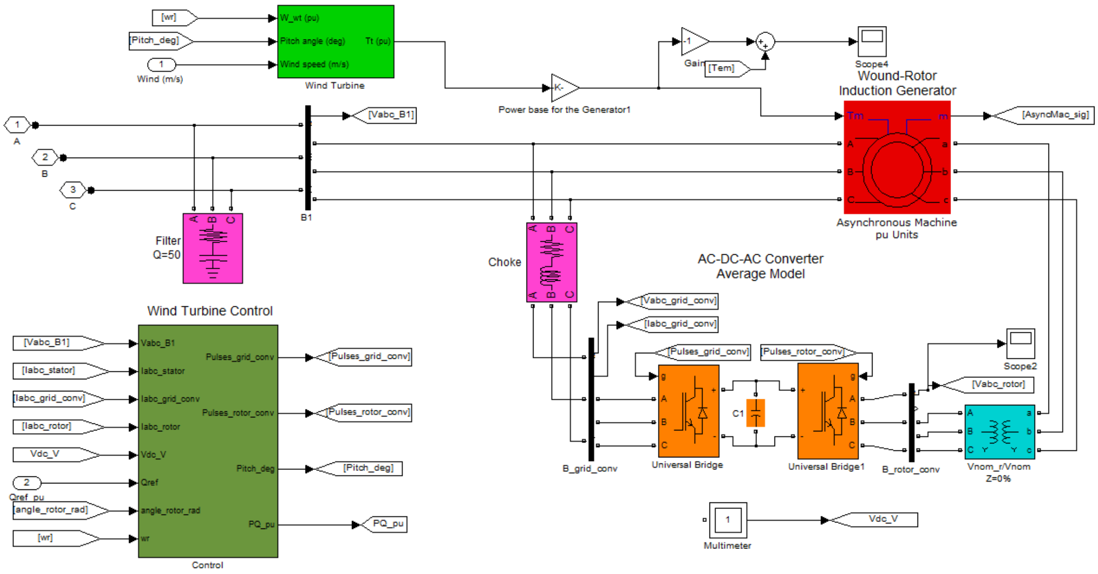

Figure 3.14 Simulation scheme of a 1.5 MW doubly-fed induction generator wind turbine-generator system

The simulation results for the WTGS are given next. Figure 3.15 shows the power verse wind speed curve. As shown in Figure 3.15, the wind speed increases from an initial condition of 2 m/s to a final condition of 15 m/s. Correspondingly, the active power is increasing and tracking its maximum value. However, when the active power reaches its rated value, it will stop increasing and stay at its rated value through the action of the control system.

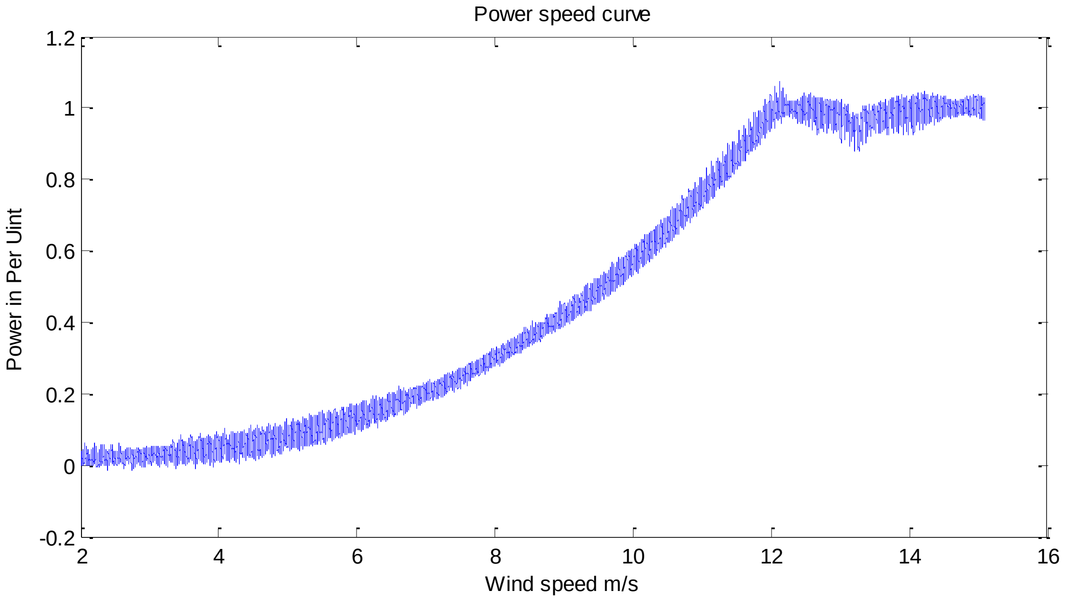

Figure 3.15 Power verse wind speed curve

In this simulation, it is assumed that the wind speed will vary from 8m/s to 15m/s, as shown in Figure 3.16, this is in order to test the system performance. Figure 3.17 shows the active power curve. It can be seen that when the wind speed equals 12 m/s, the power reaches its rated value; when the wind speed increases from 12m/s to 15 m/s, the power will first increase and then decrease to its rated value. During the time period between 0.5 seconds to1 seconds, the output active power is regulated by the pitch angle controller, and its dynamic response is slow because of the fact that the pitch angle controller is a mechanical device. Then, the wind speed decreases to 12 m/s. The active power is still kept as its rated value. When the wind speed decreases to 8m/s, the output active power also decreases too, which is due to the fact that the active power is regulated by the generator-side converter controller and will track more closely the maximum power. After 2.0 seconds, the wind speed increases to 12 m/s and the wind turbine will generate rated active power.

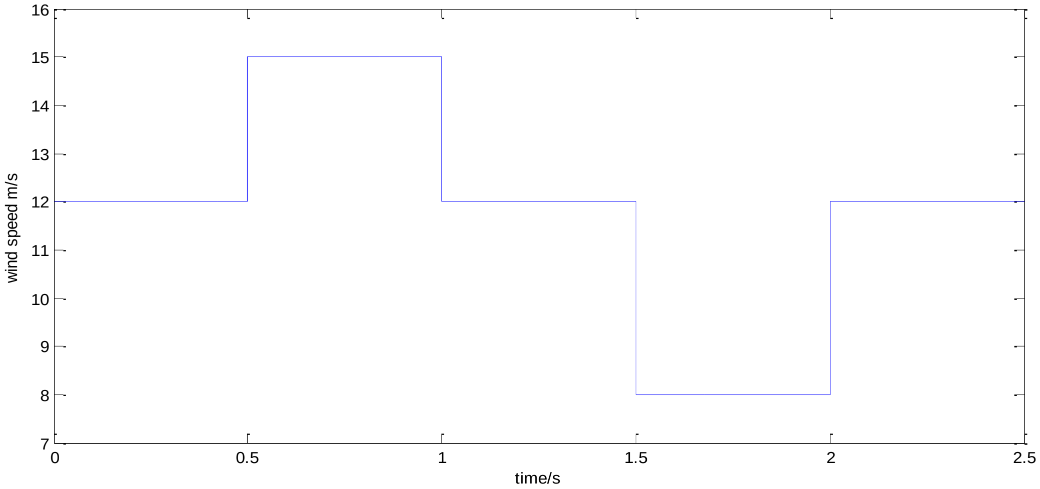

Figure 3.16 Wind speed curve

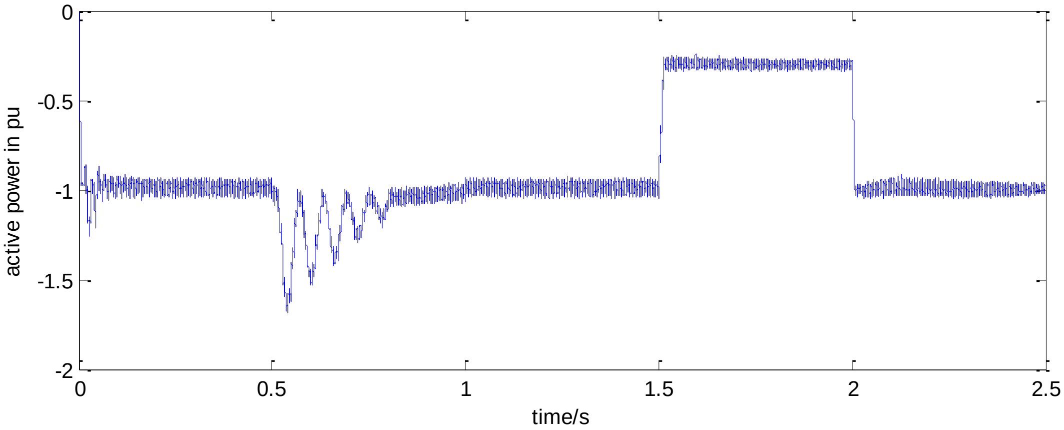

Figure 3.17 Active power profile

Since a unity power factor is expected in this system, the reactive power should stay at zero, and from the reactive power curve shown in Figure 3.18, it can be seen that no matter what the wind speed is, the reactive power tries to be kept at zero value. The role of the pitch angle controller is to regulate the pitch angle when the wind speed exceeds its rated value of 12 m/s. The pitch angle profile is shown in Figure 3.19, and it can be seen that when the wind speed reaches 12 m/s or 8m/s, the pitch angle is kept at zero value, under which case the wind turbine will capture the maximum wind power. When the wind speed increases to 15 m/s, the pitch angle will be increased to limit the captured wind power to its rated value.

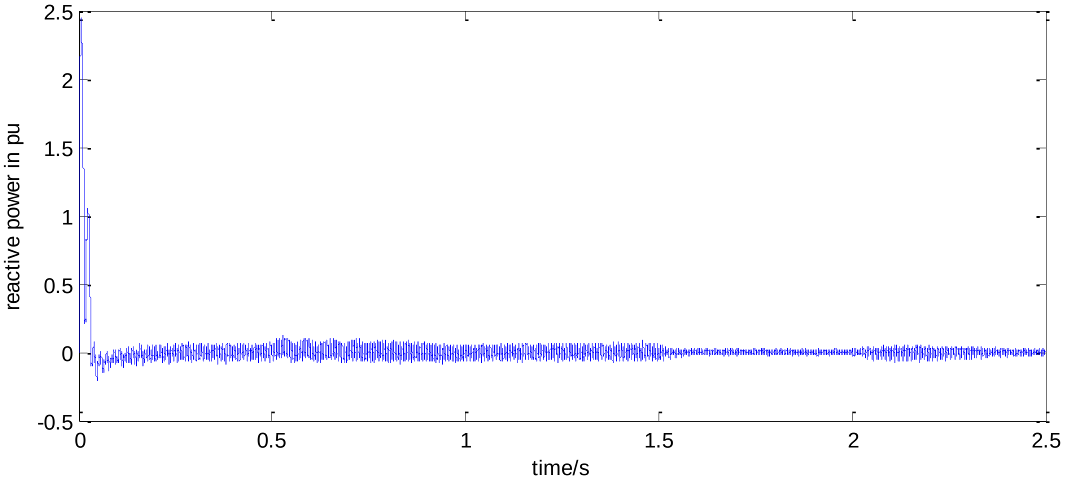

Figure 3.18 Reactive power profile

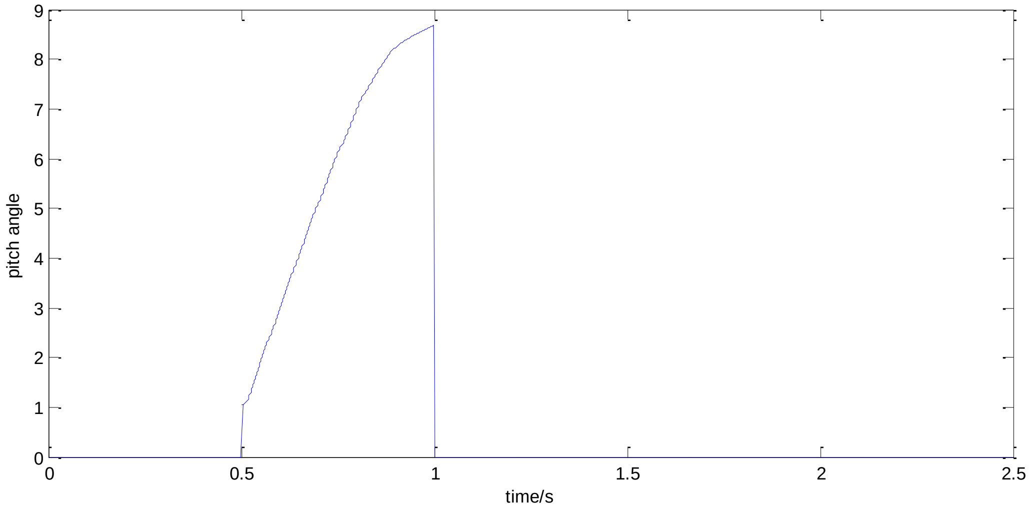

Figure 3.19 Pitch angle profile

The stator quadrature axis current profile is shown in Figure 3.20, and it can be seen that the active power and stator quadrature axis current have similar profiles. This is because of the fact that the active power is directly controlled by the stator quadrature axis current according to equation (3.37). Figure 3.21 shows the curve of the stator direct axis current. Here, based on Figure 3.18 and Figure 3.21, it can be concluded that the reactive power can be directly controlled by the stator direct axis current. Also, from equation (3.38), the same conclusion can be made.

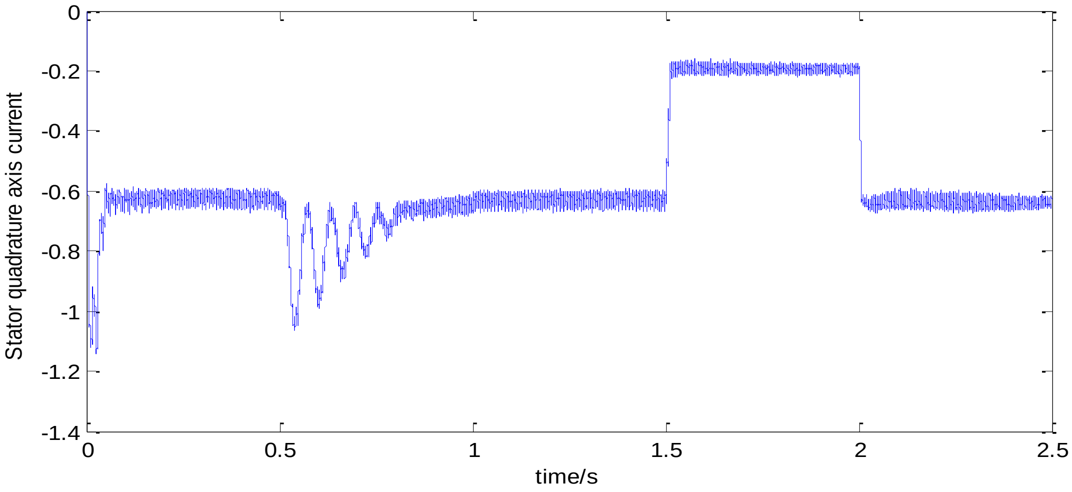

Figure 3.20 Stator quadrature axis current profile in p.u. (stator flux reference frame)

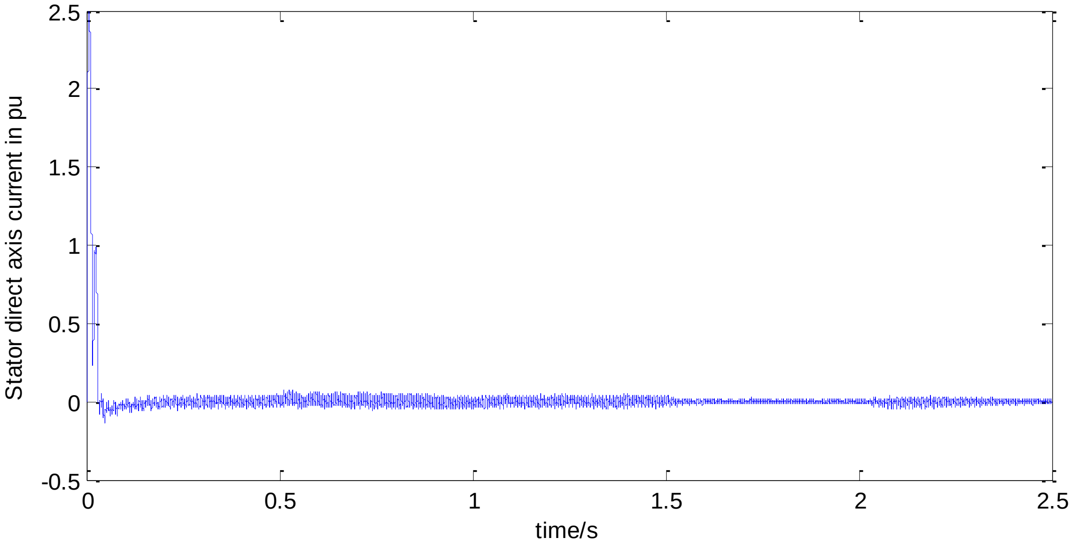

Figure 3.21 Stator direct axis current profile in p.u. (stator flux reference frame)

Under the stator flux oriented control scheme, the active power and reactive power are directly controlled by the stator quadrature and direct axes currents, respectively. From equations (3.26) and (3.28), it can be seen that the stator quadrature and direct axes currents have direct relationships to the rotor quadrature and direct axes currents, which are shown in Figure 3.22 and Figure 3.23. This explains why the rotor quadrature and direct axes currents are similar to the stator quadrature and direct axes current profiles.

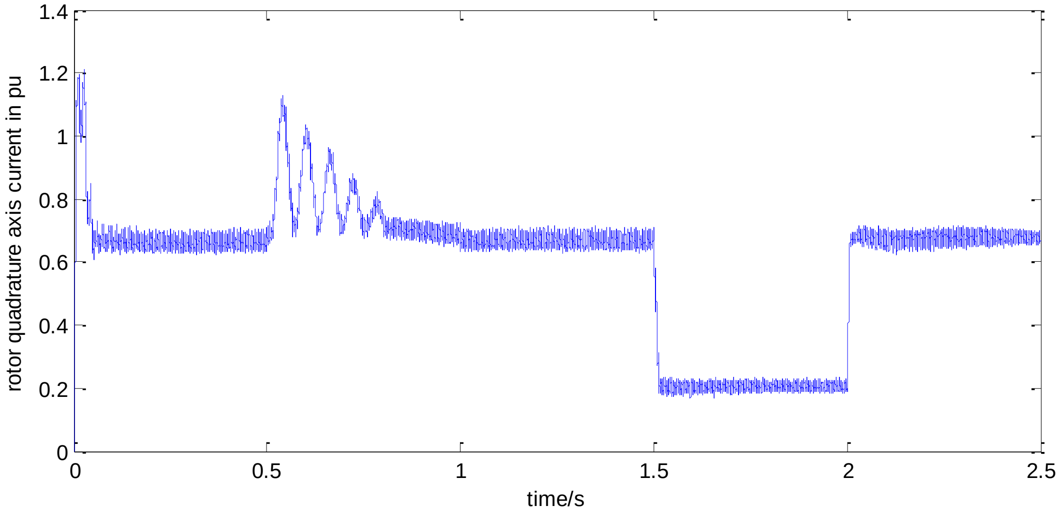

Figure 3.22 Rotor quadrature axis current profile in p.u. (stator flux reference frame)

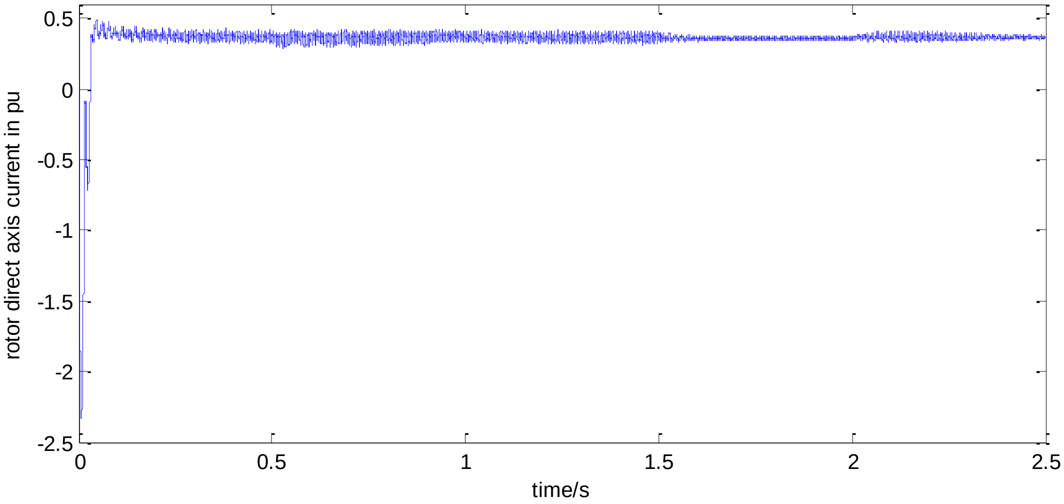

Figure 3.23 Rotor direct axis current profile in p.u. (stator flux reference frame)

Here, the profiles of the rotor and stator currents in the ABC reference frame are shown in Figure 3.24 and Figure 3.25, respectively. As shown in Figure 3.24 and Figure 3.25, the frequency of the stator currents is much higher than the rotor currents due to the reason that $f_r = s \bullet f_r$, where, s, is the slip.

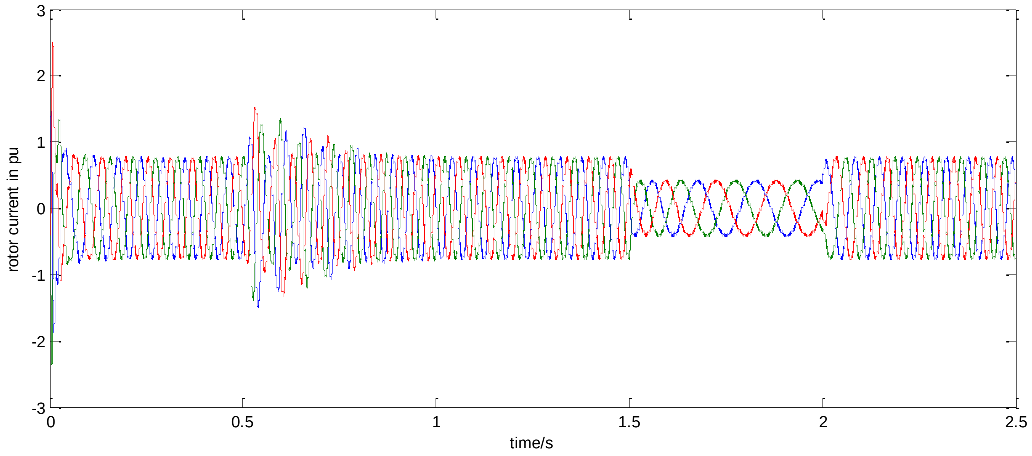

Figure 3.24 Rotor phase current profiles in p.u. (ABC reference frame)

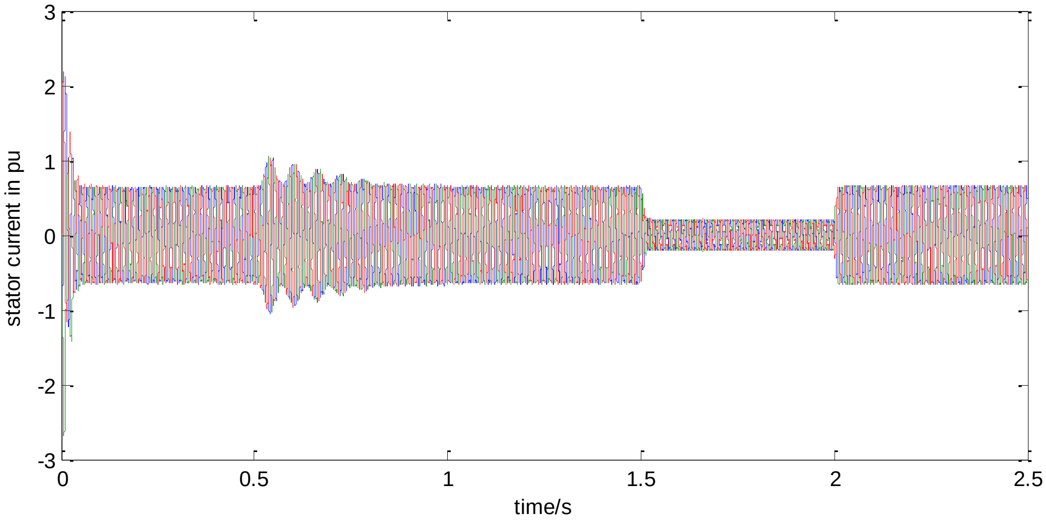

Figure 3.25 Stator phase current profiles in p.u. (ABC reference frame)

The electromagnetic torque in Figure 3.26 is also controlled by the rotor quadrature axis current. One can easily reach this conclusion through using equation (3.36). From Figure 3.27, it can be seen that the grid-side converter controller will attempt to keep the DC-link voltage as constant under various wind speed conditions. In this simulation, the ripple in the DC-link voltage was found to be as follows:

$$Ripple = \frac{1180 - 1130}{1150} = 4.34\%$$

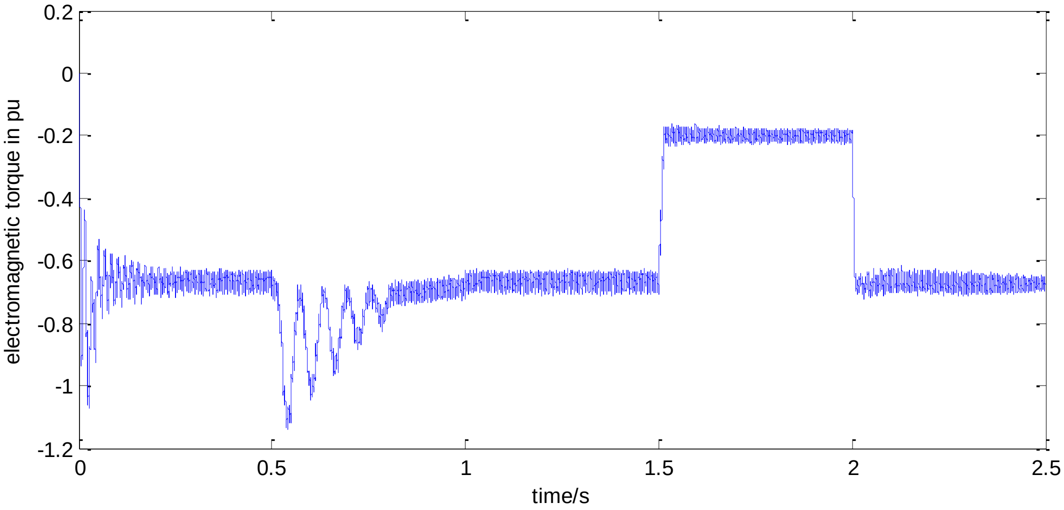

Figure 3.26 Electromagnetic torque profile in p.u.

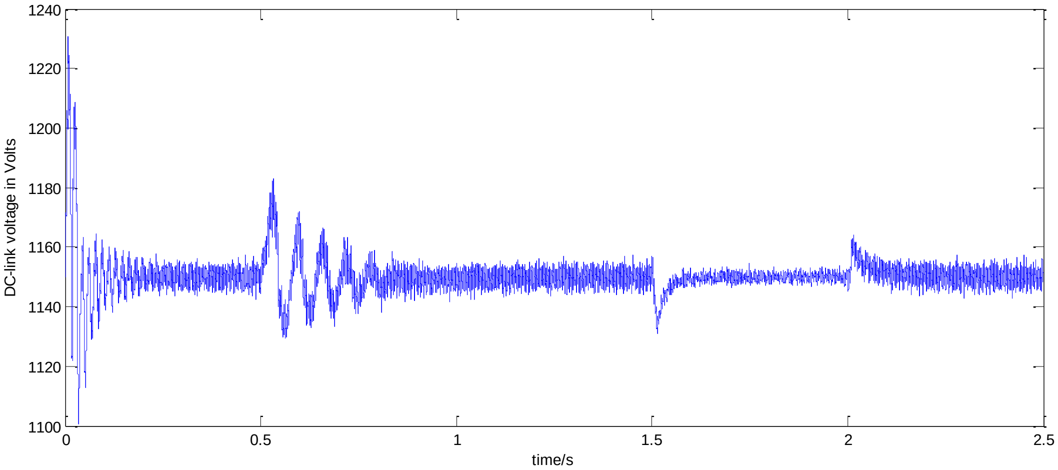

Figure 3.27 DC-link voltage profile in volts

In order to test the performance of the grid-side converter control, the generator-side converter control and the maximum power tracking, the wind turbine-generator system was simulated under a sinusoidal wind speed variation condition, which is shown in Figure 3.28. Here, the wind speed varies from 6 m/s to 12 m/s, and is below the rated wind speed. Therefore, the wind turbine should operate in the MPPT operating mode and generate the maximum power according to the specific wind speed.

Figure 3.29 and Figure 2.30 show the active power and reactive power profiles.

It can be observed that the active power is tracking its reference value and varies with the wind speed, and the reactive power is kept at zero value due to the actions of the controller. Therefore, it can be concluded that the generator-side converter control and the maximum power point tracking control also work well for a sinusoidal wind speed variation condition. Figure 3.31 through Figure 3.34 show the direct and quadrature axes currents of the stator and rotor, respectively, which verify the corresponding relationships given in equations (3.37) and (3.38). Figure 3.35 and Figure 3.36 show the stator and rotor phase currents, respectively, and it can be seen that the envelopes of the stator and rotor currents have sinusoidal response. Figure 3.37 and Figure 3.38 show the electromagnetic torque and rotational speed profiles, respectively, and their product of speed times torque should be equal to the active power. The ripple for the DC-link voltage, based on the simulation results in Figure 3.39, was found to be as follows:

$$Ripple = \frac{1157 - 1144}{1150} = 1.13\%$$

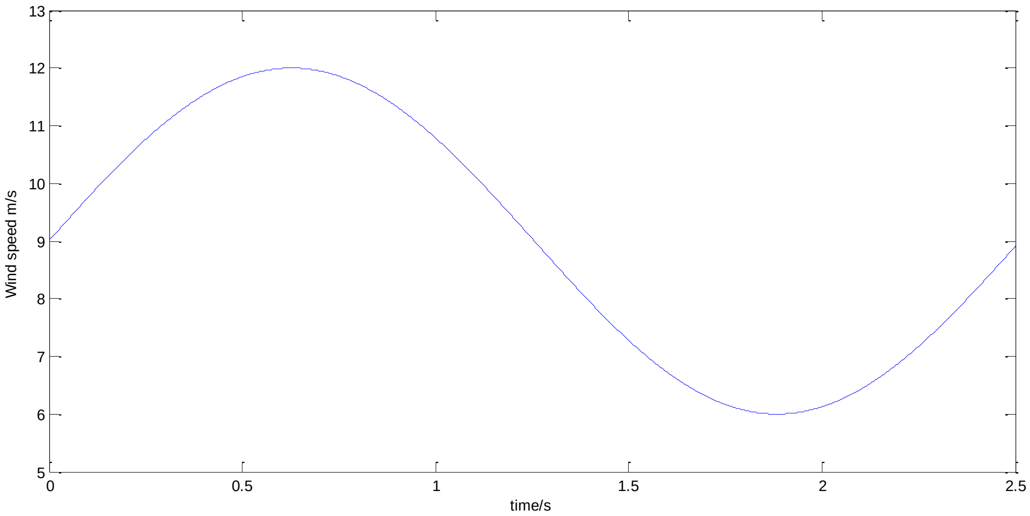

Figure 3.28 Wind speed curve

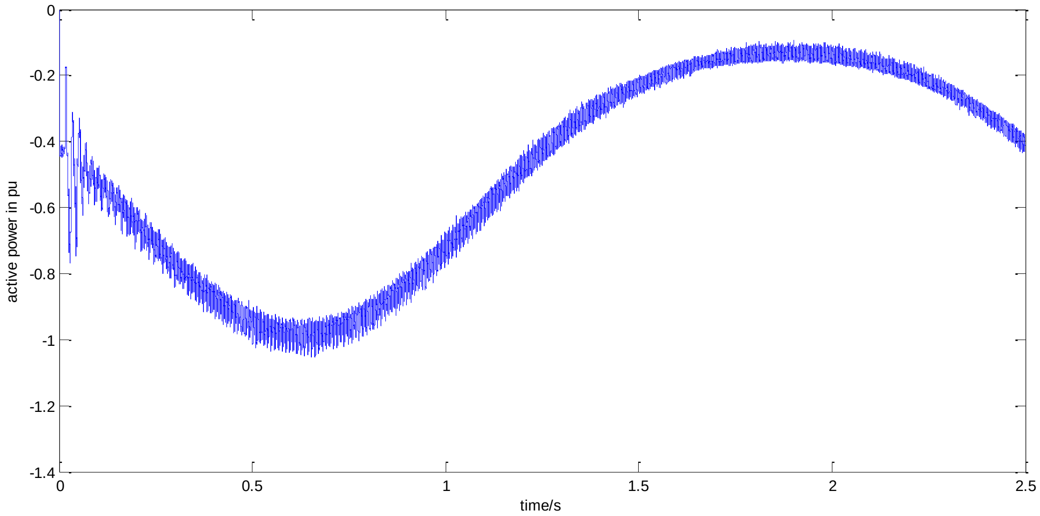

Figure 3.29 Active power profile for a sinusoidal wind speed variation condition

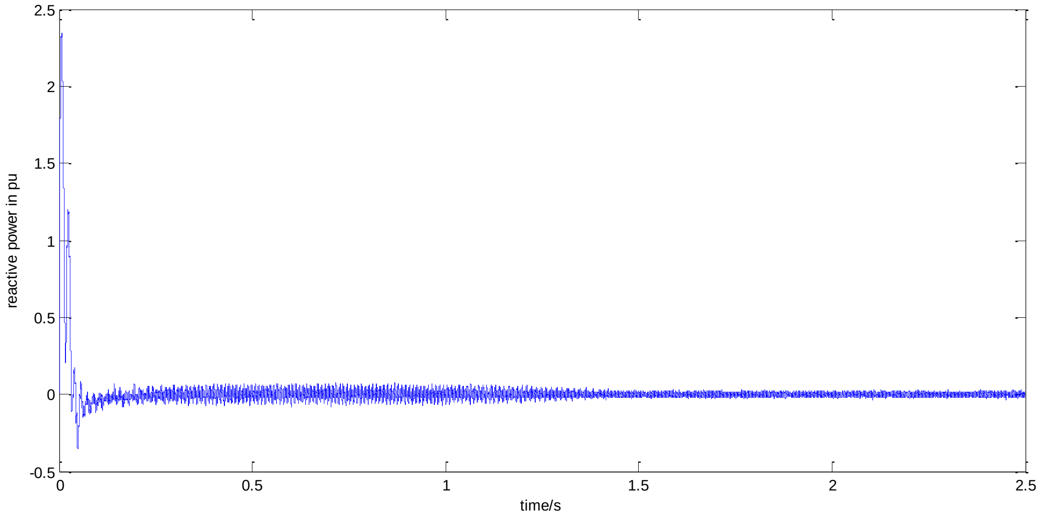

Figure 3.30 Reactive power profile for a sinusoidal wind speed variation condition

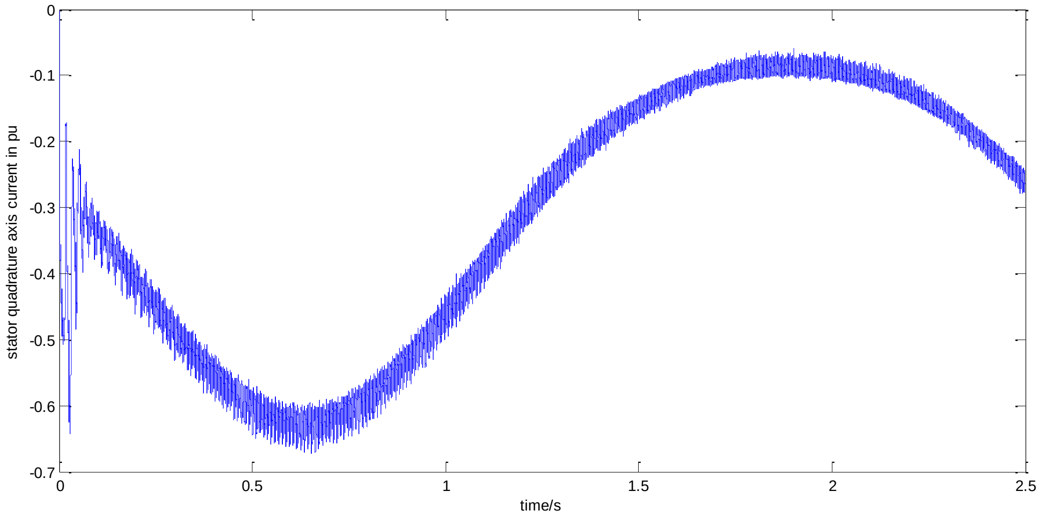

Figure 3.31 Stator quadrature axis current profile in p.u. for a sinusoidal wind speed variation condition

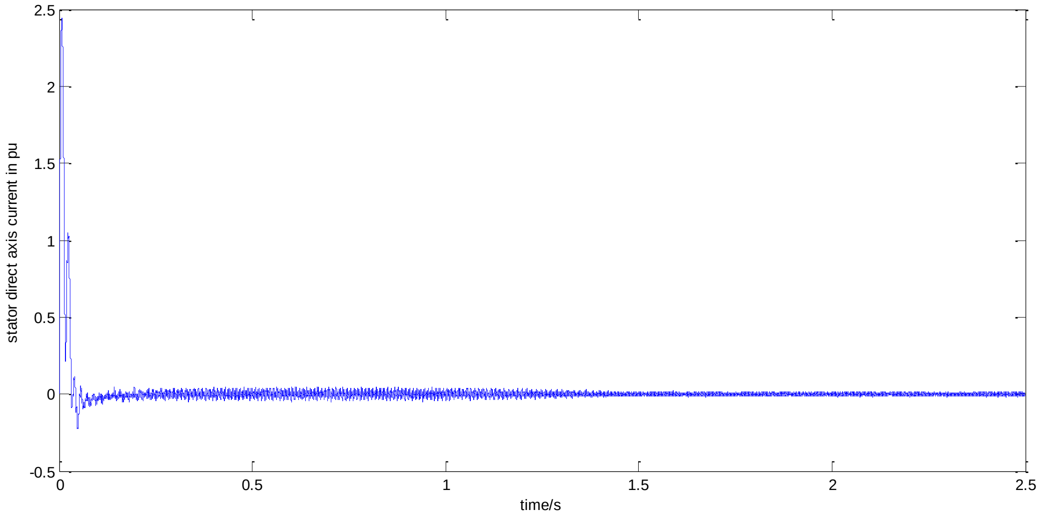

Figure 3.32 Stator direct axis current profile in p.u. for a sinusoidal wind speed variation condition

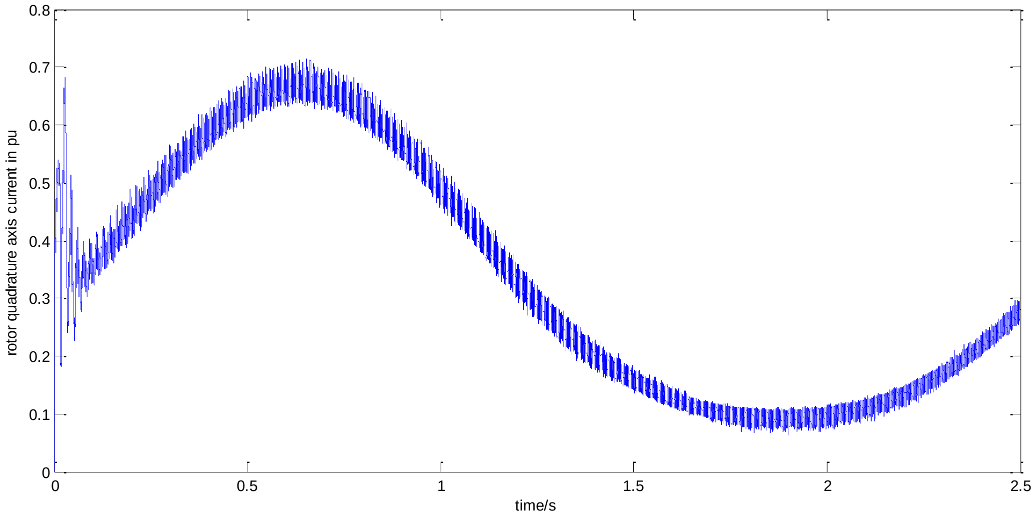

Figure 3.33 Rotor quadrature axis current profile in p.u. for a sinusoidal wind speed variation condition

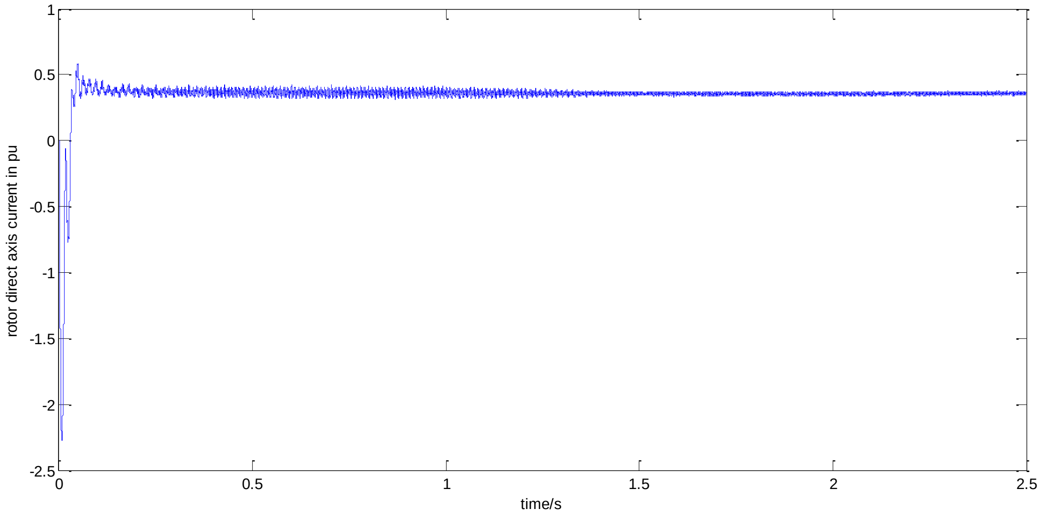

Figure 3.34 Rotor direct axis current profile in p.u. for a sinusoidal wind speed variation condition

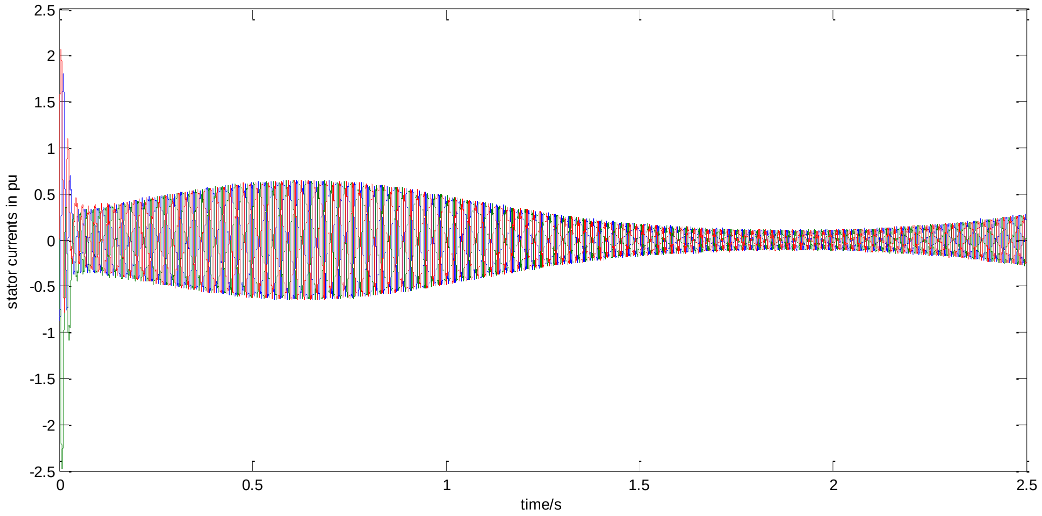

Figure 3.35 Stator phase current profiles in p.u. for a sinusoidal wind speed variation condition

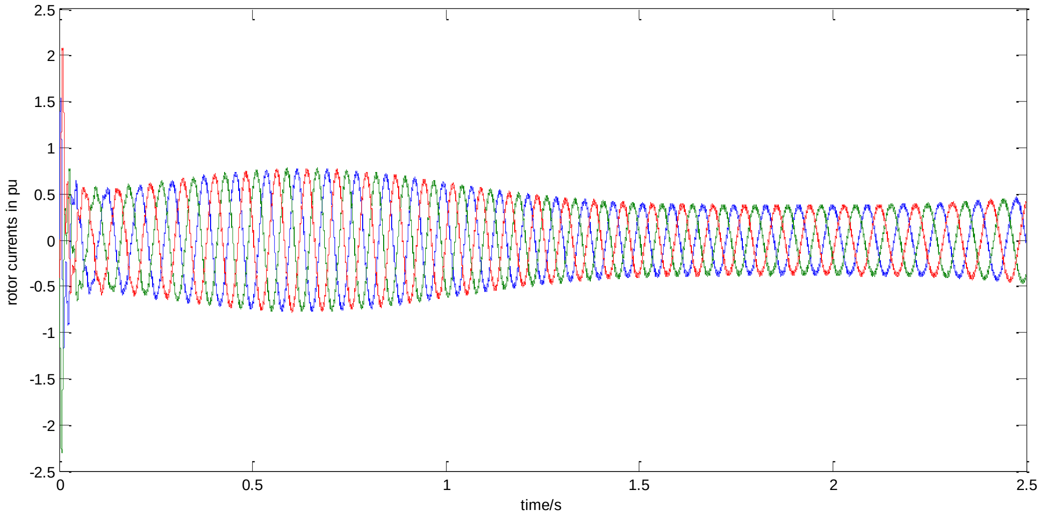

Figure 3.36 Rotor phase current profiles in p.u. for a sinusoidal wind speed variation condition

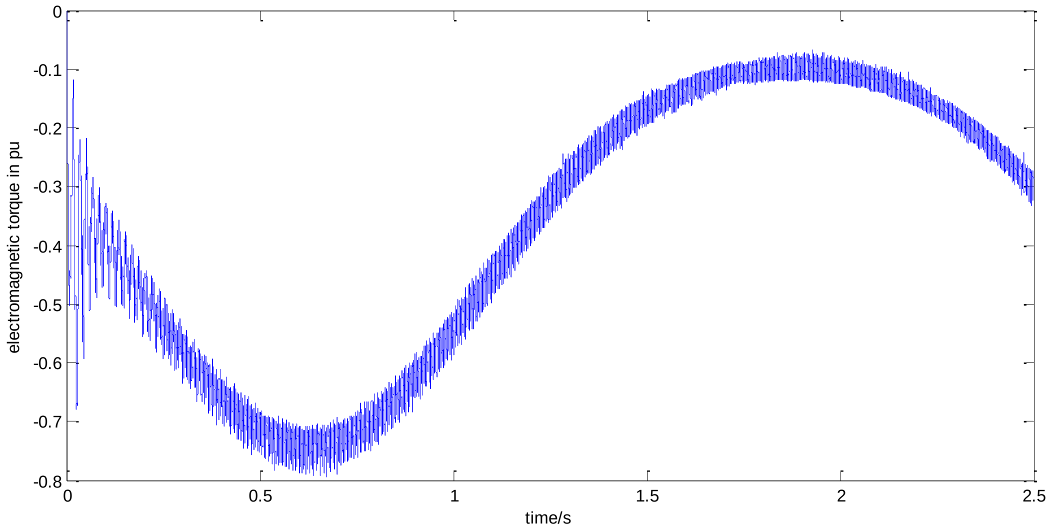

Figure 3.37 Electromagnetic torque profile in p.u. for a sinusoidal wind speed variation condition

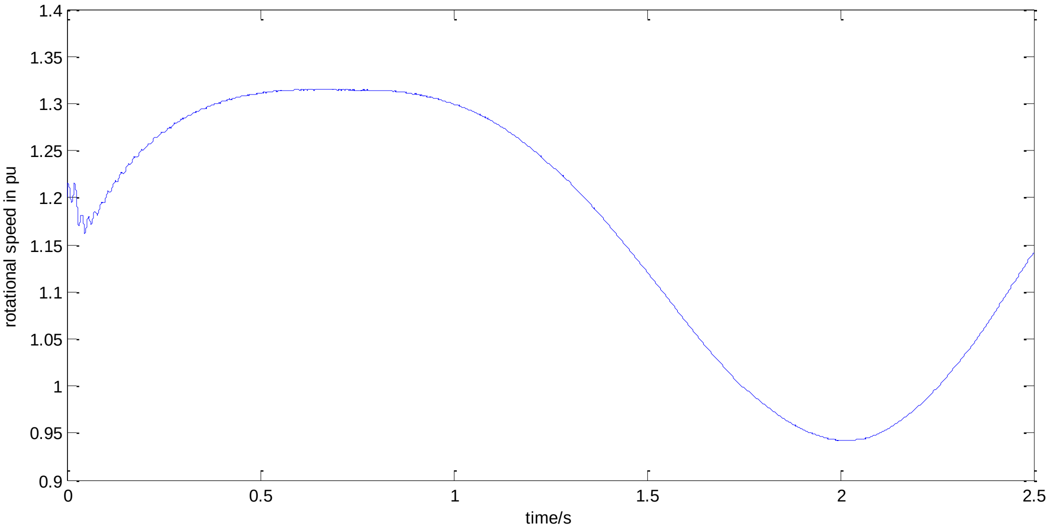

Figure 3.38 Rotational speed profile in p.u. for a sinusoidal wind speed variation condition

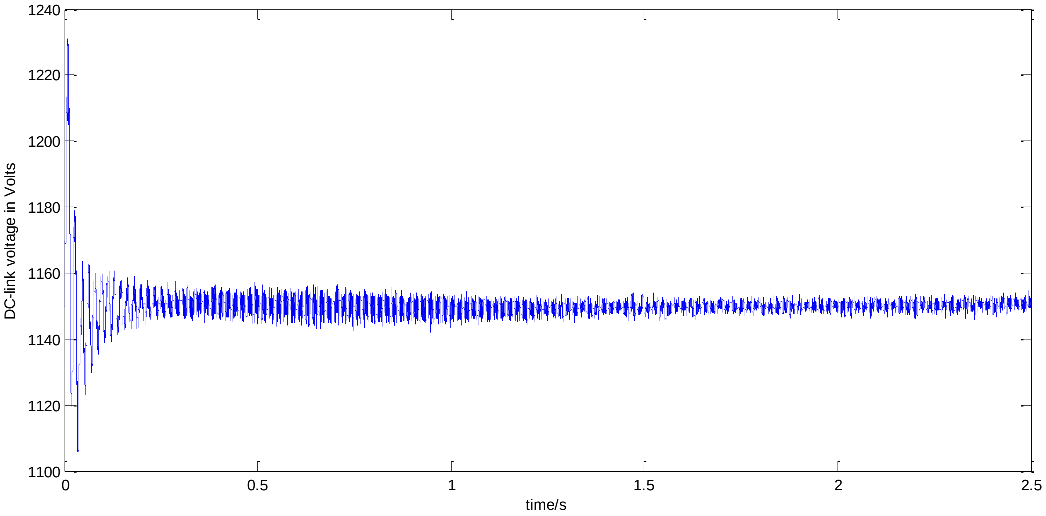

Figure 3.39 DC-link voltage profile in Volts for a sinusoidal wind speed variation condition

Chapter 4

Space Vector PWM and Multi-Level Neutral-Point-Clamped Converters

4.1 Introduction

Sinusoidal PWM (SPWM) has been widely used in AC motor control applications during the past decades. In this relatively unsophisticated method, the three-phase reference modulating signals are compared with a common triangular carrier, and their intersections determine the switching points of the power devices in the inverter. However, this method cannot fully use the inverter's supply voltage, and the asymmetrical nature of the SPWM switching characteristics produces relatively high harmonic distortion of the three-phase output voltages.

The space vector concept, which was originally derived from the rotating field of induction motors, is used in the application of pulse width modulation. Space vector PWM (SVPWM) is a more sophisticated technique for generating modulation signals, and it has many advantages, which are listed as follows: 1) reduced commutation losses, 2) higher amplitude of the modulation index, 3) greater DC-bus voltage utilization, and 4) lower total harmonic distortion (THD) of the output voltages, when compared with the conventional SPWM techniques. The above advantages have allowed this novel technique to be increasingly used in industry since last decade [133].

The multi-level neutral-point-clamped (NPC) inverter concept was first proposed by Akira Nabae in 1981 [134]. Since its introduction, the multi-level NPC voltage source inverters (VSI) have been shown to provide significant advantages over the conventional two-level VSI for medium- and high-power applications, due to their abilities to meet the increasing demand of the power ratings and power quality associated with reduced harmonic distortion, lower electromagnetic interference, and higher efficiency [135]. The advantages of the multi-level NPC voltage source converters are explained as follows:

1. The multi-level converters can generate several voltage levels for the output line-to-line voltages. As a sequence, it will reduce the output voltage and current harmonic contents.
2. The power topologies of the multi-level converters synthesize the voltage waveform with a number of semiconductor devices connected in a special arrangement, rated at a fraction of the DC-bus voltage. For three-level converters, the voltage supported by each power semiconductor will be $0.5V_{dc}$. However, for two-level converters, the voltage supported by each power semiconductor will be V_{dc} with the same DC-bus.
3. The use of multi-level converters permits a direct connection of the wind turbine to the medium voltage electric grid without using expensive, bulky, and heavy 50/60-Hz transformers. Multi-level converters can control the frequency, magnitudes and the phase angle of the output voltages, and provide a fast response and autonomous control [135].
4. The first group of the voltage harmonics is centered around twice the switching frequency, and the low frequency harmonics from the output ac voltages are cancelled. This feature enables further reduction in size, weight,

and cost of passive components while at the same time improving the quality of the output waveforms [136].

On the other hand, this topology is also limited by the following drawbacks: high number of devices, unbalance issue of the neutral-point, and typically complex control schemes [137].

The presented advantages of the multi-level converters make them alternatives to conventional two-level converters for the application in renewable energy and industry. In this thesis, the SVPWM technique is first applied in a traditional two-level converter. Second, the basic principles and features of the multi-level NPC converter will be presented. Third, the SVPWM for a three-level converter will be studied and analyzed in detail. Finally, the simulation results and comparison study of the two-level and three-level inverters, modulated by the SPWM and SVPWM, respectively, will be presented. Here, the simulation study is developed under a Matlab/Simulink environment.

4.2 Space Vector PWM for Two-level Inverters

4.2.1 Three-Phase Voltage Source Inverter Modeling Review

The circuit schematic of a typical three-phase voltage source PWM inverter is shown in Figure 4.1. The six power switches, S_1 to S_6, shape the output voltages. Here, let's define $S_k\left(k=a,b,c\right)$ as the switch function of phase, k. Hence, based on the principle that any two switches in the same leg cannot be on at the same time, the definition of S_k is given as follows:

$$S_k = \begin{cases} 1 & The \quad upper \quad IGBT \quad is \quad on \\ 0 & The \quad upper \quad IGBT \quad is \quad off \end{cases} \tag{4.1}$$

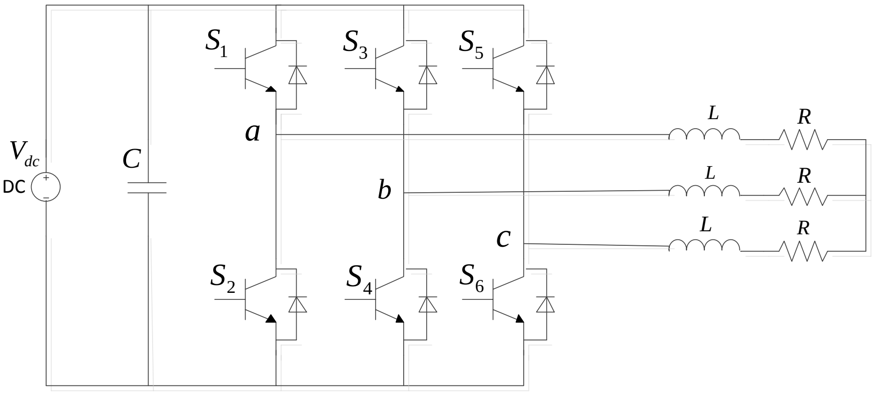

Figure 4.1 Three-phase voltage source PWM inverter scheme

For each phase, there will be two switching states. As a result, there are 2^3=8 possible switching patterns for the three-phase two-level inverter, and the output phase voltages and line-to-line voltages for different switching patterns are given in Table 4.1.

Table 4.1 Switching patterns and output voltages

Voltage vectors	Switching vectors			Line-to-neutral voltages			Line-to-line voltages		
	A	B	C	$V_{an}(V_{dc})$	$V_{bn}(V_{dc})$	$V_{cn}(V_{dc})$	$V_{ab}(V_{dc})$	$V_{bc}(V_{dc})$	$V_{ca}(V_{dc})$
$\vec{V}_0$	0	0	0	0	0	0	0	0	0
$\vec{V}_1$	1	0	0	2/3	-1/3	-1/3	1	0	-1
$\vec{V}_2$	1	1	0	1/3	1/3	-2/3	0	1	-1
$\vec{V}_3$	0	1	0	-1/3	2/3	-1/3	-1	1	0
$\vec{V}_4$	0	1	1	-2/3	1/3	1/3	-1	0	1
$\vec{V}_5$	0	0	1	-1/3	-1/3	2/3	0	-1	1
$\vec{V}_6$	1	0	1	1/3	-2/3	1/3	1	-1	0
$\vec{V}_7$	1	1	1	0	0	0	0	0	0

Here, each of the voltages in above table is scaled by " V_{dc} ".

4.2.2 Space Vector PWM

From Table 4.1, the inverter has six non-zero vectors and two zero vectors. The six non-zero vectors ($\vec{V}_1$-$\vec{V}_6$) shape the axes of a hexagon and the zero vectors ($\vec{V}_0$ and $\vec{V}_7$) sit at the origin in the stator reference frame (α-β), as depicted in Figure 4.2. The eight vectors are called the basic space vectors, and the angle between any two adjacent non-zero vectors is 60 degrees. The lengths of the six non-zero vectors are $2/3V_{dc}$ and the lengths of the two zero vectors are zero.

From Table 4.1, according to the equivalence principle, the following set of equations can be deduced [138]:

$$\left.\begin{array}{r}\vec{V}_1 = -\vec{V}_4 \\ \vec{V}_2 = -\vec{V}_5 \\ \vec{V}_3 = -\vec{V}_6 \\ \vec{V}_0 = -\vec{V}_7 = 0 \\ \vec{V}_1 + \vec{V}_3 + \vec{V}_5 = 0\end{array}\right\} \tag{4.2}$$

Based on equation (4.2), the space vectors and sectors in a stationary (α-β) reference frame are drawn in Figure 4.2.

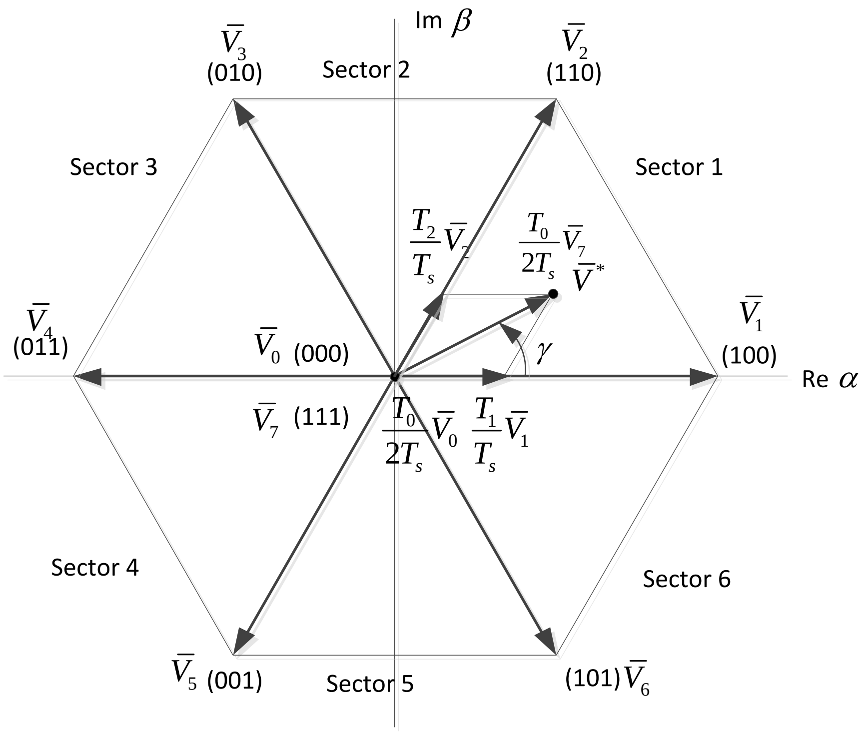

Figure 4.2 Space vectors and sectors

At any sector, the output reference voltage vector, $\vec{V}^*$, can be made up by the non-zero vectors and zero vectors, which can be written as follows:

$$\vec{V}^* = \frac{T_0}{T_s}\vec{V}_0 + \frac{T_1}{T_s}\vec{V}_1 + \cdots + \frac{T_7}{T_s}\vec{V}_7 \tag{4.3}$$

where, T_0, ..., T_7 are the turn-on time of the voltage vectors $\vec{V}_0, \cdots \vec{V}_7$, and must satisfy the following relationships: 1) T_0, T_1,... T_7>=0, 2) $\sum_{i=0}^{7} T_i = T_s$. Here, Ts, is the sample time. According to equation (4.3), there are infinite ways to compose the reference voltage vector, $\vec{V}^*$. However, it is proven that when the reference voltage vector is constructed from the two nearest adjacent voltage vectors and zero vectors, the number of switching actions can be reduced, and the active turn-on time for the space vectors can be fully used. For example, in sector 1, shown in Figure 4.2, in one sampling interval, the reference voltage vector, $\vec{V}^*$, can be expressed as follows:

$$\vec{V}^{*} = \frac{T_0}{T_s}\vec{V}_0 + \frac{T_1}{T_s}\vec{V}_1 + \frac{T_2}{T_s}\vec{V}_2 + \frac{T_7}{T_s}\vec{V}_7 \tag{4.4}$$

where, $T_s - T_1 - T_2 = T_0 + T_7 \geq 0, \quad T_0 \geq 0 \quad and \quad T_7 \geq 0$.

For the space vector modulation, the boundary between the linear modulation range and the over-modulation range in sector 1 is defined as follows:

$$T_s = T_1 + T_2 \qquad T_0 = T_7 = 0 \tag{4.5}$$

Therefore, from equation (4.5), it can be deduced that the boundary between the linear modulation range and the over-modulation range is the hexagon, shown in Figure 4.3. The linear modulation range is located within the hexagon. If the reference voltage vector exceeds the hexagon, then the summation of T_1 and T_2 will be greater than T_s, which is unrealizable.

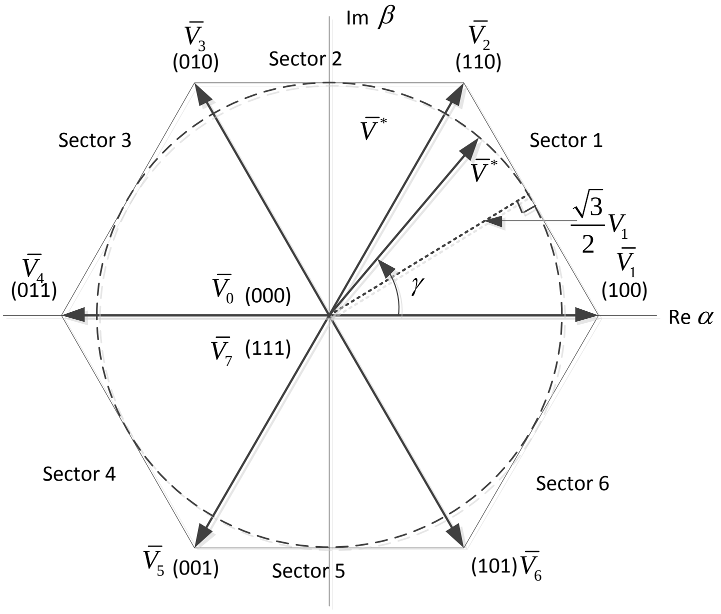

Figure 4.3 Modulation range for the SVPWM

Furthermore, it should be pointed out that in the linear modulation range, the trajectory of the reference voltage vector, $\vec{V}^{*}$, becomes the inscribed circle of the hexagon because of the fact that the amplitude of the reference voltage should be kept as constant. For the SVPWM, the maximum amplitude of the reference voltage that can be achieved is $\sqrt{3}/2V_1$ in sector 1. Therefore, the maximum amplitudes for the phase and line-to-line voltages are $1/\sqrt{3}V_{dc}$ and V_{dc}, respectively. However, for the SPWM, the maximum amplitudes for the phase and line-to-line voltages are $0.5V_{dc}$ and $\sqrt{3}/2V_{dc}$, respectively. By setting the modulation index of the SPWM as a reference, it can be deduced that the modulation index for the SVPWM is approximately 15 percent more than SPWM [139].

4.2.3 Software Implementation of the Space Vector PWM

Space vector PWM can be implemented by the following steps [140], in which the calculations for sector 1 are taken as an example:

Step 1: Determine the voltages, v_α, v_β, and the angle, γ, of the expected output voltage.

Step 2: Calculate the time durations, T_0, T_1, T_2 and T_7.

Step 3: Determine the switching sequences for all six sectors.

Step 1: The expected three-phase output voltages should be transformed to the stationary reference frame and then the angle, γ, should be determined by using the following equations:

$$\begin{bmatrix} v_\alpha \\ v_\beta \end{bmatrix} = \frac{2}{3}\begin{bmatrix} 1 & -1/2 & -1/2 \\ 0 & \sqrt{3}/2 & -\sqrt{3}/2 \end{bmatrix}\begin{bmatrix} v_{an} \\ v_{bn} \\ v_{cn} \end{bmatrix} \tag{4.6}$$

$$\left|\vec{V}^*\right| = \sqrt{v_\alpha^2 + v_\beta^2} \tag{4.7}$$

$$\gamma = \tan^{-1}\left(\frac{v_\beta}{v_\alpha}\right) \tag{4.8}$$

Step 2: Calculate the time durations, T_0, T_1, T_2 and T_7. In sector 1, there could be several alternatives to compose the reference output voltage. This thesis herein introduces the easiest method, and a more complicated method will be given later in this section. The easiest method, shown in Figure 4.2, distributes the zero vectors, $\vec{V}_0$ and $\vec{V}_7$, at the begin and end of the reference voltage vector, respectively. The non-zero vectors, $\vec{V}_1$ and $\vec{V}_2$, are distributed at the middle of the reference voltage vector. From Figure 4.2, the switching time durations for sector 1 can be calculated as follows:

$$\left.\begin{aligned} T_s \cdot \left|\vec{V}^*\right| \cdot \cos\gamma = T_1 \cdot \left|\vec{V}_1\right| + T_2 \cdot \left|\vec{V}_2\right| \cdot \cos\frac{\pi}{3} \\ T_s \cdot \left|\vec{V}^*\right| \cdot \sin\gamma = T_2 \cdot \left|\vec{V}_2\right| \cdot \sin\frac{\pi}{3} \end{aligned}\right\} \Rightarrow$$

$$T_1 = T_s \cdot m \cdot \sin\left(\frac{\pi}{3} - \gamma\right) \tag{4.9}$$

$$T_2 = T_s \cdot m \cdot \sin(\gamma) \tag{4.10}$$

$$T_0 = T_s - T_1 - T_2 \tag{4.11}$$

Here, T_0, is the total turn-on time of the zero voltage vectors, $\vec{V}_0$ and $\vec{V}_7$, and needs to be equally divided into two parts for these zero vectors. Here also, $0 \le \gamma \le \pi/3$, and *m*, is the modulation index and can be expressed as follows:

$$m = \frac{\sqrt{3}\left|\vec{V}^*\right|}{V_{dc}} \tag{4.12}$$

From previous analysis, the maximum value for the reference voltage vector, $\vec{V}^*$, can be derived as follows:

$$V_{\max}^* = \frac{\sqrt{3}}{2}\left|\vec{V}_1\right| = \frac{\sqrt{3}}{2} \times \frac{2}{3} V_{dc} = \frac{1}{\sqrt{3}} V_{dc} \tag{4.13}$$

Hence, the maximum value for the modulation index can be calculated as follow:

$$m_{\max} = \frac{\sqrt{3}V_{\max}^{*}}{V_{dc}} = \frac{\sqrt{3}}{V_{dc}} \times \frac{1}{\sqrt{3}} V_{dc} = 1 \tag{4.14}$$

From equations (4.9) through (4.11), the switching time durations of the voltage vectors, $\vec{V}_0$, $\vec{V}_n$, $\vec{V}_{n+1}$ and $\vec{V}_7$, for any sector, n, can be deduced and given as follows:

$$T_n = T_s \cdot m \cdot \sin\left(n \cdot \frac{\pi}{3} - \gamma \right) \tag{4.15}$$

$$T_{n+1} = T_s \cdot m \cdot \sin\left(\gamma - (n-1) \cdot \frac{\pi}{3} \right) \tag{4.16}$$

$$T_0 = T_s - T_n - T_{n+1} \tag{4.17}$$

where, $0 \le \gamma \le \pi/3$, and $n = 1, 2, \cdots 6$.

The switching time durations for all six sectors are given in Table 4.2.

Table 4.2 Switching time durations for all six sectors

Sector 1 (0≤ γ <π/3)	Sector 2 (π/3≤ γ <2π/3)	Sector 3 (2π/3≤ γ <π)
$T_1 = \sqrt{3}\frac{T_s \cdot \lvert\vec{V}^*\rvert}{V_{dc}}\cos(\gamma + \frac{\pi}{6})$ $T_2 = \sqrt{3}\frac{T_s \cdot \lvert\vec{V}^*\rvert}{V_{dc}}\cos(\gamma + \frac{3\pi}{2})$	$T_2 = \sqrt{3}\frac{T_s \cdot \lvert\vec{V}^*\rvert}{V_{dc}}\cos(\gamma + \frac{11\pi}{6})$ $T_3 = \sqrt{3}\frac{T_s \cdot \lvert\vec{V}^*\rvert}{V_{dc}}\cos(\gamma + \frac{7\pi}{6})$	$T_3 = \sqrt{3}\frac{T_s \cdot \lvert\vec{V}^*\rvert}{V_{dc}}\cos(\gamma + \frac{3\pi}{2})$ $T_4 = \sqrt{3}\frac{T_s \cdot \lvert\vec{V}^*\rvert}{V_{dc}}\cos(\gamma + \frac{5\pi}{6})$
Sector 4 (π≤ γ <4π/3)	Sector 5 (4π/3≤ γ <5π/3)	Sector 6 (5π/3≤ γ <2π)
$T_4 = \sqrt{3}\frac{T_s \cdot \lvert\vec{V}^*\rvert}{V_{dc}}\cos(\gamma + \frac{7\pi}{6})$ $T_5 = \sqrt{3}\frac{T_s \cdot \lvert\vec{V}^*\rvert}{V_{dc}}\cos(\gamma + \frac{\pi}{2})$	$T_5 = \sqrt{3}\frac{T_s \cdot \lvert\vec{V}^*\rvert}{V_{dc}}\cos(\gamma + \frac{5\pi}{6})$ $T_6 = \sqrt{3}\frac{T_s \cdot \lvert\vec{V}^*\rvert}{V_{dc}}\cos(\gamma + \frac{\pi}{6})$	$T_6 = \sqrt{3}\frac{T_s \cdot \lvert\vec{V}^*\rvert}{V_{dc}}\cos(\gamma + \frac{\pi}{2})$ $T_1 = \sqrt{3}\frac{T_s \cdot \lvert\vec{V}^*\rvert}{V_{dc}}\cos(\gamma + \frac{11\pi}{6})$

Step 3: Determine the switching sequences for all six sectors. From the first method mentioned in step 2, it can be seen that all the voltage vectors, $\vec{V}_0$, $\vec{V}_1$, $\vec{V}_2$ and $\vec{V}_7$, are not symmetrically distributed to compose the reference voltage vector, and this asymmetrical characteristic will generate high switching losses and harmonic components. Therefore, in order to overcome these disadvantages, reference [141] proposed another method, in which the zero state vector, $\vec{V}_0$, is equally distributed at the beginning and end of the reference voltage vector, and the zero state vector, $\vec{V}_7$, is distributed at the middle of the reference voltage vector. Besides, the non-zero vectors are equally distributed between two zero vectors, $\vec{V}_0$ and $\vec{V}_7$, and between $\vec{V}_7$ and $\vec{V}_0$, as described in Figure 4.4.

Therefore, the total switching period is divided into 7 switching states. The switching patterns for upper IGBTs in sector 1 are shown in Figure 4.5. Besides, the switching sequence is shown at the bottom of Figure 4.5, and the corresponding explanation will be given next.

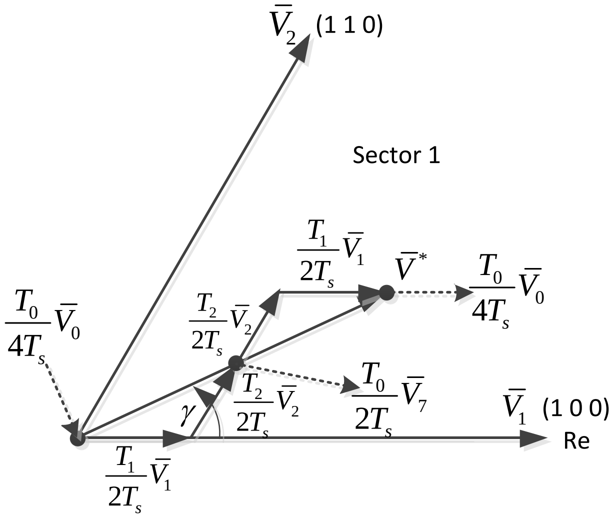

Figure 4.4 Reference vector as a combination of adjacent vectors in sector 1

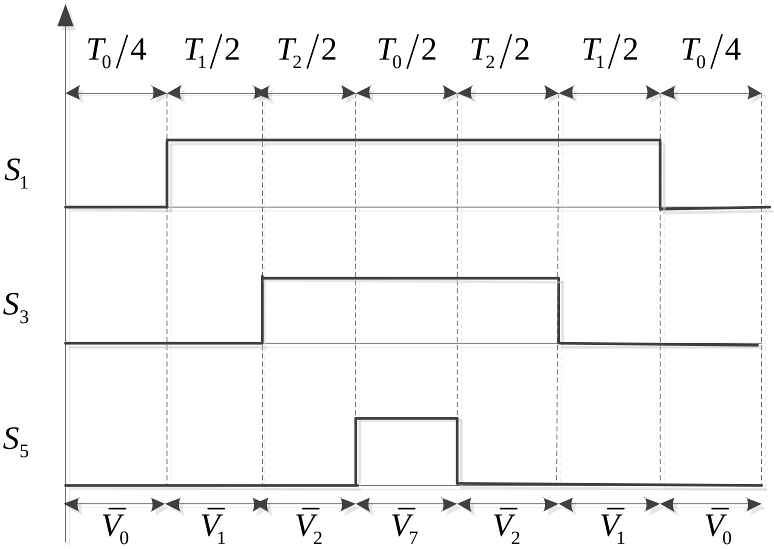

Figure 4.5 Switching patterns for upper IGBTs in sector 1

It should be noted that although this switching strategy is different from the first method, the overall switching time duration is the same. Therefore, Table 4.2 is still feasible for the second method.

To reduce the number of the inverter switching actions, it is necessary to distribute the switching states in such a way that the transition from one state to the next is performed by only switching one inverter leg at a time [142]. For example, in sector 1, the reference voltage vector is composed by $\vec{V}_0$, $\vec{V}_1$, $\vec{V}_2$ and $\vec{V}_7$, and the corresponding switching patterns of upper IGBTs for these vectors are (0, 0, 0), (1, 0, 0), (1, 1, 0) and (1, 1, 1), respectively. In order to achieve one switching action at each time duration, $\vec{V}_2$ should appear behind $\vec{V}_1$, or else, the transition from $\vec{V}_0$ to $\vec{V}_2$ needs two switching actions. Based on this principle, the switching sequence will be (0, 0, 0) $\rightarrow$ (1, 0, 0) $\rightarrow$ (1, 1, 0) $\rightarrow$ (1, 1, 1), and vice versa. Therefore, the seven-segment switching sequences for $\vec{V}^*$ residing in all six sectors are given in Table 4.3. It should be noted that all the switching sequences will start and end with switching state [000], which indicates that the transition for $\vec{V}^*$ moving from one sector to the next sector does not require any switching actions.

Table 4.3 Seven-segments switching sequences for all sectors

Sector	Switching Sequence						
	1	2	3	4	5	6	7
1	$\vec{V}_0$	$\vec{V}_1$	$\vec{V}_2$	$\vec{V}_7$	$\vec{V}_2$	$\vec{V}_1$	$\vec{V}_0$
	000	100	110	111	110	100	000
2	$\vec{V}_0$	$\vec{V}_3$	$\vec{V}_2$	$\vec{V}_7$	$\vec{V}_2$	$\vec{V}_3$	$\vec{V}_0$
	000	010	110	111	110	010	000
3	$\vec{V}_0$	$\vec{V}_3$	$\vec{V}_4$	$\vec{V}_7$	$\vec{V}_4$	$\vec{V}_3$	$\vec{V}_0$
	000	010	011	111	011	010	000
4	$\vec{V}_0$	$\vec{V}_5$	$\vec{V}_4$	$\vec{V}_7$	$\vec{V}_4$	$\vec{V}_5$	$\vec{V}_0$
	000	001	011	111	011	001	000
5	$\vec{V}_0$	$\vec{V}_5$	$\vec{V}_6$	$\vec{V}_7$	$\vec{V}_6$	$\vec{V}_5$	$\vec{V}_0$
	000	001	101	111	101	001	000
6	$\vec{V}_0$	$\vec{V}_1$	$\vec{V}_6$	$\vec{V}_7$	$\vec{V}_6$	$\vec{V}_1$	$\vec{V}_0$
	000	100	101	111	101	100	000

Based on Table 4.3, the switching pulse patterns for upper IGBTs in all six sectors are plotted in Figure 4.6.

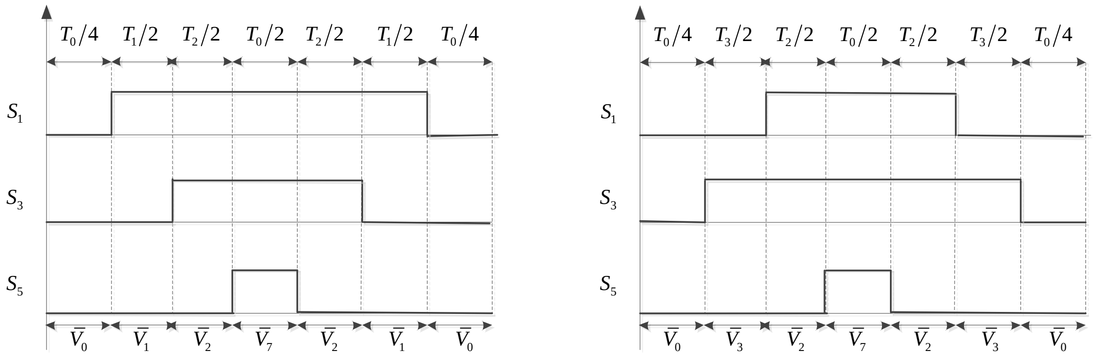

(a) Sector 1

(b) Sector 2

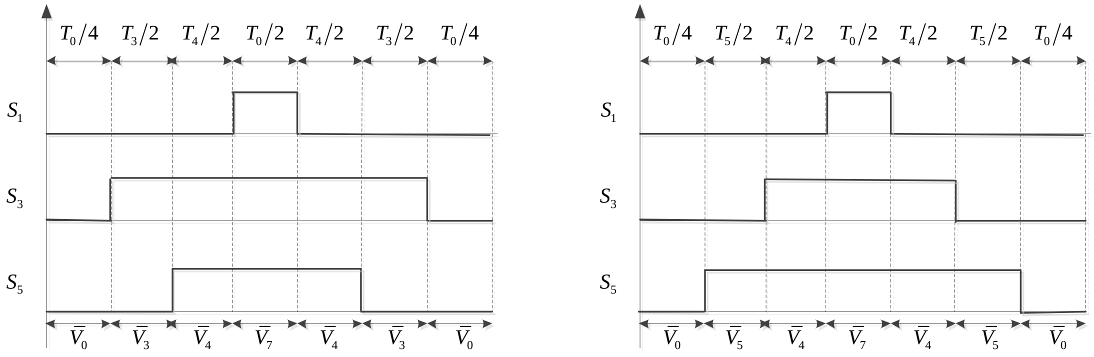

(c) Sector 3 (d) Sector 4

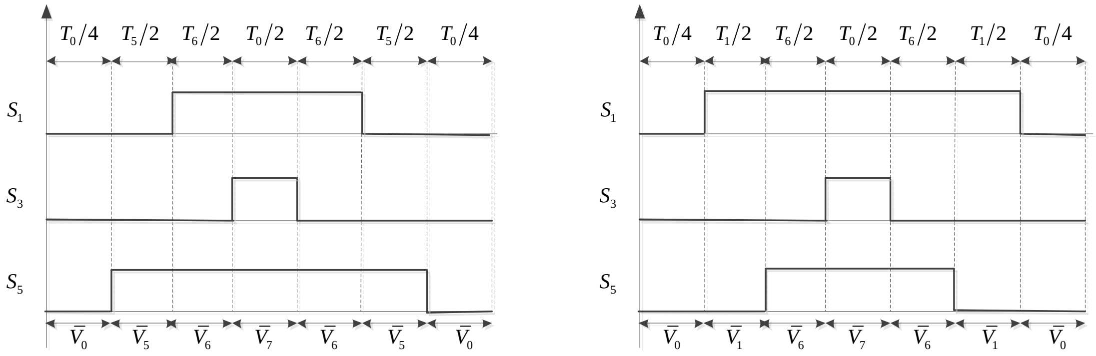

(e) Sector 5 (f) Sector 6

Figure 4.6 Switching patterns for upper IGBTs in all six sectors

4.2.4 Comparison Between SPWM and SVPWM for a Three-Phase Two-Level Inverter

In this section, the SVPWM was simulated in a Matlab/Simulink environment, in which a DC voltage source is connected to six IGBTs as well as a three-phase series RL load. Here, the gate signals for six IGBTs are generated by the SVPWM. The simulation scheme for a three-phase voltage source inverter modulated by the SVPWM is shown in Figure 4.7, and the data used in the simulation study are given in Table 4.4.

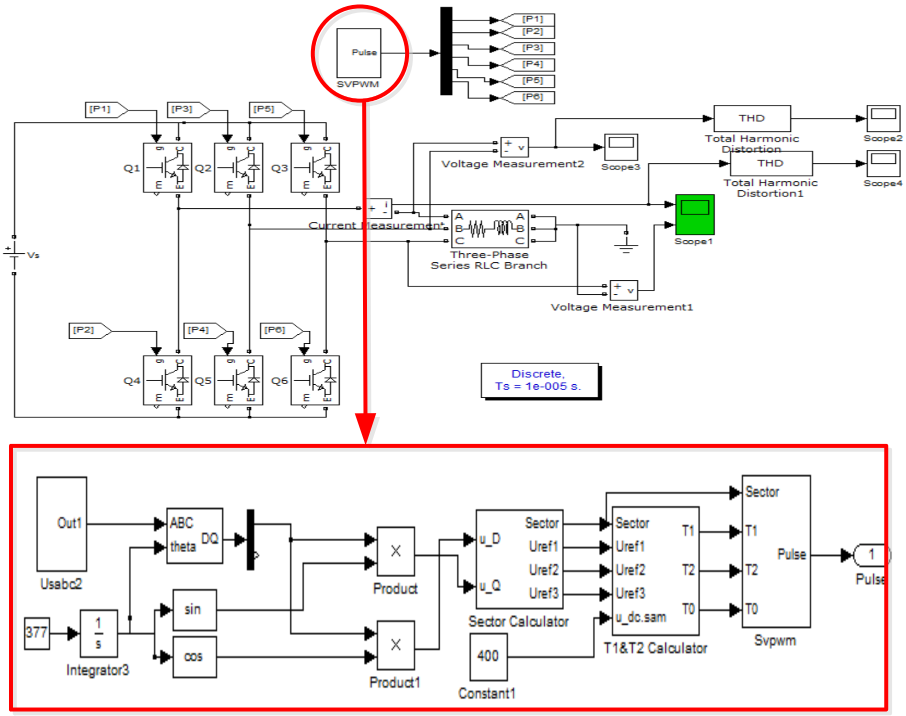

Figure 4.7 Simulation scheme for a three-phase two-level voltage source inverter

Table 4.4 Three-phase voltage source inverter data

Parameter	Value	Units
DC voltage source	400	V
R	10	ohm
L	0.05	H
Output frequency	60	Hz
T_s	1/5000	sec
Modulation index	0.8	

The simulation results for the three-phase voltage source inverter modulated by SVPWM are shown in Figure 4.8 through Figure 4.10.

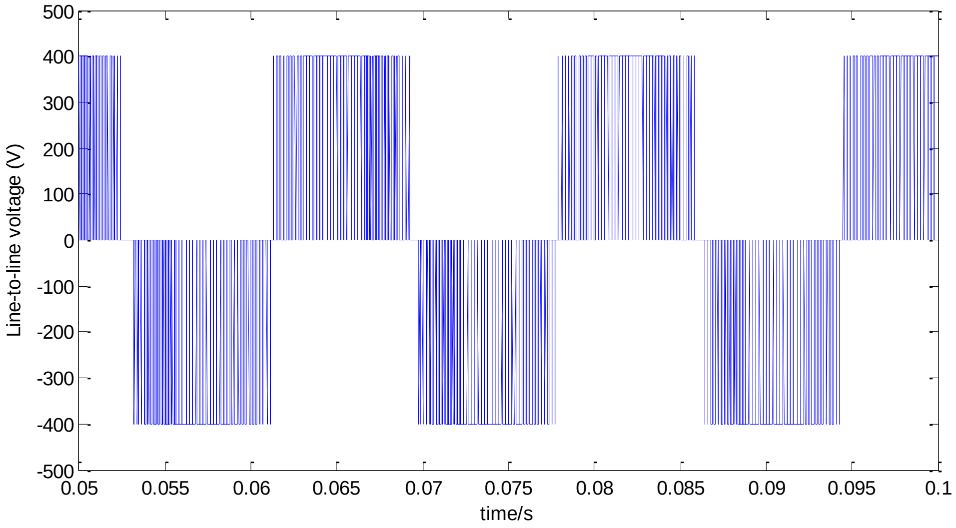

Figure 4.8 Line-to-line voltage profile

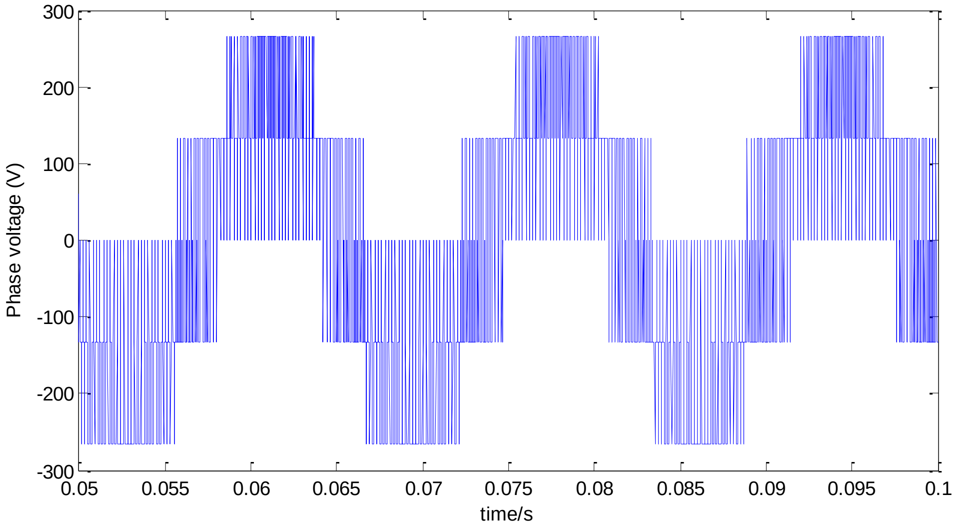

Figure 4.9 Phase voltage profile

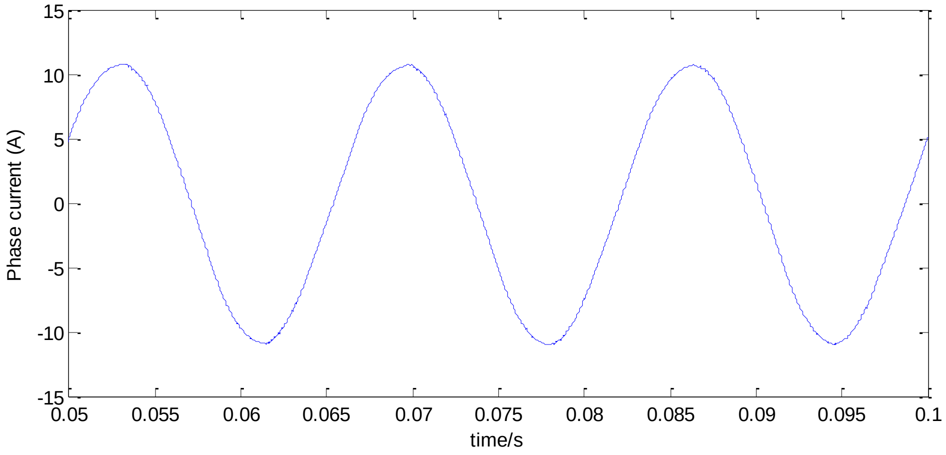

Figure 4.10 Phase current profile

To show the merit of the SVPWM, the space vector PWM is compared with SPWM under various modulation index conditions, and the comparison results are given in Table 4.5. The carrier frequency for the SPWM is 5000Hz, and all other parameters are the same as in the SVPWM simulation given in Table 4.4. Here, the modulation index for the SPWM is $m = V_m / V_T$.

Table 4.5 Comparison between SPWM and SVPWM for a two-level inverter

Modulation Style	SPWM		SVPWM	
m	Output line-to-line voltage		Output line-to-line voltage	
	Fundamental peak value	THD(%)	Fundamental peak value	THD(%)
0.2	60.53 V	251.41	80.08 V	232.16
0.4	132.5 V	160.66	160.0 V	147.61
0.6	202.8 V	117.99	240.9 V	105.46
0.8	272.7 V	89.34	320.9 V	76.83
1	343.5 V	66.17	400.0 V	52.45

From Table 4.5, it can be concluded that the SVPWM can obtain a higher peak value of the fundamental component of the output phase voltages, which means that it can utilize the DC-bus voltage more effectively, and generate less total harmonic distortion (THD) when compared with the conventional SPWM techniques.

4.3 Multi-Level Neutral-Point-Clamped Converters

Generally speaking, multi-level converters can be classified into three categories [106]: neutral-point-clamped converters, also called diode-clamped converters, flying capacitor converters and cascaded H-bridge converters. This thesis will only focus on multi-level neutral-point-clamped converters due to the fact that this type of converter is most widely used in wind turbine-generator systems recently.

A three-level diode-clamped inverter is shown in Figure 4.11(a), in which only the circuit of phase a, is described as an example. In this circuit, the DC-bus voltage is split into three levels by two series-connected bulk capacitors, C_1 and C_2. Here, the capacitors, C_1 and C_2, are identical, and the middle point of the two capacitors, *n*, is defined as the neutral point.

The definition of the switching states for the three-level diode-clamped converter is given in Table 4.6. Here, a switch status of “1” means the switch is on, and a switch status of “0” means the switch is off. Here also, when the switching state is equal to “1”, the upper two switches, S_1 and S_2, in leg *a* are conducting, and the voltage for terminal *a* with respect to the neutral point *n*, V_{an}, is $V_{dc}/2$. Similarly, when the switching state is equal to “-1”, the lower two switches, S_3 and S_4, are turned on, and the voltage, V_{an}, is equal to $V_{dc}/2$. The switching state “0” indicates that the inner two switches, S_2 and S_3, are conducting and V_{an} = 0 through the clamping diodes. In order to obtain the desired three-level voltages, the converter must ensure complementarities between the pairs of the switches: (S_1, S_3) and (S_2, S_4).

Table 4.6 Definition of the switching states

Switching State	Switch Status for Phase A				Terminal Voltage V_{an}
	S_1	S_2	S_3	S_4	
1	1	1	0	0	$V_{dc}/2$
0	0	1	1	0	0
-1	0	0	1	1	$-V_{dc}/2$

The key components that distinguish the circuit of a three-level inverter from a conventional two-level inverter are the clamped diodes, D_1 and D_2. These two diodes clamp the blocking voltage of each switch to half level of the DC-bus voltage. For example, when both switches, S_1 and S_2, are turned on, the voltage between point *a* and *0* is V_{dc}, i.e., $V_{a0} = V_{dc}$. In this case, the diode, D_2, balances out the voltage sharing between the switches, S_3 and S_4, with S_3 blocking the voltage across C_1, and S_4 blocking the voltage across C_2, as the dashed line shown in Figure 4.11 (a).

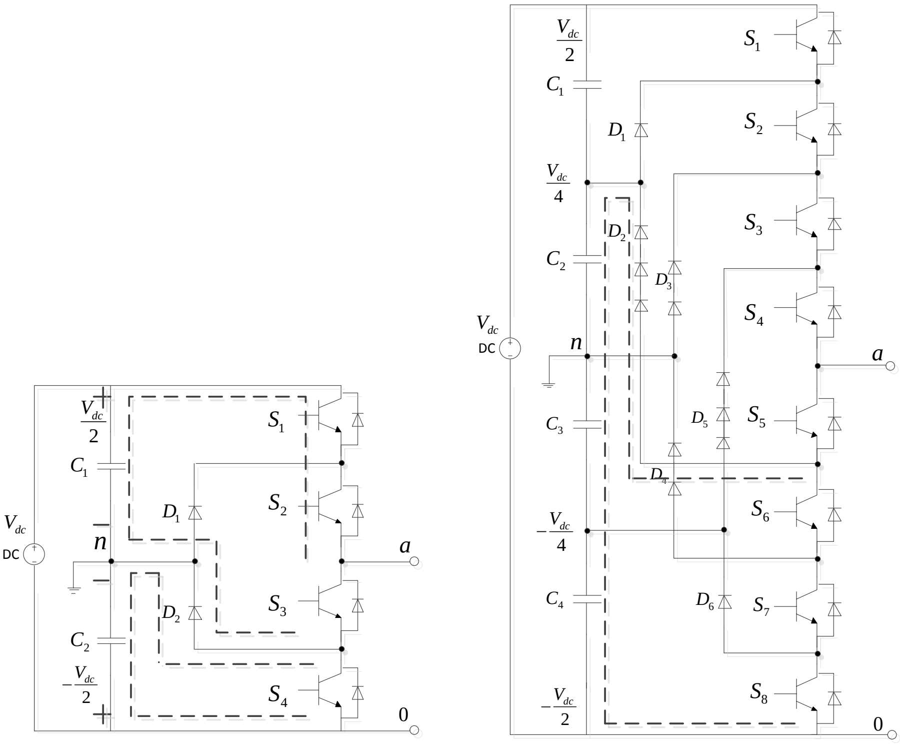

(a) (b)

Figure 4.11 Multi-level diode-clamped inverter circuit topologies: (a) three-level (b) five-level

Figure 4.11 (b) shows a five-level diode-clamped inverter, in which the DC-bus consists of four identical capacitors, C_1, C_2, C_3 and C_4. The DC-bus voltage is equally distributed on these capacitors, which means that the voltage across each capacitor is $V_{dc}/4$. Therefore, the voltage across each IGBT device will be limited to one capacitor voltage level, $V_{dc}/4$, through the clamping diodes. In order to explain how the five voltage levels of the out phase voltages are synthesized, the neutral point, *n,* is considered as the reference point, and the corresponding switching combinations across *a* and *n* are summarized as follows [143]:

1) For voltage level, $V_{dc}/2$, all upper switches, S_1 through S_4, should be turned on.
2) For voltage level, $V_{dc}/4$, three upper switches, S_2 through S_4, and one lower switch S_5 should be turned on.
3) For voltage level, 0, two upper switches, S_3 and S_4, and two lower switches, S_5 and S_6, should be turned on.
4) For voltage level, $-V_{dc}/4$, one upper switch, S_4, and three lower switches, S_5 through S_7, should be turned on.
5) For voltage level, $-V_{dc}/2$, all lower switches, S_5 through S_8, should be turned on.

For each phase, there exist four complementary switch pairs, which are defined such that turning on one of the pair switches will make the other switch be turned off. Using phase leg *a* as an example, the four complementary pairs are (S_1, S_5), (S_2, S_6), (S_3, S_7) and (S_4, S_8).

Although each active switching device is only required to block a voltage of $V_{dc}/4$, the clamping diodes must have different voltage ratings for reverse voltage blocking. As an example in Figure 4.11 (b), when the lower devices, S_6 through S_8, are turned on, the diode, D_2, needs to block three capacitor voltages, or $3V_{dc}/4$, as the dashed line shown in Figure 4.11 (b). Similarly, the diodes, D_3 and D_4, need to block

$V_{dc}/2$, and D_5 needs to block $3V_{dc}/4$. Assuming that each blocking diode has the same voltage rating, the diode which blocks multi voltage levels of $V_{dc}/4$ will need several diodes in series, as the diodes, D_2, shown in Figure 4.11 (b).

In general, an *m*-level diode-clamped converter typically consists of *m*-1 capacitors on the DC-bus, and produces *m* levels of the output phase voltages. The number of clamping diodes required for each phase will be (*m*-1)(*m*-2), the number of IGBT switches will be 2(*m*-1) and the number of antiparallel diodes will be 2(*m*-1) [137]. It can be seen that the number of devices in a multi-level inverter represents a quadratic and linear increase in *m*. When *m* is sufficiently high, it will be impractical to implement the system. In this thesis, therefore, only three-level neutral-point-clamped inverters will be studied in detail and applied in wind turbine-generator systems.

As in two-level converters, the traditional sinusoidal PWM can also be applied in the three-level NPC inverter, in which the sinusoidal reference signals are compared with two carrier signals, as shown in Figure 4.12. Here, v_{ma}, is the modulation signal for phase a, v_{tr1}, is the upper carrier signal, and v_{tr2}, is the lower carrier signal. The upper carrier signal has a triangular waveform, which varies between 0 and 1. The lower carrier signal is the reverse of the upper carrier signal.

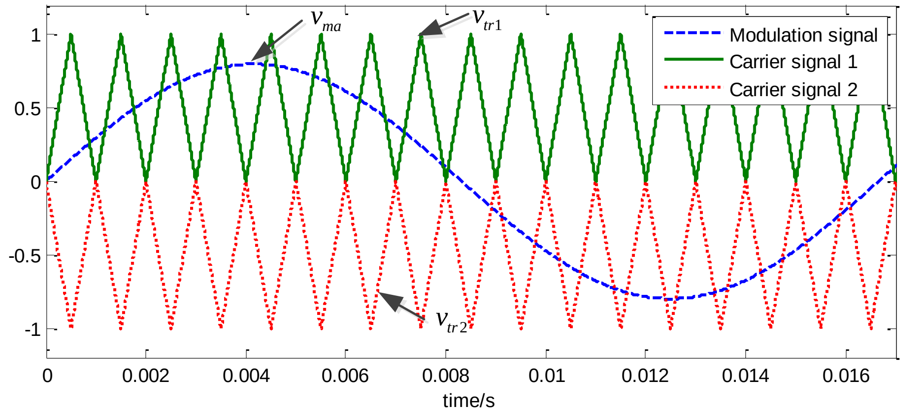

Figure 4.12 SPWM for a three-level inverter

The switching states for upper IGBTs of phase *a* can be deduced as follows [144]:

$$\begin{array}{lll} if & v_{ma} > v_{tr1} \Rightarrow S_1 = on & S_2 = on \\ if & v_{tr2} < v_{ma} < v_{tr1} \Rightarrow S_1 = off & S_2 = on \\ if & v_{ma} < v_{tr2} \Rightarrow S_1 = off & S_2 = off \end{array} \tag{4.18}$$

The switching states for the lower IGBTs of phase *a* can be derived from the switching states of the upper IGBTs because of the complementary switch pairs.

4.4 Space Vector PWM for Three-Level Inverters

4.4.1 Voltage Vector Categories

Now, consider a three-level NPC inverter shown in Figure 4.13. Here, there are two statements that should be noticed: 1) the neutral point in the load, 0, as shown in Figure 4.13, is not the same as point 0 in Figure 4.11, 2) the neutral point, n, is not the same as the neutral point in the load, 0, as shown in Figure 4.13.

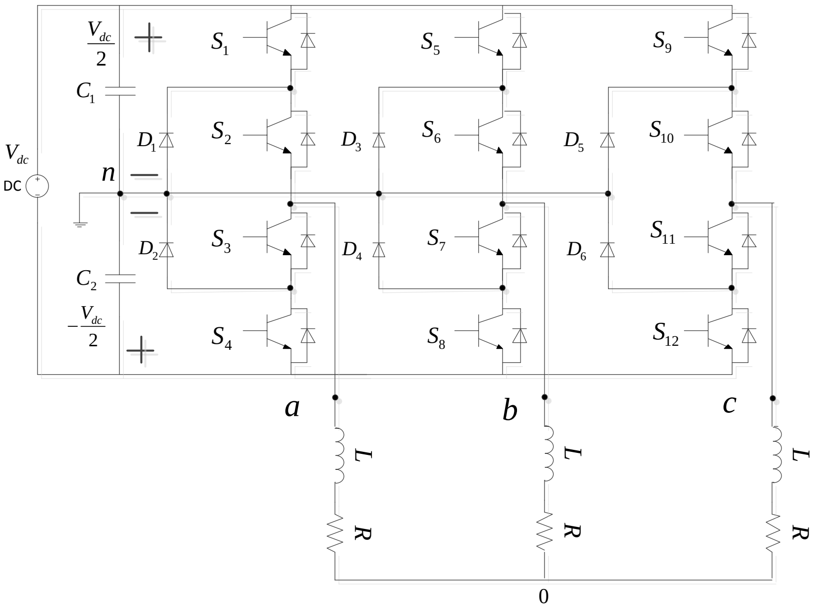

Figure 4.13 Three-phase three-level diode-clamped inverter

From Table 4.6, it can be seen that the operation of each leg has three switching states, "1", "0" and "-1". By taking all three phases into account, the inverter has a total of 27 possible switching states, which are given in Table 4.7. The voltage vectors can be classified into four groups, and given as follows [145]:

1) Zero vector ($\vec{V}_0$), representing three switching states [1 1 1], [0 0 0] and [-1 -1 -1]. The magnitude of the zero vector, $\vec{V}_0$, is zero.
2) Small vectors ($\vec{V}_1$ to $\vec{V}_6$), having a magnitude of $V_{dc}/3$. Each small vector has two switching states, one containing the switching state "1", and the other containing the switching state "-1". They are classified into P- (positive) or N- (negative) types of small vectors.
3) Medium vectors ($\vec{V}_7$ to $\vec{V}_{12}$), whose magnitude is $\sqrt{3}V_{dc}/3$.
4) Large vectors ($\vec{V}_{13}$ to $\vec{V}_{18}$), having a magnitude of $2V_{dc}/3$.

From the above four groups, it can be seen that there exist redundancies for generating the small voltage vectors and zero voltage vectors. Therefore, in all there are 18 active voltage vectors plus zero voltage vectors.

Table 4.7 Three-level inverter switching states and voltage outputs

Space Vector	Switching States		V_{an}	V_{bn}	V_{cn}	V_{a0}	V_{b0}	V_{c0}	Vector Magnitude
$\vec{V}_0$	[0 0 0]		0	0	0	0	0	0	0
	[1 1 1]		1/2	1/2	1/2	0	0	0	
	[-1-1-1]		-1/2	-1/2	-1/2	0	0	0	
	P-type	N-type							
$\vec{V}_1$	[1 0 0]		1/2	0	0	1/3	-1/6	-1/6	1/3
		[0-1 -1]	0	-1/2	-1/2	1/3	-1/6	-1/6	
$\vec{V}_2$	[1 1 0]		1/2	1/2	0	1/6	1/6	-1/3	
		[0 0 -1]	0	0	-1/2	1/6	1/6	-1/3	
$\vec{V}_3$	[0 1 0]		0	1/2	0	-1/6	1/3	-1/6	
		[-1 0 -1]	-1/2	0	-1/2	-1/6	1/3	-1/6	
$\vec{V}_4$	[0 1 1]		0	1/2	1/2	-1/3	1/6	1/6	
		[-1 0 0]	-1/2	0	0	-1/3	1/6	1/6	
$\vec{V}_5$	[0 0 1]		0	0	1/2	-1/6	-1/6	1/3	
		[-1 -1 0]	-1/2	-1/2	0	-1/6	-1/6	1/3	
$\vec{V}_6$	[1 0 1]		1/2	0	1/2	1/6	-1/3	1/6	
		[0 -1 0]	0	-1/2	0	1/6	-1/3	1/6	
$\vec{V}_7$	[1 0 -1]		1/2	0	-1/2	1/2	0	-1/2	$\sqrt{3}/3$
$\vec{V}_8$	[0 1 -1]		0	1/2	-1/2	0	1/2	-1/2	
$\vec{V}_9$	[-1 1 0]		-1/2	1/2	0	-1/2	1/2	0	
$\vec{V}_{10}$	[-1 0 1]		-1/2	0	1/2	-1/2	0	1/2	
$\vec{V}_{11}$	[0 -1 1]		0	-1/2	1/2	0	-1/2	1/2	
$\vec{V}_{12}$	[1 -1 0]		1/2	-1/2	0	1/2	-1/2	0	
$\vec{V}_{13}$	[1 -1 -1]		1/2	-1/2	-1/2	2/3	-1/3	-1/3	2/3
$\vec{V}_{14}$	[1 1 -1]		1/2	1/2	-1/2	1/3	1/3	-2/3	
$\vec{V}_{15}$	[-1 1 -1]		-1/2	1/2	-1/2	-1/3	2/3	-1/3	
$\vec{V}_{16}$	[-1 1 1]		-1/2	1/2	1/2	-2/3	1/3	1/3	
$\vec{V}_{17}$	[-1 -1 1]		-1/2	-1/2	1/2	-1/3	-1/3	2/3	
$\vec{V}_{18}$	[1 -1 1]		1/2	-1/2	1/2	1/3	-2/3	1/3	

Here, each of the voltages in the table are scaled by "V_{dc}".

In the vector space, according to the equivalence principle, these 27 voltage vectors can be drawn in the (α-β) reference frame, as illustrated in Figure 4.14. The space vector block diagram has been divided into six 60 degree sectors (1, 2, 3, 4, 5, and 6). Each sector consists of 4 regions (1, 2, 3 and 4). In any sector, the output reference voltage vector $\vec{V}^*$ can be constructed from different non-zero vectors and zero vectors according to the region in which the reference voltage vector is located.

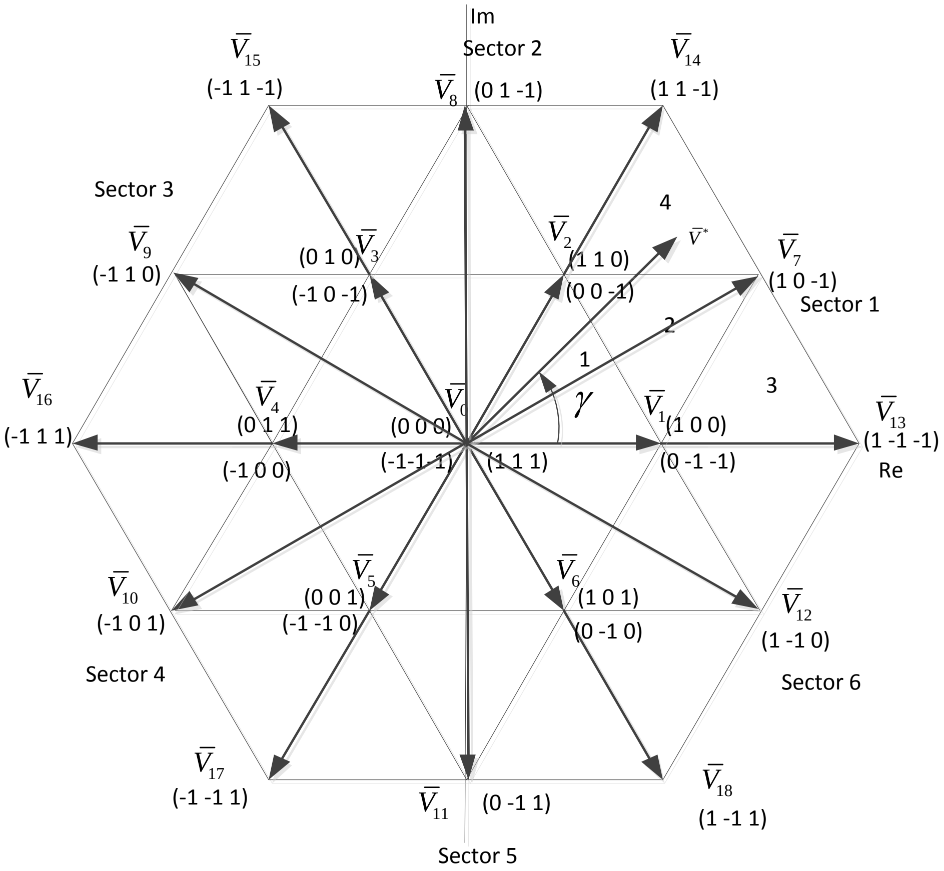

Figure 4.14 Space vectors and sectors

A careful analysis of the space vector diagram reveals that the performance of the inverter depends on the selection of the switching states and their sequences. Each small voltage vector has redundant switching states, and through selecting an appropriate switching state for each voltage vector, the switching losses can be reduced [146], and this will be explained later.

4.4.2 Time Calculations

The space vector diagram shown in Figure 4.14 can be used to calculate the time durations for each sector (1 to 6). For different regions (1 to 4), the output reference voltage vector $\vec{V}^*$ should be constructed from three nearest switching non-zero and zero vectors. For example, in sector 1, the reference voltage vector is composed by $\vec{V}_0, \vec{V}_1, \vec{V}_2$ for region 1, $\vec{V}_1, \vec{V}_7, \vec{V}_2$ for region 2, $\vec{V}_1, \vec{V}_7, \vec{V}_{13}$ for region 3, and $\vec{V}_2, \vec{V}_7, \vec{V}_{14}$ for region 4.

By using the same strategy that applied in the two-level inverter, the summation of the chosen voltage vectors multiplied by the corresponding time interval will be equal to the product of the reference voltage, $\vec{V}^*$, and the sampling period T_s. To illustrate, when the reference voltage is located in region 2 of sector 1, the nearest adjacent voltage vectors to the reference voltage vector are $\vec{V}_1$, $\vec{V}_7$ and $\vec{V}_2$, shown in Figure 4.15.

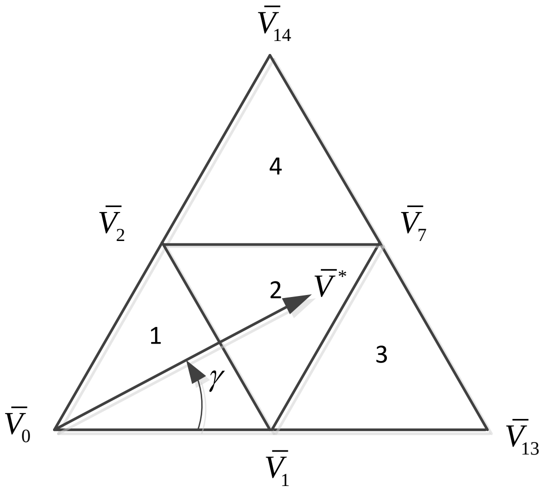

Figure 4.15 Time calculations in region 2 of sector 1

Form Figure 4.15, by resolving the voltage vectors into the real part and the imaginary part, the switching time durations of region 2 in sector 1 can be calculated as follows:

$$\left.\begin{array}{c} T_s \cdot \left|\vec{V}^*\right| \cdot \cos\gamma = T_1 \cdot \left|\vec{V}_1\right| + T_7 \cdot \left|\vec{V}_7\right| \cdot \cos\dfrac{\pi}{6} + T_2 \cdot \left|\vec{V}_2\right| \cdot \cos\dfrac{\pi}{3} \\ T_s \cdot \left|\vec{V}^*\right| \cdot \sin\gamma = T_7 \cdot \left|\vec{V}_7\right| \cdot \sin\dfrac{\pi}{6} + T_2 \cdot \left|\vec{V}_2\right| \cdot \sin\dfrac{\pi}{3} \\ T_s = T_1 + T_7 + T_2 \end{array}\right\} \Rightarrow \tag{4.19}$$

$$\left.\begin{array}{c} T_s \cdot \left|\vec{V}^*\right| \cdot \cos\gamma = T_1 \cdot \left(V_{dc}/3 \right) + T_7 \cdot \left(\sqrt{3}V_{dc}/3 \right) \cdot \cos\dfrac{\pi}{6} + T_2 \cdot \left(2V_{dc}/3 \right) \cdot \cos\dfrac{\pi}{3} \\ T_s \cdot \left|\vec{V}^*\right| \cdot \sin\gamma = T_7 \cdot \left(\sqrt{3}V_{dc}/3 \right) \cdot \sin\dfrac{\pi}{6} + T_2 \cdot \left(2V_{dc}/3 \right) \cdot \sin\dfrac{\pi}{3} \\ T_s = T_1 + T_7 + T_2 \end{array}\right\} \Rightarrow \tag{4.20}$$

$$T_1 = T_s \cdot \left[1 - 2m \cdot \sin\gamma \right] \tag{4.21}$$

$$T_7 = T_s \cdot \left[2m \cdot \sin\left(\gamma + \frac{\pi}{3} \right) - 1 \right] \tag{4.22}$$

$$T_2 = T_s - T_1 - T_7 = T_s \cdot \left[1 - 2m \cdot \sin\left(\frac{\pi}{3} - \gamma \right) \right] \tag{4.23}$$

where, $m = \dfrac{\sqrt{3}\left|\vec{V}^*\right|}{V_{dc}}$.

It should be noticed that the switching time durations, T_1, T_7 and T_2, include the time durations for the redundant switching states. For example, in region 1, T_1 is the total switching time duration for P- (positive) and N- (negative) types of small vectors, whose switching states are [1 0 0] and [0 -1 -1], respectively. By following the same procedure, the switching time durations for other regions in sector 1 can also be deduced and given in Table 4.8. The detailed calculation processes will not be shown here.

Table 4.8 Switching time durations in sector 1

Region 1	T_1		T_0		T_2	
	$\vec{V}_1$	$T_s\left[2m\sin(\frac{\pi}{3}-\gamma)\right]$	$\vec{V}_0$	$T_s\left[1-2m\sin(\frac{\pi}{3}+\gamma)\right]$	$\vec{V}_2$	$T_s\left[2m\sin\gamma\right]$
Region 2	T_1		T_7		T_2	
	$\vec{V}_1$	$T_s\left[1-2m\sin\gamma\right]$	$\vec{V}_7$	$T_s\left[2m\sin(\gamma+\frac{\pi}{3})-1\right]$	$\vec{V}_2$	$T_s\left[1-2m\sin(\frac{\pi}{3}-\gamma)\right]$
Region 3	T_1		T_7		T_{13}	
	$\vec{V}_1$	$T_s\left[2-2m\sin(\frac{\pi}{3}+\gamma)\right]$	$\vec{V}_7$	$T_s\left[2m\sin\gamma\right]$	$\vec{V}_{13}$	$T_s\left[2m\sin(\frac{\pi}{3}-\gamma)-1\right]$
Region 4	T_{14}		T_7		T_2	
	$\vec{V}_{14}$	$T_s\left[2m\sin\gamma-1\right]$	$\vec{V}_7$	$T_s\left[2m\sin(\frac{\pi}{3}-\gamma)\right]$	$\vec{V}_2$	$T_s\left[2-2m\sin(\frac{\pi}{3}+\gamma)\right]$

The time durations can also be calculated for sectors (2 to 6) by using the equations in Table 4.8 with a multiple of π/3 subtracted from the actual angular displacement, γ, such that the modified angle falls into the range between zero and π/3. Here, it should be also noticed that for each region, the reference voltage vector has a maximum value that varies with the regions.

4.4.3 Switching Sequences

To reduce the number of inverter switching actions, it is necessary to distribute the switching states in such a way that the transition from one state to the next is performed by only switching one inverter leg at a time. By obeying this rule, the thirteen segment switching sequences for the reference voltage vector, $\vec{V}^*$, residing in region 1 of all six sectors are given in Table 4.9. Table 4.10 shows nine segment switching sequences of region 2 for each sector. Table 4.11 and Table 4.12 show seven segment switching sequences of region 3 and region 4 for each sector, respectively.

In the stationary reference frame, the reference voltage vector will rotate anticlockwise, therefore, the reference voltage vector will only pass through region 1, region 1 and 2 or region 2, 3 and 4, according to its magnitude. For small magnitudes of the reference voltage vector, all the switching sequences given in Table 4.9 start and end with switching state [-1-1-1], which indicates that the transition for $\vec{V}^*$ moving from one sector to the next does not require any switching actions. For large magnitudes of the reference voltage vector, the regions that the reference voltage vector will pass through have following sequences:

$$\left.\begin{array}{l} \underbrace{3\to 2\to 4}_{Sector1}\to\underbrace{3\to 2\to 4}_{Sector2}\to\underbrace{3\to 2\to 4}_{Sector3}\cdots\cdots \\ or\quad \underbrace{1\to 2\to 1}_{Sector1}\to\underbrace{1\to 2\to 1}_{Sector2}\to\underbrace{1\to 2\to 1}_{Sector3}\cdots\cdots \end{array}\right\} \tag{4.24}$$

From Table 4.9 to Table 4.12, it can be seen that only one or zero switching action is needed for the reference voltage vector transiting from one region to another, therefore, the switching losses of the switching devices can be reduced.

Table 4.9 Thirteen segments switching sequences of region 1 for all sectors

Sector	Switching Sequence												
	1	2	3	4	5	5	6	8	9	10	11	12	13
1	$\vec{V}_0$	$\vec{V}_{1N}$	$\vec{V}_{2N}$	$\vec{V}_0$	$\vec{V}_{1P}$	$\vec{V}_{2P}$	$\vec{V}_0$	$\vec{V}_{2P}$	$\vec{V}_{1P}$	$\vec{V}_0$	$\vec{V}_{2N}$	$\vec{V}_{1N}$	$\vec{V}_0$
	-1-1-1	0-1-1	00-1	000	100	110	111	110	100	000	00-1	0-1-1	-1-1-1
2	$\vec{V}_0$	$\vec{V}_{3N}$	$\vec{V}_{2N}$	$\vec{V}_0$	$\vec{V}_{3P}$	$\vec{V}_{2P}$	$\vec{V}_0$	$\vec{V}_{2P}$	$\vec{V}_{3P}$	$\vec{V}_0$	$\vec{V}_{2N}$	$\vec{V}_{3N}$	$\vec{V}_0$
	-1-1-1	-10-1	00-1	000	010	110	111	110	010	000	00-1	-10-1	-1-1-1
3	$\vec{V}_0$	$\vec{V}_{3N}$	$\vec{V}_{4N}$	$\vec{V}_0$	$\vec{V}_{3P}$	$\vec{V}_{4P}$	$\vec{V}_0$	$\vec{V}_{4P}$	$\vec{V}_{3P}$	$\vec{V}_0$	$\vec{V}_{4N}$	$\vec{V}_{3N}$	$\vec{V}_0$
	-1-1-1	-10-1	-100	000	010	011	111	011	010	000	-100	-10-1	-1-1-1
4	$\vec{V}_0$	$\vec{V}_{5N}$	$\vec{V}_{4N}$	$\vec{V}_0$	$\vec{V}_{5P}$	$\vec{V}_{4P}$	$\vec{V}_0$	$\vec{V}_{4P}$	$\vec{V}_{5P}$	$\vec{V}_0$	$\vec{V}_{4N}$	$\vec{V}_{5N}$	$\vec{V}_0$
	-1-1-1	-1-10	-100	000	001	011	111	011	001	000	-100	-1-10	-1-1-1
5	$\vec{V}_0$	$\vec{V}_{5N}$	$\vec{V}_{6N}$	$\vec{V}_0$	$\vec{V}_{5P}$	$\vec{V}_{6P}$	$\vec{V}_0$	$\vec{V}_{6P}$	$\vec{V}_{5P}$	$\vec{V}_0$	$\vec{V}_{6N}$	$\vec{V}_{5N}$	$\vec{V}_0$
	-1-1-1	-1-10	0-10	000	001	101	111	101	001	000	0-10	-1-10	-1-1-1

6	$\vec{V}_0$	$\vec{V}_{1N}$	$\vec{V}_{6N}$	$\vec{V}_0$	$\vec{V}_{1P}$	$\vec{V}_{6P}$	$\vec{V}_0$	$\vec{V}_{6P}$	$\vec{V}_{1P}$	$\vec{V}_0$	$\vec{V}_{6N}$	$\vec{V}_{1N}$	$\vec{V}_0$
	-1-1-1	0-1-1	0-10	000	100	101	111	101	100	000	0-10	0-1-1	-1-1-1

Table 4.10 Nine segments switching sequences of region 2 for all sectors

Sector	Switching Sequence								
	1	2	3	4	5	6	7	8	9
1	$\vec{V}_{1N}$	$\vec{V}_{2N}$	$\vec{V}_7$	$\vec{V}_{1P}$	$\vec{V}_{2P}$	$\vec{V}_{1P}$	$\vec{V}_7$	$\vec{V}_{2N}$	$\vec{V}_{1N}$
	0-1-1	00-1	10-1	100	110	100	10-1	00-1	0-1-1
2	$\vec{V}_{3N}$	$\vec{V}_{2N}$	$\vec{V}_8$	$\vec{V}_{3P}$	$\vec{V}_{2P}$	$\vec{V}_{3P}$	$\vec{V}_8$	$\vec{V}_{2N}$	$\vec{V}_{3N}$
	-10-1	00-1	01-1	010	110	010	01-1	00-1	-10-1
3	$\vec{V}_{3N}$	$\vec{V}_{4N}$	$\vec{V}_9$	$\vec{V}_{3P}$	$\vec{V}_{4P}$	$\vec{V}_{3P}$	$\vec{V}_9$	$\vec{V}_{4N}$	$\vec{V}_{3N}$
	-10-1	-100	-110	010	011	010	-110	-100	-10-1
4	$\vec{V}_{5N}$	$\vec{V}_{4N}$	$\vec{V}_{10}$	$\vec{V}_{5P}$	$\vec{V}_{4P}$	$\vec{V}_{5P}$	$\vec{V}_{10}$	$\vec{V}_{4N}$	$\vec{V}_{5N}$
	-1-10	-100	-101	001	011	001	-101	-100	-1-10
5	$\vec{V}_{5N}$	$\vec{V}_{6N}$	$\vec{V}_{11}$	$\vec{V}_{5P}$	$\vec{V}_{6P}$	$\vec{V}_{5P}$	$\vec{V}_{11}$	$\vec{V}_{6N}$	$\vec{V}_{5N}$
	-1-10	0-10	0-11	001	101	001	0-11	0-10	-1-10
6	$\vec{V}_{1N}$	$\vec{V}_{6N}$	$\vec{V}_{12}$	$\vec{V}_{1P}$	$\vec{V}_{6P}$	$\vec{V}_{1P}$	$\vec{V}_{12}$	$\vec{V}_{6N}$	$\vec{V}_{1N}$
	0-1-1	0-10	1-10	100	101	100	1-10	0-10	0-1-1

Table 4.11 Seven segments switching sequences of region 3 for all sectors

Sector	Switching Sequence						
	1	2	3	4	5	6	7
1	$\vec{V}_{1N}$	$\vec{V}_{13}$	$\vec{V}_7$	$\vec{V}_{1P}$	$\vec{V}_7$	$\vec{V}_{13}$	$\vec{V}_{1N}$
	0-1-1	1-1-1	10-1	100	10-1	1-1-1	0-1-1
2	$\vec{V}_{2N}$	$\vec{V}_8$	$\vec{V}_{14}$	$\vec{V}_{2P}$	$\vec{V}_{14}$	$\vec{V}_8$	$\vec{V}_{2N}$
	00-1	01-1	11-1	110	11-1	01-1	00-1
3	$\vec{V}_{3N}$	$\vec{V}_{15}$	$\vec{V}_9$	$\vec{V}_{3P}$	$\vec{V}_9$	$\vec{V}_{15}$	$\vec{V}_{3N}$
	-10-1	-11-1	-110	010	-110	-11-1	-10-1
4	$\vec{V}_{4N}$	$\vec{V}_{10}$	$\vec{V}_{16}$	$\vec{V}_{4P}$	$\vec{V}_{16}$	$\vec{V}_{10}$	$\vec{V}_{4N}$
	-100	-101	-111	011	-111	-101	-100
5	$\vec{V}_{5N}$	$\vec{V}_{17}$	$\vec{V}_{11}$	$\vec{V}_{5P}$	$\vec{V}_{11}$	$\vec{V}_{17}$	$\vec{V}_{5N}$
	-1-10	-1-11	0-11	001	0-11	-1-11	-1-10
6	$\vec{V}_{6N}$	$\vec{V}_{12}$	$\vec{V}_{18}$	$\vec{V}_{6P}$	$\vec{V}_{18}$	$\vec{V}_{12}$	$\vec{V}_{6N}$
	0-10	1-10	1-11	101	1-11	1-10	0-10

Table 4.12 Seven segments switching sequences of region 4 for all sectors

Sector	Switching Sequence						
	1	2	3	4	5	6	7
1	$\vec{V}_{2N}$	$\vec{V}_7$	$\vec{V}_{14}$	$\vec{V}_{2P}$	$\vec{V}_{14}$	$\vec{V}_7$	$\vec{V}_{2N}$
	00-1	10-1	11-1	110	11-1	10-1	00-1
2	$\vec{V}_{3N}$	$\vec{V}_{15}$	$\vec{V}_8$	$\vec{V}_{3P}$	$\vec{V}_8$	$\vec{V}_{15}$	$\vec{V}_{3N}$
	-10-1	-11-1	01-1	010	01-1	-11-1	-10-1
3	$\vec{V}_{4N}$	$\vec{V}_9$	$\vec{V}_{16}$	$\vec{V}_{4P}$	$\vec{V}_{16}$	$\vec{V}_9$	$\vec{V}_{4N}$
	-100	-110	-111	011	-111	-110	-100
4	$\vec{V}_{5N}$	$\vec{V}_{17}$	$\vec{V}_{10}$	$\vec{V}_{5P}$	$\vec{V}_{10}$	$\vec{V}_{17}$	$\vec{V}_{5N}$
	-1-10	-1-11	-101	001	-101	-1-11	-1-10
5	$\vec{V}_{6N}$	$\vec{V}_{11}$	$\vec{V}_{18}$	$\vec{V}_{6P}$	$\vec{V}_{18}$	$\vec{V}_{11}$	$\vec{V}_{6N}$
	0-10	0-11	1-11	101	1-11	0-11	0-10
6	$\vec{V}_{1N}$	$\vec{V}_{13}$	$\vec{V}_{12}$	$\vec{V}_{1P}$	$\vec{V}_{12}$	$\vec{V}_{13}$	$\vec{V}_{1N}$
	0-1-1	1-1-1	1-10	100	1-10	1-1-1	0-1-1

From Table 4.9 through Table 4.12, it can be seen that both P- and N- types of the small vectors are used for balancing loss distribution. To illustrate, let only the P-types of the small vectors, $\vec{V}_{1P}$ through $\vec{V}_{6P}$, are considered in region 1. Based on the switching states of these small vectors given in Table 4.7, it can be seen that only switching states “0” and "1" are considered for phase a. According to the definition of the switching state, the switch, S_2, will be on all the time, and S_4, will be off all the time, which means that the S_2 has the most loss while the S4 has no loss at all. Hence, the N-types of small vectors, $\vec{V}_{1N}$ through $\vec{V}_{6N}$, need to be considered because of the fact that they include the “-1” state, which will make the switch, S_4, be on sometime, and hereby will balance the loss distribution to some extent.

Based on the switching sequences given in Table 4.9 through Table 4.12, the switching pulse patterns for upper IGBTs in all four regions of sector 1 are plotted in Figures 4.16 through 4.19.

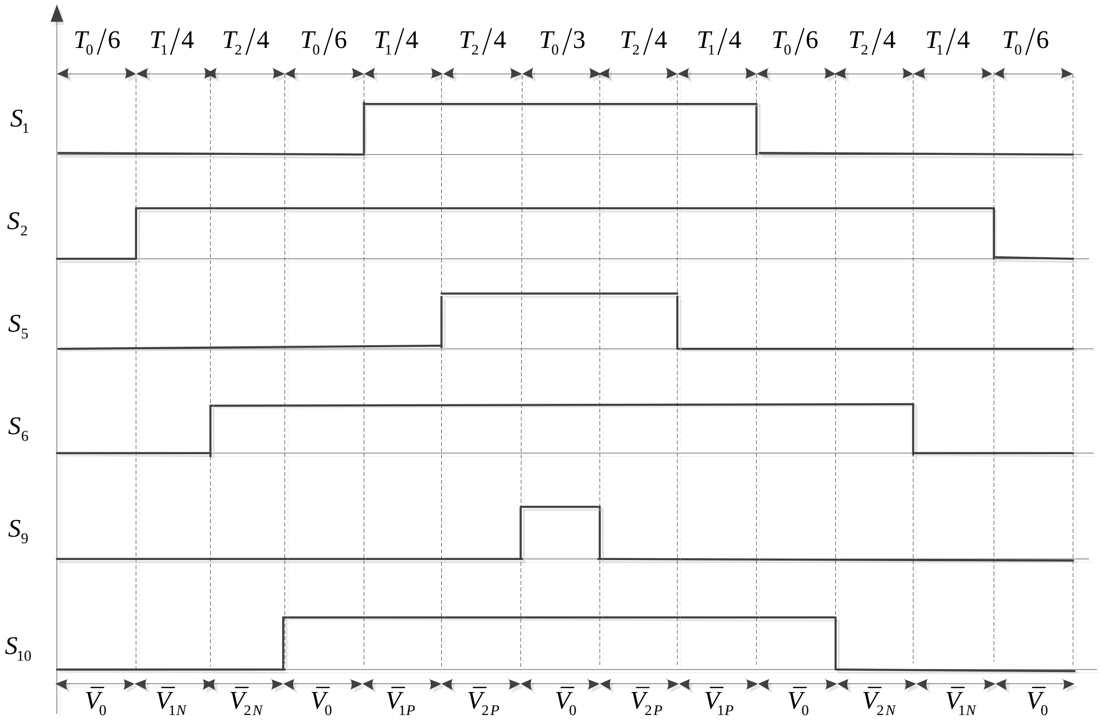

Figure 4.16 Switching patterns for upper IGBTs in region 1 of sector 1

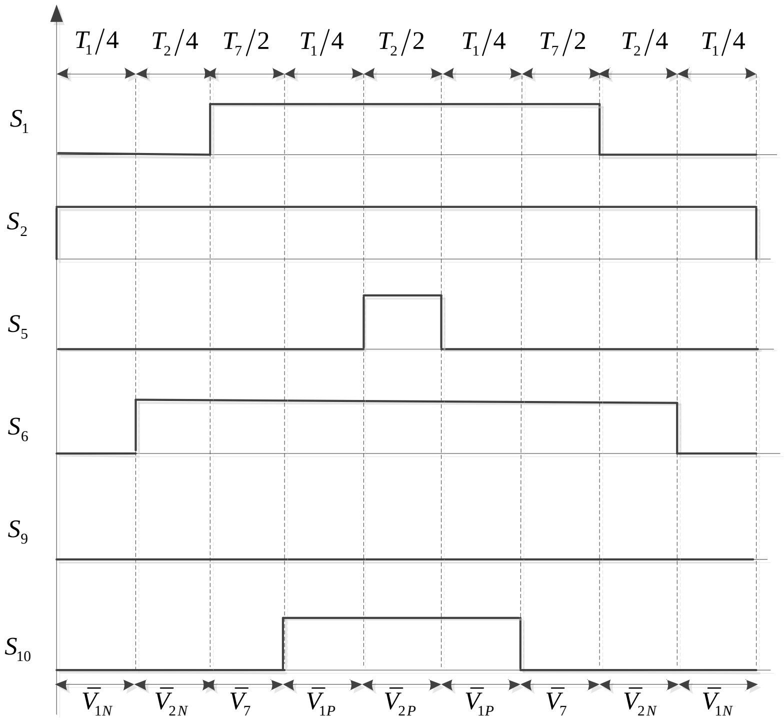

Figure 4.17 Switching patterns for upper IGBTs in region 2 of sector 1

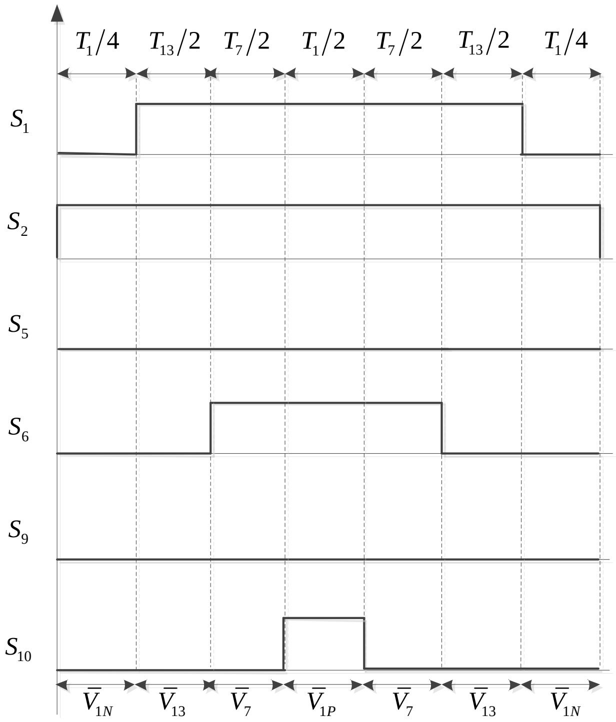

Figure 4.18 Switching patterns for upper IGBTs in region 3 of sector 1

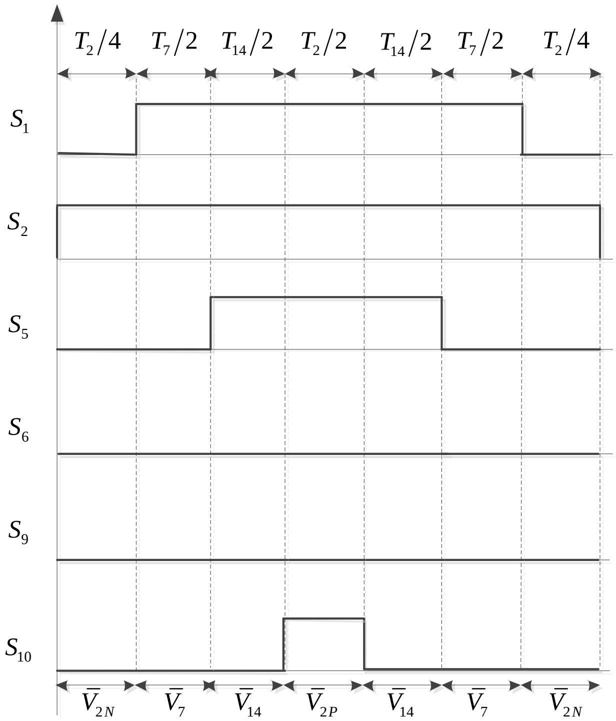

Figure 4.19 Switching patterns for upper IGBTs in region 4 of sector 1

The switching pulse patterns for other sectors could be easily derived based on these switching sequence tables, and will not be shown here.

4.4.4 Comparison Between SPWM and SVPWM for a Three-level Inverter

In this section, the SVPWM was simulated in a Matlab/Simulink environment, in which a DC voltage source is connected to twelve IGBTs as well as a three-phase series RL load, and the gate signals for these IGBTs are generated by the SVPWM. The simulation scheme for a three-phase three-level NPC inverter modulated by the SVPWM is shown in Figure 4.20. For comparison purposes, the data used in the simulation study are the same as the data used in the two-level inverter, given in Table 4.4.

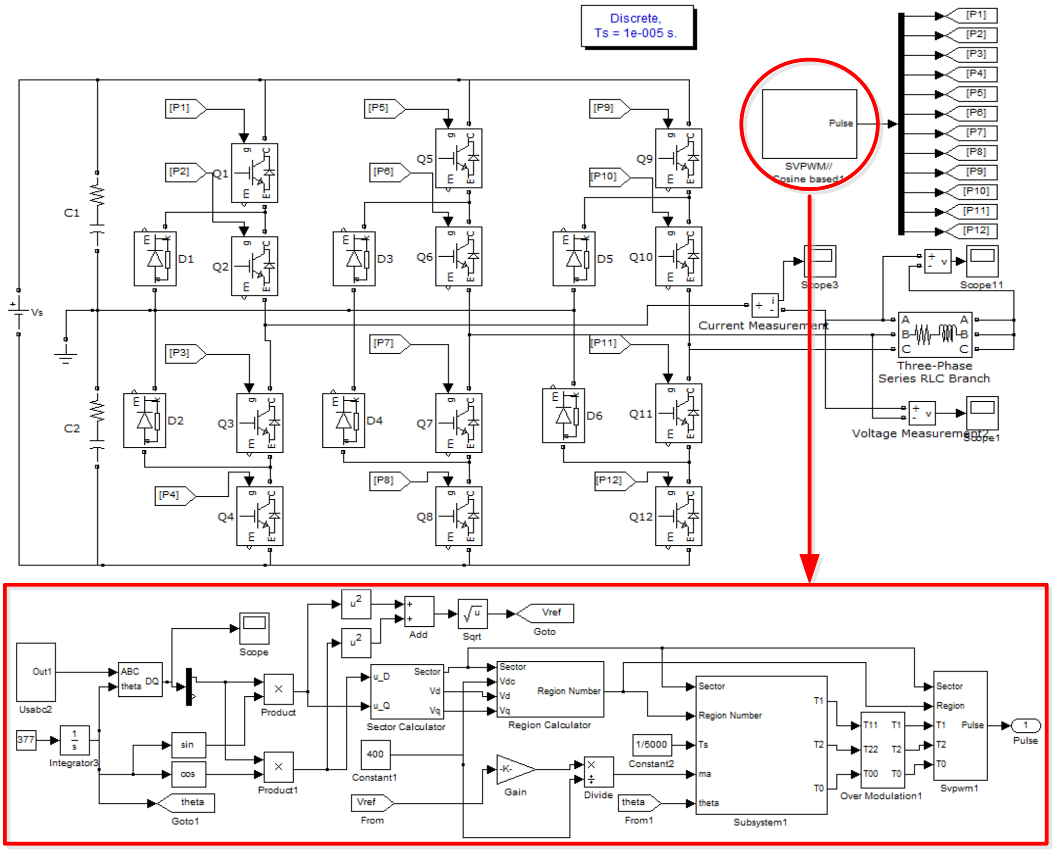

Figure 4.20 Simulation scheme for a three-phase three-level voltage source inverter

The simulation results for the three-phase three-level diode-clamped inverter modulated by the SVPWM are shown in Figure 4.21 through Figure 4.23.

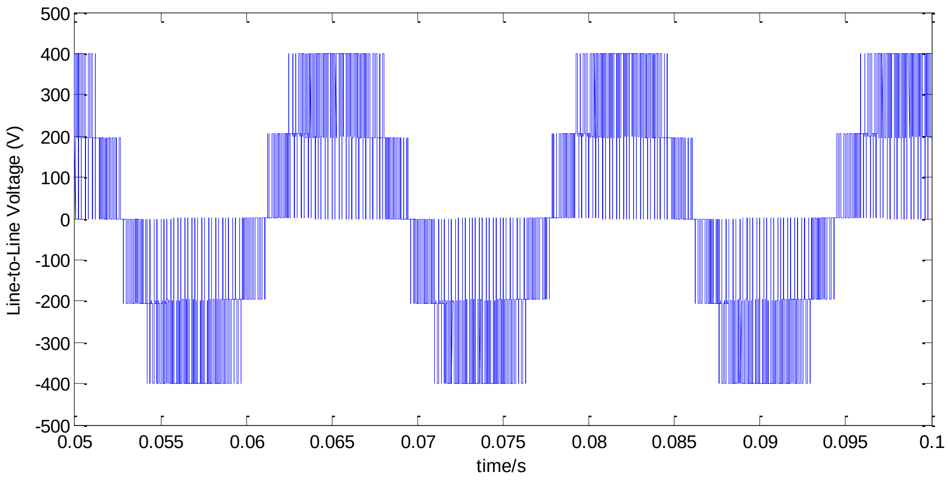

Figure 4.21 Line-to-line voltage profile

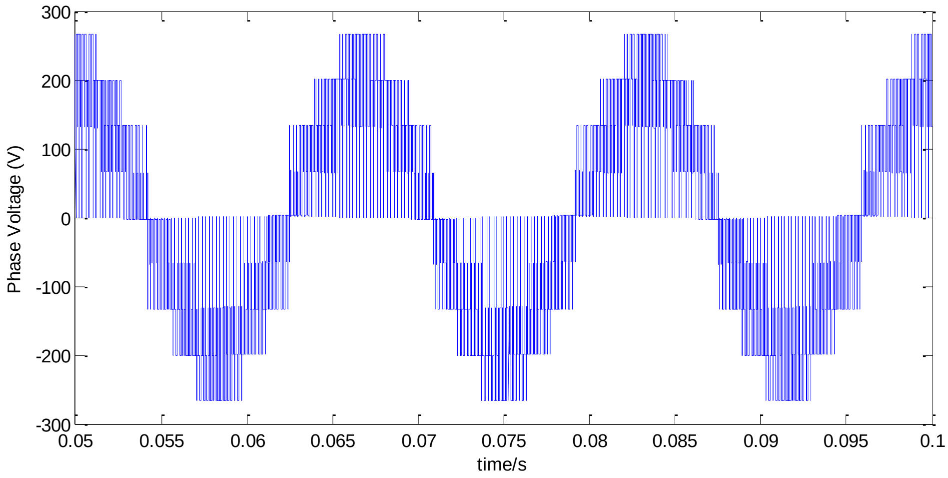

Figure 4.22 Phase voltage profile

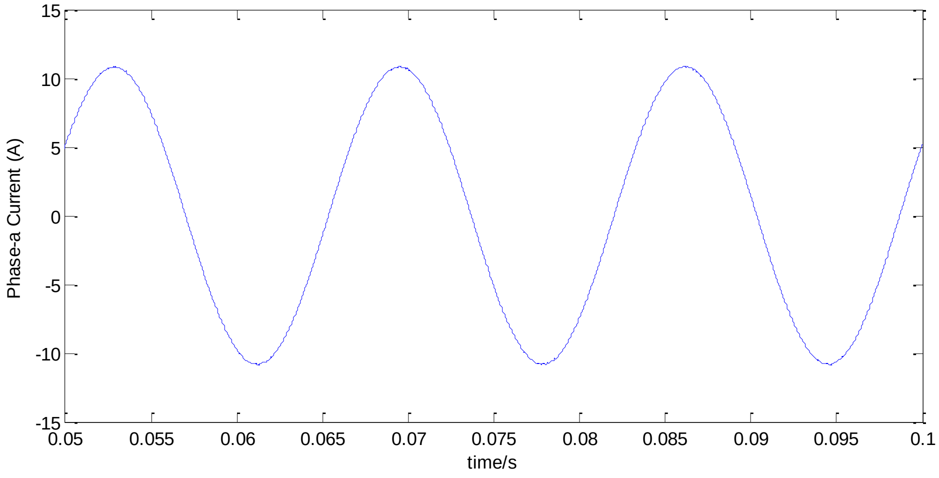

Figure 4.23 Phase current profile

To show the merit of the SVPWM, the SVPWM is compared with SPWM by varying the modulation index, and the comparison results are given in Table 4.13. The carrier frequency for SPWM is 5000Hz, and all other parameters are the same as in the simulation study of the two-level inverter.

Table 4.13 Comparison between SPWM and SVPWM for a three-level NPC inverter

Modulation Style	SPWM		SVPWM	
m	Output line-to-line voltage		Output line-to-line voltage	
	Fundamental peak value	THD(%)	Fundamental peak value	THD(%)
0.2	65.42 V	232.57	79.53V	147.85
0.4	136.2 V	140.94	158.7 V	77.00
0.6	206.1 V	98.43	238.4 V	44.74
0.8	275.7 V	68.10	319.2 V	38.68
1	344.7 V	40.94	399.6 V	27.06

Again, for the three-level NPC inverter, it can be concluded that the SVPWM can obtain a higher peak value of the fundamental component of the output phase voltages, and generate less total harmonic distortion (THD) when compared with the conventional SPWM techniques.

By comparing Table 4.13 with Table 4.5, it can be seen that the output phase voltage fundamental peak values for the two-level and three-level inverters are nearly the same, however, the three-level converters can generate three voltage levels for the output phase voltages and hence improve the quality of the output voltage waveforms. As a sequence, they will reduce the output voltage and current harmonic contents, whose feature enables further reduction in size, weight, and cost of the passive components. Moreover, as mentioned above, the three-level converters can also be suitable for medium voltage applications, hence, it is possible to directly connect the wind turbine system to the medium voltage grid without transformers.

The advantages of the three-level converters make them well suitable for the wind turbine-generator system applications, hence, in this thesis, a three-level back-to-back converter will be applied in wind turbine system and the corresponding modeling and control strategies of the three-level converter will be studied and analyzed in Chapter 5.

Chapter 5

Application of Three-level Converters in Wind Turbine-Generator Systems

5.1 Introduction

In this chapter, a three-level back-to-back converter, which is modulated by the space vector PWM, will be applied in a wind turbine-generator system (WTGS). In this system, the following modifications have been made: 1) two DC-link capacitors will be placed between the grid-side converter and the generator-side converter, 2) the original two-level back-to-back converter will be replaced by a three-level back-to-back neutral-point-clamped (NPC) converter, 3) the three-level converters will be modulated by a space vector PWM (SVPWM) method.

The main contents of this chapter are given as follows. First, the model of a three-level rectifier will be derived based on the two-level rectifier model, and the deduction results show that the model of the three-level converter is similar to the model of the two-level converter. Second, the control strategies for the two-level converters are directly used in the three-level converters, because of the similarities in their models. The corresponding details will not be given in this chapter. Moreover, to verify the validity and superiority of the three-level converters and SVPWM approach, a three-level converter-based wind turbine-generator system with SVPWM is simulated under the same wind speeds as in the two-level converter-based WTGS. The simulation results show that the two-level and three-level converter-based systems have similar simulation results for the power, torque and currents. However, through detailed analysis, the advantages of the three-level converters, for the total harmonic distortion (THD) and voltage magnitudes of the rotor terminal voltages, can be observed. Finally, based on the simulation results, a discussion and conclusions will be presented.

5.2 Modeling of a Three-level Neutral-Point-Clamped Converter

The main power circuit of a three-phase three-level PWM voltage source converter is shown in Figure 5.1. It consists of twelve IGBTs with twelve antiparallel freewheeling diodes, six neutral-point-clamped diodes, three-phase AC input inductors and resistances, and two identical DC output capacitors.

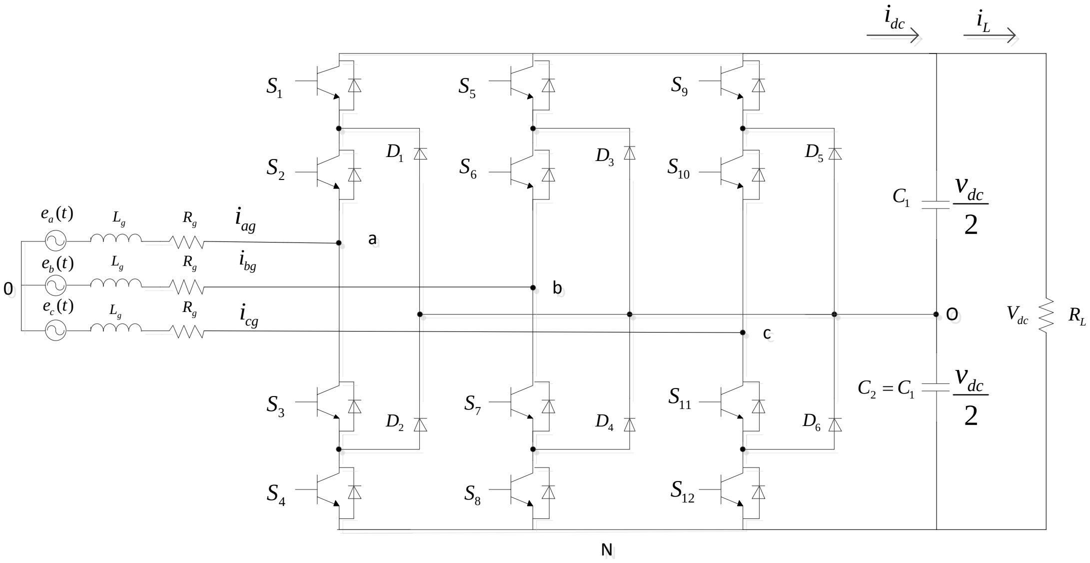

Figure 5.1 Main circuit of a three-level neutral-point-clamped rectifier

Here, in order to make comparisons with the model of a two-level converter, the same notations are adopted, but with extra point, *o*, which is defined as the neutral point between the two capacitors, C_1 and C_2. Moreover, it should be noted that the notation of the neutral point, *o*, is different from the notation for the three-level inverter mentioned in Chapter 4.

Under the assumptions that the three-phase system is balanced, and the two

DC-link capacitors are identical and have some voltage drops, the modeling and circuit analysis of the three-level PWM rectifier is given next. Applying Kirchhoff's laws to the circuit of Figure 5.1, the instantaneous values of the currents can be obtained, and written as following:

$$\begin{cases} L_g \dfrac{di_{ag}}{dt} = e_a - R_g i_{ag} - v_{(a,0)} \\ L_g \dfrac{di_{bg}}{dt} = e_b - R_g i_{bg} - v_{(b,0)} \\ L_g \dfrac{di_{cg}}{dt} = e_c - R_g i_{cg} - v_{(c,0)} \end{cases} \tag{5.1}$$

Here, $v_{(a,0)}, v_{(b,0)}$ and $v_{(c,0)}$, are the voltages from the AC side of the PWM rectifier to the power neutral point *0*, and can be obtained by using the following equations:

$$\begin{cases} v_{(a,0)} = v_{(a,N)} + v_{(N,0)} \\ v_{(b,0)} = v_{(b,N)} + v_{(N,0)} \\ v_{(c,0)} = v_{(c,N)} + v_{(N,0)} \end{cases} \tag{5.2}$$

where, $v_{(N,0)}$, is the voltage from point *N* to point *0*. Here, $v_{(a,N)}$, $v_{(b,N)}$ and $v_{(c,N)}$, are the voltages from the AC side of the PWM rectifier to point *N*.

For a balanced three-phase system, one can write:

$$v_{(a,0)} + v_{(b,0)} + v_{(c,0)} = 0 \tag{5.3}$$

Substituting from equation (5.2) into equation (5.3), the following equation can be deduced:

$$v_{(N,0)} = -\frac{v_{(a,N)} + v_{(b,N)} + v_{(c,N)}}{3} \tag{5.4}$$

According to Table 4.6, for phase-a, the switching states are defined as follows:

$$\begin{array}{ll} S_a = 1 & S_1, S_2 = 1 \\ S_a = 0 & S_2, S_3 = 1 \\ S_a = -1 & S_3, S_4 = 1 \end{array} \tag{5.5}$$

Considering phase-a, when the upper two IGBTs are on, one can write; $S_a = 1$ and $v_{(a,N)} = v_{dc}$. Similarity, when the middle two IGBTs are on, one can derive; $S_a = 0$ and $v_{(a,N)} = \frac{1}{2} v_{dc}$. Also, when the lower two IGBTs are on, one can have; $S_a = -1$ and $v_{(a,N)} = 0$. Therefore, based on the above characteristic, one can write $v_{(a,N)} = S_a \bullet \frac{1}{2} v_{dc} + \frac{1}{2} v_{dc}$. Here, $v_{(a,N)}$, $v_{(b,N)}$ and $v_{(c,N)}$, can be rewritten as follows:

$$\begin{cases} v_{(a,N)} = S_a \bullet \frac{1}{2} v_{dc} + \frac{1}{2} v_{dc} \\ v_{(b,N)} = S_b \bullet \frac{1}{2} v_{dc} + \frac{1}{2} v_{dc} \\ v_{(c,N)} = S_c \bullet \frac{1}{2} v_{dc} + \frac{1}{2} v_{dc} \end{cases} \tag{5.6}$$

Substituting from equations (5.4) and (5.6) into equation (5.2), the following set of equations can be obtained:

$$\begin{cases} v_{(a,0)} = \frac{1}{2} v_{dc} \left(S_a - \frac{1}{3} \sum\limits_{k=a,b,c} S_k \right) \\ v_{(b,0)} = \frac{1}{2} v_{dc} \left(S_b - \frac{1}{3} \sum\limits_{k=a,b,c} S_k \right) \\ v_{(c,0)} = \frac{1}{2} v_{dc} \left(S_c - \frac{1}{3} \sum\limits_{k=a,b,c} S_k \right) \end{cases} \tag{5.7}$$

Substituting from equation (5.7) into equation (5.1), one can write:

$$\begin{cases} L_g \frac{di_{ag}}{dt} = e_a - R_g i_{ag} - \frac{1}{2} v_{dc} \left(S_a - \frac{1}{3} \sum\limits_{k=a,b,c} S_k \right) \\ L_g \frac{di_{bg}}{dt} = e_b - R_g i_{bg} - \frac{1}{2} v_{dc} \left(S_b - \frac{1}{3} \sum\limits_{k=a,b,c} S_k \right) \\ L_g \frac{di_{cg}}{dt} = e_c - R_g i_{cg} - \frac{1}{2} v_{dc} \left(S_c - \frac{1}{3} \sum\limits_{k=a,b,c} S_k \right) \end{cases} \tag{5.8}$$

Applying the transformation matrix in equation (2.153) to equation (5.8), the three-phase three-level PWM rectifier model expressed in the DQ synchronous reference frame can be deduced and given as follows [147][148]:

$$\begin{aligned} L_g \frac{di_{dg}}{dt} - \omega_{gs} L_g i_{qg} + R_g i_{dg} = e_d - v_d \\ L_g \frac{di_{qg}}{dt} + \omega_{gs} L_g i_{dg} + R_g i_{qg} = e_q - v_q \end{aligned} \tag{5.9}$$

where, $v_d = 1/2 v_{dc} s_d$, $v_q = 1/2 v_{dc} s_q$. Here, s_d and s_q , are the switching functions of s_a, s_b, s_c, expressed in the DQ synchronous reference frame, while, i_{dg}, i_{qg}, e_d and e_q, are the input currents and voltages of the three-level PWM rectifier expressed in the DQ synchronous reference frame.

Compare equation (5.9) with equation (2.154), it can be seen that the three-level converter model is similar with the two-level converter model. Therefore, the same control strategies can be directly applied into the three-level converters. Besides, the space vector PWM instead of SPWM will be used to generate the gate signals for the IGBT switches.

5.3 Performance of a Doubly-Fed Induction Generator (DFIG) for Wind Turbine-Generator Systems with Three-Level Converters

In order to investigate the performance of the three-level converters and SVPWM approach, a three-level converter-based wind turbine-generator system with SVPWM is simulated under the same wind speeds as in the two-level converter-based WTGS. Here, the wind speed will vary from 8m/s to 15m/s, and is reshown in Figure 5.2 as follows:

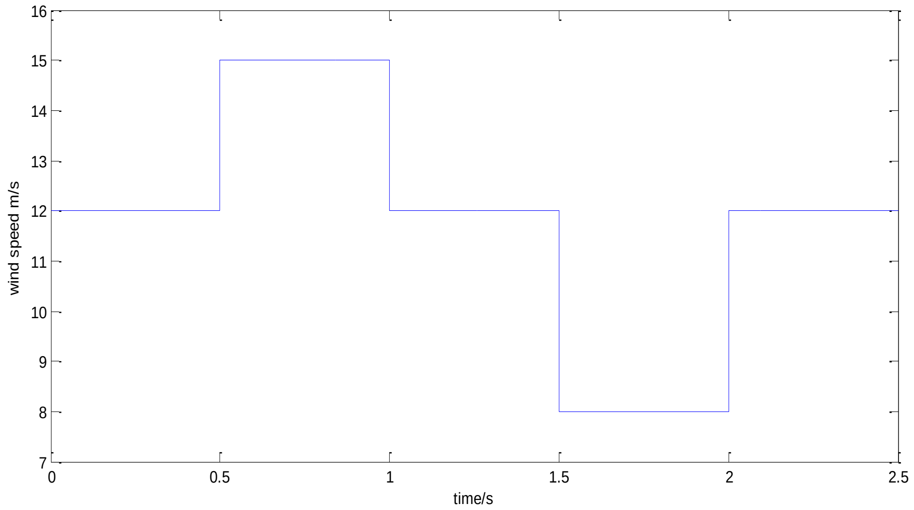

Figure 5.2 Wind speed curve

The simulation results for the three-level converter-based wind turbine-generator system are given in Figures 5.3 through 5.14 as follows:

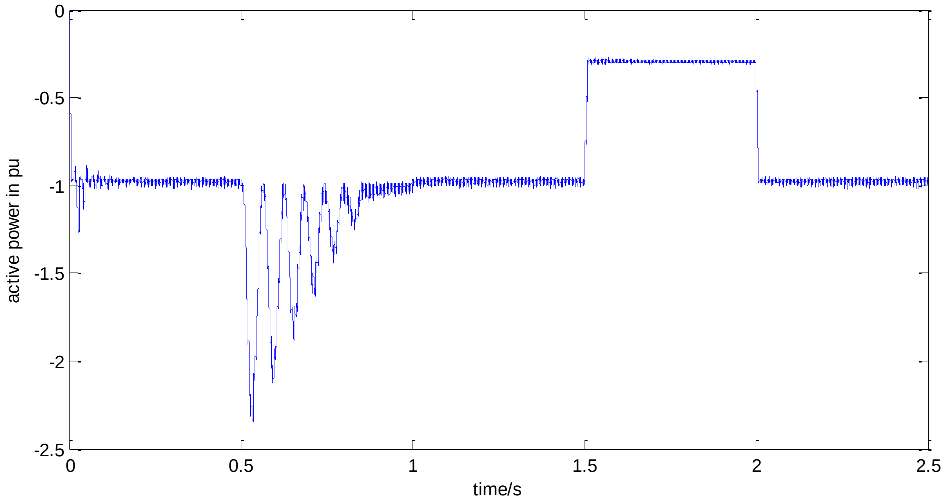

Figure 5.3 Active power profile in p.u. for a three-level converter-based WTGS

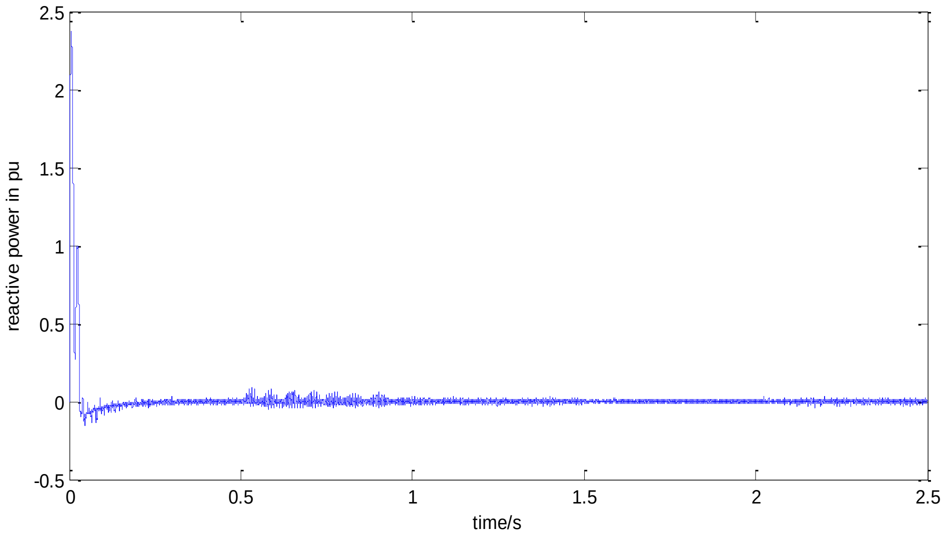

Figure 5.4 Reactive power profile in p.u. for a three-level converter-based WTGS

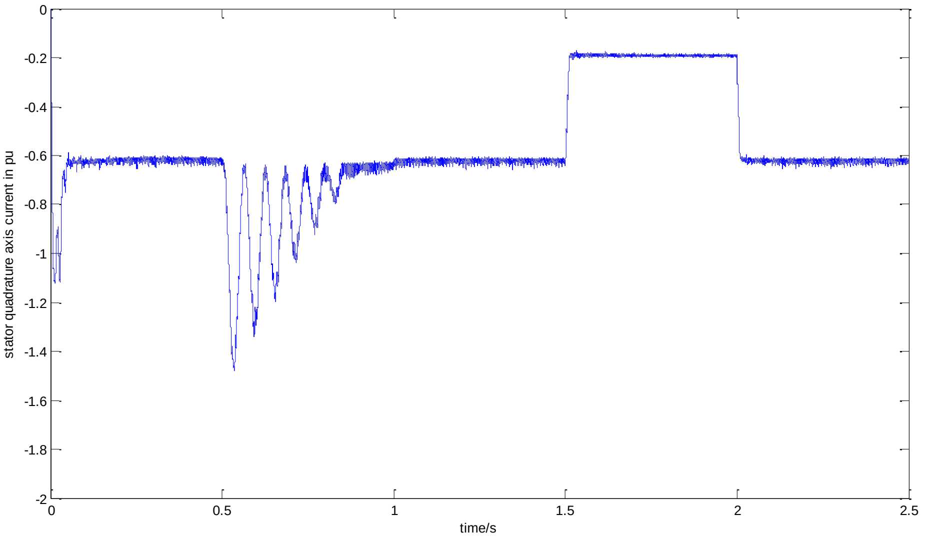

Figure 5.5 Stator quadrature axis current profile in p.u. for a three-level converter-based WTGS (stator flux reference frame)

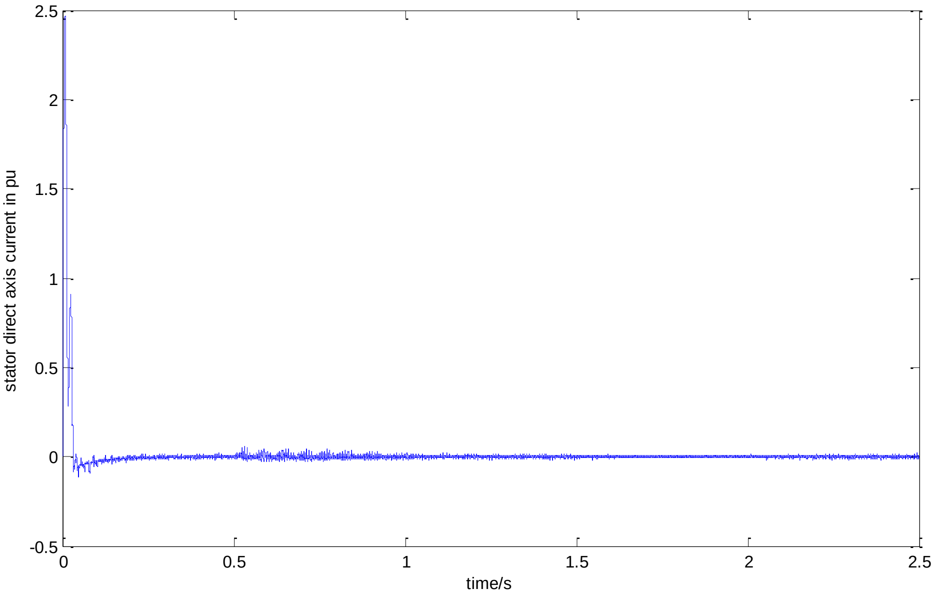

Figure 5.6 Stator direct axis current profile in p.u. for a three-level converter-based WTGS (stator flux reference frame)

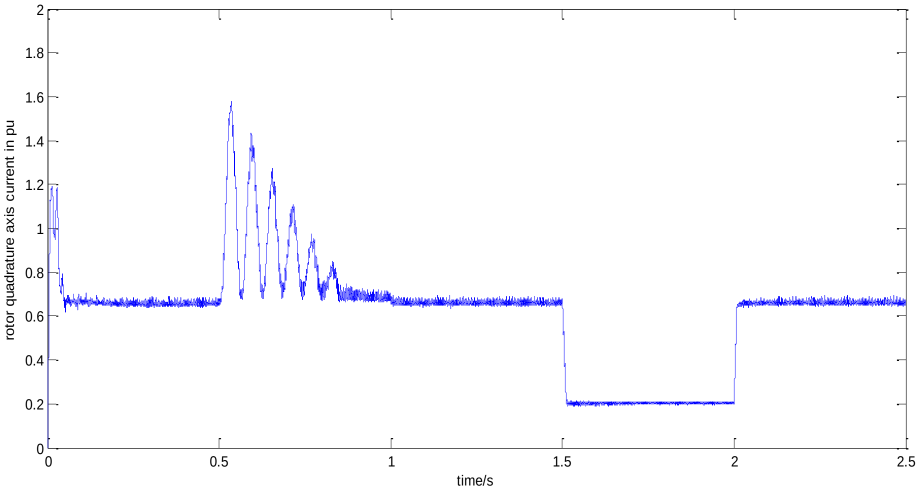

Figure 5.7 Rotor quadrature axis current profile in p.u. for a three-level converter-based WTGS (stator flux reference frame)

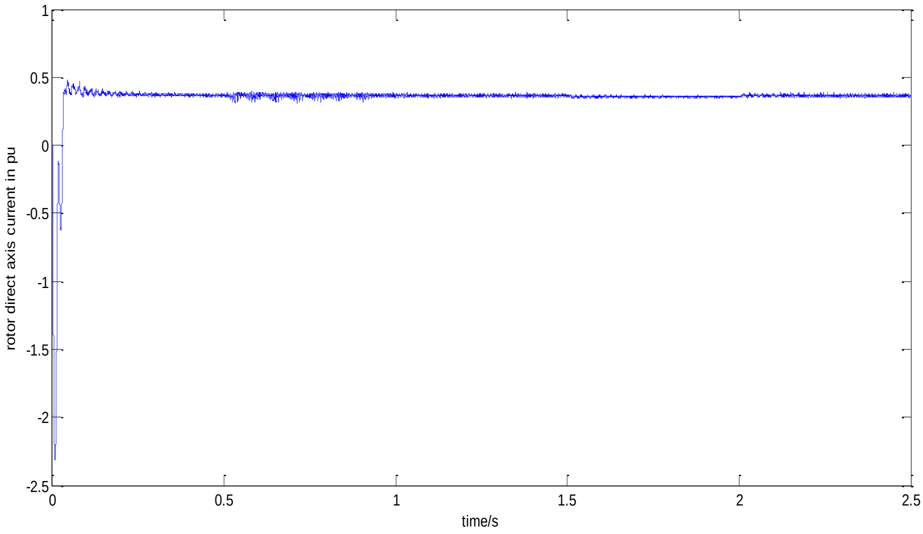

Figure 5.8 Rotor direct axis current profile in p.u. for a three-level converter-based WTGS (stator flux reference frame)

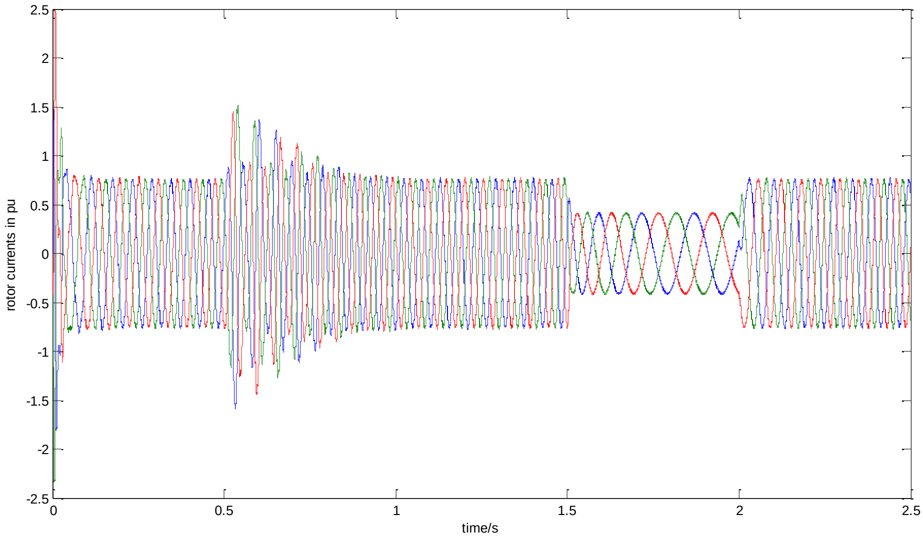

Figure 5.9 Rotor currents profiles in p.u. for a three-level converter-based WTGS (ABC reference frame)

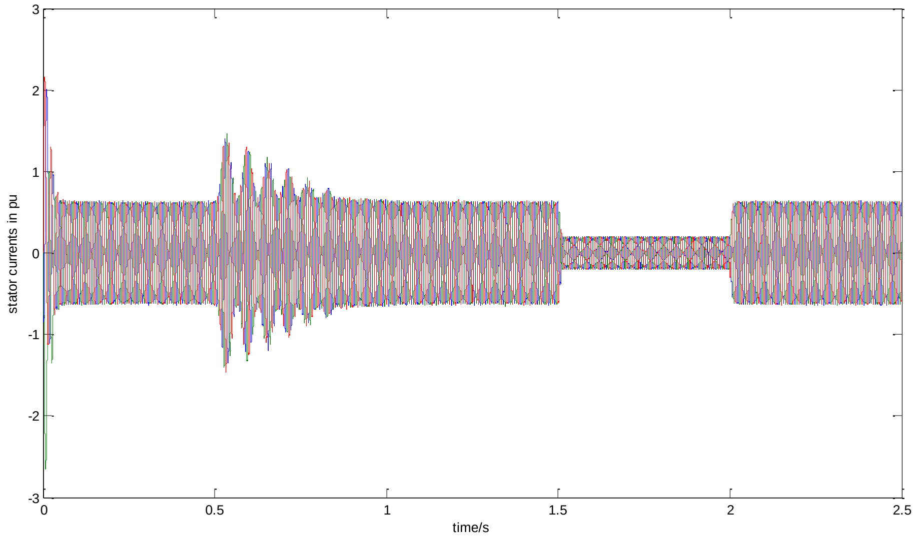

Figure 5.10 Stator currents profiles in p.u. for a three-level converter-based WTGS (ABC reference frame)

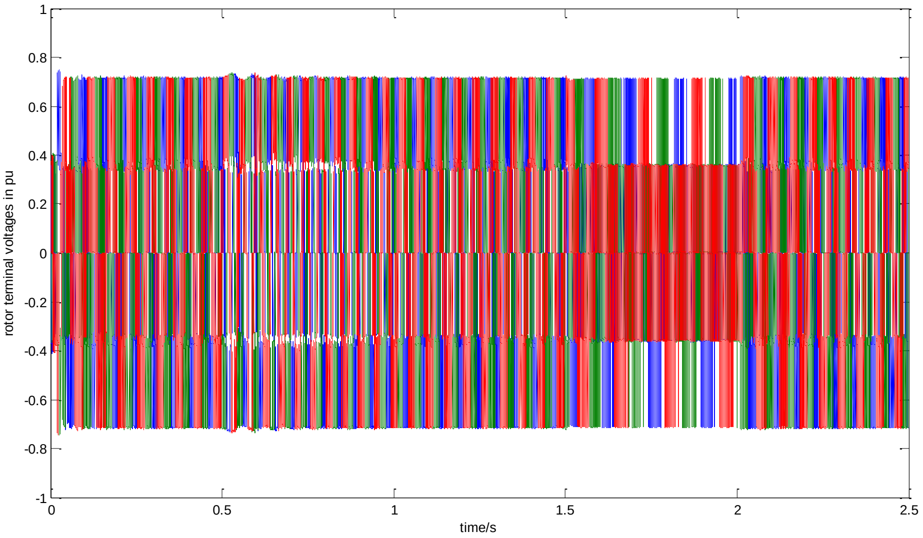

Figure 5.11 Rotor terminal voltages profiles in p.u. for a three-level converter-based WTGS (ABC reference frame)

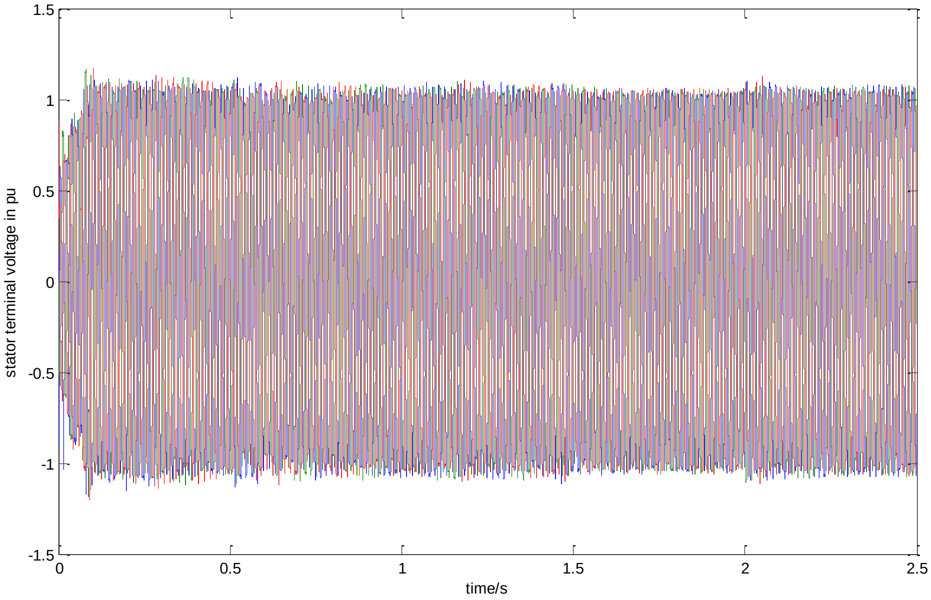

Figure 5.12 Stator terminal voltages profiles in p.u. for a three-level converter-based WTGS (ABC reference frame)

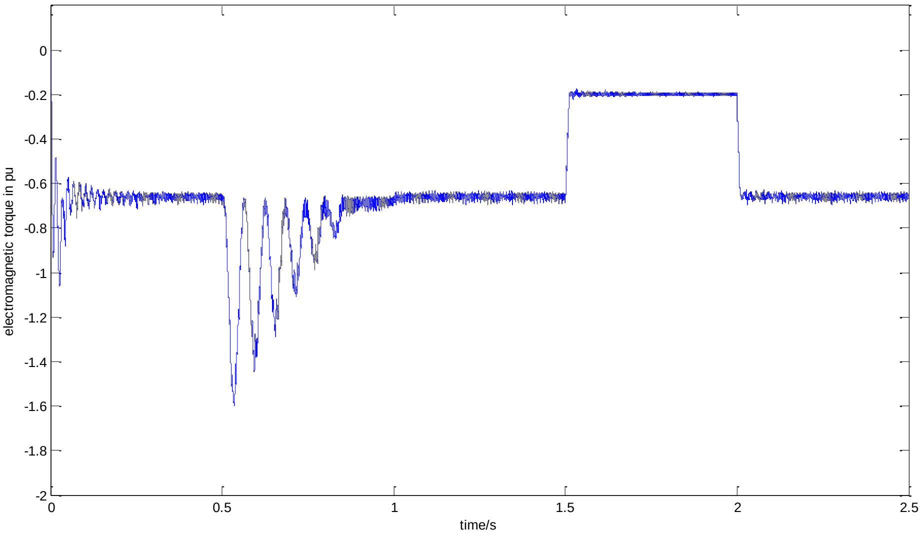

Figure 5.13 Electromagnetic torque profile in p.u. for a three-level converter-based WTGS

The ripple for the DC-link voltage, based on the simulation results in Figure 5.14, was found to be as follows:

$$Ripple = \frac{1180 - 1120}{1150} = 5.21\%$$

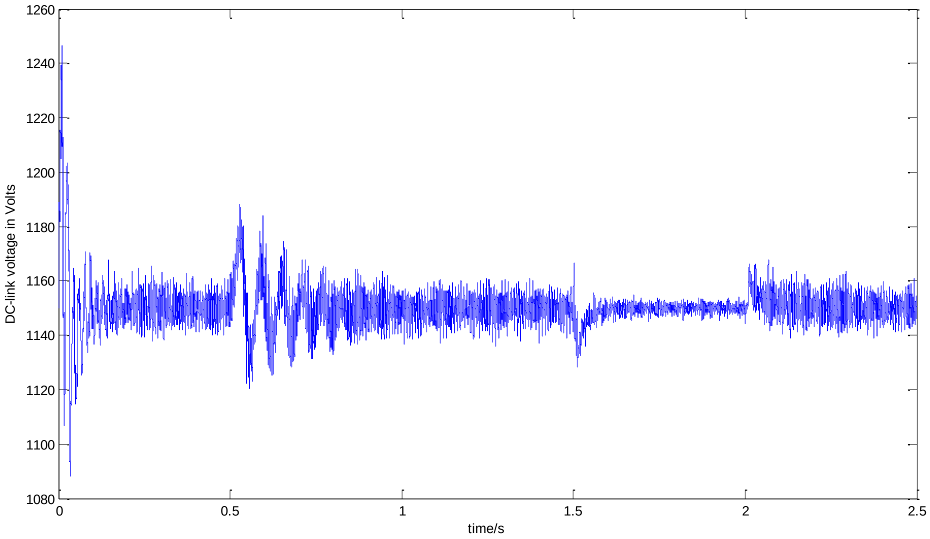

Figure 5.14 DC-link voltage profile in volts for a three-level converter-based WTGS

The above simulation results show that the two-level and three-level converter-based WTGSs have similar profiles in the power, torque and currents. However, through detailed analysis, the advantages of the three-level converter, for the total harmonic distortion (THD) and voltage magnitudes of the rotor terminal voltages, can be observed, and the comparison results are given next.

5.4 Comparison between Two-level Converters and Three-level Converters for Wind Turbine-Generator Systems

In this section, the comparison between the two-level converter- and three-level converter-based wind turbine-generator systems, which are modulated by SVPWM and SPWM, respectively, will be presented in detail. As mentioned before, the power topologies of the three-level converters synthesize the voltage waveform using a number of semiconductor devices connected in a special arrangement, rated at a fraction of the DC-bus voltage. To show this characteristic, the power switch S_1 in

Figure 4.1 and 4.13, will be taken as an example, and the IGBT voltage stresses for both systems are plotted in Figures 5.15 and 5.16 as follows:

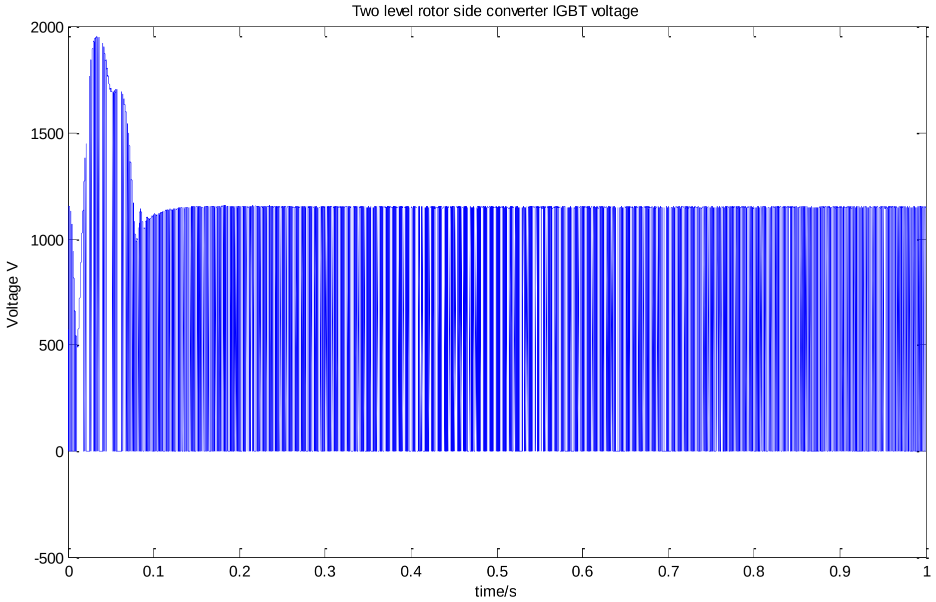

Figure 5.15 IGBT voltage stress for the two-level generator-side converter when wind speed is equal to 12m/s

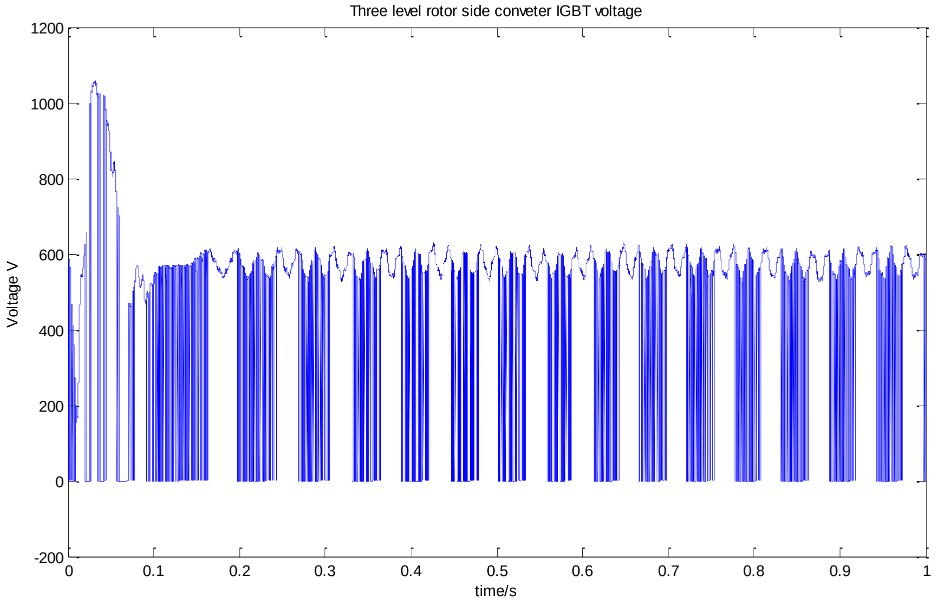

Figure 5.16 IGBT voltage stress for the three-level generator-side converter when wind speed is equal to 12m/s

From Figure 5.15 and 5.16, it can be seen that the voltage supported by the power semiconductor for the three-level converter will be half that of the two-level converter, and this characteristic makes three-level converters widely used in medium voltage applications.

Besides, the rotor terminal line-to-line voltages are plotted in Figure 5.17 and 5.18, when wind speed is equal to 12 m/s.

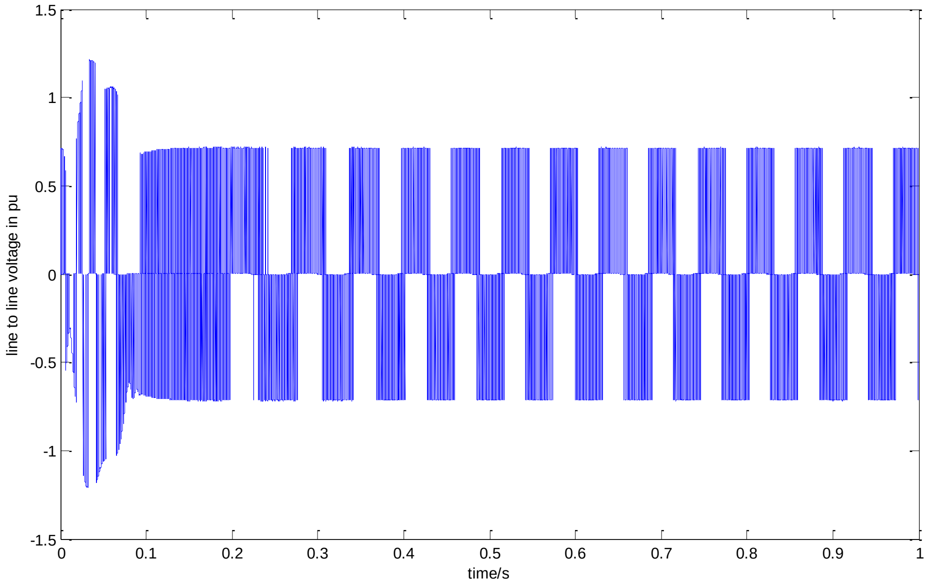

Figure 5.17 Rotor terminal line-to-line voltage for the two-level converter-based WTGS when wind speed is equal to 12m/s

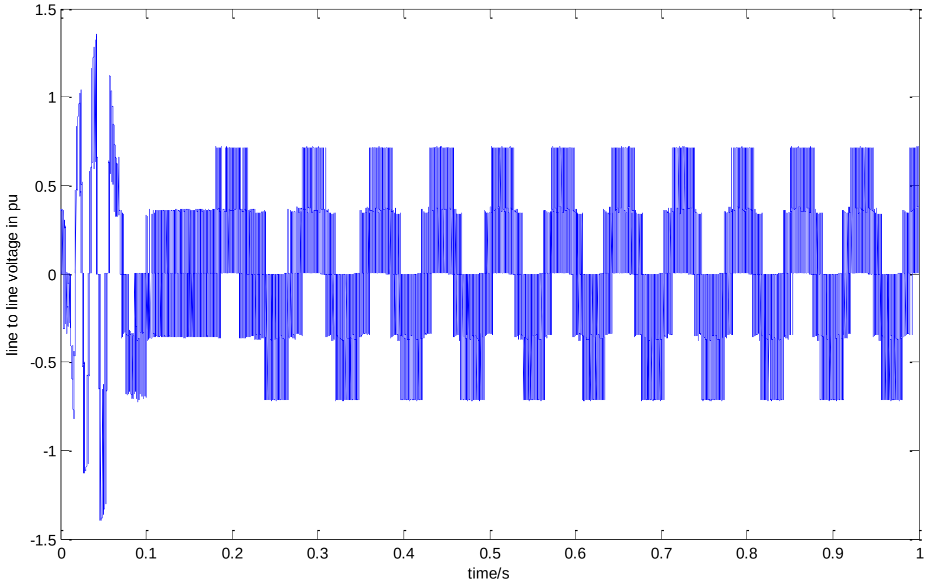

Figure 5.18 Rotor terminal line-to-line voltage for the three-level converter-based WTGS when wind speed is equal to 12m/s

From Figure 5.17 and 5.18, it can be seen that the rotor terminal line-to-line voltage for the three-level converter-based WTGS has three voltage levels, and hence has less harmonic components. Table 5.1 gives the comparison results between the three-level converter-based WTGS and the two-level converter-based WTGS, which are modulated by the SVPWM and SPWM, respectively, under various wind speed conditions.

Table 5.1 Comparison between the two-level SPWM and the three-level SVPWM for various wind speeds

Wind speed	Two-level SPWM		Three-level SVPWM	
v	Output line-to-line voltage		Output line-to-line voltage	
	Fundamental peak value (pu)	THD(%)	Fundamental peak value (pu)	THD(%)
12	0.5659	81.55	0.6274	46.74
11	0.5293	88.73	0.5967	52.39
10	0.4449	107.26	0.4951	66.56
9	0.337	140.53	0.3718	93.47

From Table 5.1, it can be concluded that the three-level converter-based system, which is modulated by SVPWM, can obtain a higher magnitude of the rotor terminal voltages and generate lower THD. The harmonic components of the rotor terminal voltage will be injected into the generator, and will further cause variations for the power profiles. Figure 5.19 through Figure 5.22 show the differences between the reference values and actual values for the active power and reactive power, respectively, when wind speed is equal to 12m/s. Here, the reference value for reactive power is 0 pu, and active power is 1 pu.

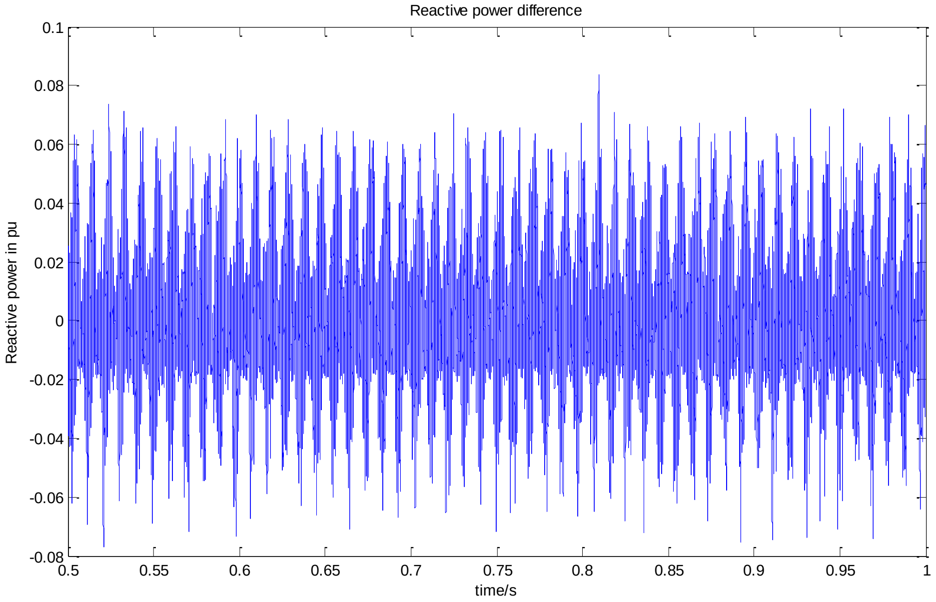

Figure 5.19 Reactive power differences for a two-level converter-based WTGS when wind speed is equal to 12m/s

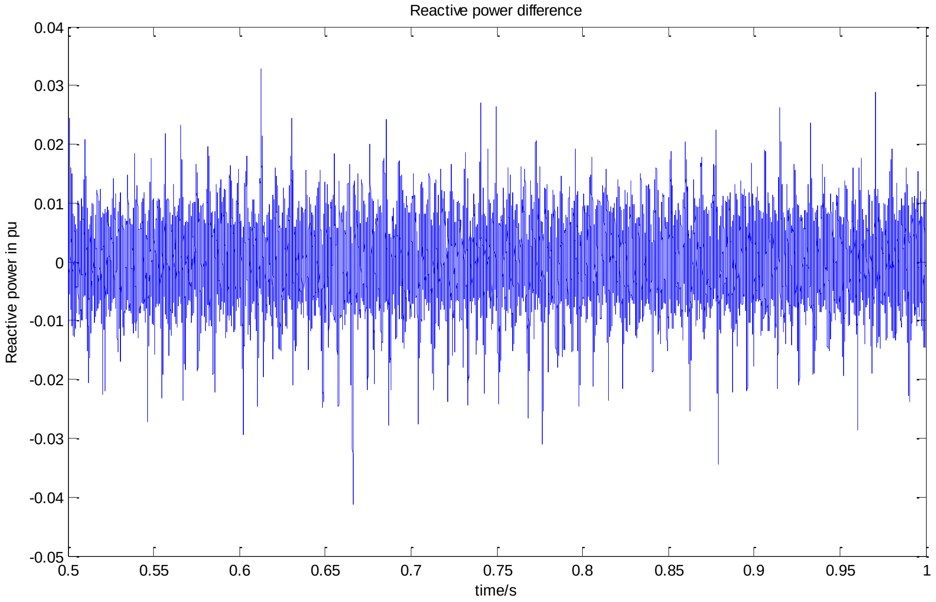

Figure 5.20 Reactive power differences for a three-level converter-based WTGS when wind speed is equal to 12m/s

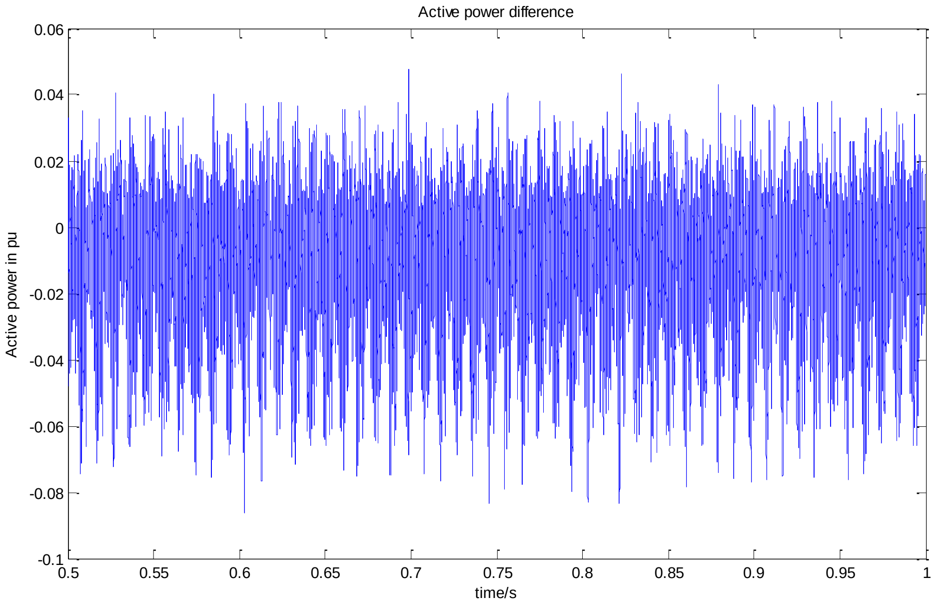

Figure 5.21 Active power differences for a two-level converter-based WTGS when wind speed is equal to 12m/s

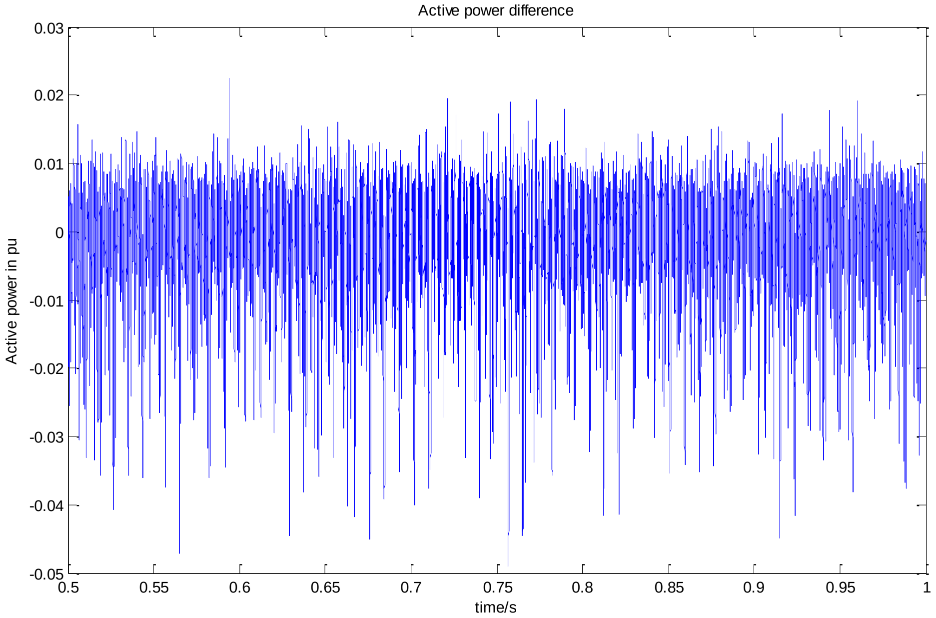

Figure 5.22 Active power differences for a three-level converter-based WTGS when wind speed is equal to 12m/s

From Figure 5.19 through Figure 5.22, it can be seen that the power difference ripples for the three-level converter-based system are much lower than those of the two-level converter-based system.

Chapter 6

Conclusions and Suggested Future Work

6.1 Summary and Conclusions

In this thesis, the modeling and control of a doubly-fed induction generator based wind turbine-generator system have been considered. More specifically, the modeling of different components, the control strategies for the back-to-back converter, the advanced modulation technology and novel type of converters have been studied and analyzed in detail.

As a basis of the research, the model of a wind turbine-generator system equipped with a doubly-fed induction generator was developed in a Matlab/Simulink environment, which simulates the dynamics of the system from the turbine rotor, where the kinetic wind energy is converted to the mechanical energy, to the generator, which transforms the mechanical power to electrical power, and then to the grid connection point, where the electric power is fed into the grid. The model of the wind turbine system includes the aerodynamic models of the wind turbine, the drive train system models, the back-to-back converter models, and the doubly-fed induction generator models.

Four control schemes were implemented in the wind turbine system, which are, the gird-side converter control, generator-side converter control, maximum power point tracking, and pitch angle control, respectively. The objective of the vector-control scheme for the grid-side converter controller is to keep the DC-link voltage constant regardless of the magnitudes of the grid voltages, and to yield a unity power factor looking into the WTGS from the grid-side. The vector-control scheme for the generator-side converter ensures a decoupling control of the stator-side active and reactive power. The maximum power point tracking scheme provides the reference value of stator active power for the generator-side converter control. The pitch angle control is used to regulate the pitch angle when the captured wind power exceeds its rated value or the wind speed exceeds its rated value. With these control schemes, the wind turbine is capable of providing satisfactory steady state and dynamic performances under various wind speed conditions.

New modulation technology, namely, SVPWM and multi-level converters, which are widely used in medium voltage applications, were presented and analyzed in detail. The simulation results and the comparison results show that the SVPWM modulation could obtain higher amplitude of the modulation index as well as generate less total harmonic distortion (THD) of the output voltages. The multi-level converters have been shown to provide significant advantages over the conventional converters for medium- and high-power applications due to their ability to meet the increasing demand of power ratings and power quality associated with reduced harmonic distortion, lower electromagnetic interference, and higher efficiency.

A three-level back-to-back converter, which is modulated by the space vector PWM, has been applied in a wind turbine-generator system. In order to show the advantages of the three-level converter and SVPWM, detailed analysis for the IGBT voltage stress, rotor terminal voltages and power differences were given. The corresponding comparison results show the superiority of the proposed system.

6.2 Future Trends in Wind Turbine-Generator Systems

The wind turbines employing doubly-fed induction generators (DFIGs) accounted for almost half of the installations back in 2001 [149]. Although, at the time, the DFIGs represented a technological advancement for the industry [150], they have two major disadvantages because they:

- Use slip-rings and brushes that require regular maintenance and replacements.
- Expose the gearboxes to large torque pulsations, which can be caused by grid faults. (Such torque pulsations may result in premature failures and increase the operational costs).

Furthermore, over the last decade, the relative cost of the power electronics in a wind turbine (WT) system has dropped. This evolution, correlated with tighter regulations imposed to grid connected WTs, led to the use of “full” power conversion systems in which the generator is electrically connected to the grid entirely through a back-to-back voltage source converter. Such a configuration is advantageous because:

- The DC link provides a decoupling of the generator side from the grid side, resulting in improved fault handling and active/reactive power control.
- The generators used are of the synchronous or squirrel cage induction type, which are superior to DFIGs in terms of efficiency, maintenance and reliability.
- Enables the implementation of direct drive train configurations that do not

employ gearboxes.

The current state of the art configuration for multi-level converters is the neutral-point-clamped (NPC) topology that was discussed in the previous chapters. A major drawback of this solution is the unequal loading of the power electronics components. Recent developments [151] suggest that industry may migrate towards cascaded H-bridge converters, which:

- Require the least number of components as compared with other topologies, due to the fact that there is no need for extra clamping diodes and capacitors
- Have a modularized circuit layout that is preferable for practical implementation in manufacturing.

6.3 Recommendations for Future Work

Although many developments have been accomplished in this thesis, several possible future investigations are interesting. Some subjects for future studies are listed as follows:

- Higher order models of the drive train system and the doubly-fed induction generator model with saturation effect should be considered in wind turbine systems.
- Wind speed sensorless control strategies should be studied, due to the fact that the anemometer may not accurately measure the wind speed.
- Direct torque control and direct power control should be considered, because of the advantages of no current regulators, no coordinate

transformations and specific modulations, and no current control loops.

- Matrix converters are another interesting topic because of their ac to ac transformation ability.
- The performances of the DFIG-based wind turbine system should be compared with a wind turbine system equipped with a multi-pole permanent magnet generator, which is connected to the grid through a full-scale power converter.
- The transient behaviors of the DFIG-based wind turbine system under disturbances of grid failures should be studied.

REFERENCES

[1] Wei Qiao, “Integrated Control of Wind Farms, FACTS Devices and the Power Network Using Neural Networks and Adaptive Critic Designs”, Georgia Institute of Technology, Ph.D. dissertation, July 2008.

[2] Jin Yang, “Fault Analysis and Protection for Wind Power Generation Systems”, University of Glasgow, Ph.D. dissertation, March 2011.

[3] Raymond W. Flumerfelt and Su Su Wang, “Wind turbines,” in AccessScience, ©McGraw-Hill Companies, 2009, http://www.accessscience.com.

[4] Bijaya Pokharel, “Modeling, Control and Analysis of a Doubly Fed Induction Generator Based Wind Turbine System with Voltage Regulation”, Tennessee Technological University, Master thesis, December 2011.

[5] F. Iov, M. Ciobotaru and F. Blaabjerg, “Power Electronics Control of Wind Energy in Distributed Power Systems”, *11th International Conference on Optimization of Electrical and Electronic Equipment*, Brasov, pp. XXIX - XLIV, May 2008.

[6] S. Muller, M. Deicke and Rik W. De Doncker, “Doubly fed induction generator systems for wind turbines”, *IEEE Industry Applications Magazine*, Vol. 8, No. 3, pp. 26-33, May/June 2002.

[7] S. Benelghali, M. E. H. Benbouzid and J. F. Charpentier, “Comparison of PMSG and DFIG for Marine Current Turbine Applications”, *XIX International Conference on Electrical Machines*, pp. 1-6, Rome, September 2010.

[8] H. Li and Z. Chen, “Overview of Different Wind Generator Systems and Their Comparisons”, *IET Renewable Power Generation*, Vol. 2, No. 2, pp.123-138, August 2008.

[9] “Wind Speed and Wind Energy”, Available on line: http://energybible.com/wind_energy/wind_speed.html.

[10] Abram Perdana, “Dynamic Models of Wind Turbines”, Ph.D. dissertation, Chalmers University of Technology, Sweden, 2008.

[11] Tao Sun, “Power Quality of Grid-Connected Wind Turbines with DFIG and Their Interaction with the Grid”, Ph.D. dissertation, Aalborg University, Denmark, May 2004.

[12] Iulian Munteanu, Antoneta Iuliana Bratcu, Nicolaos-Antonio Cutululis and Emil Ceanga, “Optimal Control of Wind Energy System”, London, Springer, 2008.

[13] Ming Yin, Gengyin Li, Ming Zhou and Chengyong Zhao, “Modeling of the Wind Turbine with a Permanent Magnet Synchronous Generator for Integration”, *IEEE Power Engineering Society General Meeting*, pp.1-6, Tampa, June 2007.

[14] J. G. Slootweg, S. W. H. de Haan, H. Polinder and W. L. Kling, “General Model for Representing Variable Speed Wind Turbines in Power System Dynamics

Simulations", *IEEE Transactions on Power Systems,* Vol.18, No.1, pp.144-151, February 2003.

[15] N. Miller, W. Price, and J. Sanchez-Gasca, "Dynamic modeling of GE 1.5 and 3.6 wind turbine-generators", General Electric Company, Technical Report, October 2003.

[16] Md. Arifujjaman, "Modeling, Simulation and Control of Grid Connected Permanent Magnet Generator (PMG)-based Small Wind Energy Conversion System", *2010 IEEE Electric Power and Energy Conference (EPEC),* pp.1-6, Halifax, August 2010.

[17] P. M. Anderson and Anjan Bose, "Stability Simulation of Wind Turbine Systems", *IEEE Transaction on Power Apparatus and Systems,* Vol.102, No.12, pp. 3791-3795, December 1983.

[18] S. M. Muyeen, Md. Hasan Ali, R. Takahashi, T. Murata, J. Tamura, Y. Tomaki, A. Sakahara and E. Sasano, "Comparative Study on Transient Stability Analysis of Wind Turbine Generator System Using Different Drive Train Models", *IET Renewable Power Generation,* Vol. 1, No, 2, pp. 131-141, June 2007.

[19] Stavros A. Papathanassiou and Michael P. Papadopoulos, "Mechanical Stresses in Fixed-Speed Wind Turbines Due to Network Disturbances", *IEEE Transactions on Energy Conversion,* Vol. 16, No. 4, pp. 361-367, December 2001.

[20] R. Melıcio, V. M. F. Mendes and J. P. S. Catala˜o, "Harmonic Assessment of Variable-Speed Wind Turbines Considering a Converter Control Malfunction", *IET Renewable Power Generation*, Vol. 4, No. 2, pp. 139-152, March 2010.

[21] H. Li and Z. Chen, "Transient Stability Analysis of Wind Turbines with Induction Generators Considering Blades and Shaft Flexibility", *33rd Annual Conference of the IEEE Industrial Electronics Society,* Chongqing, China, pp. 1604 - 1609, November 2007.

[22] Gnanasambandapillai Ramtharanand and Nicholas Jenkins, "Influence of Rotor Structural Dynamics Representations on the Electrical Transient Performance of FSIG and DFIG Wind Turbines", *Wind Energy*, Vol.10, No. 4, pp. 293-301, August 2007.

[23] Boubekeur Boukhezzar and Houria Siguerdidjane, "Nonlinear Control of a Variable-Speed Wind Turbine Using a Two-Mass Model", *IEEE Transactions on Energy Conversion,* Vol. 26, No. 1, pp.149-162, March 2011.

[24] Wei Qiao, Wei Zhou, José M. Aller, and Ronald G. Harley, "Wind Speed Estimation Based Sensorless Output Maximization Control for a Wind Turbine Driving a DFIG", *IEEE Transactions on Power Electronics,* Vol. 23, No. 3, pp. 1156-1169, May 2008.

[25] Lucian Mihet-Popa, Frede Blaabjergand and Ion Boldea, "Wind Turbine Generator Modeling and Simulation Where Rotational Speed is the Controlled Variable", *IEEE Transactions on Industry Applications,* Vol. 30, No.1, pp. 3-10, January/February 2004.

[26] Francoise Mei and Bikash Pal, “Modal Analysis of Grid-Connected Doubly Fed Induction Generators”, *IEEE Transactions on Energy Conversion*, Vol. 22, No.3, pp. 728-736, September 2007.

[27] Tomas Petru and Torbjörn Thiringer, “Modeling of Wind Turbines for Power System Studies”, *IEEE Transactions on Power Systems*, Vol. 17, No. 4, pp. 1132-1139, November 2002.

[28] G. Quinonez-Varela and A. Cruden, “Modeling and Validation of a Squirrel Cage Induction Generator Wind Turbine during Connection to the Local Grid”, *IET Generation, Transmission & Distribution*, Vol.2, No.2, pp. 301-309, March 2008.

[29] Chen Wang and George Weiss, “Integral Input-to-State Stability of the Drive-Train of a Wind Turbine”, *Proceedings of the 46th IEEE Conference on Decision and Control*, New Orleans, LA, USA, pp.6100-6105, December 2007.

[30] Yazhou Lei, Alan Mullane, Gordon Lightbody, and Robert Yacamini, “Modeling of the Wind Turbine With a Doubly Fed Induction Generator for Grid Integration Studies”, *IEEE Transactions on Energy Conversion*, Vol. 21, No. 1, pp. 257-264, March 2006.

[31] Janaka B. Ekanayake, Lee Holdsworth, Xueguang Wu and Nicholas Jenkins, “Dynamic Modeling of Doubly Fed Induction Generator Wind Turbines”, *IEEE Transactions on Power Systems*, Vol.18, No.2, pp. 803-809, May 2003.

[32] L. J. Ontiveros, P. E. Mercado and G. O. Suvire, “A New Model of the Double-Feed Induction Generator Wind Turbine”, *2010 IEEE Transmission and Distribution Conference and Exposition*, Latin America, pp. 263-269, November 2010.

[33] Daniel J. Trudnowski, Andrew Gentile, Jawad M. Khan, and Eric M. Petritz, “Fixed-Speed Wind-Generator and Wind-Park Modeling for Transient Stability Studies”, *IEEE Transactions on Power Systems*, Vol. 19, No. 4, pp. 1911-1917, November 2004.

[34] Andreas Petersson, “Analysis, Modeling and Control of Doubly-Fed Induction Generators for Wind Turbines”, Chalmers University of Technology, Ph.D. dissertation, Sweden, 2005.

[35] Kostyantyn Protsenko and Dewei Xu, “Modeling and Control of Brushless Doubly-Fed Induction Generators in Wind Energy Applications”, *IEEE Transactions on Power Electronics*, Vol. 23, No. 3, pp.1191- 1197, May 2008.

[36] Yongchang Zhang, Zhengxi Li, Jiefeng Hu, Wei Xu and Jianguo Zhu, “A Cascaded Brushless Doubly Fed Induction Generator for Wind Energy Applications Based on Direct Power Control”, *2011 International Conference on Electrical Machines and Systems* , pp.1-6, August 2011.

[37] Istvan Erlich, Jörg Kretschmann, Jens Fortmann, Stephan Mueller-Engelhardt and Holger Wrede, “Modeling of Wind Turbine Based on Doubly-Fed Induction Generators for Power System Stability Studies”, *IEEE Transactions on Power Systems*, Vol.22, No.3, pp. 909-919, August 2007.

[38] Arantxa Tapia, Gerardo Tapia, J. Xabier Ostolaza and José Ramón Sáenz, “Modeling and Control of a Wind Turbine Driven Doubly Fed Induction Generator”, *IEEE Transactions on Energy Conversion*, Vol. 18, No. 2, pp. 194-204, June 2003.

[39] I. Erlich and F. Shewarega, “Modeling of Wind Turbines Equipped with Doubly-Fed Induction Machines for Power System Stability Studies”, *2006 IEEE Power Systems Conference and Exposition*, pp. 978-985, November 2006.

[40] Alvaro Luna, Francisco Kleber de Araujo Lima, David Santos, Pedro Rodríguez, Edson H. Watanabe, and Santiago Arnaltes, “Simplified Modeling of a DFIG for Transient Studies in Wind Power Applications”, *IEEE Transactions on Industrial Electronics*, Vol. 58, No. 1, pp. 9-20, January 2011.

[41] Katherine Elkington and Mehrdad Ghandhari, “Comparison of Reduced Order Doubly Fed Induction Generator Models for Nonlinear Analysis”, *IEEE Electrical Power & Energy Conference*, pp.1-6, October 2009.

[42] P. Sørensen, A. D. Hansen, T. Lund and H. Bindner, “Reduced Models of Doubly Fed Induction Generator System for Wind Turbine Simulations”, *Wind Energy*, Vol. 9, No. 4, pp. 299-311, August 2006.

[43] A. Samuel Neto, S. L. A. Ferreira, J. P. Arruda, F. A. S. Neves, P. A. C. Rosas and M. C. Cavalcanti, “Reduced Order Model for Grid Connected Wind Turbines with Doubly Fed Induction Generators”, *IEEE International Symposium on Industrial Electronics*, pp. 2655-2660, June 2007.

[44] Alireza Abbaszadeh, Saeed Lesan and Vahid Mortezapour, “Transient Response of Doubly Fed Induction Generator Under Voltage Sag Using an Accurate Model”, *2009 IEEE PES/IAS Conference on Sustainable Alternative Energy (SAE)*, pp. 1-6, September 2009.

[45] Pablo Ledesma and Julio Usaola, “Effect of Neglecting Stator Transients in Doubly Fed Induction Generators Models”, *IEEE Transactions on Energy Conversion*, Vol. 19, No. 2, pp. 459-461, June 2004.

[46] Torbjörn Thiringer and Jorma Luomi, “Comparison of Reduced-Order Dynamic Models of Induction Machines”, *IEEE Transactions on Power Systems*, Vol.16, No. 1, pp. 119-126, February 2001.

[47] Gill G. Richards and Owen T. Tan, “Simplified Models for Induction Machine Transients under Balanced and Unbalanced Conditions”, *IEEE Transactions on Industry Applications*, Vol. IA-17, No. 1, pp. 15-21, January 1981.

[48] Jae-Ho Choi, Hyong-Cheol Kim and Joo-Sik Kwak, “Indirect Current Control Scheme in PWM Voltage-Sourced Converter”, *Proceedings of the Power Conversion Conference*, pp. 277-282, Nagaoka, August 1997.

[49] Vladimir Blasko and Vikram Kaura, “A New Mathematical Model and Control of a Three-Phase AC-DC Voltage Source Converter”, *IEEE Transactions on Power Electronics*, Vol. 12, No. 1, pp. 116-123, January1997.

[50] Bong-Hwan Kwon, Jang-Hyoun Youm and Jee-Woo Lim, "A Line-Voltage-Sensorless Synchronous Rectifier", *IEEE Transactions on Power Electronics,* Vol. 14, No. 5, pp. 966-972, September 1999.

[51] Yan Guo, Xiao Wang, Howard C. Lee and Boon-Teck Ooi, "Pole-Placement Control of Voltage-Regulated PWM Rectifiers Through Real-Time Multiprocessing", *IEEE Transactions on Industrial Engineering,* Vol. 41, No. 2, pp. 224-230, April 1994.

[52] José R. Rodríguez, Juan W. Dixon, José R. Espinoza, Jorge Pontt and Pablo Lezana, "PWM Regenerative Rectifiers: State of the Art", *IEEE Transactions on Industrial Electronics,* Vol. 52, No. 1, pp. 5-22, February 2005.

[53] N. Horiuchi and T. Kawahito, "Torque and Power Limitations of Variable Speed Wind Turbines Using Pitch Control and Generator Power Control", *2001 Power Engineering Society Summer Meeting,* Vol. 1, pp. 638-643, July 2001.

[54] Mohamed Mansour, M. N. Mansouri, and M. F. Mimouni, "Study of Performance of a Variable-Speed Wind Turbine with Pitch Control Based on a Permanent Magnet Synchronous Generator", *2011 8th International Multi-Conference on Systems, Signals & Devices*, pp. 1-6, March 2011.

[55] Eduard Muljadi and C. P. Butterfield, "Pitch-Controlled Variable-Speed Wind Turbine Generation", *IEEE Transactions on Industry Applications*, Vol. 37, No. 1, pp. 240-246, February 2001.

[56] Mohsen Faridi, Roghaiyeh Ansari, Seyed Ali Mousavi and Mahsa Dodman, "Pitch Control of Wind Turbine Blades in Noisy and Unstable Wind Conditions", *2010 9th International Conference on Environment and Electrical Engineering (EEEIC)*, pp. 22-25, May 2010.

[57] Jianzhong Zhang, Ming Cheng, Zhe Chen and Xiaofan Fu, "Pitch Angle Control for Variable Speed Wind Turbines", *2008 Third International Conference on Electric Utility Deregulation and Restructuring and Power Technologies*, pp. 2691-2696, April 2008.

[58] Tomonobu Senjyu, Ryosei Sakamoto, Naomitsu Urasaki, Toshihisa Funabashi, Hideki Fujita and Hideomi Sekine, "Output Power Leveling of Wind Turbine Generator for All Operating Regions by Pitch Angle Control", *IEEE Transactions on Energy Conversion*, Vol. 21, No. 2, pp. 467-475, June 2006.

[59] E.B. Muhando, T. Senjyu, A. Yona, H. Kinjo and T. Funabashi, "Disturbance Rejection by Dual Pitch Control and Self-Tuning Regulator for Wind Turbine Generator Parametric Uncertainty Compensation", *IET Control Theory & Applications*, Vol. 1, No. 5, pp. 1431-1440, September 2007.

[60] N. A. Schinas, N. A. Vovos and G. B. Giannakopoulos, "An Autonomous System Supplied Only by a Pitch-Controlled Variable-Speed Wind Turbine", *IEEE Transactions on Energy Conversion*, Vol. 22, No. 2, pp. 325- 331, June 2007.

[61] I. Hamzaoui, F. Bouchafaa, A. Hadjammar and A. Talha, A. "Improvement of the Performances MPPT System of Wind Generation", *2011 Saudi*

International on Electronics, Communications and Photonics Conference, pp. 1-6, April 2011.

[62] Shuhui Li, Timothy A. Haskew and Eduard Muljadi, “Integrative Characteristic Evaluation of DFIG Maximum Power Extraction using Lookup Table Approach”, *2010 IEEE Power and Energy Society General Meeting*, pp. 1-8, July 2010.

[63] H. Li, Z. Chen and John K. Pedersen, “Optimal Power Control Strategy of Maximizing Wind Energy Tracking and Conversion for VSCF Doubly Fed Induction Generator System”, *IEEE 5th International Power Electronics and Motion Control Conference*, Vol.3, pp. 1-6, August 2006.

[64] Mohamed Hilal, Mohamed Maaroufi and Mohamed Ouassaid, “Doubly Fed Induction Generator Wind Turbine Control for a maximum Power Extraction”, *2011 International Conference on Multimedia Computing and Systems*, pp. 1-7, April 2011.

[65] R. Pena, J. C. Clare and G. M. Asher, “Doubly fed induction generator using back-to-back PWM converters and its application to variable-speed wind-energy generation,” *IEE Proceedings Electric Power Applications*, Vol. 143, No. 3, pp. 231-241, May 1996.

[66] Y. Zhao, X. D. Zou, Y. N. Xu, Y. Kang and J. Chen, “Maximal Power Point Tracking under Speed-Mode Control for Wind Energy Generation System with Doubly Fed Introduction Generator”, *IEEE 5th International Power Electronics and Motion Control Conference*, Vol.1, pp. 1-5, August 2006.

[67] Xie Zhen, Zhang Xing, Yang Shuying, Li Qin and Zhai Wenfeng, “Study on Control Strategy of Maximum Power Capture For DFIG in Wind Turbine System”, *2010 2nd IEEE International Symposium on Power Electronics Distributed Generation Systems*, pp. 110-115, June 2010.

[68] Yunqi Xiao and Pengxiao Jia, “VSCF Wind Turbine Control Strategy for Maximum Power Generation”, *Proceedings of the 8th World Congress on Intelligent Control and Automation*, Jinan, China, pp. 4781-4786, July 2010.

[69] Rajib Datta and V. T. Ranganathan, “A Method of Tracking the Peak Power Points for a Variable Speed Wind Energy Conversion System”, *IEEE Transactions on Energy Conversion*, Vol. 18, No. 1, pp. 163-168, March 2003.

[70] Baike Shen, Bakari Mwinyiwiwa, Yongzheng Zhang and Boon-Teck Ooi, “Sensorless Maximum Power Point Tracking of Wind by DFIG Using Rotor Position Phase Lock Loop (PLL)”, *IEEE Transactions on Power Electronics*, Vol. 24, No. 4, pp. 942-951, April 2009.

[71] I. K. Buehring and L. L. Freris, “Control Policies for Wind Energy Conversion Systems,” *IEE Proceedings on Generation, Transmission and Distribution*, Vol. 128, No. 5, pp. 253-261, September 1981.

[72] Quincy Wang and Liuchen Chang, “An Intelligent Maximum Power Extraction Algorithm for Inverter-Based Variable Speed Wind Turbine Systems”, *IEEE Transactions on Power Electronics*, Vol. 19, No. 5, pp. 1242-1249, September 2004.

[73] Marcelo Godoy Simoes, Bimal K. Bose and Ronald J. Spiegel, "Fuzzy Logic Based Intelligent Control of a Variable Speed Cage Machine Wind Generation System", *IEEE Transactions on Power Electronics*, Vol. 12, No. 1, pp. 87-95, January 1997.

[74] Changhong Shao, Xiangjun Chen and Zhonghua Liang. "Application Research of Maximum Wind energy Tracing Controller Based Adaptive Control Strategy in WECS", *IEEE 5th International Power Electronics and Motion Control Conference*, pp. 1-5, August 2006.

[75] Eftichios Koutroulis and Kostas Kalaitzakis, "Design of a Maximum Power Tracking System for Wind-Energy-Conversion Applications", *IEEE Transactions on Industrial Electronics*, Vol. 53, No. 2, pp. 486-494, April 2006.

[76] S. Chondrogiannis and M. Barnes, "Stability of Doubly-Fed Induction Generator Under Stator Voltage Orientated Vector Control", *IET Renewable Power Generation*, Vol. 2, No. 3, pp. 170-180, September 2008.

[77] Carles Batlle, Arnau D`oria-Cerezo and Romeo Ortega, "A Stator Voltage Oriented PI Controller For The Doubly-Fed Induction Machine", *Proceedings of the 2007 American Control Conference*, New York City, USA, pp. 5438-5443, July 2007.

[78] Shuhui Li, Rajab Challoo and Marty J. Nemmers, "Comparative Study of DFIG Power Control Using Stator-Voltage and Stator-Flux Oriented Frames", *IEEE Power & Energy Society General Meeting*, pp. 1-8, July 2009.

[79] I. Takahashi and T. Noguchi, "A New Quick-Response and High Efficiency Control Strategy of an Induction Machine," *IEEE Transaction on Industry Application*, Vol. 22, No. 5, pp. 820-827, October 1986.

[80] I. Takahashi and Y. Ohmori, "High-Performance Direct Torque Control of an Induction Motor," *IEEE Transaction on Industry Application*, Vol. 25, No. 2, pp. 257-264, March/April 1989.

[81] Toshihiko Noguchi, Hiroaki Tomiki, Seiji Kondo and Isao Takahashi, "Direct Power Control of PWM Converter Without Power-Source Voltage Sensors", *IEEE Transaction on Industry Application*, Vol. 34, No. 3, pp. 473-479, May/June 1998.

[82] Jihen Arbi, Manel Jebali-Ben Ghorbal, Ilhem Slama-Belkhodja and Lotfi Charaabi, "Direct Virtual Torque Control for Doubly Fed Induction Generator Grid Connection", *IEEE Transactions on Industrial Electronics*, Vol. 56, No. 10, pp. 4163-4173, October 2009.

[83] M. Tazil, V. Kumar, R. C. Bansal, S. Kong, Z. Y. Dong, W. Freitas and H. D. Mathur, "Three-phase doubly fed induction generators: an overview", *IET Electric Power Applications*, Vol. 4, No. 2, pp. 75-89, February 2010.

[84] Domenico Casadei, Francesco Profumo, Giovanni Serra and AngeloTani, "FOC and DTC: Two Viable Schemes for Induction Motors Torque Control", *IEEE Transactions on Power Electronics*, Vol. 17, No. 5, pp. 779-787, September 2002.

[85] Thomas G. Habetler, Francesco Profumo, Michele Pastorelli and Leon M. Tolbert, “Direct Torque Control of Induction Machines Using Space Vector Modulation”, *IEEE Transactions on Industry Applications,* Vol. 28, No. 5, pp. 1045-1053, September / October 1992.

[86] S. Arnalte, J. C. Burgos and J. L. Rodríguez-Amenedo, “Direct Torque Control of a Doubly-Fed Induction Generator for Variable Speed Wind Turbines*”, Electric Power Components and Systems,* Vol. 30, No. 2, pp. 199-216, November 2002.

[87] K. C. Wong, S. L. Ho and K. W. E. Cheng, “Direct Torque Control of a Doubly-fed Induction Generator with Space Vector Modulation”, *Electric Power Components and Systems,* Vol. 36, No. 12, pp. 1337-1350, November 2008.

[88] F. Bonnet, P. E. Vidal and M. Pietrzak-David, “Direct Torque Control of Doubly Fed Induction Machine”, *Bulletin of The Polish Academy of Sciences Technical Sciences*, Vol. 54, No. 3, pp. 307-314, 2006.

[89] Z. Liu, O. A. Mohammed and S. Liu, “A Novel Direct Torque Control Induction Generator Used for Variable Speed Wind Power Generation”, *IEEE Power Engineering Society General Meeting*, pp. 1-6, June 2007.

[90] Etienne Tremblay, Sergio Atayde, and Ambrish Chandra, “Comparative Study of Control Strategies for the Doubly Fed Induction Generator in Wind Energy Conversion Systems: A DSP-Based Implementation Approach*”, IEEE Transactions on Sustainable Energy,* Vol. 2, No. 3, pp. 288-299, July 2011.

[91] Mariusz Malinowski, Marian P. Kazmierkowski and Andrzej M. Trzynadlowski, “A Comparative Study of Control Techniques for PWM Rectifiers in AC Adjustable Speed Drives”, *IEEE Transactions on Power Electronics,* Vol. 18, No. 6, pp. 1390-1396, November 2003.

[92] Rajib Datta and V. T. Ranganathan, “Direct Power Control of Grid-Connected Wound Rotor Induction Machine Without Rotor Position Sensors”, *IEEE Transactions on Power Electronics,* Vol. 16, No. 3, pp. 390-399, May 2001.

[93] David Santos-Martin, Jose Luis Rodriguez-Amenedo and Santiago Arnalte, “Direct Power Control Applied to Doubly Fed Induction Generator Under Unbalanced Grid Voltage Conditions”, *IEEE Transactions on Power Electronics,* Vol. 23, No. 5, pp. 2328-2336, September 2008.

[94] Gonzalo Abad, Miguel A´ngel Rodr´ıguez, Grzegorz Iwanskiand and Javier Poza, “Direct Power Control of Doubly-Fed-Induction-Generator-Based Wind Turbines Under Unbalanced Grid Voltage”, *IEEE Transactions on Power Electronics,* Vol. 25, No. 2, pp. 442-452, February 2010.

[95] Lie Xu and Phillip Cartwright, “Direct Active and Reactive Power Control of DFIG for Wind Energy Generation”, *IEEE Transactions on Energy Conversion,* Vol. 21, No. 3, pp. 750-758, September 2006.

[96] Mostafa Soliman, O. P. Malik, and David T. Westwick, “Multiple Model Predictive Control for Wind Turbines With Doubly Fed Induction Generators”, *IEEE Transactions on Sustainable Energy,* Vol. 2, No. 3, pp. 215- 225, July 2011.

[97] Dawei Zhi, Lie Xu and Barry W. Williams, “Model-Based Predictive Direct Power Control of Doubly Fed Induction Generators”, *IEEE Transactions On Power Electronics*, Vol. 25, No. 2, pp. 341-351, February 2010.

[98] Lie Xu, Dawei Zhi and Barry W. Williams, “Predictive Current Control of Doubly Fed Induction Generators”, *IEEE Transactions on Industrial Electronics*, Vol. 56, No. 10, pp. 4143-4153, October 2009.

[99] Jiefeng Hu, Jianguo Zhu and D. G. Dorrell, “A Comparative Study of Direct Power Control of AC/DC Converters for Renewable Energy Generation”, *37th Annual Conference on IEEE Industrial Electronics Society*, pp. 3578-3583, November 2011.

[100] B. Hopfensperger, D. J. Atkinson and R. A. Lakin, “Stator-flux-oriented control of a doubly-fed induction machine with and without position encoder”, *IEE Proceedings Electric Power Applications*, Vol.147, No. 4, pp. 241-250, July 2000.

[101] Sheng Yang and Venkataramana Ajjarapu, “A Speed-Adaptive Reduced-Order Observer for Sensorless Vector Control of Doubly Fed Induction Generator-Based Variable-Speed Wind Turbines”, *IEEE Transactions on Energy Conversion*, Vol. 25, No. 3, pp. 891-900, September 2010.

[102] G. D. Marques, V. Fern˜ao Pires, S´ergio Sousa and Duarte M. Sousa, “A DFIG Sensorless Rotor-Position Detector Based on a Hysteresis Controller”, *IEEE Transactions On Energy Conversion*, Vol. 26, No. 1, pp. 9-17, March 2011.

[103] Ralph Teichmann and Steffen Bernet, “A Comparison of Three-Level Converters versus Two-Level Converters for Low-Voltage Drives, Traction, and Utility Applications”, *IEEE Transactions on Industry Applications*, Vol. 41, No. 3, pp. 855-865, May/June 2005.

[104] Mika Ikonen, Ossi Laakkonen and Marko Kettunen, “Two-Level and Three-Level Converter Comparison in Wind Power Application”, Department of Electrical Engineering, Lappeenranta University of Technology, FI-53851, Lappeenranta, Finland, pp. 1-11, 2005.

[105] Mika Ikonen, Ossi Laakkonen, Marko Kettunen, “Two Level and Three Level Converter Comparison Wind Power Application”, available on line, http://www.elkraft.ntnu.no/-smola2005/Topics/15.pdf.

[106] Jih-Sheng Lai, and Fang ZhengPeng, “Multilevel Converters-A New Breed of Power Converters”, *IEEE Transactions on Industry Applications*, Vol. 32, No. 3, pp. 509-517, May/June 1996.

[107] Alejandro Calle, Joan Rocabert, Sergio Busquets-Monge, Josep Bordonau, Salvador, Alepuz and Joan Peracaula, “Three-Level Three-Phase Neutral-Point-Clamped Back-to-Back Converter Applied to a Wind Emulator”, *13th European Conference on Power Electronics and Applications*, pp. 1-10, September 2009.

[108] Mariusz Malinowski and Steffen Bernet, “Simple Control Scheme of Three-Level PWM Converter Connecting Wind Turbine with Grid”, Available on line: http://www.icrepq.com/-PONENCIAS/4.215.MARIUSZ.pdf.

[109] Mariusz Malinowski, Sebastian Stynski, Wojciech Kolomyjski and Marian P. Kazmierkowski, “Control of Three-Level PWM Converter Applied to Variable-Speed-Type Turbines”, *IEEE Transactions on Industrial Electronics*, Vol. 56, No. 1, pp. 69-77, January 2009.

[110] Gonzalo Abad, Miguel Ángel Rodríguez and Javier Poza, “Three-Level NPC Converter-Based Predictive Direct Power Control of the Doubly Fed Induction Machine at Low Constant Switching Frequency”, *IEEE Transactions on Industrial Electronics,* Vol. 55, No. 12, pp. 4417-4429, December 2008.

[111] Emilio J. Bueno, Santiago C´obreces, Francisco J. Rodr´ıguez, A´ lvaro Herna´ndez and Felipe Espinosa, “Design of a Back-to-Back NPC Converter Interface for Wind Turbines With Squirrel-Cage Induction Generator”, *IEEE Transactions on Energy Conversion*, Vol. 23, No. 3, pp. 932-945, September 2008.

[112] R. Melício, V. M. F. Mendes and J. P. S. Catalão, “Two-level and Multilevel Converters for Wind Energy Systems: A Comparative Study”, *13th Power Electronics and Motion Control Conference*, pp. 1682-1687, September 2008.

[113] F. Blaabjerg, M. Liserre and K. Ma, “Power Electronics Converters for Wind Turbine Systems”, *2011 IEEE Energy Conversion Congress and Exposition*, pp. 281-290, September 2011.

[114] O. S. Senturk, L. Helle, S. Munk-Nielsen, P. Rodriguez and R. Teodorescu, “Medium Voltage Three-Level Converters for the Grid Connection of a Multi-MW Wind Turbine,” *13th European Conference on Power Electronics and Applications*, pp. 1- 8, September 2009.

[115] Edris Pouresmaeil, Daniel Montesinos-Miracle and Oriol Gomis-Bellmunt, “Control Scheme of Three-level H-bridge Converter for Interfacing Between Renewable Energy Resources and AC Grid”, *Proceedings of the 2011-14th European Conference on Power Electronics and Applications*, pp. 1-9, September 2011.

[116] Paulson Samuel, Nalamati Chandrashekhar and Rajesh Gupta, “Wind Energy Conversion based on Seven-level Cascaded H-bridge Inverter using LabVIEW FPGA”, *2010 International Conference on Power, Control and Embedded Systems*, pp. 1-6, December 2010.

[117] Albert Alesina and Marc G. B. Venturini, “Analysis and Design of Optimum-Amplitude Nine-Switch Direct AC-AC Converters”, *IEEE Transactions on Power Electronics,* Vol. 4, Iss. 1, pp. 101-112, January 1989.

[118] Patrick W. Wheeler, José Rodríguez, Jon C. Clare, Lee Empringham and Alejandro Weinstein, “ Matrix Converters: A Technology Review “, *IEEE Transactions on Industrial Electronics,* Vol. 49, No. 2, pp. 276-288, April 2002.

[119] Roberto Cárdenas, Rubén Peña, Patrick Wheeler, Jon Clare and Greg Asher, “Control of the Reactive Power Supplied by a WECS Based on an Induction Generator Fed by a Matrix Converter”, *IEEE Transactions on Industrial Electronics,* Vol. 56, No. 2, pp. 429-438, February 2009.

[120] Roberto Cárdenas, Rubén Peña, Germán Tobar, Jon Clare, Patrick Wheeler and Greg Asher, "Stability Analysis of a Wind Energy Conversion System Based on a Doubly Fed Induction Generator Fed by a Matrix Converter", *IEEE Transactions on Industrial Electronics*, Vol. 56, No. 10, pp. 4194-4026, October 2009.

[121] L Zhang, C Watthanasarn and W. Shepherd, "Application of a Matrix Converter for the Power Control of a Variable-Speed Wind-Turbine Driving a Doubly-Fed Induction Generator", *23rd International Conference on industrial Electronics, Control and Instrumentation*, Vol. 2, pp. 906-911, November1997.

[122] S. Masoud Barakati, Mehrdad Kazerani and J. Dwight Aplevich, "Maximum Power Tracking Control for a Wind Turbine System Including a Matrix Converter", *IEEE Transactions on Energy Conversion*, Vol. 24, No. 3, pp. 705-713, September 2009.

[123] Majid Pahlevaninezhad, Alireza Safaee, Suzan Eren, Alireza Bakhshai and Praveen Jain, "Adaptive Nonlinear Maximum Power Point Tracker for a WECS Based on Permanent Magnet Synchronous Generator Fed by a Matrix Converter", *IEEE Energy Conversion Congress and Exposition*, pp. 2578-2583, September 2009.

[124] J. Karpagam, P. S. Mayurappriyan and Jovitha Jerome, "Application of Matrix Converter in Wind Energy Conversion System Employing Synchronous Generator", *2007 IET-UK International Conference on Information and Communication Technology in Electrical Sciences*, pp. 270-276, December 2007.

[125] Stavros A. Papathanassiou, Spyros J. Kiartzis, Michael P. Papadopoulos and Antonios G. Kladas, "Wind Turbine Flicker Calculation using Neural Networks", *Wind Engineering*, Vol. 24, No. 5, pp. 317-335, September 2000.

[126] Peter vas, "Vector control of ac machines", Oxford university press, 1990.

[127] Nabeel A. O. Demerdash, "Advance Electric Machines and Drives", class notes for EECE 6220, Department of Electrical and Computer Engineer, Marquette University, Chapter 5, pp. 1-63, 2012.

[128] Xiaoxu Fan, Yuegang Lv, Yan Bai and Daping Xu. "Hybrid System Modeling and Analysis for Power Grid Side Converter Modulated by SVPWM Technology of the Double-fed Induction Wind Power Generator", *Fourth International Conference on Natural Computation*, pp. 143-148, October 2008.

[129] Xing Zhang, "Study on the PWM Rectifier and It's Control Strategies", Hefei University of Technology, Ph.D. dissertation, 2003.

[130] Wei Qiao, "Dynamic Modeling and Control of Doubly Fed Induction Generators Driven by Wind Turbines", *Power Systems Conference and Exposition*, pp. 1-8, March 2009.

[131] Juan W. Dixon and Boon-Teck Ooi, "Indirect Current Control of a Unity Power Factor sinusoidal Current Boost Type Three-phase Rectifier", *IEEE Transactions on Industrial Electronics*, Vol. 35, No. 4, pp. 508-515, November 1988.

[132] Jianzhong Zhang, Ming Cheng, Zhe Chen and Xiaofan Fu, “Pitch Angle Control for Variable Speed Wind Turbines”, *Third International Conference on Electric Utility Deregulation and Restructuring and Power Technologies*, pp. 2691-2696, April 2008.

[133] H. Pinheiro, F. Botterbn, C. Rech, L. Schuch, R. F. Camargo, H. L. Hey, H. A. Griindling and J. R. Pinheiro, “Space Vector Modulation for Voltage-Source Inverters: A Unified Approach”, *IEEE 2002 28th Annual Conference of the Industrial Electronics Society*, Vol. 1, pp. 23 - 29, November 2002.

[134] A. Nabae, I. Takahashi and H. Akagi, “A new neutral-point clamped PWM inverter”, *IEEE Transactions on Industry Applications*, Vol. IA-17, No. 5, pp. 518-523, September/October 1981.

[135] Ramón C. Portillo, MaÁngeles Martín Prats, José I. León, Juan Antonio Sánchez, Juan M. Carrasco, Eduardo Galván and Leopoldo Garcia Franquelo, “Modeling Strategy for Back-to-Back Three-Level Converters Applied to High-Power Wind Turbines, *IEEE Transactions on Industrial Electronics*, Vol. 53, No. 5, pp. 1483-1491, October 2006.

[136] Nikola Celanovic and Dushan Boroyevich, “A Comprehensive Study of Neutral-Point Voltage Balancing Problem in Three-Level Neutral-Point-Clamped Voltage Source PWM Inverters”, *IEEE Transactions on Power Electronics*, Vol. 15, No. 2, pp. 242-249, March 2000.

[137] Andreas Nordvall, “Multilevel Inverter Topology Survey”, Chalmers University of Technology, Master Thesis, Sweden, 2011.

[138] Keliang Zhou and Danwei Wang, “Relationship between Space-Vector Modulation and Three-Phase Carrier-Based PWM: A Comprehensive Analysis”, *IEEE Transactions on Industrial Electronics*, Vol. 49, No. 1, pp. 186-196, February 2002.

[139] H. W. Van der Broeck, H. C. Skudelny and G. V. Stanke, “Analysis and Realization of a Pulse-width Modulator Based on Voltage Space Vectors”, *IEEE Transactions on Industry Applications*, Vol. 24. No. 1, pp. 142-150, January/February 1988.

[140] K. Vinoth Kumar, Prawin Angel Michael, Joseph P. John and Dr. S. Suresh Kumar, “Simulation and Comparison of SPWM and SVPWM Control for Three Phase Inverter”, *ARPN Journal of Engineering and Applied Sciences*, Vol. 5, No. 7, pp. 61-74, July 2010.

[141] Atif Iqbal, Adoum Lamine, Imtiaz Ashra and Mohibullah, “MATLAB/SIMULINK Model of Space Vector PWM for Three-Phase Voltage Source Inverter”, *Proceedings of the 41st International Universities Power Engineering Conference*, Vol. 3, pp. 1096-1100, September 2006.

[142] Dorin O. Neacsu, “Space Vector Modulation - An Introduction”, *27th Annual Conference of the IEEE Industrial Electronics Society*, pp. 1583-1592, 2001.

[143] José Rodríguez, Jih-Sheng Lai and Fangzheng Peng, “Multilevel Inverters: A Survey of Topologies, Controls, and Applications”, *IEEE Transactions on Industrial Electronics*, Vol. 49, No. 4, pp. 724-738, August 2002.

[144] Jose Rodriguez, Steffen Bernet, Peter K. Steimerand and Ignacio E. Lizama, “A Survey on Neutral-Point-Clamped Inverters”, *IEEE Transactions on Industrial Electronics*, Vol. 57, No. 7, pp. 2219-2230, July 2010.

[145] Abd Almula G. M. Gebreel, “Simulation and Implementation of Two Level and Three-Level Inverters by Matlab and Rt-Lab”, Ohio State University, Master Thesis, 2011

[146] Behzad Vafakhah, “Multilevel Space Vector PWM for Multilevel Coupled Inductor Inverters”, University of Alberta, Ph.D. dissertation, February 2010

[147] Zhang Yingchao, Zhao Zhengming, Zhang Yongchang, Lu Ting and Yuan Liqiang, “The Virtual Flux Oriented Control of Three-Level Neutral Point Clamped PWM Rectifier”, *Proceeding of International Conference on Electrical Machines and Systems*, Seoul, Korea, pp. 22-27, October 2007

[148] Chunyuan Bian, Chenglong Shi, Chonghui Song and Anna Wang, “Study of the Control System of Three-level PWM Rectifier Based on Virtual Flux Oriented”, *2011 International Conference on Intelligent Human-Machine Systems and Cybernetics (IHMSC)*, Vol. 2, pp. 53-56, August 2011.

[149] F. Blaabjerg, Z. Chen, R. Teodorescu, and F. Iov, “Power electronics in wind turbine systems”, *CES/IEEE 5th International Power Electronics and Motion Control Conference*, Vol. 1, pp. 1-11, 2006.

[150] Yao Duan and Ronald G. Harley, “Present and Future Trends in Wind Turbine Generator Designs”, *IEEE Power Electronics and Machines in Wind Applications*, pp. 1-6, 2009.

[151] Lars Helle, Osman S. Senturk, and Remus Teodorescu, “Special Tests for the Power Electronic Converters of Wind Turbine Generators”, *2011 IEEE Power and Energy Society General Meeting*, pp. 1-4, 2011.